

# Charge Dynamics in Organic Photovoltaics: Effects of Morphology on Formation, Separation and Recombination.

Inaugural dissertation  
of the Faculty of Science,  
University of Bern

presented by  
Gareth John Moore  
from South Africa

Supervisor of the doctoral thesis:  
Prof. Dr. Natalie Banerji

Department of Chemistry, Biochemistry and Pharmaceutical Sciences



This work is licensed under a Creative Commons Attribution-NonCommercial-NoDerivatives 4.0 International License

<https://creativecommons.org/licenses/by-nc-nd/4.0/>

# Charge Dynamics in Organic Photovoltaics: Effects of Morphology on Formation, Separation and Recombination.

Inaugural dissertation  
of the Faculty of Science,  
University of Bern

presented by  
Gareth John Moore  
from South Africa

Supervisor of the doctoral thesis:  
Prof. Dr. Natalie Banerji

Accepted by the Faculty of Science.

Bern, 18.02.2022

The Dean  
Prof. Dr. Zoltan Balogh







# Table of Contents

<b>1</b>	<b><i>Introduction .....</i></b>	<b><i>1</i></b>
1.1.	OPV as a usable technology.....	1
1.2.	Outline of the thesis.....	2
<b>2</b>	<b><i>Fundamental Background on Organic Photovoltaics .....</i></b>	<b><i>3</i></b>
2.1.	Working Principles of OPVs .....	4
2.1.1.	Step 1 – Exciton Formation .....	5
2.1.2.	Step 2 – Exciton Diffusion .....	5
2.1.3.	Step 3 – Exciton Dissociation and CT state formation .....	5
2.1.4.	Step 4 – CT state Separation or Recombination .....	5
2.1.5.	Step 5 – Charge Transport and Collection .....	6
2.2.	Photo-conversion Efficiency of Organic Solar Cells .....	7
2.2.1.	Short Circuit Current - $J_{sc}$ .....	8
2.2.2.	Open Circuit Voltage - $V_{oc}$ .....	9
2.2.3.	Fill Factor – FF .....	10
2.3.	Morphology.....	11
2.3.1.	Different Morphologies.....	11
2.3.2.	Different Morphologies as Model Systems.....	13
2.4.	Introduction to Machine Learning in OPVs.....	14
<b>3</b>	<b><i>Methods .....</i></b>	<b><i>21</i></b>
3.1.	Steady State Absorption Spectroscopy .....	22
3.2.	Transient Absorption Spectroscopy (TA) .....	23
3.2.1.	TA .....	23
3.2.1.	Signal processing and noise reduction.....	26
3.2.2.	TA spectral features .....	29
3.3.	TA Spectroscopy Data Analysis .....	31
3.3.1.	Multivariate Curve Resolution – Alternating Least Squares .....	31
3.3.2.	Kinetic Modelling .....	35
3.4.	Machine Learning .....	36
3.4.1.	Neural Networks (NN).....	37

3.4.2.	Convolutional Neural Networks (CNN)	39
<b>4</b>	<b><i>Ultrafast Charge Dynamics in Dilute-Donor versus Intermixed TAPC:C<sub>60</sub> Organic Solar Cell Blends</i></b>	<b>43</b>
4.1.	Introduction	45
4.2.	Results and Discussion	46
4.3.	Conclusion	56
<b>5</b>	<b><i>Following Charge Transfer State Formation and Recombination in Dilute Donor Organic Photovoltaics</i></b>	<b>61</b>
4.4.	Introduction	63
4.5.	Results and Discussion	64
4.5.1.	Transient Absorption Spectroscopy	64
4.5.2.	Theoretical Investigation of Charge Species	67
4.5.3.	Kinetic Modelling	70
4.5.4.	Reconstruction of the Transient Absorption Spectra	73
4.6.	Conclusion	75
<b>6</b>	<b><i>Pairing Non-Fullerene Acceptors with the Right Polymer: Impact of Morphology and Short-Range Mobility on Charge Generation</i></b>	<b>79</b>
6.1	Introduction	81
6.1.	Results and Discussion	83
6.2.	Conclusion	95
<b>7</b>	<b><i>Deep transfer leaning: a fast and accurate tool to predict energy levels of donor molecules for organic photovoltaics</i></b>	<b>99</b>
4.7.	Introduction	100
4.8.	Methodology	102
4.8.1.	The Deep Learning Model	102
4.8.2.	Datasets and Training	103
4.8.3.	Testing and External Validation	104
4.8.4.	The 'use-case' Dataset	105
4.9.	Results and Discussion	106
4.9.1.	Phase I	106



4.9.2.	Phase II .....	106
4.9.3.	Comparison with DFT from HOPV15 Dataset .....	109
4.9.4.	External Validation: Comparison with DFT from Literature ('use-case' Dataset).....	110
<b>4.10.</b>	<b>Conclusion .....</b>	<b>114</b>
<b>8</b>	<b><i>General Conclusions and Perspective .....</i></b>	<b><i>119</i></b>
<b>9</b>	<b><i>Appendix.....</i></b>	<b><i>123</i></b>
<b>10</b>	<b><i>Acknowledgements .....</i></b>	<b><i>163</i></b>



# 1 Introduction

## 1.1. OPV as a usable technology

With an ever-growing energy demand, the reliance on finite fossil fuel reserves is simply not sustainable for the future of humanity. Along with being limited in quantity, the burning of fossil fuels is having a direct negative effect on the earth's climate. It is clear that the development of both renewable and 'clean' methods of generating energy is beneficial for humanity in general. Most renewable energy technologies consist of capturing excess energy from naturally occurring phenomena such as wind, tidal, geothermal, and hydro. Another source of energy is radiation from the sun which bombards the earth with around 150'000 terawatts of energy, which is renewable within its roughly 5-billion-year remaining lifespan. In order to capture and use this energy it is transformed into electricity using photovoltaics (PV). Within the broad range of semi-conductor materials used in PV, crystalline Silicon dominate the market with solar to electrical energy efficiencies in the low 20 % range. Other inorganic materials such as Cadmium Telluride, hybrid organic-inorganic perovskites and organic photovoltaics (OPV) are also used.

OPVs garner special interest because of their mechanical properties. OPVs are generally light weight, flexible and semi-transparent, and although not as efficient as inorganic PV these properties allow them to be implemented in places where it is not possible for other PV types. Additionally, OPV materials are mainly solution processable, allowing for large area, high throughput roll-to-roll printing. Overall the cost of producing an OPV cell is substantially lower than its inorganic counterparts, making it potentially an economically attractive prospect. However, the challenges of efficiency and stability remain. Even though relatively high efficiencies (up to 18%) can be achieved under laboratory conditions, the production of large scale, stable arrays remain difficult. Finding organic semi-conducting materials which can be easily processed into stable high efficiency solar cells still requires an improvement in the understanding of the fundamental workings of the complex light to current conversion process.

To this end we apply state of the art spectroscopic and electrical characterisation techniques on specially designed OPV active layers. To fully understand the effects of changing the parameters of the OPV active layer we follow the energy conversion process with an ultrafast time resolution allowing each subtle effect to be observed. This results in a better understanding of what properties are desirable or undesirable when choosing new organic semiconductors to be used in future organic solar cells. On top of this we take advantage of the growing molecular

property datasets to train modern machine learning models capable of predicting a molecules properties before the decision is made to synthesise the molecule for testing. The further the techniques for measuring and to understanding of OPV materials come, the more efficient the improvement and the better the viability of this technology becomes.

## 1.2. Outline of the thesis

An introduction of the fundamentals of OPV is given in chapter 2 where we go through the main steps in light to current conversion as well as the main parameters governing the efficiency of the organic solar cell. Chapter 3 then goes through the experimental techniques used in this work, with a particular emphasis on the data processing and analysis along with a discussion of the basic principles of the machine learning techniques used. Chapters 4 and 5 follow on from previous work done on neat fullerene films where we follow the charge formation and recombination processes in dilute-donor TAPC:fullerene blends in chapter 4 and dilute-donor  $\alpha$ 6T:fullerene blends in chapter 5. Chapter 6 compares three polymers (J61, P3HT and PCDTBT) in blends with a non-fullerene acceptor molecule where the effects of blend morphology on photo-physical processes is directly tackled. Lastly, chapter 7 describes a project where a machine learning model was trained to predict properties of potential OPV materials.

# 2 Fundamental Background on Organic Photovoltaics

## Foreword

This chapter goes through the basic working principles of organic photovoltaics and gives a general background for understanding the content of this thesis.

Section 2.1 goes through the basic steps in converting absorbed light into extractable photocurrent. Section 2.2 discusses how the efficiency of light-to-current conversion is quantified and what factors determine that efficiency. We then look at how the morphology of the active layer affects the efficiency of each step of the photovoltaic process, in section 2.3 and how the different morphologies can be used to study individual steps more closely. Section 2.4 briefly summarises the work directly preceding the studies presented in the upcoming chapters and section 2.5 discusses the use of machine learning in optimising and discovering new materials for OPVs.

## 2.1. Working Principles of OPVs

The function of every photovoltaic device is the conversion of light into extractable charge carriers (photocurrent). This is usually done using an inorganic semiconductor wherein the absorption of light promotes an electron from the valence to conduction band, where it is free to be extracted. This is less trivial with organic semiconductors where, due to their low dielectric constant, absorbed light results in a strongly bound electron/hole pair called an exciton. The binding energy of the exciton is much higher than the thermal energy at room temperature and so a more complex charge separation mechanisms are required. By using a heterojunction of electron donating and electron accepting materials, the exciton can be split. The separated electron and hole are then free to be extracted as photocurrent at the electrodes.

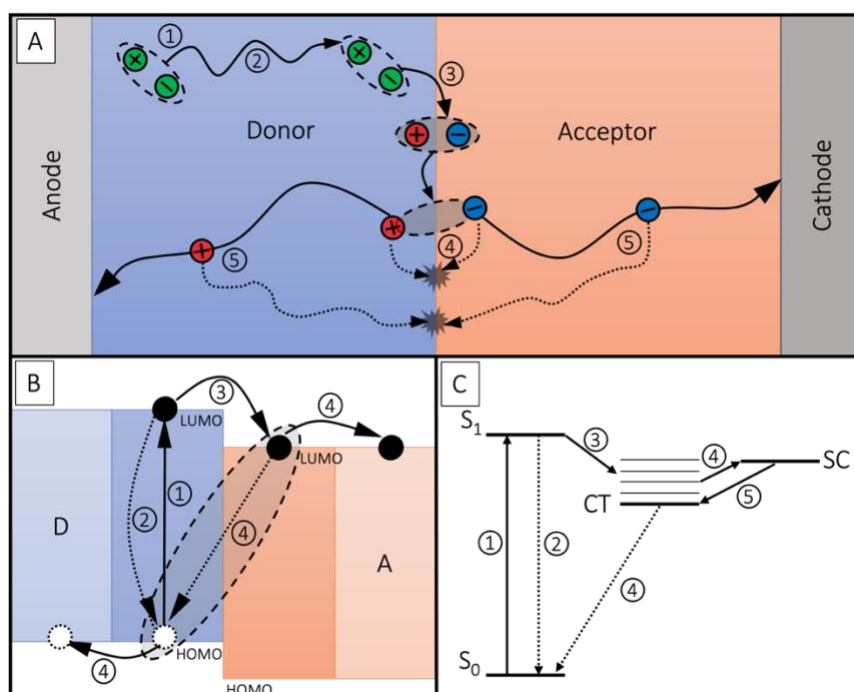


Figure 2.1-1 Illustration of the working principles of an OPV device from three perspectives: (A) Follows the process in a micro view of the interface, (B) shows the process at the donor/acceptor interface with respect to their adjacent HOMO/LUMO levels, (C) shows a Jablonski diagram which follows the energetic state of the charge carrier from absorption to separation. The numbered steps are 1) exciton formation, 2) exciton diffusion and recombination, 3) exciton dissociation and CT state formation, 4) CT state separation and geminate recombination, 5) Charge transport, non-geminate recombination, and collection.

This process is best described by splitting it into steps (discussed below) and can be illustrated from three different points of view (Figure 2-1). Figure 2-1 A shows the process in terms of the physical space and shows how the exciton and charge carriers move within a simplified active layer. Figure 2-1 B illustrates the charge transfer process at the interface of the donor and acceptor materials in terms of their relative orbital energy levels. Figure 2-1 C shows a

Jablonski diagram which follows the energy state of the charge carrier, from exciton to separation.

The charge generation can be summed up by the following steps with a note that the electron transfer and not the hole transfer process is described:

#### 2.1.1. Step 1 – Exciton Formation

The energy of an incident photon is absorbed by the donor material exciting an electron from the highest occupied molecular orbital (HOMO) to the lowest unoccupied molecular orbital (LUMO) (Figure 2-1 B, or  $S_0 \rightarrow S_1$  Figure 2-1 C). The excitation can be thought of as a neutral quasi-particle called a Frenkel exciton, when localised to a single molecule, or charge transfer (CT) exciton if delocalised over several molecules.<sup>1</sup>

#### 2.1.2. Step 2 – Exciton Diffusion

Excitons then either diffuse to a donor/acceptor interface (Figure 2-1 A) or relax back to the ground state (Figure 2-1 B,C). The excitons move (diffuse) from one molecule to the next by either Förster resonant energy transfer (FRET) or Dexter transfer.<sup>2, 3</sup> With FRET, the excited molecule transfers its energy to an adjacent molecule via Coulomb interactions of their transition dipole moments, which relies strongly on the relative orientations of the transition dipoles of both molecules. Dexter transfer occurs via a simultaneous electron and hole transfer, from the excited molecule to the adjacent molecule. Dexter transfer relies on a wave function overlap between the neighbouring molecules, requiring strong electronic coupling, suggesting FRET to be the dominant mechanism. The diffusion length then quantifies the average distance that an exciton diffuses before recombining:  $L_d = \sqrt{D\tau}$  with  $D$  the diffusivity and  $\tau$  the exciton lifetime.<sup>4</sup>

#### 2.1.3. Step 3 – Exciton Dissociation and CT state formation

Once an interface is reached by the exciton, the electron is transferred from the donor to acceptor (Figure 2-1 B). This forms a CT state (Figure 2-1 C) where the electron and hole are coulombically bound and remain in a state at the interface (Figure 2-1 A). The mechanisms governing the rate of dissociation have been hotly debated with the previous high driving force (LUMO-LUMO offset) requirement being found to not always apply.<sup>5</sup>

#### 2.1.4. Step 4 – CT state Separation or Recombination

The formed CT states, being on two different molecules, are more specially separated and have a lower binding energy than the exciton, making charge separation more realistic. The CT state

either recombines (geminate recombination) or overcomes the coulombic barrier and separates into free charges. The rate or probability of the CT state geminately recombining has been shown to related to the CT state energy ( $E_{CT}$ ) with higher lying CT states having less non-radiative recombination.<sup>6</sup> The separation of bound CT state charges is linked to the morphology and energetic landscape of the materials at and around the interface. Morphologies that facilitate CT state delocalisation have been shown to decrease its binding energy and therefore increase its chances of separating.<sup>7-11</sup>

#### 2.1.5. Step 5 – Charge Transport and Collection

Charge transport and collection describes how the free charge carriers migrate from the site of CT separation to the electrodes where they are extracted into the external circuit. This relies on percolated pathways between the interface and the electrode, use of electron and hole transporting layers, and good charge carrier mobilities. The separated charges can also undergo non-geminate recombination if they reencounter one-another. Non-geminate recombination is usually of two kinds: Langavim type bimolecular recombination, or monomolecular Shockley-Read-Hall type trap-based recombination.<sup>12-14</sup> The rate of bimolecular non-geminate recombination is dependent on the mobilities of both the electrons and holes, suggesting that the chance of charge carriers encountering each other is increased if they are highly mobile. This again creates a competition between the rate of extraction and recombination which can be optimised in the morphological design of the solar cell.



## 2.2. Photo-conversion Efficiency of Organic Solar Cells

The photo-conversion efficiency (PCE) is measured using the J-V characteristics of the illuminated solar cell (Figure 2-2).

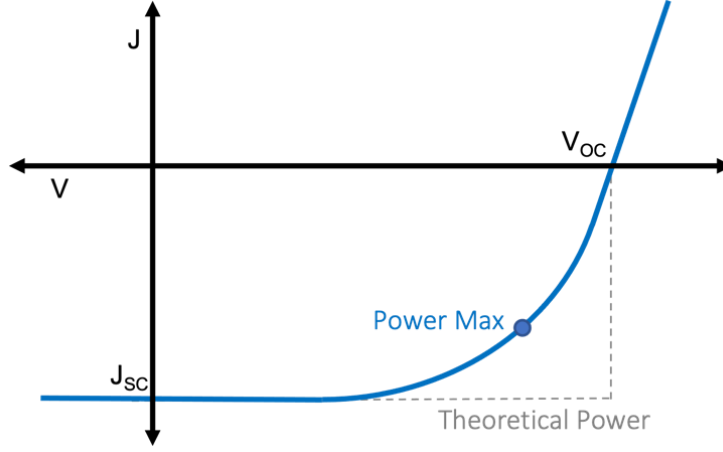


Figure 2.2-1 Theoretical J-V curve of an illuminated organic solar cell showing the short circuit photocurrent ( $J_{sc}$ ), the open circuit voltage ( $V_{oc}$ ), the maximum achieved power and the theoretically achievable maximum power.

The PCE of a device is determined by its short circuit current ( $J_{sc}$ ), its open circuit voltage ( $V_{oc}$ ) and its fill-factor ( $FF$ ). The  $J_{sc}$  is the photo-current generated when no external bias is applied. The  $V_{oc}$  is the externally applied voltage at which no current flows, or the maximum voltage that can be generated by the solar cell.  $FF$  is ratio between the realised maximum power and the theoretical maximum power. The PCE then quantifies how much of the incident radiant power is converted into realised electrical power.

$$\begin{aligned} PCE &= \frac{P_{max}}{P_{in}} \\ &= \frac{J_{sc} \times V_{oc} \times FF}{P_{in}} \end{aligned}$$

( 2-1)

$P_{in}$  is the incident radiant power. The  $J_{sc}$  can be thought of as the number of photons converted into extracted charge carriers, and so is affected by the yield of each step from absorption to extraction.  $V_{oc}$  is related to the potential energy of the extracted charges and so is related to the energy of the absorbed photon, less the energy losses at each step in the photo-conversion process. The  $FF$  is the squareness of the J-V curve and is related to the field dependence of charge generation, extraction and recombination.

### 2.2.1. Short Circuit Current - $J_{sc}$

The  $J_{sc}$  is directly related to the integral of the incident solar spectrum, at each wavelength ( $SolarSpectrum(\lambda)$ ), multiplied by the external quantum efficiency ( $EQE(\lambda)$ ), shown in Equation (2-2). The EQE is the wavelength dependent photon to extracted charge conversion efficiency and can be thought of as the probability that a photon of a specific energy is converted into an extracted charge carrier.

$$J_{sc} = q \int SolarSpectrum(\lambda) \times EQE(\lambda) d\lambda \quad (2-2)$$

The EQE of the OPV device is a combination of the efficiency of each step discussed in section 2.1 in terms of number of charges:

$$EQE = \eta_{abs} \times \eta_{diff} \times \eta_{diss} \times \eta_{sep} \times \eta_{tran} \quad (2-3)$$

The efficiency of photon absorption or exciton formation ( $\eta_{abs}$ ) depends on how well the material absorbs the light (absorption coefficient) and the spectral overlap between the incoming solar radiation and the absorption spectrum of the material. This can also be improved by having active layers thick enough to absorb all incident light and materials with broad absorption spectra. The efficiency of the exciton diffusion step ( $\eta_{diff}$ ) results from the competition between exciton relaxation and exciton quenching at a donor/acceptor interface. This is mainly determined by the difference between the average diffusion length and the average distance between excitation site and donor/acceptor interface, which can be improved with the appropriate morphology. The efficiency of exciton transfer ( $\eta_{diss}$ ) is generally very high and occurs in well under a picosecond, but is related to driving force (Marcus formalism).<sup>5</sup> The CT state separation efficiency ( $\eta_{sep}$ ) is again a competition between the CT state recombination (geminate recombination) rate and the rate of separation and is a complex function of the energetics and morphology at the interface. The CT state binding energy (energy barrier to CT separation) is given by:

$$E_b = \frac{q}{4\pi\epsilon_r\epsilon_0 r} \quad (2-4)$$

Where  $q$  is the elemental charge,  $r$  the distance between electron and hole and  $\epsilon_r\epsilon_0$  describes the local dielectric environment. Morphologies where the dielectric constant ( $\epsilon_r$ ) and electron/hole separation ( $r$ , CT state delocalisation) can be increased lower the CT state binding energy and increase the probability of CT state separation.<sup>7-11</sup> In addition, entropic effects can lower the free energy of CT state separation. The competing geminate recombination is one of the largest loss mechanisms in OPV devices. Lastly the charge transport and collection efficiency ( $\eta_{\text{tran}}$ ) is a competition between non-geminate recombination and extraction. Both collection efficiency and non-geminate recombination can be improved by morphology and device optimisation.

### 2.2.2. Open Circuit Voltage - $V_{OC}$

While  $J_{SC}$  relates to the number of photons converted to charges,  $V_{OC}$  is related to the amount of energy conserved in the charge carriers from photon absorption to extraction.

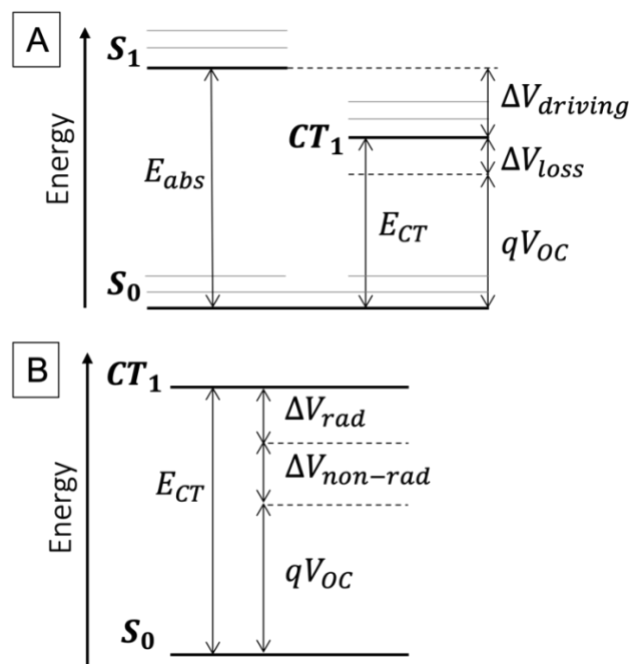


Figure 2.2-2 Illustration of the energy losses between the energy of absorbed light and the  $V_{OC}$  in panel (A) showing energy loss from driving force ( $\Delta V_{driving}$ ) and recombination losses ( $\Delta V_{loss}$ ). B shows a more complex illustration of energy losses from the CT state separating both radiative ( $\Delta V_{rad}$ ) and non-radiative ( $\Delta V_{non-rad}$ ) losses.

As illustrated in Figure 2-3 A, light is absorbed, and an electron is promoted from the ground ( $S_0$ ) to excited state ( $S_1$ ). The exciton gains potential energy relative to the wavelength/frequency of absorbed light ( $E_{abs} = h\nu$ ). The first energy loss occurs during exciton dissociation, where the electron is transferred from the donor to the acceptor (driving

force,  $\Delta V_{driving} = E_{D,LUMO} - E_{A,LUMO} = S_1 - CT$ ) to form the bound CT state. This makes the  $E_{CT}$  the first upper limit for the  $V_{OC}$ . Additional energy is lost at the interface caused by recombination processes ( $\Delta V_{loss}$ ).

These interfacial recombination losses can be further broken down into intrinsic radiative and potentially avoidable non-radiative losses ( $\Delta V_{rad}$  and  $\Delta V_{non-rad}$ , Figure 2-3 B). The radiative losses are unavoidable and depend on the coupling between the CT state and ground state. The non-radiative losses are connected to the probability that the CT state electron will recombine by tunnelling to a high vibrational level of the ground state.

The  $V_{OC}$  can then be quantified by Equation ( 2-5):

$$\begin{aligned} qV_{OC} &= E_{abs} - \Delta V_{driving} - \Delta V_{rad} - \Delta V_{non-rad} \\ &= E_{CT} - \Delta V_{rad} - \Delta V_{non-rad} \end{aligned} \quad ( 2-5)$$

All three of these general loss categories (driving force, radiative losses and non-radiative losses) depend on a wide range of parameters mainly to do with the energetics of the donor/acceptor interface. The most general effect on  $V_{OC}$  seems to be the  $E_{CT}$ , with high lying CT states resulting in lower voltage loss in charge transfer, as well as lower non-radiative recombination losses.<sup>15-18</sup>

### 2.2.3. Fill Factor – FF

The FF shows the “squareness” of the J-V curve and so the dependence of the photocurrent on the applied electric field. Excitons are effectively neutral species, and so have little field dependent splitting. FF, therefore, is mainly related to the competition between free charge extraction and charge recombination.<sup>19, 20</sup> FF is affected by the layer thickness, charge transport (including charge mobility and extraction pathways) and the rate of non-geminate charge recombination.

## 2.3. Morphology

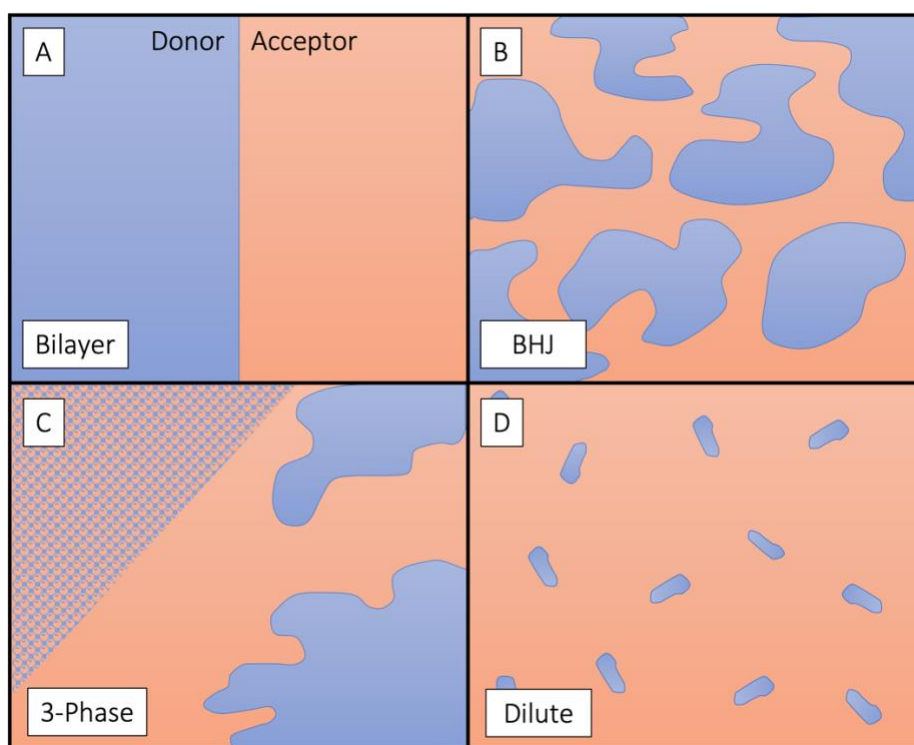


Figure 2.3-1 Illustration of donor/acceptor heterojunction morphologies. Panel A shows a planar heterojunction (bilayer) where donor and acceptor materials are completely separated. Panel B shows a bulk heterojunction (BHJ) morphology where the donor and acceptor are blended together. Panel C shows the different mixing regimes in a BHJ where completely intermixed and phases separated regions co-exist. Panel D illustrates a dilute donor blend where the mixture consists of mainly acceptor molecules with a small amount of donor material.

The active layer of an organic solar cell, as discussed before, requires a blend of donor and acceptor molecules. The way in which these two materials are arranged (which we refer to as morphology) has a major effect on the overall performance of the solar cell at each step. Originally bilayer systems, as shown in Figure 2-4 Figure A, were employed and later bulk heterojunction (BHJ) systems (Figure 2-4 Figure B).<sup>21, 22</sup>

### 2.3.1. Different Morphologies

Bilayers have the advantage of efficient CT state separation and charge carrier extraction, due to the uninterrupted neat donor and acceptor layers, as well as a low non-geminate recombination rate because of the low donor/acceptor interfacial area. However, bilayers suffer from long required exciton diffusion distances and a photocurrent that is limited by the low donor/acceptor interfacial area. BHJs on the other hand have a high interfacial area, resulting in high photocurrent, and donor/acceptor separations on the order of exciton diffusion lengths, making exciton quenching more efficient. However, BHJs suffer from inefficient CT state

separation (high geminate charge recombination) and weaker charge extraction due to the disrupted purity of the separate donor acceptor regions. BHJs also have high non-geminate recombination chance resulting from the high interfacial area (lowering FF). Nevertheless, BHJs with parameters optimised to mitigate their negative features have resulted in the most efficient organic solar cells.

Looking more closely at the morphology of the BHJ, is it clear that the two-phase description in Figure 2-3 Figure B does not completely describe the blend.<sup>23, 24</sup> BHJs exhibit a three phase morphology in which there exist neat donor and acceptor regions (either amorphous or crystalline) as well as completely intermixed regions (Figure 2-4 C).<sup>25</sup> A combination of all three phases in the morphology often leads to the highest efficiency.<sup>26-28</sup> The phase separated and intermixed regions can be controlled by the selection of solvents, additives, thermal annealing processes and by varying the donor:acceptor ratio.<sup>29-32</sup>

Many small molecule:fullerene blends have shown optimal performance with donor: acceptor ratios of around 5:95 to 1:9, known as “dilute” blends (Figure 2-4 D). These dilute blends have shown increased  $FF$  and  $V_{OC}$  compared to more traditional blend ratios of the same materials, but with naturally decreased photocurrent due to the low fullerene absorption.<sup>33</sup> At low donor concentrations, the donor molecules are often completely isolated and surrounded by acceptor molecules, requiring no exciton diffusing if the donor is excited. The isolation of donor molecules is confirmed by a linear correlation between the amplitude of CT state signatures in sensitive EQE measurements (i.e. the concentration of CT states) and the donor concentration.<sup>34, 35</sup> The main advantage of the dilute morphology is CT state delocalisation caused by electronic coupling of the fullerenes and the increased dielectric constant in the large fullerene clusters.<sup>36, 37</sup> Delocalisation of CT states results in improved CT state separation and, because recombination occurs through the CT state, non-geminate recombination is decreased by CT states reseparating after electron/hole encounter.<sup>38</sup> The delocalisation does however decrease the  $E_{CT}$ , which can increase non-radiative recombination according to the energy gap law.<sup>6</sup> The low hole mobility can also increase the chance of free electron/hole encounter (trap-based recombination). This results in a decreased  $FF$  at dilutions lower than 5% where hole mobility decreases dramatically. Hole transport has been shown to occur via long-range hole tunnelling up to 4 nm between isolated donor molecules and the clusters in fullerene acceptors have been shown to remain relatively undisturbed in blends with less than 15 % donor.<sup>35, 36</sup> Interestingly, these dilute donor devices have been shown to work without the donor forming neat phases, which was conventionally thought to be crucial for efficient charge generation.

### 2.3.2. Different Morphologies as Model Systems

Alongside trying to find the morphology which produces the most efficient solar cells, these different morphologies can be used as model systems to study individual processes. As three-phase BHJs are relatively complex, studying the extreme morphologies in bilayers or dilute blends, allows for some of the charge generation steps to be removed so that the others can be studied more closely. When studying bilayers, for example, we have a very clearly defined interface which is analogous to the phase separated interface in BHJs. Bilayers also remove many of the non-geminate recombination effects with the unimpaired charge transport and low interfacial area. Dilute blends, on the other hand, can be used as a model system for mixed phase regions in BHJ blends, with the low concentration material not forming any clusters. Dilute blends are used to remove the effects of exciton diffusion if the low concentration material is excited and so charge transfer processes can be studied independent of diffusion losses. Dilute blends also allow for the clustering and charge transport effects of the low concentration material to be removed, so that the observed processes come only from the majority material.

## 2.4. Introduction to Machine Learning in OPVs

The performance of organic solar cells continues to increase, with efficiencies having increased from 13 % to 18 % in the four years represented by this thesis.<sup>39-42</sup> This has been driven by improvements in device architecture, processing techniques but most importantly design and discovery of new materials. Material design has been informed by design rules, for selecting optimal properties, or by large scale screening. Large scale material screening and experimental work, while crucial, are expensive and time consuming, and are a clear bottle neck in the rate of development.

Understanding systems and determining the desirable properties for materials (design rules) has allowed for quantum chemical simulations to be employed in pre-synthetic determination of the materials' potential performance. Density functional theory (DFT) based calculations have proven invaluable as a tool for both understanding processes and property predictions of materials.<sup>43-45</sup> However, DFT still remains computationally relatively expensive, with any high throughput screening requiring both compromises in the quality of the results and/or access to high performance computing infrastructure. DFT also imposes assumptions in the calculations which can result in not insignificant differences between predicted and experimentally measured material property values.

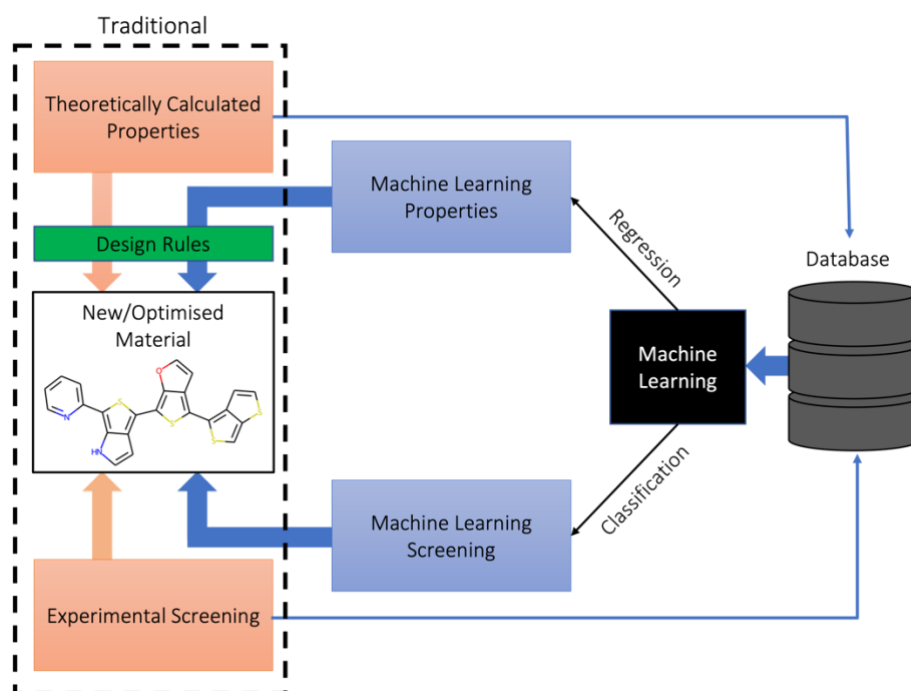


Figure 2.4-1 Illustration of traditional and machine learning (ML) based material discovery and optimisation pathways.



Many of these experimental results have been published and so many researchers are collecting this data and unifying its format into databases. This however, still required a lot of time and the quality of the databases suffers from both relatively small sizes and inconsistent experimental conditions. The improvement of DFT calculation efficiency and in computational infrastructure has made DFT based databases more reasonable in terms of creating large and consistent databases. The most widely used databases in OPVs being the Harvard Clean Energy Project (HCEP) database and the Harvard OPV (HOPV15) database.<sup>46, 47</sup> The HCEP dataset consists of 2.3 million theoretical molecules with properties calculated using DFT and the HOPV15 consists of 350 molecules with properties both measured experimentally and calculated using DFT (both datasets are described in detail in section A.4.3). These datasets are then both analysed statistically to try discovering correlations, or used as training data for machine learning (ML) models (Figure 2-5).

ML models are essentially large multi-parameter non-linear functions where the parameters can be optimised (trained) in a way that models can make predictions on incredibly complex systems, often with good generalisability and accuracy. These models require a large amount of data and allow for hidden insights and trends from the data to be revealed. ML includes a wide range of techniques which are out of the scope of this introduction.<sup>48</sup> Here, we specifically discuss supervised learning, where the input data has complete and correctly labelled features.

After the acquisition of an appropriate dataset, the second challenge is in choosing an appropriate molecular descriptor. As a ML model is purely mathematical, the input needs to be in numerical form. Molecules can be represented in a number of different ways including: fingerprints, molecular blocks with the 3D coordinates of atoms, image representations of molecules and graph networks, to name only a few.<sup>49-52</sup> Each representation has different levels of complexity and extenuates different features of the molecule. ML for OPV materials then generally falls into two categories: regression or classification (Figure 2-5). Regression models are used to numerically predict properties of a material which can then be used to determine the usefulness of the material for the application. These properties most commonly include frontier energy levels, mobility or OPV device efficiency, directly.<sup>53-56</sup> Classification models are generally used to separate out poorly and highly performing materials, usually according to their expected device efficiency.<sup>51, 57, 58</sup> This can be useful in large scale screening for determining the materials worth investigating further.

ML models have two main advantages: i.) once trained they require very little computational recourses and so are extremely fast, ii.) they are able to learn from both theoretical and

experimental data, taking advantage of both the volume of theoretical data and the relevance of the experiments. These models can also be trained continuously and so can be continually improved as new data is acquired. On the other hand, ML models represent the generality and accuracy of the training data and so are always limited by the quality of the training data. ML models can only make reliable predictions of data that is of the same type or in the same distribution as the training data. Lastly, ML models generally have no scientific input or chemical knowledge hard coded to help with predictions, the model simply finds patterns in the data. This can be a double-edged sword as, on the one hand the model becomes a black box where little scientific insights can be gained about how predictions are made, and on the other hand it becomes a tool that can learn features or trends not yet understood or explained scientifically.

## References

1. Causa', M.; Ramirez, I.; Martinez Hardigree, J. F.; Riede, M.; Banerji, N., Femtosecond Dynamics of Photoexcited C60 Films. *The Journal of Physical Chemistry Letters* **2018**, 9 (8), 1885-1892.
2. Medintz, I. L.; Hildebrandt, N., *FRET-Förster resonance energy transfer: from theory to applications*. John Wiley & Sons: 2013.
3. Lin, S.-H.; Xiao, W.; Dietz, W., Generalized Förster-Dexter theory of photoinduced intramolecular energy transfer. *Physical Review E* **1993**, 47 (5), 3698.
4. Burlingame, Q.; Coburn, C.; Che, X.; Panda, A.; Qu, Y.; Forrest, S. R., Centimetre-scale electron diffusion in photoactive organic heterostructures. *Nature* **2018**, 554 (7690), 77-80.
5. Zhong, Y.; Causa', M.; Moore, G. J.; Krauspe, P.; Xiao, B.; Günther, F.; Kublitski, J.; Shivhare, R.; Benduhn, J.; BarOr, E.; Mukherjee, S.; Yallum, K. M.; Réhault, J.; Mannsfeld, S. C. B.; Neher, D.; Richter, L. J.; DeLongchamp, D. M.; Ortman, F.; Vandewal, K.; Zhou, E.; Banerji, N., Sub-picosecond charge-transfer at near-zero driving force in polymer:non-fullerene acceptor blends and bilayers. *Nature Communications* **2020**, 11 (1), 833.
6. Collado-Fregoso, E.; Pugliese, S. N.; Wojcik, M.; Benduhn, J.; Bar-Or, E.; Perdigón Toro, L.; Hörmann, U.; Spoltore, D.; Vandewal, K.; Hodgkiss, J. M.; Neher, D., Energy-Gap Law for Photocurrent Generation in Fullerene-Based Organic Solar Cells: The Case of Low-Donor-Content Blends. *Journal of the American Chemical Society* **2019**, 141 (6), 2329-2341.
7. Zusan, A.; Vandewal, K.; Allendorf, B.; Hansen, N. H.; Pflaum, J.; Salleo, A.; Dyakonov, V.; Deibel, C., The Crucial Influence of Fullerene Phases on Photogeneration in Organic Bulk Heterojunction Solar Cells. *Advanced Energy Materials* **2014**, 4 (17), 1400922.
8. Barker, A. J.; Chen, K.; Hodgkiss, J. M., Distance Distributions of Photogenerated Charge Pairs in Organic Photovoltaic Cells. *Journal of the American Chemical Society* **2014**, 136 (34), 12018-12026.
9. Schwarz, C.; Bässler, H.; Bauer, I.; Koenen, J.-M.; Preis, E.; Scherf, U.; Köhler, A., Does Conjugation Help Exciton Dissociation? A Study on Poly(p-phenylene)s in Planar Heterojunctions with C60 or TNF. *Advanced Materials* **2012**, 24 (7), 922-925.
10. Athanasopoulos, S.; Tscheuschner, S.; Bässler, H.; Köhler, A., Efficient Charge Separation of Cold Charge-Transfer States in Organic Solar Cells Through Incoherent Hopping. *The Journal of Physical Chemistry Letters* **2017**, 8 (9), 2093-2098.
11. Pace, N. A.; Reid, O. G.; Rumbles, G., Delocalization Drives Free Charge Generation in Conjugated Polymer Films. *ACS Energy Letters* **2018**, 3 (3), 735-741.
12. Shockley, W.; Read Jr, W., Statistics of the recombinations of holes and electrons. *Physical review* **1952**, 87 (5), 835.
13. Hall, R. N., Electron-hole recombination in germanium. *Physical review* **1952**, 87 (2), 387.
14. Langevin, P., Recombinaison et mobilités des ions dans les gaz. *Ann. Chim. Phys* **1903**, 28 (433), 122.
15. Benduhn, J.; Tvingstedt, K.; Piersimoni, F.; Ullbrich, S.; Fan, Y.; Tropiano, M.; McGarry, K. A.; Zeika, O.; Riede, M. K.; Douglas, C. J.; Barlow, S.; Marder, S. R.; Neher, D.; Spoltore, D.; Vandewal, K., Intrinsic non-radiative voltage losses in fullerene-based organic solar cells. *Nature Energy* **2017**, 2 (6), 17053.
16. Vandewal, K.; Tvingstedt, K.; Gadisa, A.; Inganäs, O.; Manca, J. V., Relating the open-circuit voltage to interface molecular properties of donor:acceptor bulk heterojunction solar cells. *Physical Review B* **2010**, 81 (12), 125204.

17. Vandewal, K.; Tvingstedt, K.; Gadisa, A.; Inganäs, O.; Manca, J. V., On the origin of the open-circuit voltage of polymer–fullerene solar cells. *Nature Materials* **2009**, 8 (11), 904-909.
18. Vandewal, K.; Albrecht, S.; Hoke, E. T.; Graham, K. R.; Widmer, J.; Douglas, J. D.; Schubert, M.; Mateker, W. R.; Bloking, J. T.; Burkhard, G. F.; Sellinger, A.; Fréchet, J. M. J.; Amassian, A.; Riede, M. K.; McGehee, M. D.; Neher, D.; Salbeck, A., Efficient charge generation by relaxed charge-transfer states at organic interfaces. *Nature Materials* **2014**, 13 (1), 63-68.
19. Bartsaghi, D.; Pérez, I. d. C.; Kniepert, J.; Roland, S.; Turbiez, M.; Neher, D.; Koster, L. J. A., Competition between recombination and extraction of free charges determines the fill factor of organic solar cells. *Nature Communications* **2015**, 6 (1), 7083.
20. Mauer, R.; Howard, I. A.; Laquai, F., Effect of nongeminate recombination on fill factor in polythiophene/methanofullerene organic solar cells. *The Journal of Physical Chemistry Letters* **2010**, 1 (24), 3500-3505.
21. Tang, C. W., Two-layer organic photovoltaic cell. *Applied Physics Letters* **1986**, 48 (2), 183-185.
22. Yu, G.; Gao, J.; Hummelen, J. C.; Wudl, F.; Heeger, A. J., Polymer photovoltaic cells: enhanced efficiencies via a network of internal donor-acceptor heterojunctions. *Science (Washington, DC, U. S.)* **1995**, 270 (5243), 1789-1791.
23. Keivanidis, P. E.; Clarke, T. M.; Lilliu, S.; Agostinelli, T.; Macdonald, J. E.; Durrant, J. R.; Bradley, D. D. C.; Nelson, J., Dependence of Charge Separation Efficiency on Film Microstructure in Poly(3-hexylthiophene-2,5-diyl):[6,6]-Phenyl-C61 Butyric Acid Methyl Ester Blend Films. *The Journal of Physical Chemistry Letters* **2010**, 1 (4), 734-738.
24. Burke, T. M.; Sweetnam, S.; Vandewal, K.; McGehee, M. D., Beyond Langevin Recombination: How Equilibrium Between Free Carriers and Charge Transfer States Determines the Open-Circuit Voltage of Organic Solar Cells. *Advanced Energy Materials* **2015**, 5 (11), 1500123.
25. Westacott, P.; Tumbleston, J. R.; Shoaee, S.; Fearn, S.; Bannock, J. H.; Gilchrist, J. B.; Heutz, S.; Demello, J.; Heeney, M.; Ade, H.; Durrant, J.; McPhail, D. S.; Stingelin, N., On the role of intermixed phases in organic photovoltaic blends. *Energy & Environmental Science* **2013**, 6 (9), 2756.
26. Bartelt, J. A.; Beiley, Z. M.; Hoke, E. T.; Mateker, W. R.; Douglas, J. D.; Collins, B. A.; Tumbleston, J. R.; Graham, K. R.; Amassian, A.; Ade, H.; Fréchet, J. M. J.; Toney, M. F.; McGehee, M. D., The Importance of Fullerene Percolation in the Mixed Regions of Polymer–Fullerene Bulk Heterojunction Solar Cells. *Advanced Energy Materials* **2013**, 3 (3), 364-374.
27. Jamieson, F. C.; Domingo, E. B.; McCarthy-Ward, T.; Heeney, M.; Stingelin, N.; Durrant, J. R., Fullerenecrystallisation as a key driver of charge separation in polymer/fullerene bulk heterojunction solar cells. *Chem. Sci.* **2012**, 3 (2), 485-492.
28. Collins, B. A.; Tumbleston, J. R.; Ade, H., Miscibility, Crystallinity, and Phase Development in P3HT/PCBM Solar Cells: Toward an Enlightened Understanding of Device Morphology and Stability. *The Journal of Physical Chemistry Letters* **2011**, 2 (24), 3135-3145.
29. Shaheen, S. E.; Brabec, C. J.; Sariciftci, N. S.; Padinger, F.; Fromherz, T.; Hummelen, J. C., 2.5% efficient organic plastic solar cells. *Applied Physics Letters* **2001**, 78 (6), 841-843.
30. Ma, W.; Yang, C.; Gong, X.; Lee, K.; Heeger, A. J., Thermally Stable, Efficient Polymer Solar Cells with Nanoscale Control of the Interpenetrating Network Morphology. *Advanced Functional Materials* **2005**, 15 (10), 1617-1622.
31. Peet, J.; Kim, J. Y.; Coates, N. E.; Ma, W. L.; Moses, D.; Heeger, A. J.; Bazan, G. C., Efficiency enhancement in low-bandgap polymer solar cells by processing with alkane dithiols. *Nature Materials* **2007**, 6 (7), 497-500.

32. Causa, M.; De Jonghe-Risse, J.; Scarongella, M.; Brauer, J. C.; Buchaca-Domingo, E.; Moser, J.-E.; Stingelin, N.; Banerji, N., The fate of electron-hole pairs in polymer:fullerene blends for organic photovoltaics. *Nature Communications* **2016**, 7 (1), 12556.
33. Zhang, M.; Wang, H.; Tian, H.; Geng, Y.; Tang, C. W., Bulk heterojunction photovoltaic cells with low donor concentration. *Advanced Materials* **2011**, 23, 4960-4.
34. Vandewal, K.; Widmer, J.; Heumueller, T.; Brabec, C. J.; McGehee, M. D.; Leo, K.; Riede, M.; Salleo, A., Increased Open-Circuit Voltage of Organic Solar Cells by Reduced Donor-Acceptor Interface Area. *Advanced Materials* **2014**, 26 (23), 3839-3843.
35. Melianas, A.; Pranculis, V.; Spoltore, D.; Benduhn, J.; Inganäs, O.; Gulbinas, V.; Vandewal, K.; Kemerink, M., Charge Transport in Pure and Mixed Phases in Organic Solar Cells. *Advanced Energy Materials* **2017**, 7 (20), 1700888.
36. Bernardo, B.; Cheyns, D.; Verreet, B.; Schaller, R. D.; Rand, B. P.; Giebink, N. C., Delocalization and dielectric screening of charge transfer states in organic photovoltaic cells. *Nature Communications* **2014**, 5 (1), 3245.
37. Ramirez, I.; Causa, M.; Zhong, Y.; Banerji, N.; Riede, M., Key Tradeoffs Limiting the Performance of Organic Photovoltaics. *Advanced Energy Materials* **2018**, 8 (28), 1703551.
38. Tress, W.; Leo, K.; Riede, M., Optimum mobility, contact properties, and open-circuit voltage of organic solar cells: A drift-diffusion simulation study. *Physical Review B* **2012**, 85 (15), 155201.
39. Zhao, W.; Li, S.; Yao, H.; Zhang, S.; Zhang, Y.; Yang, B.; Hou, J., Molecular Optimization Enables over 13% Efficiency in Organic Solar Cells. *Journal of the American Chemical Society* **2017**, 139 (21), 7148-7151.
40. Yuan, J.; Zhang, Y.; Zhou, L.; Zhang, G.; Yip, H.-L.; Lau, T.-K.; Lu, X.; Zhu, C.; Peng, H.; Johnson, P. A.; Leclerc, M.; Cao, Y.; Ulanski, J.; Li, Y.; Zou, Y., Single-Junction Organic Solar Cell with over 15% Efficiency Using Fused-Ring Acceptor with Electron-Deficient Core. *Joule* **2019**, 3 (4), 1140-1151.
41. Zhang, M.; Zhu, L.; Zhou, G.; Hao, T.; Qiu, C.; Zhao, Z.; Hu, Q.; Larson, B. W.; Zhu, H.; Ma, Z.; Tang, Z.; Feng, W.; Zhang, Y.; Russell, T. P.; Liu, F., Single-layered organic photovoltaics with double cascading charge transport pathways: 18% efficiencies. *Nature Communications* **2021**, 12 (1), 309.
42. Fan, B.; Zhang, D.; Li, M.; Zhong, W.; Zeng, Z.; Ying, L.; Huang, F.; Cao, Y., Achieving over 16% efficiency for single-junction organic solar cells. *Science China Chemistry* **2019**, 62 (6), 746-752.
43. Van den Brande, N.; Van Lier, G.; Da Pieve, F.; Van Assche, G.; Van Mele, B.; De Proft, F.; Geerlings, P., A time dependent DFT study of the efficiency of polymers for organic photovoltaics at the interface with PCBM. *RSC Advances* **2014**, 4 (95), 52658-52667.
44. Refaely-Abramson, S.; Baer, R.; Kronik, L., Fundamental and excitation gaps in molecules of relevance for organic photovoltaics from an optimally tuned range-separated hybrid functional. *Physical Review B* **2011**, 84 (7), 075144.
45. Martínez, J. P.; Solà, M., Open-Circuit Voltage of Organic Photovoltaics: A Time-Dependent and Unrestricted DFT Study in a P3HT/PCBM Complex. *The Journal of Physical Chemistry A* **2020**, 124 (7), 1300-1305.
46. Hachmann, J.; Olivares-Amaya, R.; Atahan-Evrenk, S.; Amador-Bedolla, C.; Sánchez-Carrera, R. S.; Gold-Parker, A.; Vogt, L.; Brockway, A. M.; Aspuru-Guzik, A., The Harvard Clean Energy Project: Large-Scale Computational Screening and Design of Organic Photovoltaics on the World Community Grid. *The Journal of Physical Chemistry Letters* **2011**, 2 (17), 2241-2251.

47. Lopez, S. A.; Pyzer-Knapp, E. O.; Simm, G. N.; Lutzow, T.; Li, K.; Seress, L. R.; Hachmann, J.; Aspuru-Guzik, A., The Harvard organic photovoltaic dataset. *Scientific Data* **2016**, 3 (1), 160086.
48. LeCun, Y.; Bengio, Y.; Hinton, G., Deep learning. *Nature* **2015**, 521 (7553), 436-444.
49. Cereto-Massagué, A.; Ojeda, M. J.; Valls, C.; Mulero, M.; Garcia-Vallvé, S.; Pujadas, G., Molecular fingerprint similarity search in virtual screening. *Methods* **2015**, 71, 58-63.
50. Matsuzaka, Y.; Uesawa, Y., Optimization of a Deep-Learning Method Based on the Classification of Images Generated by Parameterized Deep Snap a Novel Molecular-Image-Input Technique for Quantitative Structure–Activity Relationship (QSAR) Analysis. *Frontiers in Bioengineering and Biotechnology* **2019**, 7 (65).
51. Sun, W.; Li, M.; Li, Y.; Wu, Z.; Sun, Y.; Lu, S.; Xiao, Z.; Zhao, B.; Sun, K., The Use of Deep Learning to Fast Evaluate Organic Photovoltaic Materials. *Advanced Theory and Simulations* **2019**, 2 (1), 1800116.
52. Duvenaud, D.; Maclaurin, D.; Aguilera-Iparraguirre, J.; Gómez-Bombarelli, R.; Hirzel, T.; Aspuru-Guzik, A. a.; Ryan, Convolutional Networks on Graphs for Learning Molecular Fingerprints. *arXiv pre-print server* **2015**.
53. Pereira, F.; Xiao, K.; Latino, D. A. R. S.; Wu, C.; Zhang, Q.; Aires-de-Sousa, J., Machine Learning Methods to Predict Density Functional Theory B3LYP Energies of HOMO and LUMO Orbitals. *Journal of Chemical Information and Modeling* **2017**, 57 (1), 11-21.
54. Sui, M.-Y.; Yang, Z.-R.; Geng, Y.; Sun, G.-Y.; Hu, L.; Su, Z.-M., Nonfullerene Acceptors for Organic Photovoltaics: From Conformation Effect to Power Conversion Efficiencies Prediction. *Solar RRL* **2019**, 3 (11), 1900258.
55. Peng, S.-P.; Zhao, Y., Convolutional Neural Networks for the Design and Analysis of Non-Fullerene Acceptors. *Journal of Chemical Information and Modeling* **2019**, 59 (12), 4993-5001.
56. Padula, D.; Troisi, A., Concurrent Optimization of Organic Donor–Acceptor Pairs through Machine Learning. *Advanced Energy Materials* **2019**, 9 (40), 1902463.
57. Nagasawa, S.; Al-Naamani, E.; Saeki, A., Computer-Aided Screening of Conjugated Polymers for Organic Solar Cell: Classification by Random Forest. *The Journal of Physical Chemistry Letters* **2018**, 9 (10), 2639-2646.
58. Sun, W.; Zheng, Y.; Yang, K.; Zhang, Q.; Shah, A. A.; Wu, Z.; Sun, Y.; Feng, L.; Chen, D.; Xiao, Z.; Lu, S.; Li, Y.; Sun, K., Machine learning-assisted molecular design and efficiency prediction for high-performance organic photovoltaic materials. *Science Advances* **2019**, 5 (11), eaay4275.

# 3 Methods

## Foreword

The content of this chapter describes the basic principles of methods used by myself for the research presented in the following chapters. These include steady state absorption spectroscopy, transient absorption spectroscopy and machine learning techniques. The results of other techniques performed by colleagues or collaborators are not discussed here. For completeness these include, but are not limited to: Grazing-Incidence Wide-Angle X-ray Scattering (GIWAXS), Time Dependent Density Functional Theory (TD-DFT) calculations and Electro-modulated differential absorption (EDA) spectroscopy. Full credit is given in the foreword of each chapter. The major focus of this chapter is on documenting the techniques either developed or implemented by myself through the course of this work. This includes parts of the signal processing and data analysis for transient absorption spectroscopy.

### 3.1. Steady State Absorption Spectroscopy

Steady state absorption spectroscopy is used as to get the first insight into the electronic properties of molecules or blends and the morphology of thin films. A wavelength dependent (photon energy dependant) absorption spectrum is calculated using the ratio between the intensity of incident light ( $I_0(\lambda)$ ) on a sample and the intensity of the light transmitted ( $I(\lambda)$ ) through the sample, Beer-Lambert Law:<sup>1</sup>

$$A(\lambda) = \log \frac{I_0(\lambda)}{I(\lambda)}$$

( 3-1)

This is usually done stepwise using a monochromator until the desired wavelength (energy) range is covered.

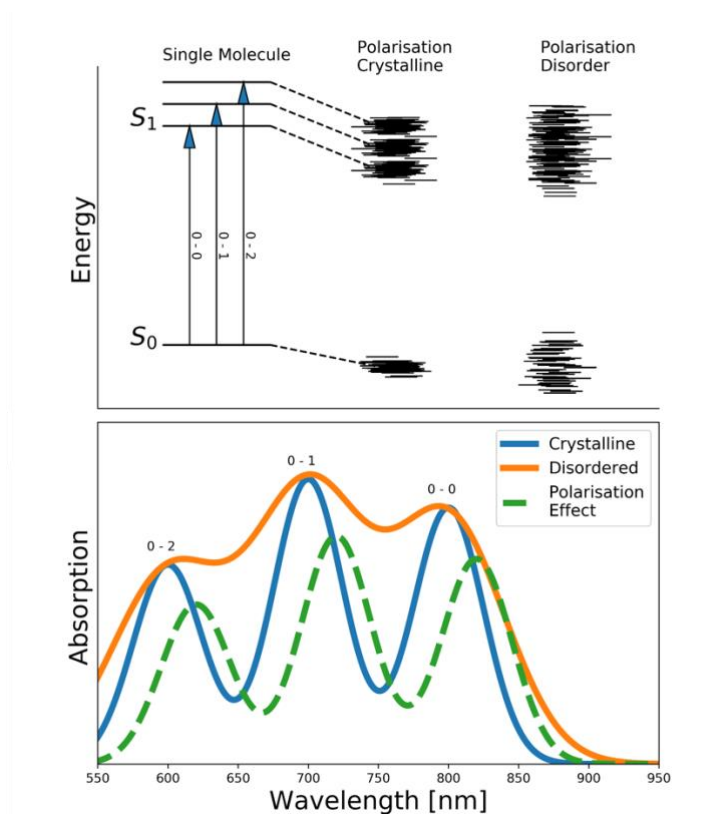


Figure 3.1-1 Energy level diagram (Top) depicting transitions from the ground state to three different vibrational levels in a single molecule (top left) and how these transitions are affected by electronic polarisation caused by molecular interactions (top middle) and by disorder (top right). The bottom panel shows the steady state absorption spectra illustrating the effects of crystallinity/disorder as well as polarisation shown in the top panel.

At its most simple, a steady state absorption spectrum shows the energy (wavelength) at which the electronic transition between the ground state ( $S_0$ ) and the first excited state ( $S_1$ ) occurs.



The features of the absorption spectrum are a result of transitions to various vibrational levels within the excited state, as illustrated in both panels of Figure 3-1 (0-0, 0-1 and 0-2 transitions). The amplitudes of these peaks are directly related to spatial transition coordinates (overlap in the wave functions of the initial and final states) according to the Frank-Condon principle and therefore the average physical orientation of the molecules. In thin films, the ratios of the amplitudes of the transitions to different vibrational levels can give an indication of crystallinity and aggregation state, especially within polymer chains.<sup>2</sup>

The absorption spectra provide information not only about individual molecules but also about their interactions. The first effect being the electrical polarisation effect where the dipole induced-dipole interactions between adjacent molecules lower the overall potential energy of the molecules.<sup>3</sup> The energy shift is larger in the excited state than in the ground state lowering the transition energies compared to a single molecule and so red-shifting the absorption spectrum. The second effect arises from a distribution of relative molecular conformations and orientations (or disorder). The polarisation effects rely on the relative orientations of molecules and when these orientations are inconsistent, the polarisation effect can vary, resulting in a spread of states and therefore available transitions. The spread of available transitions can be seen as a broadening of absorption peaks, with the more disordered packing resulting in broader peaks (Figure 3-1). These absorption features, and the information contained within, are of particular use when comparing multiple samples which have the same components but potentially different morphologies.

### 3.2. Transient Absorption Spectroscopy (TA)

#### 3.2.1. TA

The steady state absorption spectrum of an organic semiconducting system is already rich with information about its electronic and morphological properties. We now turn to TA spectroscopy to follow how this absorption spectrum changes after interaction with light.<sup>4</sup> TA spectroscopy allows for the time-resolved observation of excited states and photo-induced reactions. This is a pump-probe technique whereby a short pump laser pulse (of specific energy and intensity) excites the sample, after which a second probe pulse (of spectrally broad white light) measure the absorption spectrum. The sample is probed with and without pump with the difference in absorption being the effect of the pump alone. The time resolution is achieved by delaying the time between the pump and the probe pulses by varying the relative path lengths

of the two beams. The temporal evolution of the pump-induced absorption contains information about the dynamics of the excited states and photo-induced species present.

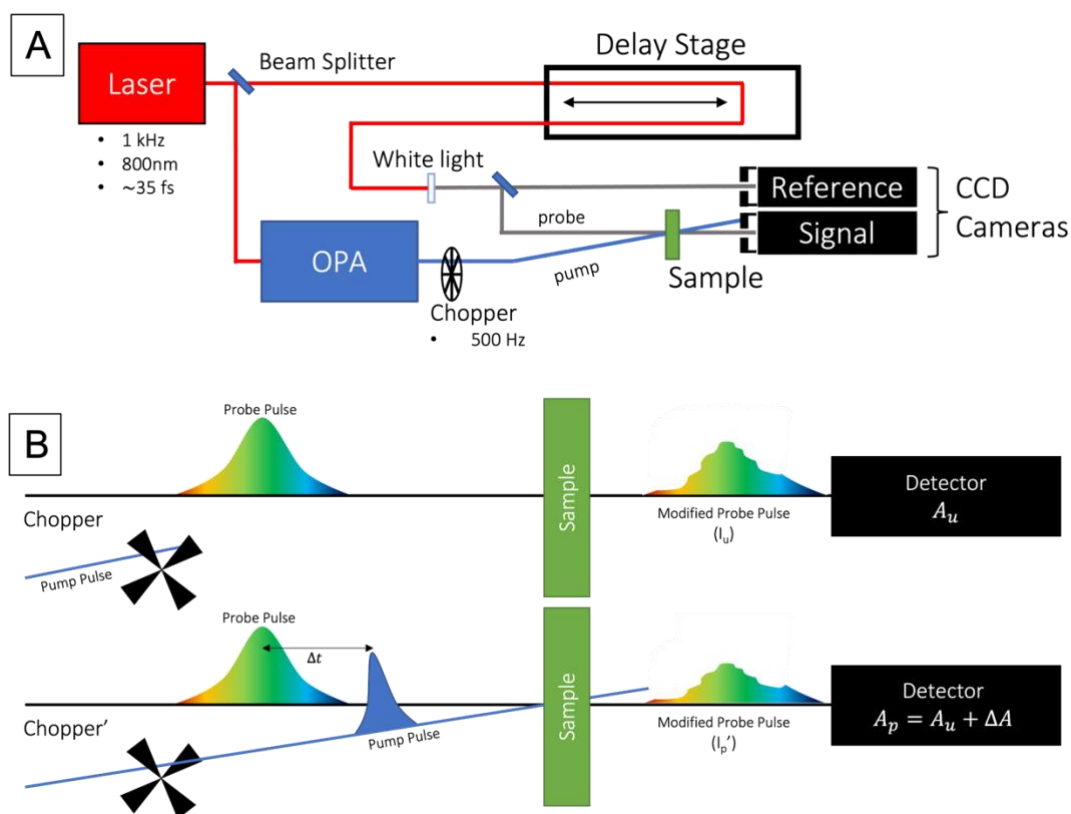


Figure 3.2-1 (A) Simplified detection schematic of transient absorption. (B) Shows the working principal of transient absorption where the absorption is measured by the probe pulse without the perturbation of the pump pulse ( $A_u$ , top) and with the perturbation of the pump pulse ( $A_p$ , bottom).

The basic experimental setup used for TA spectroscopy is shown in Figure 3-1 A. An amplified Ti:sapphire laser is used to generate around 35 fs long, high intensity pulses at a pulse frequency of 1 kHz and with a wavelength of 800 nm. The fundamental beam is split in two for the pump and probe beams. It is important that the same source is used for both the pump and probe to ensure synchronicity (alternating pulses would require ~300 km difference in path length to arrive at the sample at the same time). After the beam splitter, the probe beam is passed through a retroreflector mounted on a delay stage, where the path length of the probe beam can be varied. Varying the path length of the probe changes the time at which the probe arrives at the sample (relative to the pump) giving temporal resolution to the measurement. The 800 nm probe beam is then focused through a sapphire window generating a broad white light continuum (450 - 1200 nm)<sup>5</sup> after which it is split into a signal and reference beam. The pump beam is passed through an optical parametric amplifier (OPA) where a series of non-linear

optical frequency-mixing processes (i.e. optical parametric amplification, sum-frequency and second-harmonic generation) are used to accurately tune the wavelength (photon energy) of the pump pulse.<sup>6</sup> Having fine control of the energy of the photons in the pump pulse allows for the selective excitation of molecules, including different transitions within the molecule. The pump then passes through a chopper (500 Hz) which blocks every second pulse, allowing for the pumped and unpumped absorption measurement to be taken (Figure 3-1 B). The pump and signal probe are then spatially overlapped on the sample for the measurement with the pump coming in at a small angle so that it does not enter the detector. To ensure that minimal ambient light and scattering from the pump beam enter the detectors, both the signal and reference beams are focused through small slits blocking light which is not collinear.

The absorbance of the probe pulse by the sample is defined by Beer-Lambert Law:

$$A = -\log \frac{I}{I_{ref}} \quad (3-2)$$

with  $I$  (measured as the signal pulse) being the wavelength-dependent intensity of the transmitted probe pulse and  $I_{ref}$  the incident probe pulse (measured as the reference pulse). The absorbance of the pumped sample is the sum of the unpumped absorbance and the proportional transient population caused by the pump (subscript “p” refers to pumped absorption and “u” to unpumped).

$$\begin{aligned} A_p &= A_u + \Delta A \\ \Delta A &= A_p - A_u \end{aligned} \quad (3-3)$$

The transient absorption signal,  $\Delta A$ , is then given by Equation (3-3) (prime identifies a second pulse):

$$\Delta A = -\log \frac{I'_p}{I'_{ref}} + \log \frac{I_u}{I_{ref}} = \log \frac{I_u I'_{ref}}{I'_p I_{ref}} \quad (3-4)$$

The TA signal ( $\Delta A$ ) measured with these two pulses represents the spectrum at one specific time delay. To obtain the entire time-resolved spectral evolution, the measurement is repeated at multiple time-delays (difference in time between the pump and probe) controlled by the delay stage. The time difference can be represented and controlled by:

$$\Delta t = \frac{n\Delta L}{c}$$

( 3-5)

With  $\Delta t$  being the time-delay,  $n$  the refractive index of air ( $n \approx 1$ ),  $\Delta L$  the change in beam path length and  $c$  the speed of light.

### 3.2.1. Signal processing and noise reduction

Once the entire time resolved TA spectra are collected, there is a multistep analysis process (discussed in 3.3) that is needed to extract the relevant information from the data. While some of the spectral analysis is qualitative, a large part is quantitative (decomposition and kinetic modelling). In the quantitative analysis, the noise (or error) in the measurement can extrapolate through the calculations and affect the quality of the results. This means that exhaustive efforts are needed to ensure the best signal-to-noise ratio, both in the experimental setup and in terms of signal processing (discussed below). The signal to noise optimisation is even more critical as signals at the low pump fluences used are often close to the level of the noise, in order to ensure specific excitation densities.

#### *Shot outlier detection and discrimination*

The first signal processing step is to identify and discriminate substantially outlying shots so they can be remeasured before averaging. This step is done during the measurement as a part of the LabView acquisition software. This is done using a binning method described by Anderson et al.<sup>7</sup> in which all the shots from each pixel and from each timestep are binned into a set number of bins across their entire optical density (OD) range. The value of the bin with the highest count (or the mode value  $M$ ) and its population (mode population  $m$ ) is measured. Noisy data with a large OD range has a large  $m$  value as the bin size (a function of the range) is large around  $M$ . Inversely, clean data with a low OD range and small bins will have a small  $m$  for the same non-outlier value distribution.  $m$  is used to define a confidence integral  $P$ :

$$P = \frac{x - m}{x}$$

( 3-6)

where  $x$  is the number of shots in a timestep. A clean signal with 100 shots and an  $m = 10$  would have a  $P = 0.9$  and a noisy signal with an  $m = 90$  a  $P = 0.1$ .

The  $P$  value is then used to determine a discrimination criterion where shots outside the calculated range are deemed to be outliers and are disregarded.

$$M - n\sigma < \text{test value} < M + n\sigma$$

( 3-7)

with:

$$n = \sqrt{2} \operatorname{erf}^{-1}(P)$$

( 3-8)

$\sigma$  being the standard deviation of the shots and  $\operatorname{erf}^{-1}(P)$  the inverse error function. The process of binning and discriminating is repeated until  $m$  is sufficiently small (typically 5% of the number of remaining data values) and the data determined to be outlier free. Assuming the outlier discrimination leaves a set of normally distributed shot values, the mean of these shots at each pixel can be saved as the measured value.

#### *Reference beam*

The second step to reduce noise is the  $I'_{ref}/I_{ref}$  part of Equation ( 3-3). This factor compensates for the intensity fluctuations between shots. However, as both signal and reference intensities are wavelength dependant, the correlation between the measured wavelength and the index of the data point in the extracted data array need to be consistent for both signal and reference (the pixel to wavelength calibration needs to be identical). This is not always trivial as signal and reference beams are measured on different detectors (Figure 3-1).

#### *Background subtraction*

Since the pump pulse is chopped, any scattered light that reaches the detector is observed as a constant signal. This can be partially mitigated by proper alignment of the signal beam and with a large enough angle between the pump and probe beams. However, if scattered signal remains, subtracting it as a background can be done since the scattering signal is both constant in amplitude and appears at negative time delays (as it is not a result of photoexcitation of the sample). The background subtraction is described by Equation ( 3-7). This also subtracts any contributions of spontaneous emission from the sample.

$$\Delta A(t) = \Delta A(t) - \overline{\Delta A(t < 0)}$$

( 3-9)

### SVD noise filtering

Singular value decomposition is a common method of factorising data matrices  $\mathbf{D}$  into two unitary matrices,  $\mathbf{U}$  and  $\mathbf{V}$ , and a diagonal matrix  $\mathbf{S}$  containing the positive singular values of the data matrix.<sup>8</sup>

$$\mathbf{D} = \mathbf{U}\mathbf{S}\mathbf{V}^T$$

( 3-10)

In TA the data matrix consists of real numbers where the rows are the time dependent dynamics at a certain wavelength and the columns are the wavelength dependent spectra at a specific time-delay,  $\mathbf{D} \in \mathbb{R}^{\lambda \times t}$  with  $\lambda$  being the measured wavelength and  $t$  the timestep.  $\mathbf{U} \in \mathbb{R}^{\lambda \times \lambda}$  and  $\mathbf{V} \in \mathbb{R}^{t \times t}$  are spectral and dynamic components respectively and  $\mathbf{S} \in \mathbb{R}^{\lambda \times t}$  is the diagonal singular value matrix. This factorisation can be expanded as:

$$\mathbf{D} = \sum_{k=1}^t \mathbf{u}_k s_k \mathbf{v}_k^T$$

( 3-11)

Where the columns of  $\mathbf{u}_k$  (a single  $\lambda$  dependent component) and  $\mathbf{v}_k^T$  (a single  $t$  dependent components) are ordered (ranked) such that their corresponding singular values  $s_k$  are in descending order. This ranked decomposition of the data matrix can be used to filter out some components which have very low influence (small  $s_k$  value) on the information in the data but still contribute to the noise.

We assume that our noisy data matrix  $\tilde{\mathbf{D}}$  is simply the sum of a clean data matrix  $\bar{\mathbf{D}}$  and some normally distributed noise  $\mathbf{E}$  originating from the experimental conditions but not large enough to be discriminated by the outlier detection or scan averaging:

$$\tilde{\mathbf{D}} = \sum_{k=1}^t \tilde{\mathbf{u}}_k \tilde{s}_k \tilde{\mathbf{v}}_k^T = \bar{\mathbf{D}} + \mathbf{E}$$

( 3-12)

$\mathbf{E}$  can be calculated with the lowest number of singular values ( $r$ ) of the noisy data matrix used, such that the maximum standard deviation of the remaining error matrix  $\mathbf{E}$  is not larger than the mean standard deviation of the negative time traces of  $\tilde{\mathbf{D}}$ .

$$\mathbf{E} = \tilde{\mathbf{D}} - \bar{\mathbf{D}} = \tilde{\mathbf{D}} - \sum_{k=1}^r \tilde{\mathbf{u}}_k \tilde{s}_k \tilde{\mathbf{v}}_k^T$$

$$\{1 < r < t \mid \max(\sigma_{E(r)}) < \text{mean}(\sigma_{\tilde{\mathbf{D}}(t < 0)})\}$$

( 3-13)

This restricts the maximum of noise removed from  $\tilde{\mathbf{D}}$  (in  $\mathbf{E}$ ) to significantly less than the noise in the negative time delays already in  $\tilde{\mathbf{D}}$ . This ensures that only the normally distributed noise is removed and that no spectral information is lost.

The clean data  $\bar{\mathbf{D}}$  is reconstructed using the determined subset ( $r$ ) of the singular values of noisy data  $\tilde{\mathbf{D}}$ :

$$\bar{\mathbf{D}} = \sum_{k=1}^r \tilde{\mathbf{u}}_k \tilde{s}_k \tilde{\mathbf{v}}_k^T$$

( 3-14)

### 3.2.2. TA spectral features

Once the TA data has been processed, it can be plotted either as dynamics (evolution of signal at a specific wavelength over time) or as spectra at specific time delays. The spectra can be complex and are a combination of spectral features, with each feature representing a specific photo-physical process.

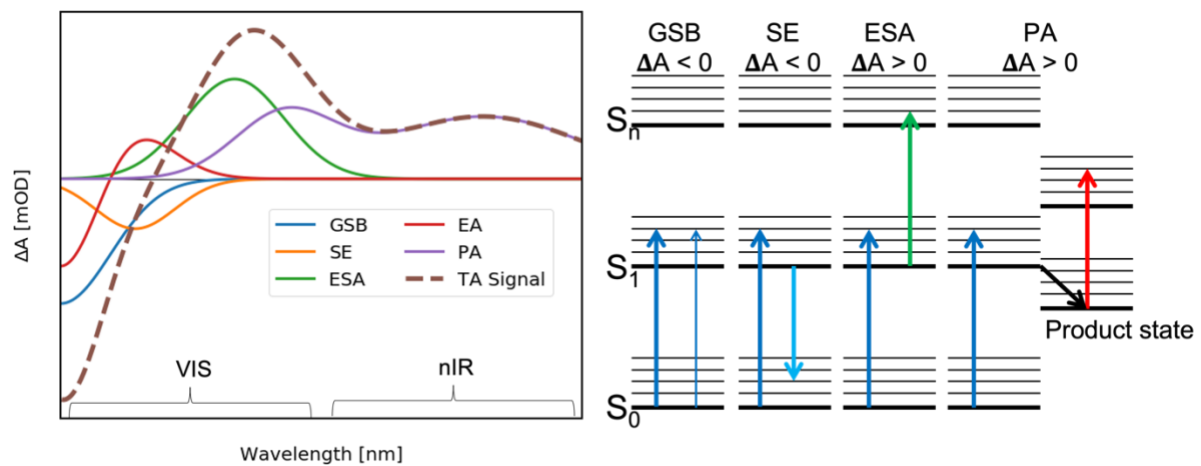


Figure 3.2-2 Illustration of TA spectral features (left) and representative energy diagrams (right). Figure partly adapted.<sup>9</sup>

#### *Ground State Bleaching (GSB)*

Once the system is excited by the pump beam, the population of excited molecules increases while the population of molecules in the ground state decreases (compared to the unpumped system). Probing this system leads to less light being absorbed in the spectral region of the  $S_0 \rightarrow S_1$  transition resulting in a negative ( $\Delta A < 0$ ) TA signal. GSB is identifiable as its shape is the inverse of the steady state absorption spectrum.

#### *Stimulated Emission (SE)*

The probe pulse can trigger a radiative relaxation of excited states to the ground state (usually to higher vibrational levels of the ground state). The radiative relaxation results in the illusion of a higher transmitted probe intensity and so a negative ( $\Delta A < 0$ ) TA signal. SE can be identified as a negative signal slightly red-shifted from the GSB and overlapping with the steady-state emission.

#### *Excited State Absorption (ESA)*

Molecules in the excited state can be further excited to higher-lying electronic or vibrational states by the probe pulse. This leads to less light being transmitted and so a positive ( $\Delta A > 0$ ) TA signal. ESA can be identified as a positive signal (in the VIS or nIR range) which is present from the earliest non-negative time-delays, always with a corresponding GSB and SE signal. In the study of organic photovoltaic thin film active layers, the ESA usually represents the population of excitons in the film.

#### *Product Absorption (PA)*

The products of photo-chemical reactions are often also able to absorb light in the spectral range of the measurement. This results in more of the probe being absorbed and so a positive ( $\Delta A > 0$ ) TA signal. PA can be identified as a positive TA signal in VIS or nIR range with a corresponding GSB signal of the involved molecules. In the study of organic photovoltaic thin film active layers, the PA usually represents the population of charges in the film with individual peaks for both the charge carriers.

#### *Electroabsorption (EA)*

Electroabsorption arises from a Stark-shift of the absorption bands resulting from an electric field across the absorbing molecules. When the electric field is a result of the pump pulse (i.e. the electric field between two separating photo-generated charges, the EA shows up as an oscillatory signal which follows the shape of the first or second derivative of the absorption spectrum of the molecules close to the charges and affected by their field.



### 3.3. TA Spectroscopy Data Analysis

#### 3.3.1. Multivariate Curve Resolution – Alternating Least Squares

The TA spectroscopy measurement is, as discussed above, the measurement of the transient absorption spectra at a series of time delays with respect to excitation. The resultant data is, therefore, in the form of a matrix which is absorption wavelength ( $\lambda$ ) and time delay ( $t$ ) dependent  $\mathbf{D}(\lambda, t)$ . This data matrix is the cumulative signal of multiple components i.e., exciton and charge spectral signatures, and so the total data matrix  $\mathbf{D}(\lambda, t)$  can be represented as the sum of the TA spectra of each component  $\mathbf{D}(\lambda, t)_i$  plus an error matrix which contains the unexplained variance and non-spectral noise of the measurement  $\mathbf{E}(\lambda, t)$  (3-14).<sup>10-13</sup>

$$\mathbf{D}(\lambda, t) = \sum_i \mathbf{D}(\lambda, t)_i + \mathbf{E}(\lambda, t) \quad (3-15)$$

$$\mathbf{D}(\lambda, t) = \sum_i \mathbf{c}(t)_i \mathbf{s}(\lambda)_i^T + \mathbf{E}(\lambda, t) \quad (3-16)$$

$$\mathbf{D}(\lambda, t) = \mathbf{C}(t) \mathbf{S}(\lambda)^T + \mathbf{E}(\lambda, t) \quad (3-17)$$

Each component  $\mathbf{D}(\lambda, t)_i$  can then be further broken down into its concentration profile (referred to as dynamics)  $\mathbf{c}(t)$  multiplied by the transpose of its pure spectral signature  $\mathbf{s}(\lambda)$  (3-15). In combination, the matrix  $\mathbf{C}$  contains the dynamics and  $\mathbf{S}^T$  the spectra of each component such that the product of the two recreates the original TA data matrix  $\mathbf{D}$  with  $\mathbf{E}$  being the error (3-16).

The general optimisation problem of multivariate curve resolution with alternating least squares (MCR-ALS) is represented as follows:

$$\begin{aligned} & \min \|\mathbf{D} - \mathbf{C}\mathbf{S}^T\| \\ & \text{or} \\ & \min \|\mathbf{E}\| \end{aligned} \quad (3-18)$$

This minimisation is done iteratively using least squared optimisation, alternating between the optimisation of the  $\mathbf{C}$  and  $\mathbf{S}^T$ , hence the name MCR-Alternating Least Squares.<sup>14</sup> Convergence criteria are specified, and constraint functions applied before the loss function allowing some control over the resulting spectra and dynamics. Selected spectra or dynamics can also be held constant during the optimisation, which is especially useful when the spectral shapes of some components are known. The Python library pyMCR is used for the decomposition with a template shown in section A.1.1.<sup>15</sup>

The process of decomposing the TA data matrix proceeds as follows:<sup>10</sup>

1. Determining the number of components (species) present.
2. Supplying initial guesses for the components.
3. Optimising the components until convergence

#### *Number of components*

The number of components present is best determined by understanding the measured system and by qualitative analysis of the TA spectrum. In OPV systems there are a limited number of species with distinct spectral signatures. Excitons with distinct signatures originate from either the acceptor or donor and can be CT or Frenkel in nature. Choosing excitation energies which selectively excite a subset of the exciton types allows for the disregarding of the rest, for example selectively exciting the donor at energies low enough to excite only Frenkel excitons means that there is most likely only one exciton species. After either ET or HT, charges have the same spectral signature, with bound and free charges very rarely having different signatures, resulting (most often) in only one charge signature. Allowing for exceptions, the number of components can usually be determined by understanding the system and experimental setup.

Alternatively, or to confirm the previous choice, SVD can be used to give an idea of the number of components in the TA data matrix. After applying SVD to the TA data matrix (as described in SVD Noise Filtering) the singular values can be compared. The number of singular values significantly higher than the mean can indicate the number of components.

#### *Component initial guesses and fixing components*

The MCR-ALS requires either a spectral or dynamics guess for each of the components. As above, the best spectral guess will be made when drawing from measured spectra as their shapes can be physically justified. The best guesses typically result from two methods: the

exciton spectra from a TA measurement of a neat donor or acceptor film can be used as a guess for the exciton of the same material in a blend, and scaled late time spectra of the measured blend can be used as the guess for the charge signature, assuming that all the excitons (and so their signatures) have either decayed to the ground state or have been quenched by ET/HT.

Spectral or dynamics guesses can be fixed (held constant) during the MCR optimisation if there is a high degree of confidence in their shape. Holding components decreases the degrees of freedom in the calculation and so increases the likelihood of meaningful results after convergence.

Lastly, if no appropriate guesses can be found, the first columns of the  $\mathbf{U}$  and  $\mathbf{V}$  matrix from the SVD of the TA data matrix (Equation ( 3-13)) can be used as the dynamics or spectral guesses respectively, remembering that they are sign invariant.

#### *Constraints, Optimisers and Convergence criteria*

Constraints are placed on the spectral and dynamics results of the MCR-ALS with the purpose of imposing some physical rules to the results. As TA spectra can be either positive or negative and of irregular shape, there are rarely constraints placed on them. The dynamics, however, only make sense if when some basic conditions are met, and so these conditions can be implemented as constraints. The two most common constraints for TA data are non-negativity and unimodality for dynamics of components where the back transformation of one species to said species is physically unlikely. Custom constraints can be created and are shown in section A.1.2.

The optimisation function for the spectral and dynamics components can be individually specified. An ordinary least squared function is employed for the spectral optimisation, while the need for the non-negativity constraint for the dynamics is negated using the non-negative least square optimiser.

The role of the convergence criteria is to determine whether the optimisation problem from Equation ( 3-17) has been sufficiently minimised. As the objective is to reach the lowest error value possible, a minimal error threshold is not specified but rather a threshold for the number of iterations allowed without a specified amount of improvement, assuming that when the error value stops improving it is at its optimum. The error value is also allowed to increase for a specified number of iterations allowing for the optimisation to potentially leave local minima in search of a more global minimum. The convergence criteria for the best optimisation needs to be balanced by the limitations of computational power and time, and so a maximum total

iterations threshold is also set such that the optimisation can be stopped if convergence takes too much time.

### *Limitations of MCR-ALS*

The main warning about both SVD and MCR-ALS is that the results are simply mathematical features of the input data matrix. The results have no (outside of constraints and fixed components) information about, or consideration for, the physics of system measured. Therefore, any result needs to have an arguable physical interpretation before further analysis can be done and conclusions about the system made.

The largest uncertainty in MCR-ALS optimisation is brought on by the ambiguity phenomenon, where the same data matrix can be equally well represented by a combination of different spectral and dynamics components.

There are three main types of ambiguity:<sup>16,17</sup>

#### *1. Permutation ambiguity.*

The order of the components has no effect on the data reconstruction and so could be shuffled during optimisation. This could cause problems if some guesses are fixed and not allowed to be shuffled in a way that best facilitates optimisation.

#### *2. Intensity ambiguity.*

The amplitudes of both the spectral and dynamics components are arbitrary provided that their ratio remains constant (Equation (3-18)).

$$\mathbf{D}(\lambda, t) = \sum_i (\mathbf{c}(t)_i k_i) (\mathbf{s}(\lambda)_i^T \frac{1}{k_i}) + \mathbf{E}(\lambda, t)$$

(3-19)

It is, therefore, imperative that the absolute amplitudes of the spectra are known (from their absorption coefficients) so that the correct amplitude of the dynamics can be determined. The relative amplitudes of the dynamics represent the relative populations of the species (exciton, charge etc.), which is crucial for kinetic modelling.

#### *3. Rotational ambiguity.*

Spectral and dynamics components with different shapes can fit the data matrix equally well. This is best illustrated by applying a transform matrix  $\mathbf{T}$  to both  $\mathbf{C}$  and  $\mathbf{S}$ :

$$\mathbf{D}(\lambda, t) = (\mathbf{C}(t)\mathbf{T})(\mathbf{T}^{-1}\mathbf{S}(\lambda)^T) + \mathbf{E}(\lambda, t)$$

(3-20)

This kind of ambiguity specifically emphasises the need for physical justification before the results can be trusted and conclusions derived from them.

The final notable feature of MCR-ALS is its inability to model spectral shifts or broadening over time due to the necessarily static nature of spectral components. This could be potentially overcome by breaking the initial and final states (before and after the shift or shape change) into two separate components with the intermediate states being a combination of the two. This needs to then be consciously considered when choosing the number of components to use.

### 3.3.2. Kinetic Modelling

To better understand and quantify the mechanisms involved in the processes that lead from excitons to free charges, including recombination steps, a kinetic model is fit to the time-dependent species population dynamics extracted from the MCR-ALS decomposition.

The process of setting up and fitting the model requires these steps:

1. Defining the system of species and their kinetic interactions.
2. Defining the corresponding set of linked differential equations.
3. Fitting the set of equations to the dynamics data.

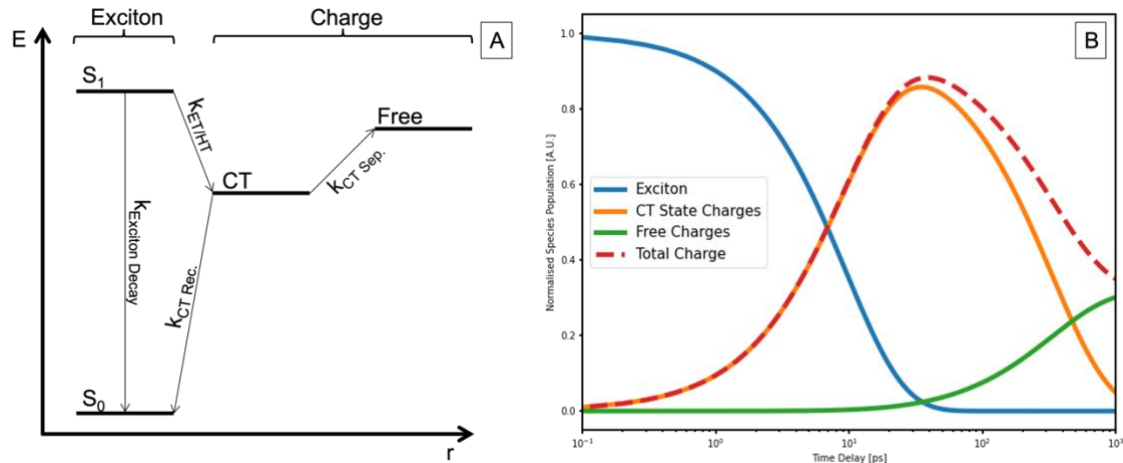


Figure 3.3-1 (A) Jablonski Diagram of typical species and mechanisms in an OPV. (B) The species population dynamics corresponding to the Jablonski diagram including the CT state, Free and Total Charge dynamics. The rates used in this illustration were:  $k_{Exciton\ Decay} = 1/200\ ps$ ,  $k_{ET/HT} = 1/10\ ps$ ,  $k_{CT\ Rec.} = 1/500\ ps$  and  $k_{CT\ Free} = 1/1000\ ps$ .

#### Defining the system and linked differential equations

Describing the system in a Jablonski diagram including interactions, as in Figure 3-3 A,<sup>18</sup> allows us to visualise the competing mechanisms and more easily define the kinetic equations. To define the kinetic equations, a differential rate equation is set up describing the temporal evolution of each species. For the Jablonski diagram in Figure 3-3 A:

$$\frac{d[S_1]}{dt} = -k_{Exciton\ Decay} * [S_1](t) - k_{ET/HT} * [S_1](t)$$

( 3-21)

$$\frac{d[CT]}{dt} = k_{CT/HT} * [S_1](t) - k_{CT\ Rec.} * [CT](t) - k_{CT\ Sep.} * [CT](t)$$

( 3-22)

$$\frac{d[Free]}{dt} = k_{CT\ Sep.} * [CT](t)$$

( 3-23)

As these differential equations are necessarily linked, sharing both rates and concentrations, all three equations need to be fit to the data simultaneously. Rather than fitting the analytically solved equations (which can become extremely complex), a stepwise ODE integrator is used as the function minimised against the experimental data.

#### *CT/Free charge problem, custom loss functions and fitting*

As discussed in 3.3.1.1, the bound charges (CT state charges) and free charges are typically spectrally indistinguishable. Not only do they share a spectral component, from the MCR-ALS decomposition, but also a single dynamics component. Therefore, the charge dynamic is fit by the sum of the separately integrated CT and Free kinetic equations and so the loss function (normally a least squares function) needs to be modified. Custom loss functions are explained in section A.1.3. The loss function is then minimised until the convergence criteria are met. The minimizer used is usually gradient descent based and can implement bounds for rates and hold some rates constant. This allows some predetermined physical understanding to assist in getting less ambiguous results, for example holding predetermined exciton lifetimes constant or bounding CT state lifetimes to realistic values. After fitting the goodness of fit is calculated, normally using  $R^2$ , allowing the viability of the model to be assessed.

### 3.4. Machine Learning

Chapter 7 of this thesis breaks from experimental work and applies machine learning techniques to large molecular datasets. These machine learning techniques are in the realm of reinforcement learning, where the model is trained on data with perfect input-output mapping and where that mapping is learnt. The basic machine learning methods are summarised below.

### 3.4.1. Neural Networks (NN)

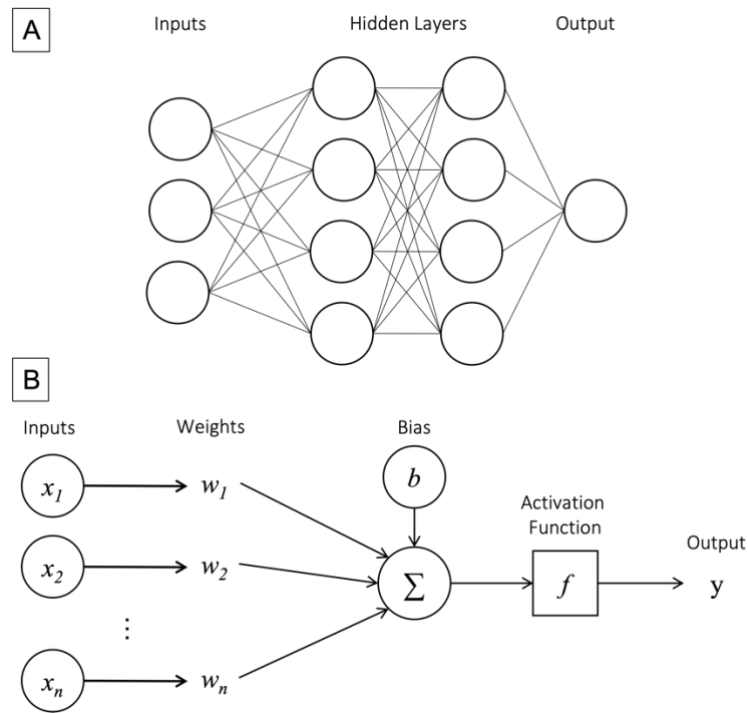


Figure 3.4-1 (A) The architecture of a basic Neural Network including input, hidden and output layers. (B) An illustration of the input, weights, bias, activation function and output of a single neuron in a neural network.

Neural networks (NN) are essentially a large nonlinear function which takes a numerical input and produces an output. The distinction of a NN from a classic mathematical function is its ability to improve the quality of its output by training. The network consists of three parts: input layer, generally an array of real numbers; hidden layers, a series of layers with fully connected neurons; and an output layer as illustrated in Figure 3-5 A. Each neuron in a hidden or output layer receives the output of every neuron in the previous layer (Figure 3-5 B). The output of each neuron from the previous layer is multiplied by a weight which is unique to that specific connection, a bias (unique to that specific neuron) is added to the sum of all the connections and an activation function is applied to the result. The output of a neuron is calculated from Equation ( 3-25):

$$y = f(\mathbf{W}^T \mathbf{X} + b)$$

( 3-24)

With  $y$  the output of the neuron,  $f$  the activation function,  $\mathbf{W}$  a matrix containing all the weights from the previous layer,  $\mathbf{X}$  a matrix containing the output values of each neuron from the previous layer and  $b$  the bias associated to the neuron. The activation function introduces

nonlinearity to the network, with the rectified linear unit (ReLU) and Sigmoid functions ( 3-26) being popular.<sup>19,20</sup>

$$ReLU(x) = \max(0, x)$$

$$Sigmoid(x) = \frac{1}{1 + e^{-x}}$$

( 3-25)

Once the input has been processed through all hidden layers, the quality of the output can be quantified by a loss function which compares the output to the true value and returns a “score”. The loss function used in this work is the mean squared error function, shown in Equation ( 3-27):

$$L(y, \hat{y}) = \frac{1}{N} \sum_{i=0}^N (y_i - \hat{y}_i)^2$$

( 3-26)

Where  $L(y, \hat{y})$  is the loss function,  $y_i$  the true value,  $\hat{y}_i$  the output of the NN and  $N$  the number of calculations made in the batch. The lower the result of the loss function, the higher the quality of output of the NN, and so the training process is one where the weights associated to each connection and the biases associated to each neuron are adjusted to minimise the output of the loss function. The weights and biases are adjusted using a process called back propagation and gradient decent optimisation. Gradient decent algorithms use the partial derivative of the loss function with respect to each weight and each bias to adjust the value of each weight and bias respectively. A single iteration of gradient decent is represented in Equation ( 3-28):

$$w_{i+1} = w_i - \alpha \frac{\partial L}{\partial w_i}$$

$$b_{i+1} = b_i - \alpha \frac{\partial L}{\partial b_i}$$

( 3-27)

With  $w_{i+1}$  and  $b_{i+1}$  being the adjusted weights and biases respectively and  $\alpha$  the learning rate. The learning rate is a constant factor used to scale the effect of the gradient on the weight or bias. More complex optimisation algorithms such as SGD, RMSprop and Adam are used more often, but all involve a form of gradient decent.<sup>21</sup> Using back propagation and enough properly labelled training data (where inputs are linked to correct outputs), the NN is able to optimise



its weights and biases in a way that consistent and high quality outputs can be achieved for appropriate inputs. The quality of the outputs of the NN, in terms of accuracy and precision of prediction as well as generalisability, are strictly limited to the quality and scope of the training data. Input data for post training use of the NN, as well as input data for testing, must therefore be subsets of a superset to which the training data also belongs.

During the training process the data set is split into three parts: training, validation and testing sets. The NN has its weights and biases randomly initialised at the beginning of the training process. The training data is fed forward through the network in batches (subsets of the training data), with back propagation and parameter optimisation steps being done after each batch until the NN has been exposed to the entire training set (called an epoch). After each epoch, the unseen validation set is fed through the network and the value of the loss function is used to judge the performance of NN on unseen data. The training is usually stopped if one of three conditions are met: the specified number of epochs are complete (done to limit training time or to stop a non-converging network); the validation loss value reaches a specified “low enough” value; or if the validation loss value starts to increase with more epochs. Increasing validation loss is a sign of overfitting. Overfitting is when the network starts to simply learn the training set “off by hart” as opposed to learning to calculate the relationship between the input and output, this limits the generalisability of the network and so the quality of outputs for unseen inputs.<sup>22</sup>

#### 3.4.2. Convolutional Neural Networks (CNN)

A Convolutional Neural Network (CNN) is a network architecture which is able to take images (or 2D/3D matrices) as an input to the network and learn to produce appropriate outputs. The CNN is broken into two parts: the convolutional network and the neural network. The convolutional network is able to extract features of an image and convert them in to an appropriate input for the neural network which then performs the regression or classification. The convolution layers transform the image such that features can be extracted. An image is convolved with a randomly initialized kernel (or filter) by sliding said kernel across the image through every special position and extracting the dot product of the kernel and the specific region of the image. An activation function and bias are then applied to the convolved feature-set, resulting in a feature map. The activation function introduces nonlinearity to the network and adjusting the bias creates ability to train the value or importance of each kernel, producing more meaningful feature maps. The feature maps are then subsequently treated as inputs for the next convolutional layer moving through the network. After a series of convolutional layers

are applied, the feature map is reduced in size by a max-pooling layer where only the maximum value in each region of the feature map is carried through. Pooling is used both to reduce the computational burden of calculation, to speed up training, and to make prominent features more robust by only taking the feature with the highest value, reducing overfitting. It is however important to note that the kernels are randomly initialized and none of them are designed to intentionally extract specific features. Lastly, a global average pooling layer is applied, where the average value of each feature map is taken such that the features are converted into a single array that can be passed through the fully connected network.

## References

- (1) Swinehart, D. F. The beer-lambert law. *Journal of chemical education* **1962**, 39, 333.
- (2) Dimitriev, O. P.; Blank, D. A.; Ganser, C.; Teichert, C. Effect of the Polymer Chain Arrangement on Exciton and Polaron Dynamics in P3HT and P3HT:PCBM Films. *The Journal of Physical Chemistry C* **2018**, 122, 17096-17109.
- (3) Köhler, A.; Bässler, H.: *Electronic processes in organic semiconductors: An introduction*; John Wiley & Sons, 2015.
- (4) Berera, R.; van Grondelle, R.; Kennis, J. T. Ultrafast transient absorption spectroscopy: principles and application to photosynthetic systems. *Photosynthesis research* **2009**, 101, 105-118.
- (5) Majus, D.; Jukna, V.; Pileckis, E.; Valiulis, G.; Dubietis, A. Rogue-wave-like statistics in ultrafast white-light continuum generation in sapphire. *Opt. Express* **2011**, 19, 16317-16323.
- (6) Baumgartner, R.; Byer, R. Optical parametric amplification. *IEEE Journal of Quantum Electronics* **1979**, 15, 432-444.
- (7) Anderson, K. E. H.; Sewall, S. L.; Cooney, R. R.; Kambhampati, P. Noise analysis and noise reduction methods in kilohertz pump-probe experiments. *Review of Scientific Instruments* **2007**, 78, 073101.
- (8) Van Loan, C. F. Generalizing the singular value decomposition. *SIAM Journal on numerical Analysis* **1976**, 13, 76-83.
- (9) Shivhare, R. R. Investigation of Low Optical-Gap Donor and Acceptor Materials for Organic Solar Cells. **2019**.
- (10) de Juan, A.; Tauler, R.: Chapter 2 - Multivariate Curve Resolution-Alternating Least Squares for Spectroscopic Data. In *Data Handling in Science and Technology*; Ruckebusch, C., Ed.; Elsevier, 2016; Vol. 30; pp 5-51.
- (11) Lawton, W. H.; Sylvestre, E. A. Self modeling curve resolution. *Technometrics* **1971**, 13, 617-633.
- (12) Rutan, S. C.; de Juan, A.; Tauler, R.: Introduction to Multivariate Curve Resolution. In *Comprehensive Chemometrics*, 2009; Vol. 2; pp 249-259.
- (13) De Juan, A.; Rutan, S. C.; Tauler, R.: Two-Way Data Analysis: Multivariate Curve Resolution - Iterative Resolution Methods. In *Comprehensive Chemometrics*, 2009; Vol. 2; pp 325-344.
- (14) Leng, L.; Zhang, T.; Kleinman, L.; Zhu, W. In *Tilte2007*; IOP Publishing.
- (15) Jr., C. H. C. pyMCR: A Python Library for Multivariate Curve Resolution Analysis with Alternating Regression (MCR-AR). *Journal of Research of National Institute of Standards and Technology* **2019**, 124.
- (16) Tauler, R.; Maeder, M.: 2.20 - Two-Way Data Analysis: Multivariate Curve Resolution – Error in Curve Resolution. In *Comprehensive Chemometrics*; Brown, S. D., Tauler, R., Walczak, B., Eds.; Elsevier: Oxford, 2009; pp 345-363.
- (17) Tauler, R.; Smilde, A.; Kowalski, B. Selectivity, local rank, three-way data analysis and ambiguity in multivariate curve resolution. *Journal of Chemometrics* **1995**, 9, 31-58.
- (18) Jablonski, A. Efficiency of Anti-Stokes Fluorescence in Dyes. *Nature* **1933**, 131, 839-840.
- (19) Abien. Deep Learning using Rectified Linear Units (ReLU). *arXiv pre-print server* **2019**.
- (20) Narayan, S. The generalized sigmoid activation function: Competitive supervised learning. *Information Sciences* **1997**, 99, 69-82.
- (21) Ruder, S. An overview of gradient descent optimization algorithms. *arXiv pre-print server* **2017**.

(22) Salman, S.; Liu, X. Overfitting Mechanism and Avoidance in Deep Neural Networks. *arXiv pre-print server* **2019**.

# 4 Ultrafast Charge Dynamics in Dilute-Donor versus Intermixed TAPC:C<sub>60</sub> Organic Solar Cell Blends

## Foreword

The work in this chapter is the second part of a series of three works. The series starts with the photo physics of neat C<sub>60</sub> films and then continues to dilute donor systems with C<sub>60</sub> as acceptor. Firstly with a non-aggregating, symmetric donor (TAPC) with consistent CT state energies and now with an aggregating, not completely symmetric donor ( $\alpha$ 6T) whose CT state energies decrease with increased donor concentration.

The first part is published in the Journal of Physical Chemistry Letters by Martina Causa' et al. titled *Femtosecond Dynamics of Photoexcited C<sub>60</sub> Films*<sup>1</sup>.

The work by Causa' et al. on neat C<sub>60</sub> films showed the presence of both CT and Frenkel excitons which were selectively excited at 450 nm and 610 nm respectively. The spectral shapes and dynamics of the two exciton species were presented, where the CT exciton has a pronounced EA signal owing to its delocalization over multiple molecules. The fast relaxation of CT to Frenkel excitons was also elucidated and a time constant of 0.18 ps deduced along with a Frenkel exciton lifetime of 150 ps. Lastly the spectral shape of the C<sub>60</sub> anion was related to its delocalisation with a sharper peak indicating a less localised electron.

The contents of this chapter is published in the Journal of Physical Chemistry Letters titled:  
*Ultrafast Charge Dynamics in Dilute-Donor versus Highly Intermixed TAPC:C60 Organic Solar Cell Blends.*<sup>2</sup>

Gareth John Moore<sup>1</sup>, Martina Causa<sup>1</sup>, Josue F. Martinez Hardigree<sup>2</sup>, Safakath Karuthedath<sup>3</sup>, Ivan Ramirez<sup>2</sup>, Anna Jungbluth<sup>2</sup>, Frédéric Laquai<sup>3</sup>, Moritz Riede<sup>2</sup> and Natalie Banerji<sup>1</sup>

<sup>1</sup>Department of Chemistry and Biochemistry, University of Bern, Freiestrasse 3, 3012 Bern, Switzerland.

<sup>2</sup>Clarendon Laboratory, Department of Physics, University of Oxford, Parks Road, OX1 3PU, Oxford, UK.

<sup>3</sup>King Abdullah University of Science and Technology (KAUST), KAUST Solar Center (KSC), Physical Science and Engineering Division (PSE), Thuwal 23955-6900, Kingdom of Saudi Arabia.

#### AUTHOR CONTRIBUTIONS:

N.B. and M.R. conceived the project, which was led by N.B. Samples were prepared by I.R., A.J. and J.F.M.H, who also did the GIWAXS measurements. TA experiments were carried out by G.M., M.C. and N.B (< 1 ns time scale, room temperature), and by S.K. in the group of F.L. (long time scales, low temperature). EQE spectra were recorded by I.R. during a STEM visit to TU Dresden. G.M. and N.B. analysed and interpreted the spectroscopic data, and wrote the manuscript with input from all other authors.

The supporting information is published in the Appendix chapter of this thesis.

## 4.1. Introduction

For our studies, a TAPC:C<sub>60</sub> blend is selected, since it shows similar interfacial CT state energy of 1.4-1.5 eV and negligible donor aggregation over a wide range of compositions (5-50 wt.% TAPC),<sup>3-5</sup> good solar cell performance and high V<sub>oc</sub> at dilute donor concentrations,<sup>6</sup> as well as distinct donor absorption allowing selective C<sub>60</sub> excitation. The morphology of the 5 wt.% BHJ consists of large C<sub>60</sub> domains with TAPC molecules isolated and dispersed throughout the blend, while the 50 wt.% BHJ is notably without large C<sub>60</sub> domains and presents an intermixed donor:acceptor morphology (Figure 4-1).<sup>5,7</sup> Coherence lengths of ~65 Å and ~12 Å were found for the two samples, respectively, using Grazing-Incidence Wide-Angle X-ray Scattering (GIWAXS, Figure A.2-1). Thus, we can tune the C<sub>60</sub> domain size from the low-donor (5 wt.% TAPC) to the completely intermixed (50 wt.% TAPC) regime, while maintaining constant interfacial energetics. Relevant to both dilute and standard solar cell systems, we gain valuable insights into the effect of excitation energy on exciton dissociation, the local energetic landscape near the interface, and we identify different recombination mechanisms.

## 4.2. Results and Discussion

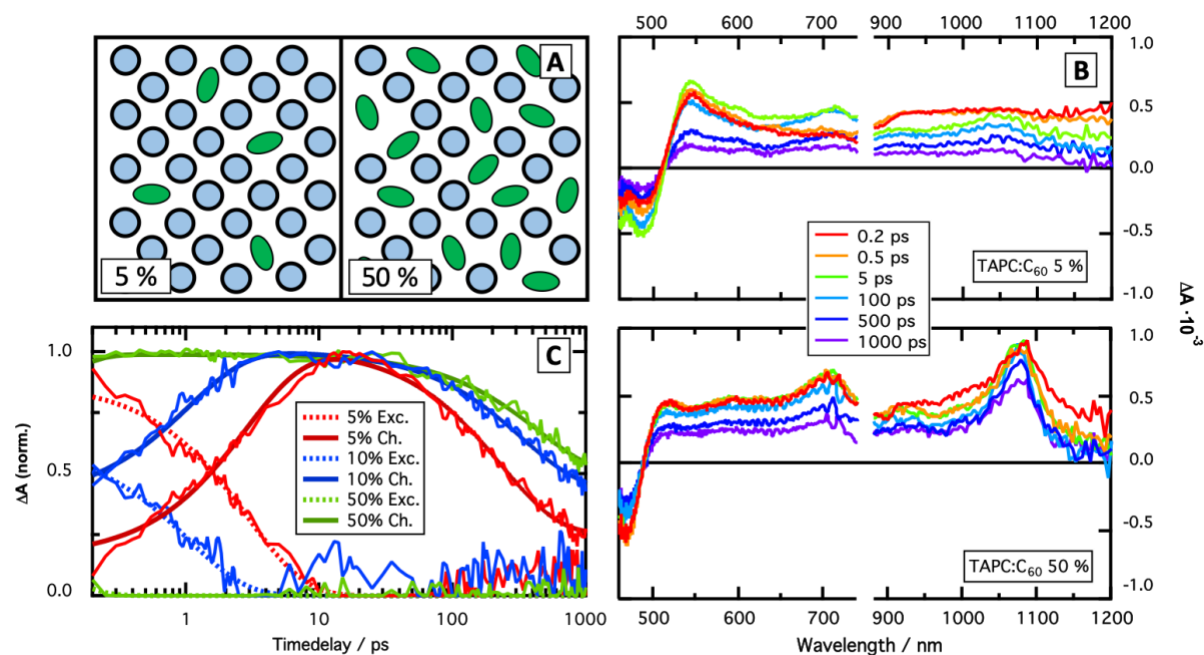


Figure 4.2-1 Transient absorption (TA) spectra of TAPC:C<sub>60</sub> blends with a weight ratio of 5 wt.% and 50 wt.% (B) at selected time delays (0.2 ps, 0.5 ps, 5 ps, 100 ps, 500 ps and 1 ns) at 610 nm pump excitation. The MCR-ALS decomposition into the dynamics of Frenkel exciton and charge signatures is shown in (C) for 5 wt.% (red), 10 wt.% (blue) and 50 wt.% (green) blends, with a kinetic model analysis of both, excitons (dashed lines) and charges (solid lines). (A) shows a 2D representation of the expected packing inside the bulk-heterojunctions, with C<sub>60</sub> represented as blue circles and TAPC as green ellipsoids in 5 wt.% and 50 wt.% blends.

The transient absorption (TA) spectra of TAPC:C<sub>60</sub> blends with donor weight ratios of 5 wt.% (A) and 50 wt.% (B) excited at 610 nm (selectively generating intramolecular C<sub>60</sub> Frenkel excitons) are shown in Figure 4-1. All TA spectra were recorded at a low excitation density of  $<10^{18} \text{ cm}^{-3}$ , so that many-body interactions between excitons and charges can be neglected on the investigated time scale. At early times ( $< 1 \text{ ps}$ ), the features of the 5 wt.% TA spectra are dominated by C<sub>60</sub> Frenkel exciton signatures at 920 and 450 nm, similar to 610 nm excitation of a neat C<sub>60</sub> film (Figure A.2-2). At later times ( $> 5 \text{ ps}$ ), following diffusion-limited hole transfer (HT) from the C<sub>60</sub> Frenkel excitons to TAPC, we observe the rise of charge-induced signatures at  $\sim 700 \text{ nm}$  for TAPC cation and  $\sim 1050 \text{ nm}$  for C<sub>60</sub> anion and the resulting oscillatory Electro-Absorption (EA) peaking at 485 nm and 545 nm.<sup>1</sup> The anion in C<sub>60</sub> is highly delocalized into the large fullerene clusters and therefore shows a relatively broad peak, as previously shown by Causa' et al.<sup>1</sup> The EA signature is a result of a field-induced shift in the ground state absorption of inter-C<sub>60</sub> CT transitions that occur in large C<sub>60</sub> clusters in the 400-500 nm region, with the field created by photogenerated charges and/or highly-delocalized



excitons (see discussion below). Figure 4-1B shows the TA spectra of the 50 wt.% blend, in which we see prompt charge signatures, since, unlike in dilute blends, the intermixed morphology does not require exciton diffusion before HT to TAPC. The anion peak (~1050 nm) is notably sharper and more pronounced because of the anion being localized on isolated C<sub>60</sub> molecules.<sup>1,8</sup> Therefore, as the morphology of the 50 wt.% blend does not allow for many large C<sub>60</sub> clusters, the ground state bleaching (GSB) dominates the negative band at 450 nm, with the EA having a smaller amplitude and being blue-shifted compared to the 5 wt.% blend. This is a result of the blue-shifted and less pronounced onset of inter-C<sub>60</sub> CT exciton absorption, as seen in the steady-state absorption spectra (Figure A.2-3).

*Table 4-1 Outcome of the kinetic modelling of the MCR-ALS decomposition dynamics from the TA data for all three TAPC:C<sub>60</sub> blends (5 wt.%, 10 wt.%, and 50 wt.%): Initial charge population at 0.2 ps ( $C_{init}$ ) expressed as a fraction of the total excitation density, intrinsic exciton lifetime ( $\tau_{exciton}$ ) and fraction of excitons decaying to the ground state, hole transfer time constant ( $\tau_{HT}$ ) and fraction of excitons undergoing hole transfer, charge recombination time constant ( $\tau_{rec}$ ) and fraction of charges undergoing recombination, offset due to long-lived charges ( $C_{long}$ ) expressed as a fraction of the total charge population.*

	5 wt.% Blend	10 wt.% Blend	50 wt.% Blend
$C_{init}$	20%	50%	97%
$\tau_{exciton}$ (ps)	150 (2%)	150 (1%)	150 (0%)
$\tau_{HT}$ (ps)	2.9 (98%)	1.1 (99%)	<0.1 (100%)
$\tau_{rec}$ (ps)	280 (75%)	280 (53%)	280 (42%)
$C_{long}$	25%	47%	58%

The dynamics of excitons and charges, obtained from the decomposition of the TA spectra into the two corresponding spectral components using Multivariate Curve Resolution with Alternating Least Squares (MCR-ALS),<sup>9-12</sup> are shown for 5 wt.%, 10 wt.% and 50 wt.% blends in Figure 4-1C. These dynamics were subsequently analysed with a kinetic model, which accounts for the evolution of the excitonic and charge species (Figure A.2-4). In brief, the C<sub>60</sub> Frenkel excitons undergo HT to TAPC in competition with their intrinsic decay to the ground state. The HT generates charges that either recombine within the time window of the experiment (< 1 ns) or that are long-lived. Intrinsic exciton lifetimes in C<sub>60</sub> were fixed in the model to 150 ps, as previously determined for neat C<sub>60</sub> films (Table 4-1).<sup>1</sup> Since intrinsic decay is negligible compared to the predominant quenching by HT, any differences in the intrinsic

exciton lifetime due to the blend morphology were not accounted for. In the dilute blends, we expect that Frenkel excitons need to diffuse through C<sub>60</sub> clusters in order to reach TAPC donors prior to HT. In support of this, the time constant for diffusion-limited HT follows the trend expected from the morphology, with HT times decreasing from 3 ps (5 wt.% blend) to 1 ps (10 wt.% blend) as the size of the C<sub>60</sub> clusters decreases (Table 4-1 and Figure 4-1C). Since no exciton diffusion is required in the molecularly intermixed 50 wt.% blend, charge signatures are present at the earliest time delays and the HT time constant reduces to <100 fs. Therefore, the fraction of charges generated by prompt HT within the 0.2 ps time resolution of our analysis increases from 20% to 97% when going from the 5 wt.% to the 50 wt.% blend (Table 4-1).

In our TA experiments, relatively fast recombination of charges is seen in all films on the hundreds of picoseconds timescale. Surprisingly, this charge recombination is more pronounced in the 5 wt.% than the 50 wt.% BHJ with, respectively, 75% and 42 % of charges recombining within the 1 ns time window of our experiment (Table 4-1, Figure 4-1C). In contrast, the 5 wt.% system shows the best solar cell performance of all blends, with short circuit current density, fill factor and overall PCE of 5.94 mAcm<sup>-2</sup>, 0.52 and 2.81 %, respectively.<sup>4,13</sup> We can rule out bimolecular recombination of free charges as the origin of this effect, since all measurements were carried out at excitation fluences where the dynamics are density-independent (Figure A.2-5). Typically, sub-nanosecond charge recombination in organic donor:acceptor blends is assigned to geminate charge recombination (gCR) of charges that have not entirely escaped their mutual attraction at the donor-acceptor interface.<sup>14</sup> This process is indeed expected in the 50 wt.% blend, since intimately mixed systems lead to poor charge dissociation and enhanced gCR.<sup>14-16</sup> In contrast, neat fullerene regions are known to assist free charge generation, which is ultrafast in fullerene-based blends.<sup>14,15,17-19</sup> We therefore expect that the electrons in the dilute TAPC:C<sub>60</sub> blends can dissociate from the holes into the C<sub>60</sub> domains, allowing efficient and ultrafast separation into free charges, as well as limiting gCR. Moreover, the work by Collado-Fregoso et al. confirms that, in dilute TAPC:C<sub>60</sub> blends, the interfacial CT states dissociate faster than they recombine.<sup>6</sup>

We suggest that the sub-nanosecond recombination mechanisms are different in the 5 wt.% and 50 wt.% blends, and that the phenomenon observed in the 5 wt.% sample is a peculiarity of thin films (without electrodes) with dilute morphologies. Thus, we assume that the recombination in the 50 wt.% blend is predominantly geminate and concerns bound electron-hole pairs, while the recombination in the dilute blends involves free electrons that recombine with trapped holes. In the dilute BHJs, holes move predominantly via long-range tunnelling

between isolated donor molecules,<sup>5,20</sup> so that their mobility is orders of magnitude lower than that of the electrons in the C<sub>60</sub> domains. This has been shown for both the steady-state mobilities and the relevant transient mobilities on the < 1 ns time scale (by TREFISH - time-resolved electric-field-induced second harmonic generation experiments).<sup>13,20</sup> We can therefore consider the holes to be trapped on isolated TAPC molecules during the time window probed in our TA experiments, while highly mobile free electrons can encounter them, leading to monomolecular trap-based recombination.<sup>21</sup> For the few free charges that manage to separate at the interface of the intermixed 50 wt.% blend, trap-assisted recombination plays a lesser role, since the electron mobility decreases due to disruption of the C<sub>60</sub> crystallinity at higher TAPC concentration,<sup>13,22</sup> while the hole mobility increases due to improved hole percolation pathways.<sup>20</sup> TA cannot distinguish between bound and free charges, but the extent of the fast recombination can be evaluated from the offset caused by long-lived charges (which recombine much slower than our measurement window). This offset is lower in the dilute blends than it is in the intermixed 50 wt.% blend, indicating that the trap-assisted mechanism leads to an even higher charge loss than gCR (Table 4-1). While charges remain mostly bound in interfacial CT states in the 50 wt.% BHJ, CT dissociation is much more efficient in the 5 wt.% blend, but the free electrons can also readily find trapped holes and reform CT states. In both systems, the overall recombination is therefore rate limited by CT decay to the ground state, which proceeds with a similar time constant of 280 ps, since TAPC:C<sub>60</sub> CT states are of the same energy independently of the donor concentration.<sup>23</sup>

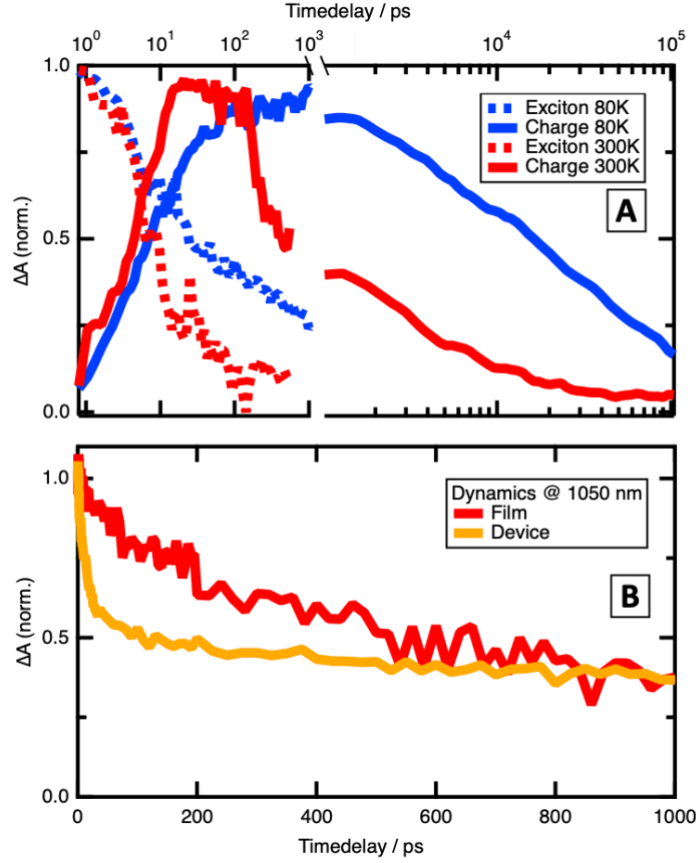


Figure 4.2-2 (A) MCR-ALS decomposition dynamics of the exciton (dashed lines) and charge (solid lines) components of a 5 wt.% TAPC:C<sub>60</sub> thin film excited at 532 nm at 80 K (blue lines) and at 300 K (red lines). (B) TA dynamics probed at the C<sub>60</sub> anion peak (~1050 nm) for a 5 wt.% TAPC:C<sub>60</sub> film without contacts (red) and the corresponding device (orange), both excited at 450 nm.

To gain further insights to the processes occurring in the dilute 5 wt.% TAPC:C<sub>60</sub> film, we have measured temperature-dependent TA dynamics at short ( $< 1$  ns) and long ( $< 10 \mu s$ ) time scales. The exciton and charge dynamics from the MCR-ALS analysis at low (80K) and high (300K) temperature are shown in Figure 4-2A. Both charge formation and especially recombination are markedly slower at 80K. We hypothesize that it is related to freezing of exciton diffusion and reduced electron mobility leading to reduced encounter rates, while other parameters such as the intrinsic charge transfer/recombination rates and the CT state lifetime are also affected at low temperature. Supporting the trap-assisted recombination mechanism, we see that when the electron motion is slowed at 80 K (from  $\sim 10^0 \text{ cm}^2 \text{V}^{-1} \text{s}^{-1}$  at 300 K to  $\sim 10^{-3} \text{ cm}^2 \text{V}^{-1} \text{s}^{-1}$  at 80 K in transistor measurements),<sup>24</sup> they encounter fewer trapped holes and the  $< 1$  ns recombination is absent.

Coming back to the discrepancy between the important sub-nanosecond trap-based recombination (seen by TA spectroscopy in the dilute thin films without electrodes) and the

good performance of the corresponding devices, we performed TA measurements on the 5 wt.% blend in a full device structure with semi-transparent back electrode: ITO / MoO<sub>x</sub> (2 nm) / 5 wt.% TAPC:C<sub>60</sub> (50 nm) / BPhen (6 nm)/ Al (10 nm) (at V<sub>OC</sub>, no external circuit). The device was excited at 450 nm to avoid strong scattering of the pump in the TA probe range. In the device configuration, mobile photogenerated electrons can be collected at the Al cathode. The notably faster decay of the C<sub>60</sub> anion peak at 1050 nm observed in the device compared to the thin film (Figure 4-2B) supports some electron extraction from the active layer into the electrode on the < 1 ns time scale. Such fast electron extraction is consistent with previous TREFISH measurements, which have revealed that electrons are extracted from dilute BHJ devices on the 20 ps to 1 ns time scale, while hole extraction occurs only after 200 ns.<sup>20</sup> Since electrons are extracted on a time scale relevant to trap-assisted recombination, we suggest that in devices, the highly mobile electrons rapidly leave the active layer and are thus not able to recombine with trapped holes. However, we could not unambiguously confirm reduced trap-assisted recombination and slower decay of the hole population in the device structure, since a large EA signature (caused by additional fields in the device) dominates the visible spectral range of the TA probe spectrum (Figure A.2-6 A). The slower decay of this EA signal compared to the one of the neat film could nevertheless be an indication that some charges live longer in the device (Figure A.2-6 B). In OPV operating conditions, the faster electron than hole extraction rate results in a lower steady-state electron density in the active layer, suppressing trap-based recombination that we see by TA spectroscopy in the un-contacted films. This allows the higher photocurrent and PCE in dilute (5 wt.%) blends compared to intermixed morphologies (50 wt.%), where charges are lost due to gCR even in device configuration.

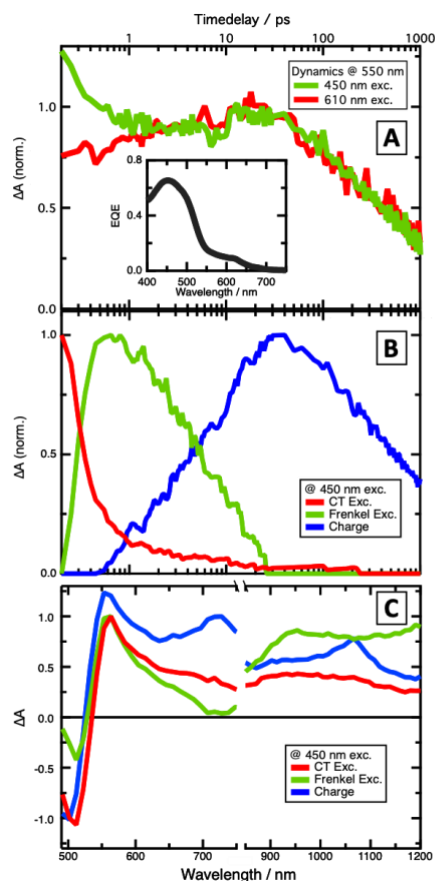


Figure 4.2-3 (A) Dynamics of the TA spectra probed at 550 nm (EA peak overlapping with photo-induced absorption) of the 5 wt.% TAPC:C<sub>60</sub> blend excited at 450 nm (green line) and 610 nm (red line, see Figure 4-1A), normalized to the maximum of the dynamics with 610 nm excitation. The inset shows the EQE spectrum of the dilute TAPC:C<sub>60</sub> blend. (B) MCR-ALS decomposition of the TA spectra of the 5 wt.% TAPC:C<sub>60</sub> blend excited at 450 nm, with the dynamics of inter-C<sub>60</sub> CT excitons in red, of Frenkel excitons in green and of charges in blue. The spectra of those MCR-ALS components are shown in (C) with the same colour coding.

We now turn to the excitation wavelength dependence in the dilute TAPC:C<sub>60</sub> blends. As previously discussed for neat C<sub>60</sub> films by Causa' et al.,<sup>1</sup> excitation of C<sub>60</sub> clusters at 610 nm yields localized Frenkel excitons, while excitation at 450 nm yields delocalized inter-C<sub>60</sub> CT excitons (not to be confused with interfacial CT states in donor:acceptor blends), which are characterized by a pronounced EA signature peaking at 550 nm.<sup>1</sup> In neat C<sub>60</sub> films, these inter-C<sub>60</sub> CT excitons decay to Frenkel excitons within 0.2 ps, while they can dissociate to charges in neat C<sub>60</sub> devices.<sup>1,25</sup> Inter-C<sub>60</sub> CT excitons can also be generated in the fullerene domains of dilute-donor BHJs. To evaluate their impact on the HT mechanism to donor molecules, we measured the TA spectra of the 5 wt.% TAPC:C<sub>60</sub> film excited at 450 nm. Figure 4-3A shows the TA dynamics of this blend probed at 550 nm (EA signal overlapped with photoinduced absorption of both inter-C<sub>60</sub> CT excitons and charges), for excitation at 450 nm and 610 nm.

There is a notable decay in the signal with 450 nm excitation on the 1 ps time scale, after which, the rise corresponding to HT and subsequent decay due to charge recombination are the same at both excitation wavelengths. The amplitude spectra from a multiexponential global analysis of the TA data, shown in Figure A.2-7 confirm that the diffusion-limited HT (1 ps), trap-assisted charge recombination (512 ps), and long-lived charge component (offset) are equivalent for excitation at 450 nm (inter-C<sub>60</sub> CT excitons) and 610 nm (Frenkel excitons). It has been suggested that direct charge generation via CT excitons in neat fullerene domains contributes to photocurrent generation in organic solar cells,<sup>37, 26</sup> but our results show that the inter-C<sub>60</sub> CT excitons do not significantly affect the charge generation mechanism, disproving that bulk-ionization and intermolecular exciton delocalization are relevant for the operation of C<sub>60</sub>-based dilute-donor systems. The EQE spectrum (Figure 4-3A, inset) agrees with efficient photocurrent generation from spectral regions of both inter-C<sub>60</sub> CT and Frenkel transitions, and a similar field-independence of charge generation has also been demonstrated by TDCF measurements on dilute blends.<sup>6</sup> This is in contrast to neat C<sub>60</sub> devices, where only inter-C<sub>60</sub> CT excitons yield photocurrent.<sup>1</sup> It allows to exploit the entire Frenkel and CT spectral range of the fullerene absorption to generate charges in dilute-donor BHJs.

Figure 4-3B shows the MCR-ALS decomposition dynamics obtained from the TA data. The corresponding component spectra (Figure 4-3C) are assigned to inter-C<sub>60</sub> CT excitons characterized by their pronounced EA signal, Frenkel excitons showing photoinduced absorption at 550 nm and 950 nm, and the charge-induced spectrum consisting of a shifted EA signal together with the TAPC cation absorption (710 nm) and the C<sub>60</sub> anion band (1050 nm). There is a rapid decay (<1 ps) of the inter-C<sub>60</sub> CT excitons and concomitant rise of Frenkel excitons, which in turn convert to the charge component. The 0.2 ps amplitude spectrum of the 5 wt.% TAPC blends supports that inter-C<sub>60</sub> CT excitons localize to Frenkel excitons, similar as is observed in neat C<sub>60</sub> films with 450 nm excitation (Figure A.2-7). This fast relaxation is absent when Frenkel excitons are directly generated at 610 nm and in the 50 wt.% BHJ at both excitation wavelengths, since no C<sub>60</sub> clusters are present in the intermixed blend. We conclude that the initially generated inter-C<sub>60</sub> CT excitons in C<sub>60</sub> clusters first undergo ultrafast relaxation to Frenkel excitons before the latter diffuse to TAPC molecules and undergo HT. Although we cannot exclude that some inter-C<sub>60</sub> CT excitons generated near TAPC molecules directly undergo HT, the majority of HT occurs from Frenkel excitons that are generated from inter-C<sub>60</sub> CT excitons faster than exciton diffusion to an interface.

Finally, we turn our attention to the EA signatures generated in our systems. Upon 450 nm excitation of the 5 wt.% TAPC:C<sub>60</sub> blend, two sources of electric field can be identified, which both provoke an EA response in neighbouring C<sub>60</sub> clusters: First, the short-lived inter-C<sub>60</sub> CT excitons and second, the charges formed between the TAPC donor and C<sub>60</sub> acceptor. In Figure 4-4A, we compare the TA spectra at an early time delay (0.2 ps), where we have predominantly inter-C<sub>60</sub> CT excitons, and at 100 ps, where the EA signal is generated by TAPC<sup>+</sup>/C<sub>60</sub><sup>-</sup> charges. At early times, the oscillatory EA signature corresponds to the spectral position of the steady-state bulk EA signal recorded on a neat C<sub>60</sub> device under reverse bias (red dotted line), while the position of the EA signal is clearly blue-shifted at the later time delay (the manually shifted steady-state EA is shown as a dotted blue line to illustrate this). By taking the zero-crossing of the TA spectra, we have time-resolved the gradual shift of the EA (Figure 4-4B), which occurs within a few picoseconds and corresponds to the decay of inter-C<sub>60</sub> CT excitons (Figure 4-3B). EA signatures, and their corresponding spectral positions, have been previously used to probe the energetics of the local environment of charges.<sup>14,27,28</sup> Therefore, we interpret the shift in EA as a difference in the energetics of the C<sub>60</sub> clusters causing the EA. As the EA at early times is caused by inter-C<sub>60</sub> CT excitons in bulk C<sub>60</sub> clusters, we assign the EA position to the local energy environment within these clusters. In the same way, as the later time EA is caused by charges formed at the TAPC:C<sub>60</sub> interface (with the holes remaining on TAPC), the shifted EA position is assigned to a different local energy environment in C<sub>60</sub> clusters near the TAPC donors (Figure 4-4D).

As shown in Figure 4-4C, by integrating both the early and late EA signals twice (since the EA in C<sub>60</sub> has a second derivative line-shape compared to the absorption),<sup>29-31</sup> we are able to reconstruct the absorption spectra of the C<sub>60</sub> clusters both in the bulk and close to the TAPC donor. The calculated absorption spectrum at early times fits well with the steady-state CT absorption of neat C<sub>60</sub>, because the EA originates from bulk C<sub>60</sub> clusters. At later delay times, the calculated absorption spectrum from C<sub>60</sub> clusters near a TAPC molecule is blue shifted by 10 nm (or 4.5 meV). The energetic shift between C<sub>60</sub> clusters near and far from a TAPC donor is likely due to either the disruption of crystallinity in the clusters or the inter-C<sub>60</sub> interactions between C<sub>60</sub> and TAPC molecules.<sup>4,32</sup> Therefore, our results provide the opportunity to selectively monitor the absorption of interfacial C<sub>60</sub> clusters, which is not possible with bulk techniques. Since C<sub>60</sub> molecules near TAPC are at higher energy than those in the bulk, an energetic driving force exists that aids electrons to separate from positively-charged TAPC molecules after HT. The benefits of such an energetic gradient have been evoked earlier as an



important factor promoting free charge generation in organic solar cells,<sup>33-36</sup> together with other parameters such as enhanced charge delocalization into the C<sub>60</sub> clusters.<sup>17,27,37</sup>

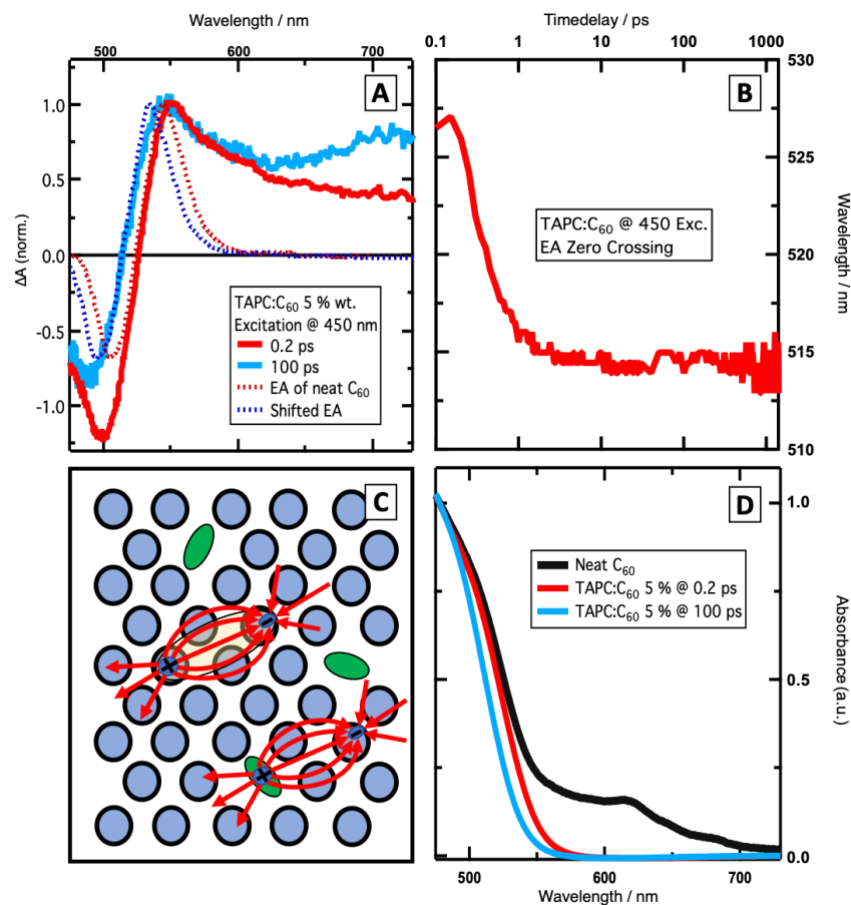


Figure 4.2-4 (A) Normalized TA spectra of the 5 wt.% TAPC:C<sub>60</sub> blend excited at 450 nm, at 0.2 ps (solid red) and 100 ps (solid blue), together with the steady-state EA signature recorded in a neat C<sub>60</sub> device (dotted red line), which is also shown manually shifted to match the zero crossing point at 100 ps (dotted blue line). (B) Time evolution of the zero-crossing point of the EA signal from the TA spectra. (C) Calculated absorption spectra of C<sub>60</sub> clusters from double integration of the EA signal at different times (0.2 ps red, 100 ps blue), with the absorption spectrum of neat C<sub>60</sub> film for comparison (black). (D) Schematics of the electric fields responsible for the EA, as produced by inter-C<sub>60</sub> CT excitons in C<sub>60</sub> clusters and by charges generated by HT to TAPC molecules.

### 4.3. Conclusion

In conclusion, we have investigated vapor-deposited organic solar cells based on TAPC:C<sub>60</sub> blends with low (5 wt.%, 10 wt.%) and high (50 wt.%) TAPC concentration, creating dilute and molecularly mixed morphologies, respectively. In agreement with previous work on solution-processed solar cells, we find that large C<sub>60</sub> domains in the dilute blends lead to exciton diffusion-limited hole transfer and assist the generation of free electrons by enhancing electron delocalization and transport. In addition, we directly visualize, via a gradual shift of the electro-absorption, an energetic gradient driving electrons away from the TAPC site into the C<sub>60</sub> bulk, further favoring free charge generation. We show that charge transfer excitons within C<sub>60</sub> clusters (and any related intermolecular delocalization and auto-ionization) do not play a primordial role in the hole transfer process, since they undergo rapid localization to Frenkel excitons before dissociating. The entire Frenkel and charge transfer range of the fullerene absorption can thus be exploited for charge generation. Finally, we identify a fast monomolecular trap-based recombination mechanism in thin films containing 5 wt.% TAPC, where free electrons recombine with holes that are trapped on isolated TAPC molecules. Dilute TAPC:C<sub>60</sub> devices nevertheless have good solar cell efficiency,<sup>6</sup> because this recombination is suppressed when electrons are rapidly extracted. In contrast, hole transfer in the intermixed 50 wt.% blend leads to bound electron-hole pairs that geminately recombine, causing poor device performance. In general, the fast trap-based recombination can harm the performance of dilute solar cells, if charge extraction cannot effectively compete. For C<sub>60</sub>-based systems containing different dilute donors, this might contribute to the observed strong field-dependence, low fill factor and poor efficiency of systems with low-lying interfacial CT states, where the intrinsic recombination rate is enhanced (energy gap law),<sup>6</sup> increasing the probability of recombination when a free electron encounters a trapped hole. Overall, dilute morphologies present an opportunity to promote free charge generation in organic solar cells compared to intermixed blends, but the fast trap-based recombination that we evidence must be overcome by rapid extraction.

## Reference

- (1) Causa', M.; Ramirez, I.; Martinez Hardigree, J. F.; Riede, M.; Banerji, N. Femtosecond Dynamics of Photoexcited C60 Films. *The Journal of Physical Chemistry Letters* **2018**, *9*, 1885-1892.
- (2) Moore, G. J.; Causa', M.; Martinez Hardigree, J. F.; Karuthedath, S.; Ramirez, I.; Jungbluth, A.; Laquai, F.; Riede, M.; Banerji, N. Ultrafast Charge Dynamics in Dilute-Donor versus Highly Intermixed TAPC:C60 Organic Solar Cell Blends. *The Journal of Physical Chemistry Letters* **2020**, *11*, 5610-5617.
- (3) Vandewal, K.; Albrecht, S.; Hoke, E. T.; Graham, K. R.; Widmer, J.; Douglas, J. D.; Schubert, M.; Mateker, W. R.; Bloking, J. T.; Burkhard, G. F.; Sellinger, A.; Fréchet, J. M. J.; Amassian, A.; Riede, M. K.; McGehee, M. D.; Neher, D.; Salleo, A. Efficient charge generation by relaxed charge-transfer states at organic interfaces. *Nature materials* **2014**, *13*, 63-68.
- (4) Vandewal, K.; Benduhn, J.; Schellhammer, K. S.; Vangerven, T.; Rückert, J. E.; Piersimoni, F.; Scholz, R.; Zeika, O.; Fan, Y.; Barlow, S.; Neher, D.; Marder, S. R.; Manca, J. V.; Spoltore, D.; Cuniberti, G.; Ortmann, F. Absorption tails of donor:C60 blends provide insight into thermally activated charge-transfer processes and polaron relaxation. *Journal of the American Chemical Society* **2017**, *139*, 1699-1704.
- (5) Lee, T.; Sanzogni, A.; Zhangzhou, N.; Burn, P. L.; Mark, A. E. Morphology of a Bulk Heterojunction Photovoltaic Cell with Low Donor Concentration. *ACS Appl Mater Interfaces* **2018**, *10*, 32413-32419.
- (6) Collado-Fregoso, E.; Pugliese, S. N.; Wojcik, M.; Benduhn, J.; Bar-Or, E.; Perdigón Toro, L.; Hörmann, U.; Spoltore, D.; Vandewal, K.; Hodgkiss, J. M.; Neher, D. Energy-Gap Law for Photocurrent Generation in Fullerene-Based Organic Solar Cells: The Case of Low-Donor-Content Blends. *Journal of the American Chemical Society* **2019**, *141*, 2329-2341.
- (7) Vandewal, K.; Widmer, J.; Heumueller, T.; Brabec, C. J.; McGehee, M. D.; Leo, K.; Riede, M. K.; Salleo, A. Increased Open-Circuit Voltage of Organic Solar Cells by Reduced Donor-Acceptor Interface Area. *Advanced Materials* **2014**, *26*, 3839-3843.
- (8) Yamamoto, S.; Guo, J.; Ohkita, H.; Ito, S. Formation of Methanofullerene Cation in Bulk Heterojunction Polymer Solar Cells Studied by Transient Absorption Spectroscopy. *Advanced Functional Materials* **2008**, *18*, 2555-2562.
- (9) Jaumot, J.; Gargallo, R.; de Juan, A.; Tauler, R. A graphical user-friendly interface for MCR-ALS: a new tool for multivariate curve resolution in MATLAB. *Chemometr Intell Lab* **2005**, *76*, 101-110.
- (10) de Juan, A.; Tauler, R. Chemometrics applied to unravel multicomponent processes and mixtures: Revisiting latest trends in multivariate resolution. *Analytica Chimica Acta* **2003**, *500*, 195-210.
- (11) Amrhein, M.; Srinivasan, B.; Bonvin, D.; Schumacher, M. M. On the rank deficiency and rank augmentation of the spectral measurement matrix. *Chemometr Intell Lab* **1996**, *33*, 17-33.
- (12) Tauler, R. Multivariate curve resolution applied to second order data. *Chemometr Intell Lab* **1995**, *30*, 133-146.
- (13) Zhang, M.; Wang, H.; Tian, H.; Geng, Y.; Tang, C. W. Bulk heterojunction photovoltaic cells with low donor concentration. *Advanced Materials* **2011**, *23*, 4960-4964.
- (14) Causa', M.; De Jonghe-Risse, J.; Scarongella, M.; Brauer, J. C.; Buchaca-Domingo, E.; Moser, J.-E.; Stingelin, N.; Banerji, N. The fate of electron-hole pairs in polymer:fullerene blends for organic photovoltaics. *Nature Communications* **2016**, *7*, 12556.

- (15) Scarongella, M.; De Jonghe-Risse, J.; Buchaca-Domingo, E.; Causa, M.; Fei, Z.; Heeney, M.; Moser, J. E.; Stingelin, N.; Banerji, N. A close look at charge generation in polymer:fullerene blends with microstructure control. *J Am Chem Soc* **2015**, *137*, 2908-2918.
- (16) Howard, I. A.; Mauer, R.; Meister, M.; Laquai, F. Effect of morphology on ultrafast free carrier generation in polythiophene: fullerene organic solar cells. *Journal of the American Chemical Society* **2010**, *132*, 14866-14876.
- (17) Bittner, E. R.; Silva, C. Noise-induced quantum coherence drives photo-carrier generation dynamics at polymeric semiconductor heterojunctions. *Nat Commun* **2014**, *5*, 3119.
- (18) Gélinas, S.; Rao, A.; Kumar, A.; Smith, S. L.; Chin, A. W.; Clark, J.; van der Poll, T. S.; Bazan, G. C.; Friend, R. H. Ultrafast Long-Range Charge Separation in Organic Semiconductor Photovoltaic Diodes. *Science* **2014**, *343*, 512.
- (19) Provencher, F.; Bérubé, N.; Parker, A. W.; Greetham, G. M.; Towrie, M.; Hellmann, C.; Côté, M.; Stingelin, N.; Silva, C.; Hayes, S. C. Direct observation of ultrafast long-range charge separation at polymer–fullerene heterojunctions. *Nature Communications* **2014**, *5*, 4288.
- (20) Melianas, A.; Pranculis, V.; Spoltore, D.; Benduhn, J.; Inganäs, O.; Gulbinas, V.; Vandewal, K.; Kemerink, M. Charge Transport in Pure and Mixed Phases in Organic Solar Cells. *Advanced Energy Materials* **2017**, 1700888, 1700888.
- (21) Street, R. A.; Schoendorf, M.; Lee, J. Y.; Roy, A. Interface state recombination in organic solar cells. *Physical Review B* **2010**, *81*, 205307.
- (22) Pandey, R.; Gunawan, A. A.; Mkhoyan, K. A.; Holmes, R. J. Efficient Organic Photovoltaic Cells Based on Nanocrystalline Mixtures of Boron Subphthalocyanine Chloride and C60. *Advanced Functional Materials* **2012**, *22*, 617-624.
- (23) Vandewal, K.; Benduhn, J.; Schellhammer, K. S.; Vangerven, T.; Rückert, J. E.; Piersimoni, F.; Scholz, R.; Zeika, O.; Fan, Y.; Barlow, S.; Neher, D.; Marder, S. R.; Manca, J.; Spoltore, D.; Cuniberti, G.; Ortmann, F. Absorption Tails of Donor:C60 Blends Provide Insight into Thermally Activated Charge-Transfer Processes and Polaron Relaxation. *Journal of the American Chemical Society* **2017**, *139*, 1699-1704.
- (24) Singh, T. B.; Marjanović, N.; Matt, G. J.; Günes, S.; Sariciftci, N. S.; Montaigne Ramil, A.; Andreev, A.; Sitter, H.; Schwödiauer, R.; Bauer, S. High-mobility n-channel organic field-effect transistors based on epitaxially grown C60 films. *Organic Electronics* **2005**, *6*, 105-110.
- (25) Zou, Y.; Holmes, R. J. The Role of Exciton Ionization Processes in Bulk Heterojunction Organic Photovoltaic Cells. **2015**, *5*, n/a-n/a.
- (26) Burkhard, G. F.; Hoke, E. T.; Beiley, Z. M.; McGehee, M. D. Free carrier generation in fullerene acceptors and its effect on polymer photovoltaics. *Journal of Physical Chemistry C* **2012**, *116*, 26674-26678.
- (27) Gélinas, S.; Rao, A.; Kumar, A.; Smith, S. L.; Chin, A. W.; Clark, J.; van der Poll, T. S.; Bazan, G. C.; Friend, R. H. Ultrafast Long-Range Charge Separation in Organic Semiconductor Photovoltaic Diodes. *Science* **2014**, *343*, 512-516.
- (28) Jakowetz, A. C.; Böhm, M. L.; Sadhanala, A.; Huettnner, S.; Rao, A.; Friend, R. H. Visualising Excitations at Buried Heterojunctions in Organic Semiconductor Blends. *Nature Materials* **2017**.
- (29) Kazaoui, S.; Minami, N.; Tunabe, Y.; Byrne, H. J.; Eilmes, A.; Petelenz, P. Comprehensive analysis of intermolecular charge-transfer excited states in C60 and C70 films. *Phys. Rev. B* **1998**, *58*.
- (30) Petelenz, P.; Slawik, M.; Pac, B. Electro-absorption spectrum of buckminsterfullerene—evidence for the existence of charge transfer states. *Synthetic metals* **1994**, *64*, 335-339.

- (31) Jeglinski, S.; Vardeny, Z. V.; Moses, D.; Srdanov, V. I.; Wudl, F. Electroabsorption studies of undoped C60 thin films. *Synthetic metals* **1992**, *50*, 557-563.
- (32) Jamieson, F. C.; Domingo, E. B.; McCarthy-Ward, T.; Heeney, M.; Stingelin, N.; Durrant, J. R. Fullerene crystallisation as a key driver of charge separation in polymer/fullerene bulk heterojunction solar cells. *Chemical Science* **2012**, *3*, 485-492.
- (33) Burke, T. M.; McGehee, M. D. How high local charge carrier mobility and an energy cascade in a three-phase bulk heterojunction enable >90% quantum efficiency. *Adv Mater* **2014**, *26*, 1923-1928.
- (34) Izawa, S.; Nakano, K.; Suzuki, K.; Hashimoto, K.; Tajima, K. Dominant Effects of First Monolayer Energetics at Donor/Acceptor Interfaces on Organic Photovoltaics. *Advanced Materials* **2015**, *27*, 3025-3031.
- (35) Nakano, K.; Suzuki, K.; Chen, Y.; Tajima, K. Roles of Energy/Charge Cascades and Intermixed Layers at Donor/Acceptor Interfaces in Organic Solar Cells. *Scientific Reports* **2016**, *6*, 29529.
- (36) Sweetnam, S.; Graham, K. R.; Ngongang Ndjawa, G. O.; Heumuller, T.; Bartelt, J. A.; Burke, T. M.; Li, W.; You, W.; Amassian, A.; McGehee, M. D. Characterization of the polymer energy landscape in polymer:fullerene bulk heterojunctions with pure and mixed phases. *J Am Chem Soc* **2014**, *136*, 14078-14088.
- (37) Jakowetz, A. C.; Böhm, M. L.; Zhang, J.; Sadhanala, A.; Huettnner, S.; Bakulin, A. A.; Rao, A.; Friend, R. H. What Controls the Rate of Ultrafast Charge Transfer and Charge Separation Efficiency in Organic Photovoltaic Blends. *Journal of the American Chemical Society* **2016**, *138*, 11672-11679.



# 5 Following Charge Transfer State Formation and Recombination in Dilute Donor Organic Photovoltaics

## Foreword

The work in this chapter is the third part of a series of three works. The series starts with the photo physics of neat C<sub>60</sub> films and then continues to dilute donor systems with C<sub>60</sub> as acceptor. Firstly with a non-aggregating, symmetric donor (TAPC) with consistent CT state energies and now with an aggregating, not completely symmetric donor ( $\alpha$ 6T) whose CT state energies decrease with increased donor concentration.

The first part is published in the Journal of Physical Chemistry Letters by Martina Causa' et al. titled *Femtosecond Dynamics of Photoexcited C<sub>60</sub> Films*<sup>1</sup>.

The second part is published in Chapter 4 of this thesis and the Journal of Physical Chemistry Letters by Gareth John Moore et al. titled *Ultrafast Charge Dynamics in Dilute-Donor versus Highly Intermixed TAPC: C<sub>60</sub> Organic Solar Cell Blends*.<sup>2</sup>

The work by Causa' et al. on neat C<sub>60</sub> films showed the presence of both CT and Frenkel excitons which were selectively excited at 450 nm and 610 nm respectively. The spectral shapes and dynamics of the two exciton species were presented, where the CT exciton has a pronounced EA signal owing to its delocalization over multiple molecules. The fast relaxation of CT to Frenkel excitons was also elucidated and a time constant of 0.18 ps deduced along with a Frenkel exciton lifetime of 150 ps. Lastly the spectral shape of the C<sub>60</sub> anion was related to its delocalisation with a sharper peak indicating a less localised electron.

The work by Moore et al. on dilute TAPC blends first, we show that intermolecular charge-transfer (CT) excitons in the C<sub>60</sub> clusters of dilute BHJs rapidly localize to Frenkel excitons

prior to dissociating at the donor:acceptor interface. Thus, both Frenkel and CT excitons generate photocurrent over the entire fullerene absorption range. Second, we selectively monitor interfacial and bulk C<sub>60</sub> clusters via their electro-absorption, demonstrating an energetic gradient that assists free charge generation. Third, we identify a fast (<1 ns) recombination channel, whereby free electrons recombine with trapped holes on isolated TAPC molecules. This can harm the performance of dilute solar cells unless the electrons are rapidly extracted in efficient devices.

The work in this chapter is done by:

Gareth John Moore<sup>1</sup>, Florian Günther<sup>2</sup>, Martina Causa<sup>1</sup>, Anna Jungbluth<sup>3</sup>, Josue F. Martinez Hardigree<sup>3</sup>, Ivan Ramirez<sup>3</sup>, Moritz Riede<sup>3</sup>, Frank Ortmann<sup>2</sup> and Natalie Banerji<sup>1</sup>

<sup>1</sup>Department of Chemistry and Biochemistry, University of Bern, Freiestrasse 3, 3012 Bern, Switzerland.

<sup>2</sup>Department of Chemistry, Technische Universität München, 85748 Garching b. München, Germany

<sup>3</sup>Clarendon Laboratory, Department of Physics, University of Oxford, Parks Road, OX1 3PU, Oxford, UK.

#### AUTHOR CONTRIBUTIONS:

N.B. and M.R. conceived the project, which was led by N.B. Samples were prepared by I.R., A.J. and J.F.M.H. TA experiments were carried out by G.M., M.C. and N.B. TD-DFT simulations were performed by F.G and F.O. G.M. and N.B. analysed and interpreted the spectroscopic data, G.M., F.G., F.O and N.B. wrote the manuscript.



#### 4.4. Introduction

Even with a well-chosen sample set, transient absorption (TA) spectroscopy is usually unable to spectrally resolve bound charge transfer (CT) states and separated charges (SC), making following the charge separation and recombination processes more difficult.

In this study, we investigate thermally evaporated thin films intended for use as active layers in organic solar cells with morphologies controlled by the donor:acceptor ratios as well as by intentionally separating the materials in a bilayer. Bulk heterojunctions (BHJs) with more than 90% fullerene acceptor material and small molecule donors, ‘dilute-donor organic solar-cells’, create a morphology where the donors are completely isolated and surrounded by acceptor molecules.<sup>3,4</sup> Here, we use both TA spectroscopy and time-dependent density functional theory (TD-DFT) simulations to investigate the charge separation process in dilute-donor, phase separated and bilayer  $\alpha$ -sexithiophene ( $\alpha$ 6T): C<sub>60</sub> blends. The dilution of the donor (5% and 10%) was chosen because of the complete homogeneous dispersion and isolation of  $\alpha$ 6T within the large C<sub>60</sub> regions as compared to the strong donor aggregation seen in 50% blends and the completely separated bilayers.<sup>5</sup> The CT state energy has also been shown to decrease rapidly with the onset of  $\alpha$ 6T aggregation in higher donor content blends.<sup>6</sup> The dilute-donor  $\alpha$ 6T: C<sub>60</sub> blends show a similar Voc (0.93 and 0.92 V for 5% and 10% blend), Jsc (6.07 and 6.14 mA/cm<sup>2</sup> for 5% and 10% blend) and PCE (3.18 and 3.18 % for 5% and 10% blend), which are all larger than for the phase separated 50% blend and bilayer.<sup>5, 6</sup> This selection of morphologies allows us to obtain well-defined interfaces which give insight into CT state and SC properties and their effect on the final solar cell properties.

We observe two spectrally separable charge components in the TA spectra of the dilute thin films. TD-DFT is then used to simulate charged species at the interface, particularly in a configuration representing CT states and SCs. Using the simulated absorption spectra of the CT state and SCs we are able to attribute the two charge components, seen in the TA spectra, to bound CT state charges and SCs. This then allows a kinetic model to be fit to the TA data with separated CT and SC population dynamics. The result of the kinetic modelling gives insight into the hole transfer (HT) process, the CT state lifetime, the CT separation, the fast trap-based bimolecular recombination processes and how they are affected by the slightly different morphologies. The 50 % blend and bilayer show relatively little CT state separation, in line with their much lower CT state energies. Finally, the entire TA spectrum is reconstructed using the simulated absorption spectra and lifetimes obtained from kinetic modelling.

## 4.5. Results and Discussion

### 4.5.1. Transient Absorption Spectroscopy

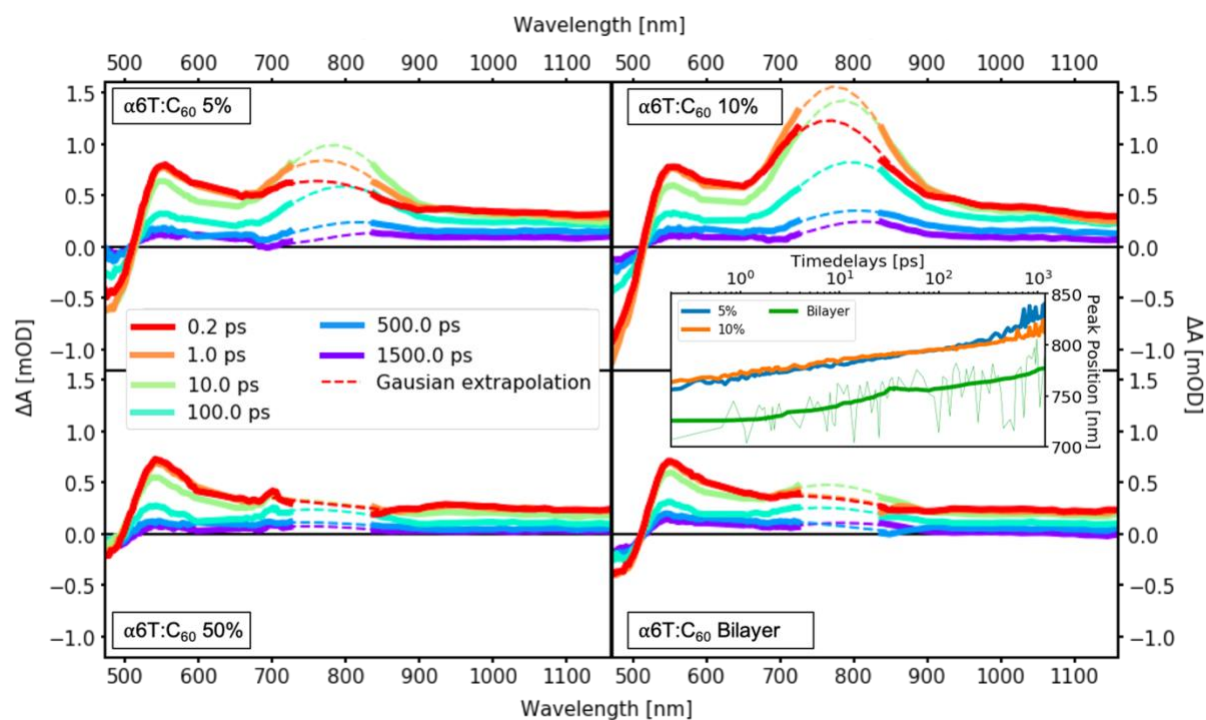


Figure 4.5-1 Transient absorption (TA) spectra of  $\alpha 6T:C_{60}$  blends with a weight ratio of 5%, 10% and 50% as well as a bilayer at selected time delays (0.2 ps, 1 ps, 10 ps, 100 ps, 500 ps, and 1.5 ns) with 610 nm pump excitation. The spectral cuts at around 800 nm (at the fundamental laser output) are fit and extrapolated with Gaussian functions (dashed lines). The inset shows how the centre of the Gaussian fits shift over time for the 5%, 10% and Bilayer.

TA spectra were measures of the  $\alpha 6T:C_{60}$  blends excited at 610 nm to selectively excite the  $C_{60}$  acceptor (absorption distinct from  $\alpha 6T$ ) and at an excitation density low enough ( $<10^{18} \text{ cm}^{-3}$ ) as to avoid non-linear many-bodied interactions. Excitation of  $C_{60}$  at 610 nm results in Frenkel type excitons localized to single  $C_{60}$  molecules and does not result in any self-ionization, even under an applied electric field.<sup>1, 7</sup> In the top left and top right of Figure 5-1 the TA spectra of  $\alpha 6T:C_{60}$  blends containing 5% and 10% donor, respectively, are shown. At early times we see a mixture of both  $C_{60}$  exciton and charge signatures. The  $C_{60}$  Frenkel exciton shows negative ground state bleaching (GSB) at wavelengths lower than 500 nm, as well as excited state absorption peaks at  $\sim 550 \text{ nm}$  and  $\sim 950 \text{ nm}$  (shown in appendix A.2-2 for neat  $C_{60}$  film).<sup>1, 2</sup> The charge features consist of the GSB, the  $C_{60}$  anion with a broad signature in the near infra-red (NIR) with a peak at  $\sim 1070 \text{ nm}$  (best seen in the 10 % blend),<sup>1, 8, 9</sup> and the  $\alpha 6T$  cation absorption at around 650-900 nm, which grows and red shifts over time.<sup>10, 11</sup> Charge signatures feature an oscillatory electro-absorption (EA) signature at 485 and 545 nm, a result

of the electric field between the electron and hole (which causes the Stark shift and therefore the EA in neighbouring neat  $C_{60}$  clusters).<sup>1, 2</sup> Evidence of long-lived charges is seen with non-zero spectra at times as long as 1.5 ns. The bottom left and bottom right panels of Figure 5-1 show the TA spectra of a 50 % blend and bilayer respectively with the  $C_{60}$  in the bilayer being excited from the  $\alpha 6T$  side. The spectrum of the 50% blend is completely dominated by the  $C_{60}$  exciton spectrum with very little evidence for charge formation, while the bilayer (still dominated by  $C_{60}$  excitons) shows some charges formed at early times with a slight charge offset at the longest time delays.

A strong red shift of the cation peaks is observed from approximately 755 to 830 nm for the 5 % blend, 765 to 815 nm for the 10 % blend and 730 to 780 nm for the bilayer, as illustrated in the inset of Figure 5-1. These peak shifts correspond to about 145, 100 and 110 meV for the 5 %, 10 % blends and bilayer, respectively. While the energy shifts are similar for the bilayer and blends, the entire range of the bilayer cation spectrum is at a lower wavelength, most likely because of the vastly different morphological landscape of the  $\alpha 6T$  cation in the bilayer, being essentially bulk  $\alpha 6T$  as opposed to isolated molecules or small clusters in the blends.<sup>5, 10, 12, 13</sup>

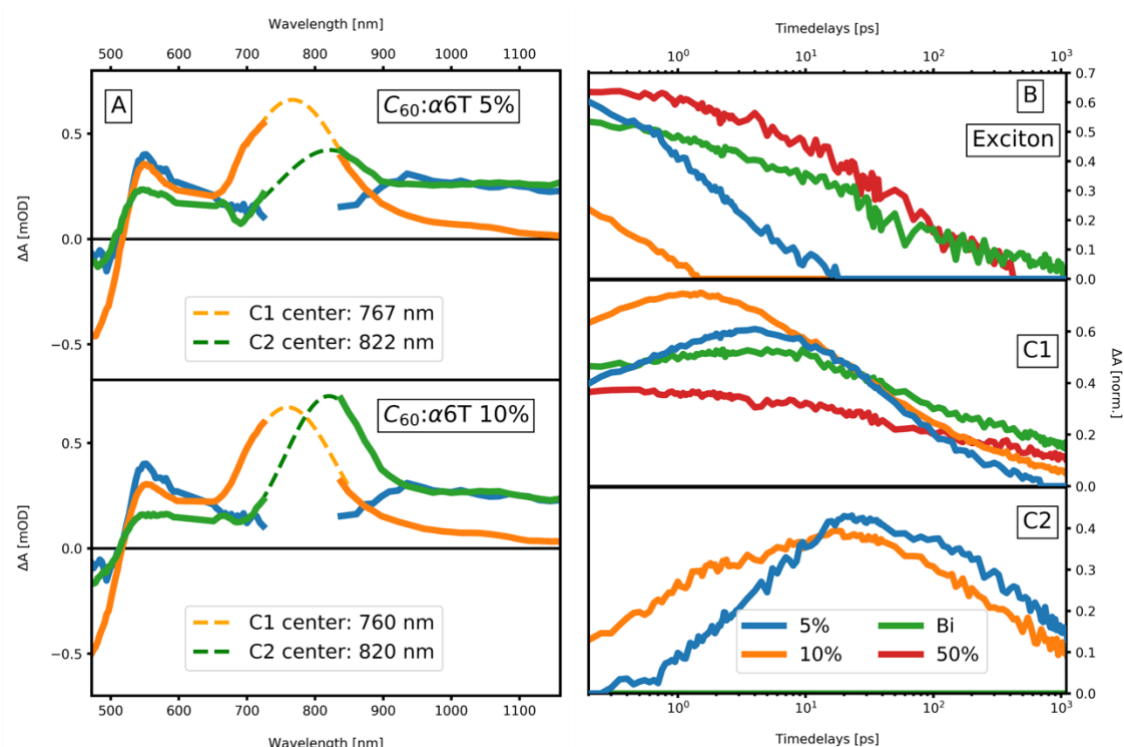


Figure 4.5-2 (A) The spectral components of the MCR-ALS decomposition of  $\alpha 6T:C_{60}$  5% and 10% blends with the  $C_{60}$  exciton (blue), early charge (C1, orange) and late charge signatures (C2, green). The 800 nm gap is fit and extrapolated with Gaussian functions (dashed lines) for both charge species. The position of the centre of the Gaussians is shown (in nm). (B) shows the

*dynamics of the three components of the MCR-ALS decomposition in each of the blends (5% in blue, 10% in orange, 50% in red and Bilayer in green), with the top being the exciton dynamics, the middle being the dynamics of the first charge species (C1) and the bottom being the dynamics of the second charge species (C2).*

Figure 5-2A shows the spectral components resulting from the Multivariate Curve Resolution with Alternating Least Squares (MCR-ALS) decomposition of the 5% blend (top) and 10% blend (bottom).<sup>14, 15</sup> The spectra were best decomposed into three components (confirmed by SVD) representing the exciton, first charge species (C1) and second charge species (C1). The initial exciton component was taken from an early time TA measurement of a neat C<sub>60</sub> film and was fixed during the decomposition as its spectral shape is known.<sup>1</sup> The initial guesses for the charge components were taken from the early (0.2 ps) and late (1 ns) time TA spectra with the exciton shape subtracted from the early charge species. The oscillatory EA signature can be seen for both the charge species peaking at 550 nm with the amplitude of the EA signature being distinctly larger in the first charge species than the second charge species in both blends. The decrease in amplitude of the EA signal can be explained by both the decreasing charge population through recombination and the dissociation of the charges causing a weaker electric field as electrons and holes separate. The slightly more pronounced C<sub>60</sub> anion signature (around 1070 nm in Figure 2A) in the first charge species, as opposed to the broad band in the second charge species, suggests a more localised anion at early times. To quantify the magnitude of the shift in the  $\alpha$ 6T cation peaks we once again fit a gaussian function to the data around the spectral gap at 800 nm. A shift in charge peak position from 767 nm to 822 nm and 760 nm to 820 nm is seen for the 5% and 10% blends respectively. The shift picked up by the MCR-ALS spectral components matches reasonably well with the shifts measured by fitting the raw TA spectra. The shape and amplitude of the spectra for each component is similar between the 5% and 10% blends, indicating that the nature of the species is likely the same in both blends. A small difference can be seen when comparing the second charge component of the two blends in the cation band around 850 nm where the 10 % blend shows a sharper and more pronounced peak suggesting a more localised charge.

The dynamics of the spectral components obtained from the MCR-ALS decomposition are shown in Figure 5-2B with the exciton, first and second charge species shown in the top, middle and bottom panel, respectively. Excitons from the 5% and 10% blends are quenched completely and relatively quickly, with the 5% excitons having more than double the population at 0.2 ps and surviving longer than the 10% blend excitons. In the case of the 5 % and 10% blends, the excitons in the C<sub>60</sub> diffuse to the  $\alpha$ 6T molecules and undergo hole transfer

(HT) where they form charge transfer (CT) states or separate directly into free charges. As there is more  $\alpha 6T$  in the 10% blend than the 5% blend, the average diffusion length needed to find an  $\alpha 6T$  site is shorter resulting in a faster quenching of the excitons. In the case of the 50% blend and bilayer, we see that the exciton signature lasts roughly as long as it would in a neat  $C_{60}$  film (150 ps lifetime).<sup>1</sup> In the 50% and bilayer, excitons are quenched either very rapidly (if formed near an  $\alpha 6T$  cluster) or are not quenched at all because of the almost complete phase separated morphology with very large  $C_{60}$  and  $\alpha 6T$  clusters, as opposed to the homogeneously diluted 5% and 10% blends.<sup>16</sup> As the  $C_{60}$  in the bilayer is excited through the  $\alpha 6T$ , a portion of the excitons are formed directly at the interface resulting in approximately 40% of the excitons undergoing HT to the  $\alpha 6T$  within the first 0.2 ps with only very few excitons diffusing to the interface after the initial excitation. The same observation can be made for the 50% blend only with even less initial HT and charge formation. The first charge species (C1) is formed quicker in the 10% blend than in the 5% blend as expected in a diffusion-controlled exciton quenching. The C1 population reaches a higher value in the 10% blend due, most likely, to the higher  $C_{60}:\alpha 6T$  interfacial area.<sup>5</sup> The rise of the second charge species is also affected by exciton diffusion but reaches a maximum at around 20 ps for both dilute blends. The CT state separation in the bilayer and 50 % blend is expected to be extremely inefficient due to its low lying CT state. The results of the MCR-ALS decomposition suggest that there is no shift of the charge peak in the 50% and the bilayer blends. This could be a result of poor CT state separation due to their low lying CT states and therefore enhanced non-radiative geminate recombination. Since a shift is visible in the TA spectra of the bilayer, we expect this to not be the case and rather that the second charge species was simply not prominent enough to be picked up by the MCR-ALS fitting. The slight spectral shift in the bilayer and not in the 50 % blend could be a result of slightly enhanced CT state delocalisation in the bilayer and so slightly more CT state separation.

#### 4.5.2. Theoretical Investigation of Charge Species

In order to understand the origin of the two charge species observed in the TA spectra the absorption of the  $\alpha 6T$  cation species is simulated with TD-DFT in a number of configurations. The configurations that are considered are (i)  $\alpha 6T$  cations in CT states with  $C_{60}$  anions at the D-A-interface, (ii)  $\alpha 6T$  cations at the D-A interface in the absence of charge in  $C_{60}$ , and (iii) isolated  $\alpha 6T$  cations in the bulk phase of  $\alpha 6T$ . However, the species (ii) and (iii) should be rather similar apart from a possible slight shift due to different local dielectrics. This shift, however, is smaller ( $\sim 5$  meV) than our applied gauss broadening (35 meV) of the oscillator

strengths used to simulate the absorption spectra.<sup>17</sup> Not considering bulk phase  $\alpha 6T$  is further justified by the fact that  $\alpha 6T$  molecules are said to be completely isolated at dilutions less than 15 %, seen in their linear external quantum efficiency growth with increased  $\alpha 6T$  fraction.<sup>5</sup> We therefore simulate the fingerprints of  $\alpha 6T$  cation either alone or with a  $C_{60}$  anion (represented as a negative point charge) in its vicinity. The system where the  $C_{60}$  anion is in the vicinity of the  $\alpha 6T$  cation represents a bound CT state, as the anion and cation are within the coulombic capture radius. The system with the isolated  $\alpha 6T$  cation represents the SCs where they are no longer coulombically bound. The absorption of the  $C_{60}$  is not considered as no spectral shifts are observed, and the absorption is far enough away from the  $\alpha 6T$  cation not to have an effect.

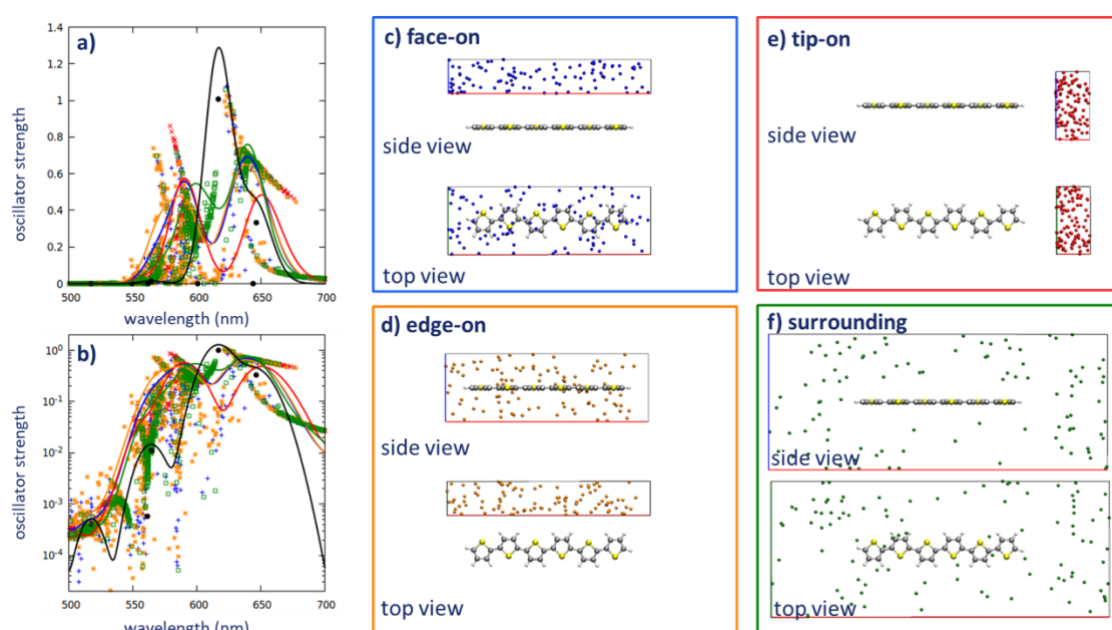


Figure 4.5-3 (a),(b) Wavelengths and oscillator strengths for cation (black) and CT states in face-on (blue), edge-on (orange), tip-on (red), and fully surrounding (green) as obtained from TD-DFT/B3LYP/6-31G\* and corrected by a rigid red shift (0.42 eV). Symbols represent individual simulation results. Lines represent the average over the 100 different CT orientations for each case broadened by Gauss curves of 35 meV width. (c)-(f) individual, random positions of the point charge.

For a representative absorption study of the  $\alpha 6T$  cation in the CT state, it is important to densely sample the microscopic D-A interface geometries. This is done by considering different  $\alpha 6T^+/C_{60}^-$  configurations, namely: face-on, tip-on, edge-on, and finally completely surrounded (Figure 5-3(c)-(f)), with only one  $C_{60}^-$  considered at a time. The resulting spectra are summarized in Figure 5-3(a)-(b). We find that the transition energies and oscillator strengths depend only weakly on the location of the point charge such that averaging over different arrangements results in spectra with the double-peak structure for all classes (face-on, tip-on, edge-on or surrounding). The only noticeable difference is the longer wavelength peak for the tip-on orientation having a weaker oscillation strength than the rest. The orientation



independence of the absorption shape suggests that the model is applicable for any of the system morphologies, including the bilayer. The resulting spectrum, which is obtained by averaging over all considered point charge positions, is representative for the CT state and is plotted in Figure 5-4 B (red). It is clearly different from the cationic absorption in neutral environment (bulk  $\alpha 6T$ ) (blue line). The absorption spectrum of the cation is observed at 780 nm with a shoulder at 830 nm. In the presence of a negative counter charge, however, the absorption maximum is blue shifted to about 730 nm, a shift of approximately 100 meV corresponding roughly to the observed shifts in TA spectrum. The absorption at 830 nm largely remains. In general, the  $\alpha 6T$  cation with the negative charge in the vicinity is blue shifted with respect to the  $\alpha 6T$  cation without the point charge (bulk  $\alpha 6T$  cation absorption).

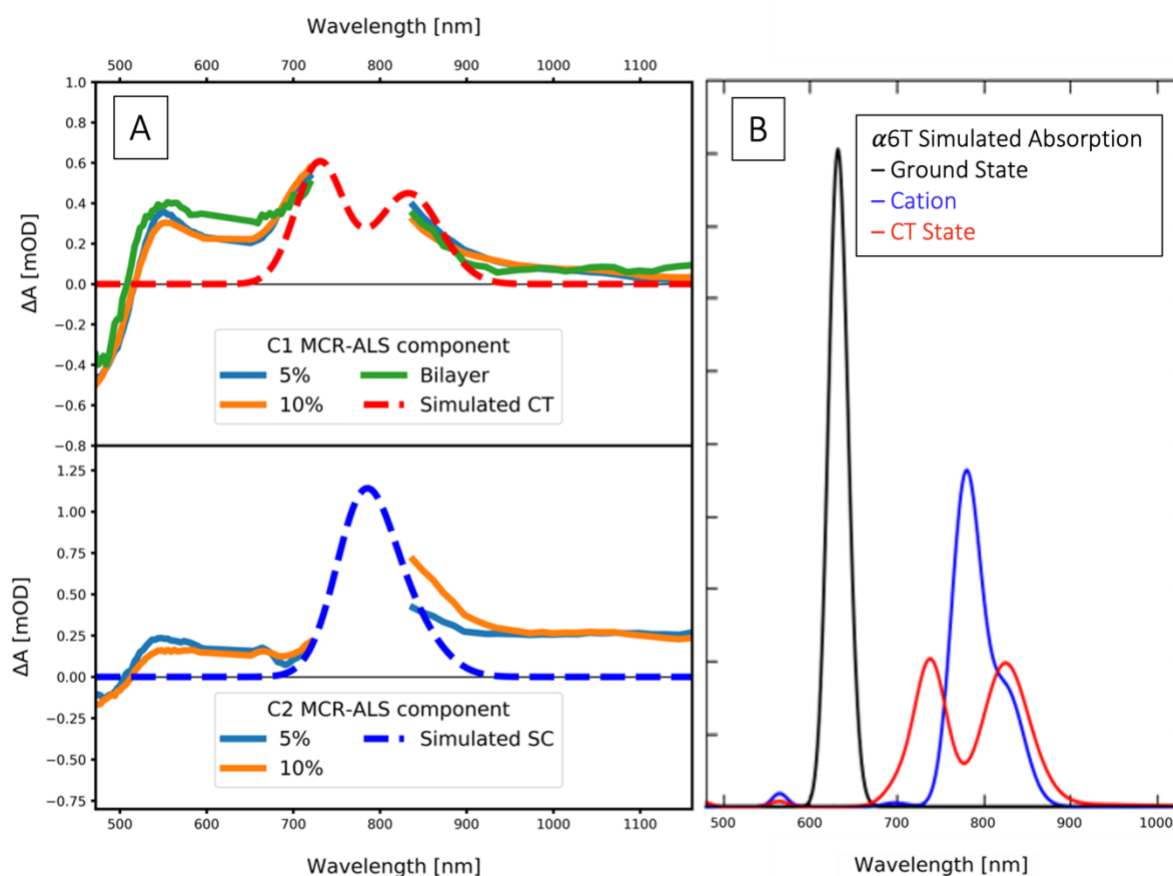


Figure 4.5-4 (A) Comparison of simulated absorption spectra to first (C1 top) and second (C2 bottom) charge spectra from MCR-ALS decomposition for 5% and 10% blends as well as bilayers. (B) Simulated absorption spectra for  $\alpha 6T$  in the ground state (black), cation (blue), and CT state (red) as obtained from TD-DFT/B3LYP/6-31G\* and corrected by a 0.42 eV red shift.

Comparing the simulated absorption spectra of CT and SC charges from TD-DFT with the two charge components extracted from the experimental TA data with the MCR-ALS

decomposition (Figure 5-4 A) we see a reasonable agreement in spectral shape between the first component (C1) with the simulated CT spectrum and the second component (C2) with the simulated SC spectrum. These correlations are most obvious around 700 nm, with the broad  $C_{60}^-$  absorption distorting the spectra in the nIR. The two charge species C1 and C2 are therefore attributed to interfacial CT state charges and SC, respectively.

#### 4.5.3. Kinetic Modelling

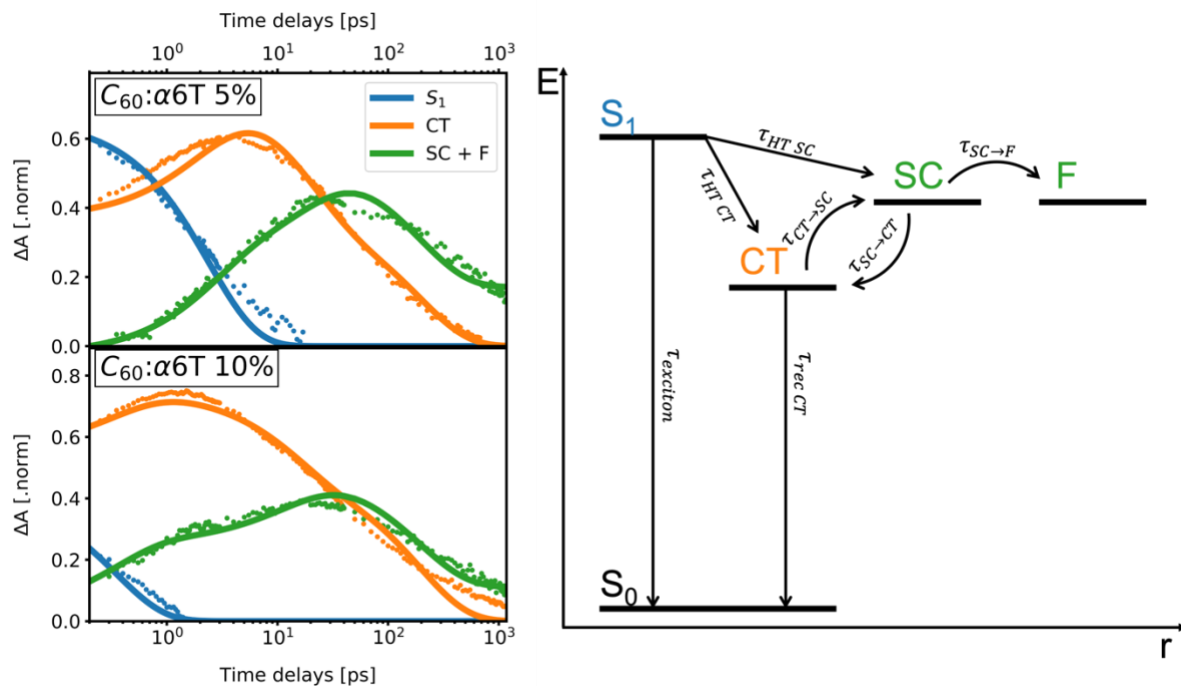


Figure 4.5-5 The dynamics of the exciton (blue), CT state and separated charge species (orange and green) for 5 % (top) and 10 % (bottom)  $\alpha 6T:C_{60}$  blends as determined by MCR-ALS decomposition are shown on the left, together with the fits obtained from the kinetic modelling. On the right, a Jablonski diagram summarizing the relaxation pathways in the blends used as the basis for the kinetic model is shown.

With the attribution of the first and second charge species to the CT and separated charges (SCs), a kinetic model was designed to model the sequence of processes undergone upon excitation of the blends. The kinetic model was then fit to dynamics obtained from the MCR-ALS decomposition in order to quantify the time constants associated with each step. Figure 5-7 shows a Jablonski diagram associated to the kinetic model as well as the fitting of the model onto the 5% and 10% blends, while Table 5-1 summarises the results of the fit. The Jablonski diagram is expressed as a set of linked differential equations for each population which are used to fit the dynamics of each species. The set of equations used for fitting are shown here:

$$\frac{dS_1}{dt} = -\tau_{exciton}^{-1}S_1(t) - \tau_{HT\ CT}^{-1}S_1(t) - \tau_{HT\ SC}^{-1}S_1(t)$$



( 5-1)

$$\frac{dCT}{dt} = \tau_{HT}^{-1} CT S_1(t) - \tau_{CT \rightarrow SC}^{-1} CT(t) - \tau_{rec}^{-1} CT(t) + \tau_{SC \rightarrow CT} SC(t)$$

( 5-2)

$$\frac{dSC}{dt} = \tau_{HT}^{-1} SC S_1(t) + \tau_{CT \rightarrow SC}^{-1} CT(t) - \tau_{SC \rightarrow CT}^{-1} SC(t) + \tau_{SC \rightarrow F}^{-1} F(t)$$

( 5-3)

$$\frac{dF}{dt} = \tau_{SC \rightarrow F}^{-1} F(t)$$

( 5-4)

Equation ( 5-1) is then fit to the exciton (S1) dynamic, equation ( 5-2) to the CT state dynamic and the sum of ( 5-3) and ( 5-4) to the SC + F dynamic.

Table 5-1 Outcome of the Kinetic Modelling of the MCR-ALS Decomposition Dynamics from the TA Data for  $\alpha 6T:C_{60}$  Blends (5% and 10%)<sup>a</sup>

	<b><math>\alpha 6T:C_{60}</math> 5%</b>	<b><math>\alpha 6T:C_{60}</math> 10%</b>
CT <sub>initial</sub>	40%	65%
SC <sub>initial</sub>	0%	15%
$\tau_{exciton}$ (ps)	150.0 (6%)	150.0 (1%)
$\tau_{HT CT}$ (ps)	4.2 (55%)	0.8 (45%)
$\tau_{HT SC}$ (ps)	5.8 (39%)	0.6 (54%)
$\tau_{rec CT}$ (ps)	97.4	106.6
$\tau_{CT \rightarrow SC}$ (ps)	38.6	33.2
$\tau_{SC \rightarrow CT}$ (ps)	47.7	30.7
$\tau_{SC \rightarrow F}$ (ps)	600.6	858.6

<sup>a</sup>Initial charge population at 0.2 ps of both charge species ( $CT_{initial}$ ,  $SC_{initial}$ ) expressed as a fraction of the total exciton density; intrinsic exciton lifetime ( $\tau_{exciton}$ ) and the fraction of excitons decaying to the ground state, hole-transfer (HT) time constant ( $\tau_{HT CT}$ ,  $\tau_{HT SC}$ ) to both charge species along with the fraction of excitons undergoing HT to each; charge recombination time

*for CT species ( $\tau_{rec-CT}$ ); time constants associated with charges separating and undergoing fast trap-based recombination ( $\tau_{CT \rightarrow SC}$ ,  $\tau_{SC \rightarrow CT}$ ); time constants associated with separated charges remaining free at long time delays ( $\tau_{SC \rightarrow F}$ ).*

After excitation, the exciton (S1 state) decays to the ground state (S0) with a time constant of 150 ps, as determined by previous studies on neat C<sub>60</sub> films.<sup>1</sup> If the exciton is able to diffuse to an  $\alpha 6T:C_{60}$  interface, it undergoes hole-transfer (HT) to either form a CT state or directly SCs.<sup>18</sup> Charges in CT states then either recombine to the ground state or separate. The SCs either remains in a region where fast trap-based recombination is possible, or move to a region where they remain free (F in model) for the 1.5 ns time window of the measurement. We have already shown that this fast trap-based recombination, while dominating in thin films, is suppressed in a device configuration by the fast extraction of mobile electron to the electrodes explaining the high efficiency at low donor concentration.<sup>2</sup> As SC and F are spectrally indistinguishable, the sum of their populations is fit to the second charge component dynamic from the MCR-ALS decomposition. There are more initial charges (at 0.2 ps) in the 10% blend (65 % CT and 15% SC) than the 5% blend (40% CT and 0% SC). Faster HT is also observed in the 10% blend, with HT to CT having a time constant of 0.8 ps and HT to SC of 0.6 ps, as opposed to the 5% blend where HT to CT has a time constant of 4.2 ps and HT to SC of 5.8 ps. The higher relative population of initial charges and faster HT in the 10% blend agrees with a diffusion-controlled HT model where excitons require, on average, shorter diffusion lengths to reach a donor molecule.

The essentially equal CT lifetime of around 100 ps for both 5% and 10% blends is due to their similar CT energy levels.<sup>3, 5</sup> Also, the CT dissociation to SC is similar for both blends blend (38.6 ps in 5% and 33.2 ps in 10%), which can be related to the comparable local dielectric environment and electron delocalization in C<sub>60</sub>.

The SC to CT recombination is monomolecular trap-based recombination where the holes are trapped on the isolated  $\alpha 6T$  molecules. Hole transport has been shown to occur by long range tunnelling from one  $\alpha 6T$  molecule to the next.<sup>5</sup> However, over the 1.5 ns time-window of this measurement the holes are essentially immobile, while the electron mobility in C<sub>60</sub> remains unperturbed by the  $\alpha 6T$  for blends  $\leq 10\%$ .<sup>5</sup> The fast trap-based SC recombination is therefore faster in the 10% blend than the 5% blend (47.7 and 30.7 ps for 5 % and 10 % respectively) owing to the increase in trap site density ( $\alpha 6T$  density). Finally the 5 % blend shows slightly faster SC to free rate than the 10 % resulting in the comparable external quantum efficiency despite the 10 % blend having double the interfacial area.<sup>5</sup> The attribution of the two charge

species to CT states and SC is therefore further validated both by the goodness of fit and by the physically meaningful time constants extracted from the kinetic model.

#### 4.5.4. Reconstruction of the Transient Absorption Spectra

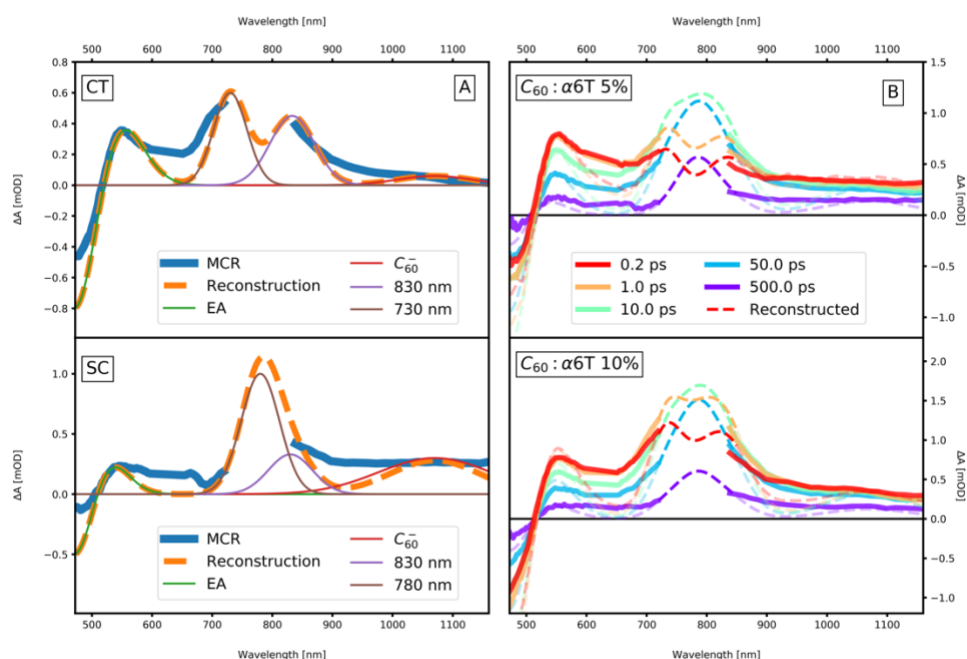


Figure 4.5-6 (A) Simulation of MCR-ALS charge components for the CT state (top) and SCs (bottom). The components are simulated using Gaussian bands with centres at charge transition absorption wavelengths for the  $\alpha 6T$  cation and  $C_{60}$  anion. The EA is simulated by the second derivative of a Gaussian centred at the  $C_{60}$  CT state exciton (470 nm). (B) experimental (solid lines) and reconstructed (dashed lines) TA spectra of the 5% (top) and 10% (bottom) blends using the reconstructed MCR-ALS components and the component dynamics obtained from the kinetic modelling.

Using the energies of the most active transitions obtained from the TD-DFT simulations, the spectra of both the CT charges and SCs can be simulated (Figure 5-8A). The  $\alpha 6T$  cation is simulated by summing Gaussians with centres at wavelengths corresponding to the energies of the two most active transitions (CT 830 nm, 730 and SC 830 nm, 780 nm) with relative amplitudes according to their oscillator strengths. The  $C_{60}$  anion is simulated by a Gaussian at 1070 nm with the anion in the SC spectrum being substantially broader, motivated by the difference in delocalisation. The EA signal is a result of the shift in absorption of large  $C_{60}$  clusters in the vicinity of the charges, and so was simulated by taking the second derivative of a Gaussian centred at the absorption of the  $C_{60}$  intermolecular CT state exciton (470 nm).<sup>1</sup> The reconstructed spectra are compared to the spectra extracted from MCR-ALS decomposition for the 5% blend in Figure 5-8A. Using the dynamics fit in the kinetic model and the reconstructed

spectral components, the entire TA spectral evolution for both the 5% and 10% blends can be reconstructed (Figure 5-8B).

#### 4.6. Conclusion

In summary, thermally evaporated  $\alpha 6T:C_{60}$  bilayer and bulk-heterojunction blends of different ratios are investigated using both experimental methods (TA spectroscopy) and theoretical simulations (TD-DFT). TA spectra of the blends showed predominantly excitonic signatures in the bilayer and 50% blend, with the bilayer showing some charge signature and the 50% showing very little. The dilute-donor blends (5% and 10% blends), however, exhibit a strong charge character, especially for the  $\alpha 6T$  cation, agreeing with the much higher photocurrent reported for the dilute blends. The  $\alpha 6T$  cation peak showed a definite and measurable red shift over time. An MCR-ALS decomposition was performed on the TA spectra of the blends which resulted in an excitonic spectrum and split the shifting charge peak into two separate components for the dilute blends. TD-DFT simulations were done to simulate the  $\alpha 6T$  cation transition energies in different configurations. The  $\alpha 6T$  cation was simulated both in the vicinity of the  $C_{60}$  anion (represented by a point charge) and without the presence of the anion, representing the CT state and SCs respectively. The transition energies of the  $\alpha 6T$  cation were indeed different in the presence of the  $C_{60}$  anion and were shown to be reasonably invariant to their relative orientations. The absorption spectra of the two cationic species were then simulated with the physical origins of the peaks discussed. It was therefore concluded that the early time charge species (C1) is attributed to the CT state charges at the donor:acceptor interface and the later time charge species (C2) attributed to the SCs. With the identity of the charge species in mind, a kinetic model was developed to model the interconversion processes of the excitonic and charge species. The model was fit to the dynamics of the spectral species extracted in the MCR-ALS decomposition for both dilute blends. The model fit well, and resultant time constants matched expected values, further validating the attribution of the charge species to CT and SC. The spectral components from the MCR-ALS decomposition were then reconstructed using the simulated absorption spectra from the TD-DFT calculations. The entire TA spectrum was then reconstructed using the reconstructed spectral components and the dynamics resulting from the kinetic model.

These results not only give insight into the charge generation mechanisms and the differences in charge absorption character, but constitute the first observation of spectrally resolved CT state and separated charges confirmed by simulation. This allows the opportunity to fit more complete and nuanced kinetic models and understand the charge generation, separation, and recombination in more detail.

## Reference

1. Causa', M.; Ramirez, I.; Martinez Hardigree, J. F.; Riede, M.; Banerji, N., Femtosecond Dynamics of Photoexcited C60 Films. *The Journal of Physical Chemistry Letters* **2018**, 9 (8), 1885-1892.
2. Moore, G. J.; Causa', M.; Martinez Hardigree, J. F.; Karuthedath, S.; Ramirez, I.; Jungbluth, A.; Laquai, F.; Riede, M.; Banerji, N., Ultrafast Charge Dynamics in Dilute-Donor versus Highly Intermixed TAPC:C60 Organic Solar Cell Blends. *The Journal of Physical Chemistry Letters* **2020**, 11 (14), 5610-5617.
3. Collado-Fregoso, E.; Pugliese, S. N.; Wojcik, M.; Benduhn, J.; Bar-Or, E.; Perdigón Toro, L.; Hörmann, U.; Spoltore, D.; Vandewal, K.; Hodgkiss, J. M.; Neher, D., Energy-Gap Law for Photocurrent Generation in Fullerene-Based Organic Solar Cells: The Case of Low-Donor-Content Blends. *Journal of the American Chemical Society* **2019**, 141 (6), 2329-2341.
4. Vandewal, K.; Albrecht, S.; Hoke, E. T.; Graham, K. R.; Widmer, J.; Douglas, J. D.; Schubert, M.; Mateker, W. R.; Bloking, J. T.; Burkhard, G. F.; Sellinger, A.; Frechet, J. M.; Amassian, A.; Riede, M. K.; McGehee, M. D.; Neher, D.; Salleo, A., Efficient charge generation by relaxed charge-transfer states at organic interfaces. *Nat Mater* **2014**, 13 (1), 63-8.
5. Melianas, A.; Pranculis, V.; Spoltore, D.; Benduhn, J.; Inganäs, O.; Gulbinas, V.; Vandewal, K.; Kemerink, M., Charge Transport in Pure and Mixed Phases in Organic Solar Cells. *Advanced Energy Materials* **2017**, 1700888, 1700888.
6. Benduhn, J.; Tvingstedt, K.; Piersimoni, F.; Ullbrich, S.; Fan, Y.; Tropiano, M.; McGarry, K. A.; Zeika, O.; Riede, M. K.; Douglas, C. J.; Barlow, S.; Marder, S. R.; Neher, D.; Spoltore, D.; Vandewal, K., Intrinsic non-radiative voltage losses in fullerene-based organic solar cells. *Nature Energy* **2017**, 2 (6), 17053.
7. Kazaoui, S.; Minami, N.; Tanabe, Y.; Byrne, H. J.; Eilmes, A.; Petelenz, P., Comprehensive analysis of intermolecular charge-transfer excited states in  $\text{C}_{60}$  and  $\text{C}_{70}$  films. *Physical Review B* **1998**, 58 (12), 7689-7700.
8. Yamamoto, S.; Guo, J.; Ohkita, H.; Ito, S., Formation of methanofullerene cation in bulk heterojunction polymer solar cells studied by transient absorption spectroscopy. *Adv Funct Mater* **2008**, 18 (17), 2555-2562.
9. Nakanishi, I.; Ohkubo, K.; Fujita, S.; Fukuzumi, S.; Konishi, T.; Fujitsuka, M.; Ito, O.; Miyata, N., Direct detection of superoxide anion generated in C60-photosensitized oxidation of NADH and an analogue by molecular oxygen. *Journal of the Chemical Society, Perkin Transactions 2* **2002**, (11), 1829-1833.
10. Dong, Y.; Nikolis, V. C.; Talnack, F.; Chin, Y.-C.; Benduhn, J.; Londi, G.; Kublitski, J.; Zheng, X.; Mannsfeld, S. C. B.; Spoltore, D.; Muccioli, L.; Li, J.; Blase, X.; Beljonne, D.; Kim, J.-S.; Bakulin, A. A.; D'Avino, G.; Durrant, J. R.; Vandewal, K., Orientation dependent molecular electrostatics drives efficient charge generation in homojunction organic solar cells. *Nature Communications* **2020**, 11 (1).
11. Ramirez, I.; Privitera, A.; Karuthedath, S.; Jungbluth, A.; Benduhn, J.; Sperlich, A.; Spoltore, D.; Vandewal, K.; Laquai, F.; Riede, M., The role of spin in the degradation of organic photovoltaics. *Nature Communications* **2021**, 12 (1).
12. Duhm, S.; Heimel, G.; Salzmann, I.; Glowatzki, H.; Johnson, R. L.; Vollmer, A.; Rabe, J. P.; Koch, N., Orientation-dependent ionization energies and interface dipoles in ordered molecular assemblies. *Nat. Mater.* **2008**, 7 (4), 326-32.

13. Yang, Y.; Zhang, Z. G.; Bin, H.; Chen, S.; Gao, L.; Xue, L.; Yang, C.; Li, Y., Side-Chain Isomerization on an n-type Organic Semiconductor ITIC Acceptor Makes 11.77% High Efficiency Polymer Solar Cells. *J Am Chem Soc* **2016**, *138* (45), 15011-15018.
14. Rutan, S. C.; de Juan, A.; Tauler, R., 2.06 - Introduction to Multivariate Curve Resolution☆. In *Comprehensive Chemometrics (Second Edition)*, Brown, S.; Tauler, R.; Walczak, B., Eds. Elsevier: Oxford, 2020; pp 85-94.
15. de Juan, A.; Tauler, R., Chemometrics applied to unravel multicomponent processes and mixtures: Revisiting latest trends in multivariate resolution. *Analytica Chimica Acta* **2003**, *500* (1), 195-210.
16. Melianas, A.; Pranculis, V.; Spoltore, D.; Benduhn, J.; Inganäs, O.; Gulbinas, V.; Vandewal, K.; Kemerink, M., Charge transport in pure and mixed phases in organic solar cells. *Advanced Energy Materials* **2017**, *7* (20), 1700888.
17. Ortstein, K.; Hutsch, S.; Hambsch, M.; Tvingstedt, K.; Wegner, B.; Benduhn, J.; Kublitski, J.; Schwarze, M.; Schellhammer, S.; Talnack, F.; Vogt, A.; Bäuerle, P.; Koch, N.; Mannsfeld, S. C. B.; Kleemann, H.; Ortmann, F.; Leo, K., Band gap engineering in blended organic semiconductor films based on dielectric interactions. *Nature Materials* **2021**, *20* (10), 1407-1413.
18. Gélinas, S.; Rao, A.; Kumar, A.; Smith, S. L.; Chin, A. W.; Clark, J.; Poll, T. S. v. d.; Bazan, G. C.; Friend, R. H., Ultrafast Long-Range Charge Separation in Organic Semiconductor Photovoltaic Diodes. *Science* **2014**, *343* (6170), 512-516.





# 6 Pairing Non-Fullerene Acceptors with the Right Polymer: Impact of Morphology and Short-Range Mobility on Charge Generation

## Foreword

This work is a follow-up recombination study on a work done exploring charge transfer in low driving force polymer:non-fullerene-acceptor blends by Zhong and Causa' et al.<sup>1</sup> In the first study, the charge transfer process in blends with varying driving forces for electron and hole transfer was investigated using transient absorption spectroscopy. The charge transfer rates in bilayers, BHJs and dilute morphologies were compared to disentangle the intrinsic charge transfer rates from exciton diffusion. It was then shown that hole transfer occurs at sub-picosecond time scales even with a negligible driving force. Electron transfer was shown to be even faster than hole transfer at comparable driving force, likely due to stronger electronic coupling for electron transfer. The main conclusion being that a large driving force, which increases  $V_{OC}$  losses, is not necessary for efficient CT state formation.

The first part is published in Nature Communications by Yufei Zhong and Martina Causa' et al. titled *Sub-picosecond charge-transfer at near-zero driving force in polymer:non-fullerene acceptor blends and bilayers*.<sup>1</sup>

The work in this chapter is done by:

Gareth John Moore<sup>1</sup>, Yufei Zhong<sup>1</sup>, Martina Causa'<sup>1</sup> and Natalie Banerji<sup>1</sup>

<sup>1</sup>Department of Chemistry and Biochemistry, University of Bern, Freiestrasse 3, 3012 Bern, Switzerland.

#### AUTHOR CONTRIBUTIONS:

N.B led the project. Y.Z. prepared the samples and performed the steady state absorption spectroscopy. G.J.M, M.C and Y.Z. performed TA measurements. EDA was carried out by M.C. and Y.Z. The manuscript was written by G.J.M., Y.Z. and N.B.

## 6.1 Introduction

The PCE of OPVs has rapidly improved in recent years, with records over 18% to date.<sup>2,3</sup> This rapid increase in efficiency has been a result of the development of non-fullerene acceptors (NFAs).<sup>4</sup> NFAs have tuneable absorption spectra and energy levels allowing them to rapidly outcompete the previously ubiquitous fullerene acceptors, whose PCE has peaked at 11.5%.<sup>5</sup> Compared to the weak absorption of fullerene molecules in the visible region, NFAs can be tuned to absorb strongly in the nIR range, leading to a significant contribution to the photocurrent from NFA absorption. The nIR absorption of NFAs also allows the use of relatively wide bandgap donor polymers whose complimentary absorption in the VIS region results in a broad coverage of the solar spectrum for light harvesting.

This naturally brings the choice of polymers back to the relatively wide bandgap systems used in the early stages of OPVs, specifically as Poly(3-hexylthiophene-2,5-diyl) (P3HT). When P3HT was initially combined with NFAs (IDTBR, BTA3 and BTP-4Cl), a clear improvement of open circuit voltage ( $V_{OC}$ ) was observed because of the optimized interfacial energetics. However, despite the broad light harvesting, the improvement in short circuit current ( $J_{SC}$ ) was much lower than expected.<sup>6-10</sup> The best PCE of a P3HT:NFA solar cell achieves only 9.4 % to date,<sup>6</sup> compared to 6.5 % in P3HT:PCBM.<sup>11</sup> This modest improvement suggest that polymers that are efficient in fullerene blends do not necessarily work well in NFA blends.

High performance with NFAs is typically found when paired with donor-acceptor (D-A) type polymers with absorption in the VIS range. Initial trials with polymers based on the benzotriazole (BTA) structure gave efficiencies of around 10%, with simultaneous improvement of  $V_{OC}$  and  $J_{SC}$ .<sup>4, 12</sup> These polymers were then further optimised by fluorination of the polymer backbone, side-chain engineering and interfacial optimization which lead to efficiencies of 13%.<sup>4</sup> Finally efficiencies over 18% were achieved using polymer structures such as PM6, based on the 1,3-bis(thiophen-2-yl)-5,7-bis(2-ethylhexyl)benzo[1,2-c:4,5-c']dithiophene-4,8-dione (BDD) acceptor unit, combined with BTP-4F and its derivatives as NFA.<sup>3, 13</sup> Nevertheless, compared to the polymers previously used in fullerene blends, we find the choice of core structures (D or A building blocks) of polymers that perform well with NFAs to be quite limited. More investigation into these polymers is needed in order to identify desirable donor properties for the generalized design of efficient NFA blends, with a focus on high charge generation yield. A high morphological tolerance, of these donor properties, is also critical since morphology control is hard to achieve in randomly mixed bulk heterojunctions

(BHJs). This is even more pertinent for large area processing, in which careful control of the drying kinetics is almost impossible.<sup>14-16</sup>

In this work, we aim to find what properties define a good polymer for pairing with a prototypical ITIC-type NFA (m-ITIC), with a particular focus on the system's ability to maintain efficient charge generation in different morphologies. We combine the acceptor with two amorphous D-A type polymers (J61 and PCDTBT) as well as state-of-the-art semi-crystalline P3HT (Figure 6-1 A). To obtain a broad set of morphologies, we compare four sample configurations: a bilayer, a 1:1 polymer:m-ITIC BHJ blend, a dilute-acceptor 5:1 blend and a dilute-donor 1:10 blend (blend ratios are given by weight), as shown in Figure 6-1 B. We have previously addressed the impact of the energetic offset between the excited state and the interfacial charge transfer (CT) state on the intrinsic exciton dissociation dynamics, and demonstrated efficient (sub-picosecond) and slightly driving-force dependent charge transfer in all systems.<sup>17</sup> Here, we concentrate on the early geminate charge recombination dynamics measured by transient absorption (TA) spectroscopy and on the time-resolved transport properties accessed via the electro-modulated differential absorption (EDA) technique. We relate this to device measurements and explain the high performance of the J61 polymer by the absence of geminate recombination, which is independent of the sample configuration thanks to a robust amorphous polymer morphology. Moreover, J61 maintains excellent charge separation despite being amorphous thanks to high short-range charge mobility, which is not the case for PCDTBT. For semi-crystalline P3HT, the charge generation is highly morphology-dependent and recombination can only be avoided in the phase-separated bilayer, where high crystallinity is achieved. We therefore conclude that amorphous polymers, with high lying CT states and intrinsically high short-range mobility, are desirable for efficient and easily processed NFA blends. Our results explain why BTA-based polymers can be efficiently paired with NFAs and also point towards the future rules for designing and selecting polymeric donors.

## 6.1. Results and Discussion

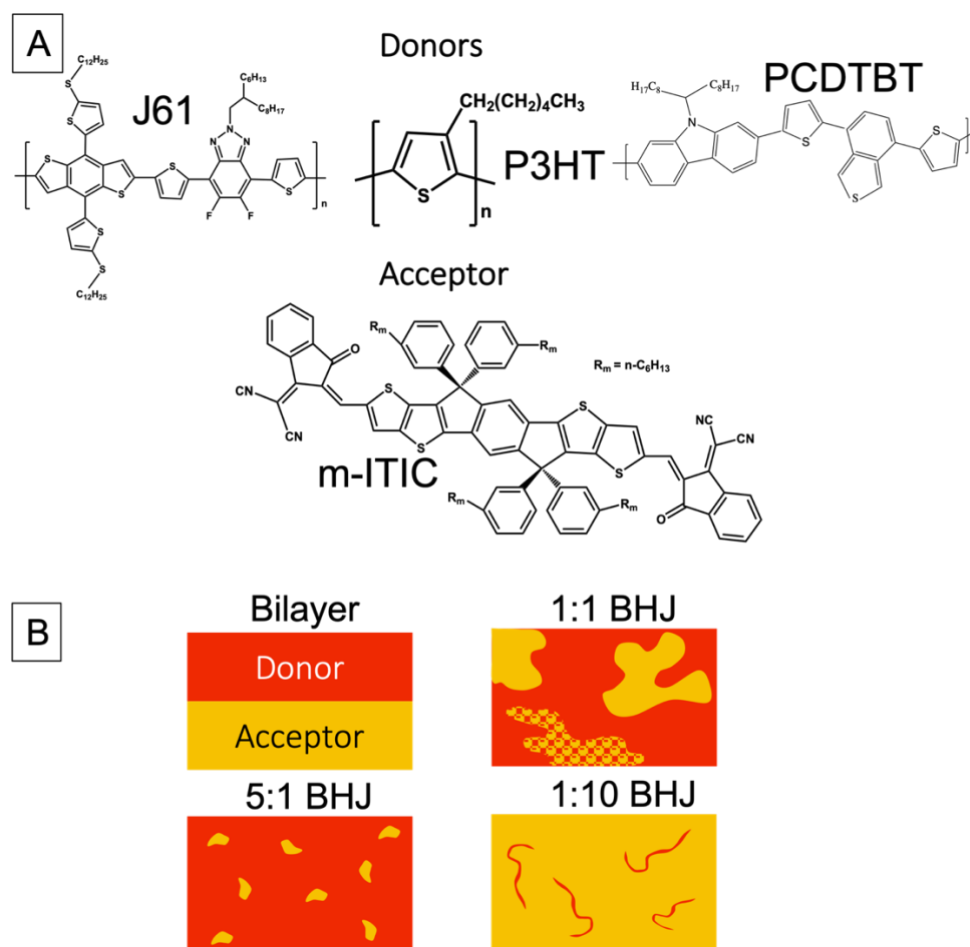


Figure 6.1-1 (A) Chemical structure of the polymers and NFA used in this work. (B) Schematic sample configurations: bilayer, 1:1 (donor:acceptor ratio) BHJ, 5:1 BHJ and 1:10 BHJ

It is well known that BHJs generally exhibit a three-phase morphology where there are both completely intermixed regions along-side phase-separated neat donor and neat acceptor regions.<sup>18, 19</sup> The different interfaces can then be simulated by carefully selecting various blend compositions (Figure 6-1 B). Here, the phase-separated interfaces are analogous to a bilayer morphology, the intermixed acceptors near neat donor regions are simulated with the 5:1 blend, and intermixed donors near neat acceptors with the 1:10 blend. In this way, the different morphological regimes of the BHJ can be studied separately.

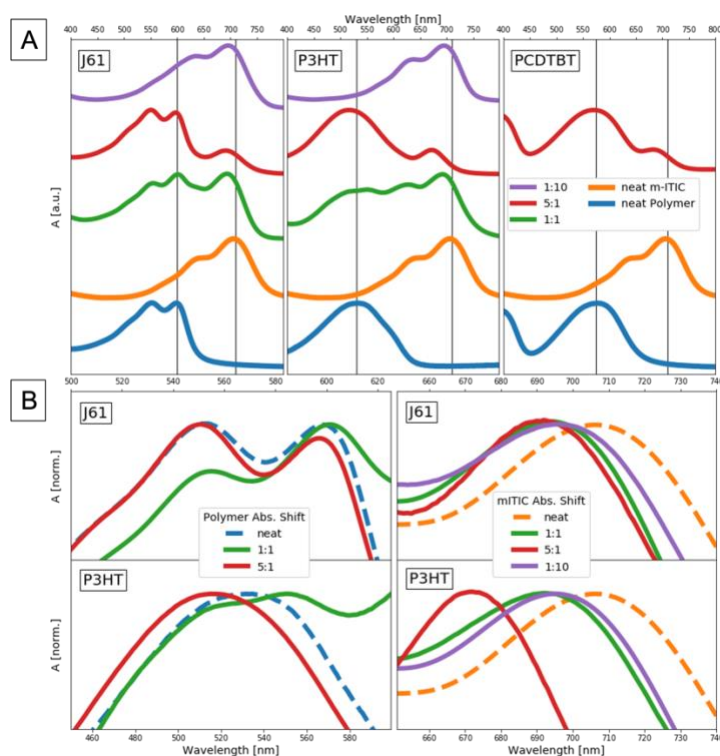


Figure 6.1-2 The absorption spectra of polymer:m-ITIC blends for J61, P3HT and PCDTBT including neat polymer, neat m-ITIC, 1:1 blend, 5:1 blend and 1:10 blends are shown in panel A. Panel B shows a normalised view of absorption peaks for the polymer regions of J61 and P3HT for the neat, 1:1 and 5:1 samples as well as the m-ITIC regions for J61 and P3HT blends for neat m-ITIC, 1:1 blend, 5:1 blend and 1:10 blend.

Comparing the absorption spectra of the blends to the bilayer (layers of bilayer represented by neat films), we gain an insight to the effect of blending on the morphology, order and dielectric environment within the film (Figure 6-2 A). As shown in Figure 6-2 (A and B), the absorption peak (around 710 nm) of neat m-ITIC is blue-shifted when blended with J61 (1:1, 5:1 and 1:10 blends, Figure 6-2 B top right). This is due to weakened inter-m-ITIC interaction and/or change in dielectric environment upon mixing with the polymer. It has already been shown that the 1:1 blend of J61:m-ITIC exhibits a three-phase morphology where there exist both completely intermixed and phase separated regions. The 5:1 J61:m-ITIC blend, on the other hand, was found to be completely intermixed with m-ITIC not forming clusters.<sup>17</sup> The positions of the J61 absorption peaks (550 nm and 600 nm) remain unchanged upon blending with m-ITIC (Figure 6-2 B top left), indicating that the polymer remains amorphous regardless of the blend. Furthermore, for the J61 blends we see a rather consistent m-ITIC blue shift in all three blends, indicating that the dielectric environment remains invariant to blending type. Looking closely at the shape of m-ITIC absorption when blended with J61 (Figure 6-2 B top right) we see that the 1:1 blend is slightly broader than the 5:1 blend resulting from the increased variation of states in the three-phase morphology (phase-separated and intermixed in 1:1 blend) as opposed

to the completely intermixed morphology (5:1 blend). We also see that the m-ITIC absorption in the 1:10 blend is slightly less blue-shifted because of the naturally larger neat m-ITIC regions. A very similar trend is observed in the amorphous PCDTBT 5:1 blend, where the absorption of the polymer (575 nm) remains constant and the absorption of the m-ITIC shifts in a similar way to the J61 blend (Figure 6-2 A).

Neat P3HT displays small shoulders due to the 0-0 and 0-1 vibronic features, typical for this semi-crystalline polymer.<sup>20, 21</sup> Those vibronic transitions are only weakly pronounced, pointing to limited ordering of the polymer chains, likely due to the solvent used to process these films (chloroform, with short time for self-assembly during drying). Upon blending with m-ITIC in the 1:1 ratio, the P3HT peak position remains constant, with the apparent structure in the absorption coming mainly from the underlying m-ITIC absorption. This shows that in the 1:1 blend, the order of the P3HT remains similar to the neat. In the m-ITIC absorption (Figure 6-2 B bottom right) we see the blue shift of the 1:1 and 1:10 blends following the same trends as in the J61 blends, further indicating that the ordering of the P3HT is similar in 1:1 and neat films. In the P3HT:m-ITIC 5:1 blend, however, we observe a large blue shift in the absorption of the P3HT. This shows that the order maintained in the 1:1 blend is lost upon mixing in a 5:1 ratio.<sup>22</sup> The m-ITIC absorption in the 5:1 blend is also greatly blue shifted, most likely due to the change in dielectric environment caused by the change in the order of the P3HT.

As well as describing the morphology of the blends, we can see overall that the amorphousness of the J61 and PCDTBT polymers is invariant to blend morphology, staying the same regardless of blend ratio. Semi-crystalline P3HT on the other hand is unable to maintain its order under some blend morphologies, particularly in the 5:1 blend ratio. This allows us to compare the effects of changing and consistent polymer order on charge separation and recombination.

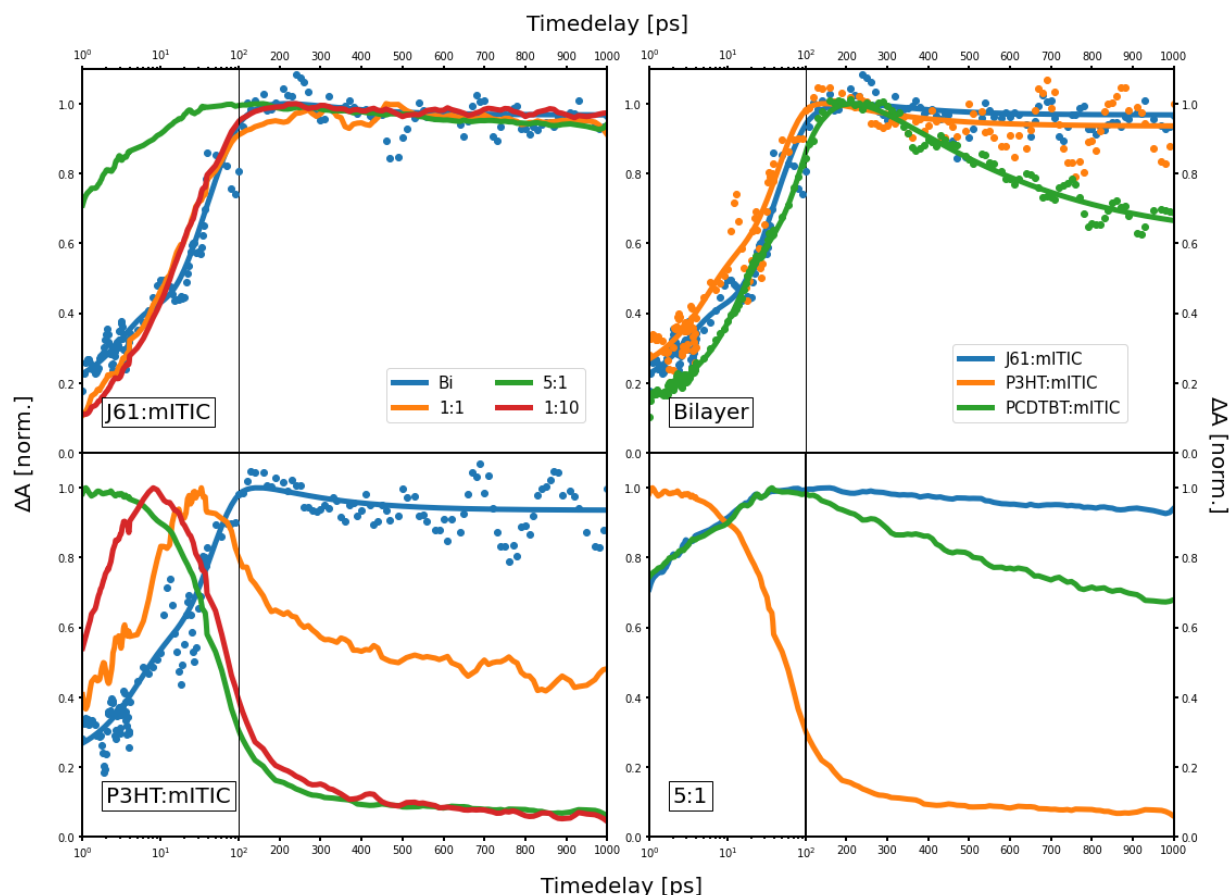


Figure 6.1-3 Normalised dynamics of the charge components from TA measurements of J61, P3HT and PCDTBT blends with *m*-ITIC. The first 100 ps shown on log scale and time delays 100 to 1000 ps on a linear scale. Top left panel shows all J61:*m*-ITIC blends, bottom left shows all P3HT:*m*-ITIC blends. Top right panel compares all three bilayers and bottom right compared all three 5:1 blends. All samples were excited with a 700 or 730 nm pulse, exclusively generating excitons in *m*-ITIC.

With the morphology controlled, we turn to the charge dynamics extracted from the TA measurements of the blends. Figure 6-3 traces the charge population dynamics within the 1 ns timeframe of the measurement and focuses on the recombination of charges, since charge formation occurs in less than 100 ps.<sup>17</sup> Exciton quenching and charge transfer for these blends are exhaustively discussed in a previous work by Zhong and Causa' et.al. The TA spectra on which the decomposition was performed are shown in section A.3.1. There are two main things to keep in mind when discussing these charge dynamics: 1. TA measurements are not able to distinguish between bound CT state charges and free charges; 2. the type of recombination observed on the 1 ns timescale is predominately geminate recombination (CT state recombination) and is the major loss mechanism in OPVs. Some trap-based recombination can also take place in the dilute blends. Bimolecular recombination also takes place and results



in losses but generally occurs at later times and so is not considered, especially since we did not observe any fluence-dependence in the dynamics.

We observe negligible geminate charge recombination in all J61 blends (Figure 6-3 top left), suggesting an efficient and essentially morphology-independent charge separation to free charges (within the 1 ns time window). This is in sharp contrast to the P3HT:m-ITIC blends, where the geminate charge recombination is clearly dependent on the morphology (Figure 6-3 bottom left). The most efficient charge separation (absence of recombination) in P3HT:m-ITIC samples lies in bilayer configuration, where the donor and acceptor are completely phase-separated. Once the donor and acceptor start to blend, in the 1:1 sample for instance, around half of the charges are lost due to geminate recombination and almost all charges are lost when the donor or acceptor is dispersed in the other (5:1 or 1:10 blends). The different charge recombination behaviour between the 1:1 and dilute blends in the P3HT samples lies in the phase-separated regions present in the 1:1 blend. A 3-phase morphology exists in the 1:1 blend, where a combination of phase-separated and intermixed regions exist. The presence of phase-separated regions helps charge separation both at the interface and in terms of transport away from the interface, as in the extreme example of the bilayer and as reported previously in polymer:fullerene blends.<sup>19, 23</sup> At the interface of the phase-separated domains, the interface is clearly defined and interfacial ordering of donor and acceptor is preserved due to the absence of mixing.<sup>24-29</sup> Additionally, the order of the adjacent neat domains at the phase-separated interface promotes delocalisation and efficient separation of CT states. Interestingly, the requirement of neat domains includes both donor and acceptor. In the 5:1 P3HT:m-ITIC blend, the majority of charges recombines even though we expect large P3HT regions, this could be a result of the break in order of the P3HT observed in the absorption spectrum (Figure 6-2). The recombination in the P3HT 1:10 blends could also be a result of the poor delocalisation of holes in the polymer as well as some disruption of m-ITIC regions by the P3HT.

In the blends, the J61:m-ITIC samples show J61 order that is similar to that of the bilayer (or neat film, as evidenced by absorption data), suggesting that the morphology is dominated by phase-separated interfaces regardless of the blend ratios. P3HT:m-ITIC blends, on the other hand, clearly show that the amount of phase separated-regions and interfaces is dependent on the mixing ratio. This shows that charge separation in P3HT:m-ITIC blends would not be robust to morphology and mixing variations in less controllable large-scale applications. Despite having a similar amorphous nature to J61, we observe charge recombination in PCDTBT:m-ITIC bilayer and 5:1 blends, as shown in Figure 6-3 (right). The recombination in

PCDTBT is, however, still substantially less than that of P3HT in 5:1 blends, but more in the bilayer. This suggests that under the ideal charge separation conditions of the bilayer, P3HT is more efficient than PCDTBT, but that the morphological robustness of PCDTBT allows it to separate charges more efficiently in more realistic intermixed morphologies of the 5:1 blend. This provides a basic argument for using amorphous polymers with NFAs for OPV applications.

Lastly, since TA shows the dynamics of both bound CT state charges and separated charges, the effect of the  $E_{CT}$  on the geminate recombination needs to be taken into consideration. The  $E_{CT}$  of the J61 and PCDTBT blends are significantly higher than that of the P3HT blends (PCDTBT 5:1 1.62 eV, J61 5:1 1.55 eV and P3HT 5:1 1.2 eV).<sup>17</sup> We know that blends with higher  $E_{CT}$  typically show slower non-radiative CT state recombination, and so the competition between recombination and separation is more in favour of the separation for high  $E_{CT}$  blends.<sup>30</sup> This could partially explain the large difference in recombination between P3HT and the amorphous blends, but not why we still see recombination in PCDTBT (with the highest  $E_{CT}$ ) and not in J61. This suggests that, as well as being amorphous and having slower CT state recombination, there are other requirements for efficient charge separation.

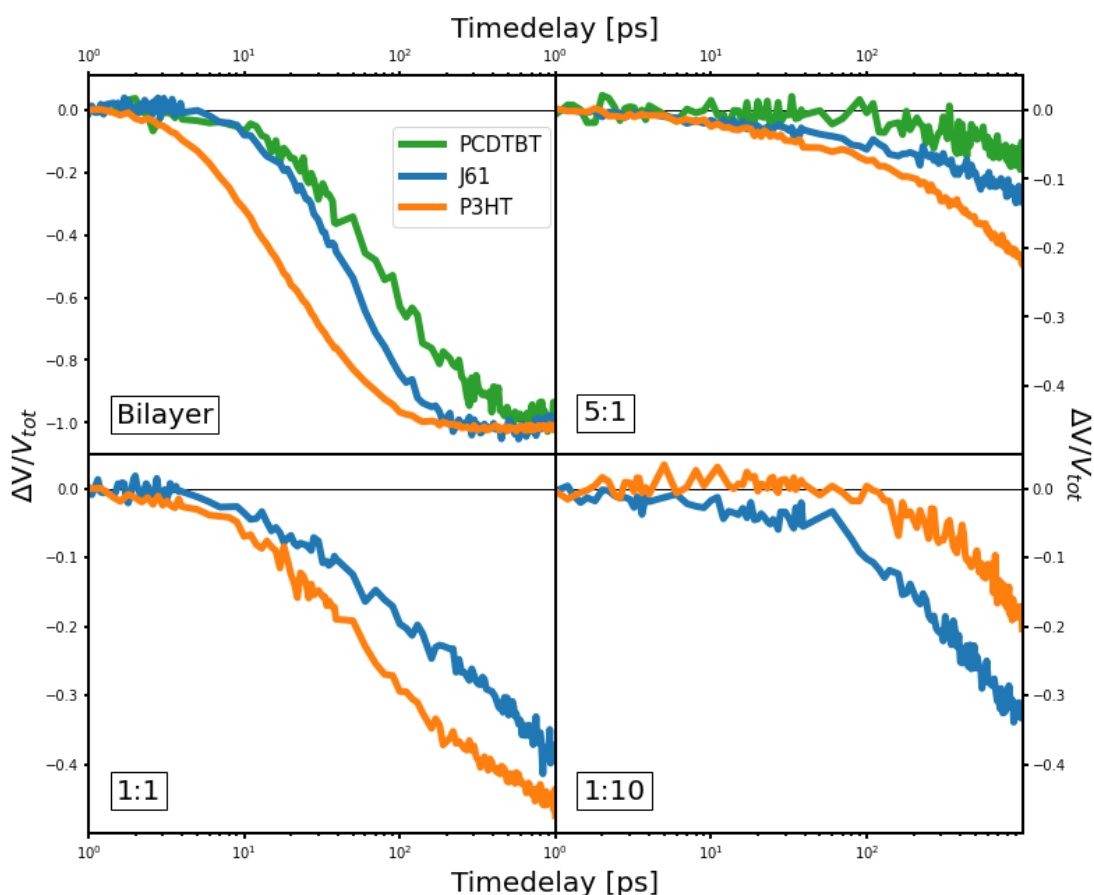


Figure 6.1-4 Normalised voltage drop from EDA measurements of PCDTBT, J61 and P3HT blends and bilayers with m-ITIC. The normalised voltage drop represents the charge collection over time, with -1 indicating that all the charge is collected ( $V_{tot}$  is the total extracted charge obtained from a photocurrent measurement). All devices are excited at 700 nm, selectively exciting m-ITIC exciton. Top left shows the voltage drop for the bilayers with layer thicknesses and applied voltage of: PCDTBT (10 nm, 6V), P3HT (10 nm, 5V), J61 (9 nm, 1.7V), m-ITIC (9 nm). Top right shows 5:1 polymer:m-ITIC blends with thicknesses and applied voltage of: PCDTBT 120 nm and 8V, J61 130 nm and 7V, P3HT 85 nm and 10V. Bottom left shows 1:1 polymer:m-ITIC blends with thicknesses and applied voltage of: J61 150 nm and 4.3V, P3HT 97 nm 6V. Bottom right shows 1:10 polymer:m-ITIC blends with thicknesses and applied voltage of: J61 78 nm and 6V, P3HT 99 nm and 4V.

In order to follow the charge separation and transport processes more closely, we employ our previously reported EDA measurement (Figure 6-4).<sup>19</sup> This measurement essentially captures the change in electro-absorption induced by the generation/transport of free charges and so represents the percentage of the total charges collected at each timestep. It is important to note that the EDA measures only the unbound or free charge carriers, excluding charges that undergo geminate charge recombination, in this way we see the separation and transport of the surviving charges. Using the different blend ratios and bilayers, we can observe the transport properties in three scenarios: 1. both electrons and holes can be transported in percolated regions in the bilayer; 2. both electrons and holes can be transported but in a less efficient way in a 3-phase morphology (mixed phase and 2 pure phases) in the 1:1 BHJ; 3. one of the carriers

will be essentially trapped in dilute blends, we therefore only see holes in 5:1 BHJ and electrons in 1:10 BHJ (hole might also migrate along polymer chains in 1:10 sample, but not further).

The EDA dynamics of the three bilayer devices are plotted in the top left of Figure 6-4 where we see a rapid collection of all generated charges (-1 on the normalised voltage drop scale) within the 1 ns time scale, owing to the efficient charge separation and the thinness of the layers (9-10 nm) used to construct all bilayer samples. The charge transfer is very similar in all three bilayers making the formation of CT states comparable (Figure 6-3 B top right). The thicknesses of the bilayers are roughly the same but the EDA was measured using different applied voltages (J61 at 1.7V, P3HT at 5V and PCDTBT at 6V), however we do not observe any voltage dependence in the normalised EDA traces. Among the three bilayer samples, the P3HT sample shows the fastest charge separation and collection with all charges being collected within 100 ps. This is due to good ordering and packing of the P3HT chains being preserved in the bilayer configuration, allowing efficient charge separation and transport. The J61 bilayer shows slightly slower CT state separation and collects all charges in 200 ps. The PCDTBT sample, however, shows the slowest separation and takes over 500 ps to complete charge collection even with the highest applied voltage. Since the sample configuration and thickness in these bilayer samples is the same, such striking differences suggest that the lower short-range mobility in the PCDTBT sample jeopardizes its charge separation. When comparing the P3HT and J61 bilayers, where there is no disruption of order and unhindered percolation pathways, we see comparable separation and extraction efficiencies, with P3HT being slightly more efficient.

In the 1:1 blends (Figure 6-4 bottom left) we see a notably faster charge collection in the P3HT blend compared to the J61 blend, despite the higher recombination. This confirms that the EDA is only able to observe charges which separate from the favourable phase separated regions of the P3HT blend. However, in both the bilayers and 1:1 blends we have different exciton diffusion which would have an effect on the charge rise time and so we turn to the 5:1 samples where the exciton diffusion is minimised. In the 5:1 blends (Figure 6-4 top right) we still see a faster charge collection in P3HT compared to the amorphous polymers. This can be related to the fact that the few charges that separate in P3HT are generated in very ordered regions, where the mobility is higher than in J61 and PCDTBT. Notably we see a much slower extraction in the PCDTBT blend than in the J61 blend even though their charge rise time is the same in TA, indicating that the lower mobility of PCDTBT indeed hinders the charge separation. Since the electrons are essentially trapped on the isolated m-ITIC in the dilute 5:1 blends, the primary

charge carriers observed are the holes moving through the polymers.<sup>31</sup> In order to see the effect of morphology on the electron transport we look at the 1:10 blends of P3HT and J61. In the 1:10 blends we see that the electron dominated separation is faster in the J61 blend. This suggests that the J61 polymer not only maintains its order when blended with m-ITIC (in 1:1 and 5:1 blends) but also most likely allows for better hole delocalisation (intrachain transport) than P3HT resulting in better CT separation in the J61 1:10 blend as well as potentially less m-ITIC disruption.

We close our discussion by again mentioning that TA does not differentiate between CT states and free charges, while EDA only detects free charges. This allows us to get an idea of the lifetime of CT states by comparing the TA and EDA results. The TA dynamics in Figure 6-3 (top right) clearly show CT/free charges at 1 ps (approximately 20% of excitons quenched) in all three bilayers, while EDA shows free charges only after 3-4 ps (Figure 6-4 top left) even in such favourable morphological conditions. This effect is accentuated in the 5:1 dilute blends (where exciton diffusion is mitigated but the blend morphology becomes less favourable to charge separation), where we see between 75 and 100% exciton quenching in TA after 1 ps but free charges only after 5-10 ps (around 100 ps for PCDTBT). We therefore conclude a relatively slow intrinsic charge separation in the polymer:NFA blends (even in favourable morphology) compared to ultrafast (femtosecond) charge separation in polymer: fullerene blends.<sup>19, 32</sup> We speculate this difference might be associated with the different electronic coupling between polymers and NFAs compared to that in polymer:fullerene blends, as well as the effect of electron delocalisation in fullerene clusters on charge separation. This again brings us to the competition between CT state recombination and separation, where even blends with slow CT recombination (like J61 and PCDTBT with high  $E_{CT}$ ) require high short-range mobility to ensure efficient separation and mitigate geminate charge recombination.

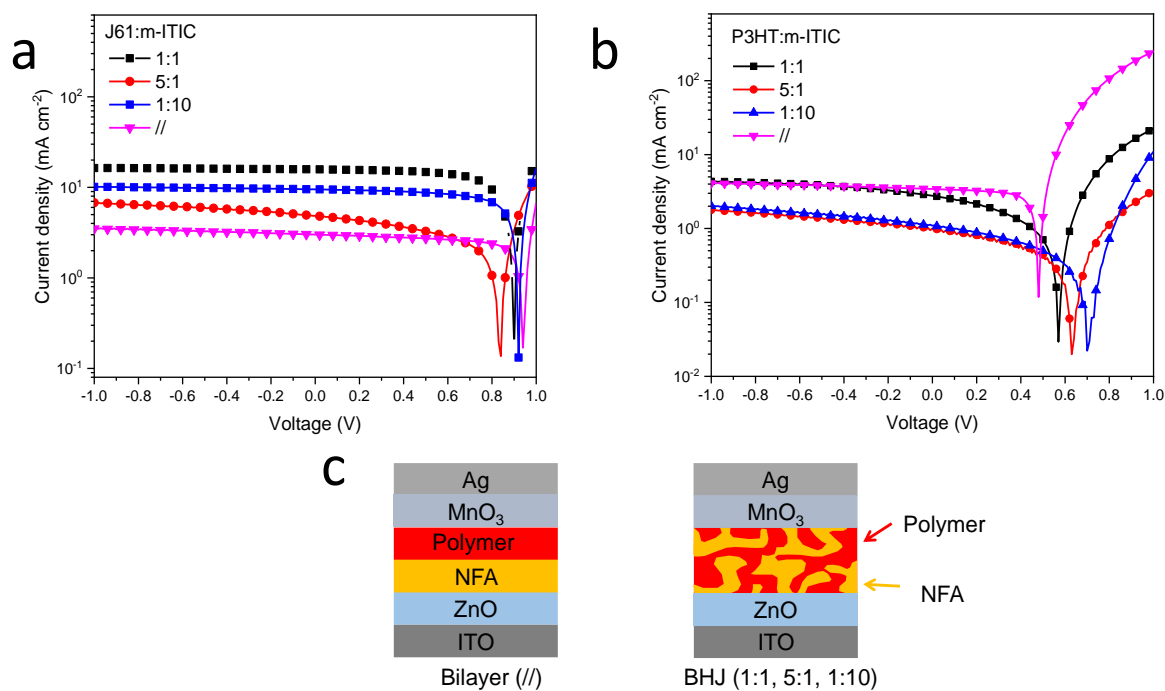


Figure 6.1-5 J-V curves of (a) J61:m-ITIC based samples and (b) P3HT:m-ITIC based samples. (c) Structure of bilayer and BHJ photovoltaic devices. Both the polymer and NFA layers in bilayer devices are around 9 nm thick; the thickness of the BHJs is around 100 nm.

Table 6-1 Figures of merit for devices based on J61:m-ITIC and P3HT:m-ITIC bilayers and blends.

Sample	$V_{OC}$ (V)	$J_{SC}$ (mA cm <sup>-2</sup> )	FF	PCE (%)
J61//m-ITIC	0.93±0.01	2.90±0.10	66.55±2.02	1.81±0.13
J61:m-ITIC (1:1)	0.90±0.01	17.65±0.03	63.45±0.41	10.01±0.07
J61:m-ITIC (5:1)	0.84±0.01	4.68±0.12	41.51±1.29	1.62±0.09
J61:m-ITIC (1:10)	0.92±0.01	10.40±0.16	64.58±0.23	6.20±0.06
P3HT//m-ITIC	0.47±0.01	3.06±0.45	64.23±0.65	0.94±0.17
P3HT:m-ITIC (1:1)	0.56±0.01	2.42±0.24	33.10±0.47	0.45±0.05
P3HT:m-ITIC (5:1)	0.62±0.02	0.87±0.08	35.90±1.50	0.20±0.03
P3HT:m-ITIC (1:10)	0.68±0.04	1.01±0.10	33.76±0.54	0.23±0.04

Devices based on the J61:m-ITIC and P3HT:m-ITIC blends and bilayers were fabricated in order to compare their performance in the different configurations. The J-V curves measured from the devices are shown in Figure 6-2 (J61 in A and P3HT in B) along with the device composition (Figure 6-2 C) and the figures of merit are summarised in Table 6-1. There are clear trends of the device parameters in J61 and P3HT based samples. The overall higher  $V_{OC}$  in the J61 samples is simply explained by the higher lying CT state energy ( $E_{CT}$ ) of the J61 blends (1.55 eV for J61 1:1 and 1.20 eV for P3HT 1:1).<sup>17</sup> We first compare the  $V_{OC}$  in the J61:m-ITIC based devices, where only minor changes (tens of mV) are observed as the donor and acceptor start to blend or one component dilutes in the other. Contrastingly, the P3HT:m-ITIC samples show a significant increase (0.47 to 0.68 V) in  $V_{OC}$  when P3HT is blended with m-ITIC. The large increase of  $V_{OC}$  in the P3HT samples can be explained by the decreased packing between P3HT chains when mixed with m-ITIC, which increases the bandgap (as observed in the absorption spectrum) and increases  $E_{CT}$ , and/or changes in charge delocalization. According to a previous report, crystalline and amorphous regions are simultaneously present in the P3HT films and different bandgaps in the bulk and at the interface are possible.<sup>33</sup> Further reports have also shown crystalline P3HT to have an up to 0.3 eV higher HOMO (highest occupied molecular orbital) level than amorphous P3HT, which explains the large difference in  $V_{OC}$  between the more ordered bilayer and more disordered 5:1 blend.<sup>34</sup> CT state delocalisation is expected to be largest in the bilayer which lowers the  $E_{CT}$  and so can increase non-radiative recombination induced energy losses. Additionally, since J61 remains relatively amorphous in the bilayer and BHJ samples, the slight decrease of  $V_{OC}$  in the blended J61 based samples could be partially explained by the change order in m-ITIC (seen by the shift of absorption) particularly in the 5:1 blend. Note that  $V_{OC}$  is a comprehensive term reflecting many interfacial properties, we here only screen few of the factors governing  $V_{OC}$ . The above  $V_{OC}$  trends agree well with the trends in our absorption.

The phenomenon is even more pronounced in the other device parameters like  $J_{SC}$  and FF. Upon blending J61 and m-ITIC,  $J_{SC}$  increases due to the increase of interfacial area in the BHJ and decrease in required exciton diffusion distance.<sup>17</sup> This is, however, not true in P3HT blends. The drop of  $J_{SC}$  in P3HT based BHJs shows that the advantage of an increased donor/acceptor interfacial area for exciton splitting and more efficient exciton quenching is negated by the substantial increase in geminate charge recombination at these interfaces (evidenced by our TA data in Figure 6-3). Similarly, the FF in P3HT based BHJ devices is only

half of that in bilayer device. The FF is related to non-geminate charge recombination and charge extraction. In the P3HT bilayer minimal non-geminate recombination is expected and charge extraction is essentially unhindered resulting in a high FF. In the P3HT blends non-geminate recombination is aided by trap-based recombination, where electrons are trapped on isolated or intermixed m-ITIC molecule in the 1:1 and 5:1 and holes on the P3HT, in the 1:10 blend, which requires good packing for inter/intrachain transport. The FF of J61 remains consistent for all blends except the 5:1 blend. This suggests that there is limited non-geminate recombination and efficient charge extraction in J61 based samples unless electrons are trapped on isolated m-ITIC molecules (5:1 blend) where trap-based recombination takes effect, decreasing the FF. The compromise of FF in the J61 BHJs, upon blending/dilution, is not as pronounced as in P3HT, again showing the benefit of morphology tolerance.

Starting from the bilayer devices, both J61 and P3HT show essentially the same  $J_{SC}$  and FF, due to the same device structure, layer thickness and similar absorption region. The only difference observed is  $V_{OC}$ , which is mainly a consequence of the difference in  $E_{CT}$ . Upon blending, however, charge recombination dominates the P3HT samples, leading to a sharp decrease of  $J_{SC}$  and FF. J61 based samples, on the other hand, present a decent improvement in  $J_{SC}$  and minor compromise in FF. The factors which result in the higher PCE in the J61 1:1 blend are the high lying CT state and high mobility in all morphological scenarios, which results in both efficient charge separation and charge extraction.



## 6.2. Conclusion

We have, in this work, studied the impact of morphology, and charge separation efficiency (short-range mobility) on charge generation in three different polymer:NFA systems. We find that blends with a high lying  $E_{CT}$ , and polymers with a relatively amorphous nature with high intrinsic short-range carrier mobility lead to efficient charge generation. Being amorphous allows polymers to maintain similar packing regardless of morphology, preventing morphology dependent charge recombination. The main loss in these polymer:NFA blends is geminate CT state charge recombination. This can be also somewhat mitigated by choosing a polymer:NFA combination with a high lying  $E_{CT}$ , and so a slower CT state recombination rates, so that the competition between separation and recombination becomes less fierce (J61 and PCDTBT with m-ITIC). High short-range carrier mobility, even with an amorphous nature, is key to aid charge separation and counteract geminate charge recombination (J61 with m-ITIC). On the other hand, a semi-crystalline polymer can also eliminate recombination when interfacial order is preserved (P3HT bilayer for example, where short-range mobility remains high) but can also lead to substantial charge recombination when the aggregation (and ordering) of the polymer is disrupted by the NFA. The benefit of choosing an amorphous polymer with high short-range mobility is that significant morphology tolerant charge generation can be achieved. Morphology tolerance will be highly desirable for large area applications and with a wide range of acceptor materials where strict morphology control is not cost-effective. The ideal polymer properties discovered here serve as guidelines for designing and selecting materials to further push the efficiency of NFA based devices both under laboratory and industrial processing conditions and offers new insight into the important effects of morphology on charge generation in the age of non-fullerene acceptors.

## Reference

1. Zhong, Y.; Causa', M.; Moore, G. J.; Krauspe, P.; Xiao, B.; Günther, F.; Kublitski, J.; Shivhare, R.; Benduhn, J.; BarOr, E.; Mukherjee, S.; Yallum, K. M.; Réhault, J.; Mannsfeld, S. C. B.; Neher, D.; Richter, L. J.; DeLongchamp, D. M.; Ortmann, F.; Vandewal, K.; Zhou, E.; Banerji, N., Sub-picosecond charge-transfer at near-zero driving force in polymer:non-fullerene acceptor blends and bilayers. *Nature Communications* **2020**, *11* (1), 833.
2. Li, C.; Zhou, J.; Song, J.; Xu, J.; Zhang, H.; Zhang, X.; Guo, J.; Zhu, L.; Wei, D.; Han, G.; Min, J.; Zhang, Y.; Xie, Z.; Yi, Y.; Yan, H.; Gao, F.; Liu, F.; Sun, Y., Non-fullerene acceptors with branched side chains and improved molecular packing to exceed 18% efficiency in organic solar cells. *Nat. Energy* **2021**, *6*, 605-613.
3. Xu, Y.; Cui, Y.; Yao, H.; Zhang, T.; Zhang, J.; Ma, L.; Wang, J.; Wei, Z.; Hou, J., A New Conjugated Polymer that Enables the Integration of Photovoltaic and Light-Emitting Functions in One Device. *Adv. Mater.* **2021**, 2101090.
4. Cui, C.; Li, Y., High-performance conjugated polymer donor materials for polymer solar cells with narrow-bandgap nonfullerene acceptors. *Energy Environ. Sci.* **2019**, *12* (11), 3225-3246.
5. Zhao, J.; Li, Y.; Yang, G.; Jiang, K.; Lin, H.; Ade, H.; Ma, W.; Yan, H., Efficient organic solar cells processed from hydrocarbon solvents. *Nat. Energy* **2016**, *1* (2), 15027.
6. Yang, C.; Zhang, S.; Ren, J.; Gao, M.; Bi, P.; Ye, L.; Hou, J., Molecular design of a non-fullerene acceptor enables a P3HT-based organic solar cell with 9.46% efficiency. *Energy Environ. Sci.* **2020**, *13* (9), 2864-2869.
7. Holliday, S.; Ashraf, R. S.; Wadsworth, A.; Baran, D.; Yousaf, S. A.; Nielsen, C. B.; Tan, C.-H.; Dimitrov, S. D.; Shang, Z.; Gasparini, N.; Alamoudi, M.; Laquai, F.; Brabec, C. J.; Salleo, A.; Durrant, J. R.; McCulloch, I., High-efficiency and air-stable P3HT-based polymer solar cells with a new non-fullerene acceptor. *Nat. Commun.* **2016**, *7* (1), 11585.
8. Baran, D.; Ashraf, R. S.; Hanifi, D. A.; Abdelsamie, M.; Gasparini, N.; Röhr, J. A.; Holliday, S.; Wadsworth, A.; Lockett, S.; Neophytou, M.; Emmott, C. J. M.; Nelson, J.; Brabec, C. J.; Amassian, A.; Salleo, A.; Kirchartz, T.; Durrant, J. R.; McCulloch, I., Reducing the efficiency–stability–cost gap of organic photovoltaics with highly efficient and stable small molecule acceptor ternary solar cells. *Nat. Mater.* **2017**, *16* (3), 363-369.
9. Tang, A.; Zhan, C.; Yao, J.; Zhou, E., Design of Diketopyrrolopyrrole (DPP)-Based Small Molecules for Organic-Solar-Cell Applications. *Adv. Mater.* **2017**, *29* (2), 1600013.
10. Xiao, B.; Tang, A.; Zhang, J.; Mahmood, A.; Wei, Z.; Zhou, E., Achievement of High Voc of 1.02 V for P3HT-Based Organic Solar Cell Using a Benzotriazole-Containing Non-Fullerene Acceptor. *Adv. Energy Mater.* **2017**, *7* (8), 1602269.
11. Lee, S.-H.; Kim, D.-H.; Kim, J.-H.; Lee, G.-S.; Park, J.-G., Effect of Metal-Reflection and Surface-Roughness Properties on Power-Conversion Efficiency for Polymer Photovoltaic Cells. *J. Phys. Chem. C* **2009**, *113* (52), 21915-21920.
12. Bin, H.; Zhang, Z.-G.; Gao, L.; Chen, S.; Zhong, L.; Xue, L.; Yang, C.; Li, Y., Non-Fullerene Polymer Solar Cells Based on Alkylthio and Fluorine Substituted 2D-Conjugated Polymers Reach 9.5% Efficiency. *J. Am. Chem. Soc.* **2016**, *138* (13), 4657-4664.
13. Yuan, J.; Zhang, Y.; Zhou, L.; Zhang, G.; Yip, H.-L.; Lau, T.-K.; Lu, X.; Zhu, C.; Peng, H.; Johnson, P. A.; Leclerc, M.; Cao, Y.; Ulanski, J.; Li, Y.; Zou, Y., Single-Junction Organic Solar Cell with over 15% Efficiency Using Fused-Ring Acceptor with Electron-Deficient Core. *Joule* **2019**, *3* (4), 1140-1151.
14. Zhong, M.; Li, Y.; Du, G.; Li, Y.; Chang, K.; Lau, T.-K.; Lu, X.; Sun, H.; Guo, X.; Guo, Y.-F.; Zhao, X.; Deng, W., Soft Porous Blade Printing of Nonfullerene Organic Solar Cells. *ACS Appl. Mater. Interfaces* **2020**, *12* (23), 25843-25852.

15. Zhang, L.; Zhao, H.; Yuan, J.; Lin, B.; Xing, Z.; Meng, X.; Ke, L.; Hu, X.; Ma, W.; Yuan, Y., Blade-coated efficient and stable large-area organic solar cells with optimized additive. *Org. Electron.* **2020**, *83*, 105771.
16. Gu, X.; Zhou, Y.; Gu, K.; Kurosawa, T.; Guo, Y.; Li, Y.; Lin, H.; Schroeder, B. C.; Yan, H.; Molina-Lopez, F.; Tassone, C. J.; Wang, C.; Mannsfeld, S. C. B.; Yan, H.; Zhao, D.; Toney, M. F.; Bao, Z., Roll-to-Roll Printed Large-Area All-Polymer Solar Cells with 5% Efficiency Based on a Low Crystallinity Conjugated Polymer Blend. *Adv. Energy Mater.* **2017**, *7* (14), 1602742.
17. Zhong, Y.; Causa, M.; Moore, G. J.; Krauspe, P.; Xiao, B.; Günther, F.; Kublitski, J.; Shivhare, R.; Benduhn, J.; BarOr, E.; Mukherjee, S.; Yallum, K. M.; Réhault, J.; Mannsfeld, S. C. B.; Neher, D.; Richter, L. J.; DeLongchamp, D. M.; Ortmann, F.; Vandewal, K.; Zhou, E.; Banerji, N., Sub-picosecond charge-transfer at near-zero driving force in polymer:non-fullerene acceptor blends and bilayers. *Nat. Commun.* **2020**, *11* (1), 833.
18. Westacott, P.; Tumbleston, J. R.; Shoaee, S.; Fearn, S.; Bannock, J. H.; Gilchrist, J. B.; Heutz, S.; deMello, J.; Heeney, M.; Ade, H.; Durrant, J.; McPhail, D. S.; Stingelin, N., On the role of intermixed phases in organic photovoltaic blends. *Energy & Environmental Science* **2013**, *6* (9), 2756-2764.
19. Causa, M.; De Jonghe-Risse, J.; Scarongella, M.; Brauer, J. C.; Buchaca-Domingo, E.; Moser, J.-E.; Stingelin, N.; Banerji, N., The fate of electron-hole pairs in polymer:fullerene blends for organic photovoltaics. *Nat. Commun.* **2016**, *7* (1), 12556.
20. Yamagata, H.; Spano, F. C., Interplay between intrachain and interchain interactions in semiconducting polymer assemblies: The HJ-aggregate model. *J. Chem. Phys.* **2012**, *136* (18), 184901.
21. Yamagata, H.; Spano, F. C., Vibronic coupling in quantum wires: Applications to polydiacetylene. *J. Chem. Phys.* **2011**, *135* (5), 054906.
22. Moulé, A. J.; Neher, D.; Turner, S. T., P3HT-Based Solar Cells: Structural Properties and Photovoltaic Performance. In *P3HT Revisited – From Molecular Scale to Solar Cell Devices*, Ludwigs, S., Ed. Springer Berlin Heidelberg: Berlin, Heidelberg, 2014; pp 181-232.
23. Chen, D.; Nakahara, A.; Wei, D.; Nordlund, D.; Russell, T. P., P3HT/PCBM Bulk Heterojunction Organic Photovoltaics: Correlating Efficiency and Morphology. *Nano Lett.* **2011**, *11* (2), 561-567.
24. Zhong, Y.; Ma, J.; Hashimoto, K.; Tajima, K., Electric Field-Induced Dipole Switching at the Donor/Acceptor Interface in Organic Solar Cells. *Adv. Mater.* **2013**, *25* (7), 1071-1075.
25. Zhong, Y.; Tada, A.; Geng, Y.; Wei, Q.; Hashimoto, K.; Tajima, K., Donor/Acceptor Interface Modifications in Organic Solar Cells. *J. Photopolym. Sci. Technol.* **2013**, *26* (2), 181-184.
26. Tada, A.; Geng, Y.; Wei, Q.; Hashimoto, K.; Tajima, K., Tailoring organic heterojunction interfaces in bilayer polymer photovoltaic devices. *Nat. Mater.* **2011**, *10* (6), 450-455.
27. Zhong, Y.; Tada, A.; Izawa, S.; Hashimoto, K.; Tajima, K., Enhancement of VOC without Loss of JSC in Organic Solar Cells by Modification of Donor/Acceptor Interfaces. *Adv. Energy Mater.* **2014**, *4* (5), 1301332.
28. Zhong, Y.; Suzuki, K.; Inoue, D.; Hashizume, D.; Izawa, S.; Hashimoto, K.; Koganezawa, T.; Tajima, K., Interface-induced crystallization and nanostructure formation of [6,6]-phenyl-C61-butyric acid methyl ester (PCBM) in polymer blend films and its application in photovoltaics. *J. Mater. Chem. A* **2016**, *4* (9), 3335-3341.
29. Wei, Q.; Miyanishi, S.; Tajima, K.; Hashimoto, K., Enhanced Charge Transport in Polymer Thin-Film Transistors Prepared by Contact Film Transfer Method. *ACS Appl. Mater. Interfaces* **2009**, *1* (11), 2660-2666.

30. Collado-Fregoso, E.; Pugliese, S. N.; Wojcik, M.; Benduhn, J.; Bar-Or, E.; Perdigón Toro, L.; Hörmann, U.; Spoltore, D.; Vandewal, K.; Hodgkiss, J. M.; Neher, D., Energy-Gap Law for Photocurrent Generation in Fullerene-Based Organic Solar Cells: The Case of Low-Donor-Content Blends. *Journal of the American Chemical Society* **2019**, *141* (6), 2329-2341.
31. Moore, G. J.; Causa', M.; Martinez Hardigree, J. F.; Karuthedath, S.; Ramirez, I.; Jungbluth, A.; Laquai, F.; Riede, M.; Banerji, N., Ultrafast Charge Dynamics in Dilute-Donor versus Highly Intermixed TAPC:C60 Organic Solar Cell Blends. *The Journal of Physical Chemistry Letters* **2020**, *11* (14), 5610-5617.
32. Gélinas, S.; Rao, A.; Kumar, A.; Smith, S. L.; Chin, A. W.; Clark, J.; van der Poll, T. S.; Bazan, G. C.; Friend, R. H., Ultrafast Long-Range Charge Separation in Organic Semiconductor Photovoltaic Diodes. *Science* **2014**, *343* (6170), 512-516.
33. Ohkita, H.; Ito, S., Transient absorption spectroscopy of polymer-based thin-film solar cells. *Polymer* **2011**, *52* (20), 4397-4417.
34. Tsoi, W. C.; Spencer, S. J.; Yang, L.; Ballantyne, A. M.; Nicholson, P. G.; Turnbull, A.; Shard, A. G.; Murphy, C. E.; Bradley, D. D. C.; Nelson, J.; Kim, J.-S., Effect of Crystallization on the Electronic Energy Levels and Thin Film Morphology of P3HT:PCBM Blends. *Macromolecules* **2011**, *44* (8), 2944-2952.

# 7 Deep transfer leaning: a fast and accurate tool to predict energy levels of donor molecules for organic photovoltaics

## Foreword

This work demonstrates a machine learning based predictive quantitative structure-property relationship model for organic semiconductors intended as donor molecules in OPV systems. The model is trained to predict the HOMO and LUMO energy levels of a molecule comparable to experimental values. While the work in the chapter does not rely on the spectroscopic experimental work which dominates the previous chapters, the motivation clearly stems from the importance these energy levels for predicting and explaining the properties of OPV devices. This model shows good predictability when compared to traditional DFT based calculations and most importantly has very well defined limitations. The hope would be that this or similar models make both effective tools screening of new high efficiency materials and are incorporated as tools for research into the photo-physics of these materials.

The work in this chapter is done by:

Gareth John Moore<sup>1</sup>, Olivier Bardagot<sup>1</sup> and Natalie Banerji<sup>1</sup>

<sup>1</sup>Department of Chemistry and Biochemistry, University of Bern, Freiestrasse 3, 3012 Bern, Switzerland.

## AUTHOR CONTRIBUTIONS:

G.M. conceived and led the project. G.M. designed, trained, and validated the model. O.B. compiled the ‘use-case’ dataset with the help of G.M. O.B. identified the and classified represented/unrepresented building blocks in ‘use-case’ dataset. The manuscript was written by G.M. with the help of O.B. and the supervision and help of N.B.

The supporting information is published in the Appendix chapter of this thesis.

#### 4.7. Introduction

With the burning of fossil fuels massively contributing to the current global warming crisis, the design, optimization and implementation of renewable alternatives for energy generation is critical to curb its already devastating effects.<sup>1</sup> Organic photovoltaics (OPV) offer a cost-effective, lightweight, flexible and renewable light-to-electrical energy conversion process, and with efficiencies over 19%,<sup>2</sup> show promise as one of the viable alternatives to fossil fuels.<sup>3-7</sup> Much of these efficiency improvements have come from molecular engineering based on empirically determined design rules and trial-and-error methods. It has been shown, however, that the energies of the frontier molecular orbitals (Highest Occupied Molecular Orbital or HOMO, and Lowest Unoccupied Molecular Orbital or LUMO) can be used as a good approximation of the expected power conversion efficiency of materials in OPV devices<sup>8-10</sup>. Consequently, a pre-synthetic determination of these energies makes screening of potential materials more efficient. The theoretical determination of the HOMO/LUMO levels of organic molecules is traditionally achieved using Density Functional Theory (DFT) based calculations.<sup>11-13</sup> However, the accuracy of DFT simulations is limited by the inherent trade-off between over-delocalization and under-binding.<sup>14,15</sup> Besides, DFT simulations are computationally expensive and time consuming, thereby limiting the usefulness of DFT for large scale OPV power conversion efficiency predictions and material screening. To address these limitations, deep learning methods,<sup>16,17</sup> along with the development of ever larger datasets, has emerged as a promising alternative for the development of highly predictive quantitative structure-property relationship (QSPR) models in the field of OPV.<sup>18-23</sup>

In this work a QSPR deep learning model, in the form of a deep convolutional neural network, is developed to predict the HOMO/LUMO levels of organic molecules intended for use in OPV applications. The deep learning model takes the SMILES (simplified molecular-input line-entry system) of a molecule as input, converts it to a 2D RGB image, uses the convolutional layers of the network to extract features from the image and then converts the features into energy levels using a deep dense neural network. The model takes advantage of a machine learning technique called transfer learning,<sup>24,25</sup> whereby it is first trained on a large dataset (500'000 molecules) with HOMO/LUMO estimated by DFT simulations and then fine-tuned on a smaller dataset (180 molecules) with experimentally measured HOMO/LUMO levels. The deep learning model shows an accuracy below 200 meV, with accuracy and precision superior to DFT-estimated energies. The validity of the QSPR model was carefully evaluated and confirmed using commercially available polymers (such as P3HT, PTB7-Th, PNTz4T, J71,

PM6, D18 (Figure 7-5 D)) to ensure its practical utility. As a result, the deep learning model offers an efficient way to accurately and almost instantly (~ 170 ms on a personal computer) predict the frontier energy levels of molecules, without the need for molecular geometry optimization and large computing clusters, thereby allowing fast and reliable screening of donor molecules for OPV applications. This model, and models of this kind, are expected to find rapid use in both academic and industrial laboratories to realize molecular engineering at a lower cost and in a fraction of the time.

## 4.8. Methodology

### 4.8.1. The Deep Learning Model

Deep learning has emerged as a powerful tool for solving a variety of problems of machine learning and artificial intelligence, both in everyday<sup>26,27</sup> and scientific applications.<sup>28-32</sup> Deep learning makes use of multilayer stacks of modules (in our case convolutional layers and fully connected neurons, Figure 7-1 A) that map an input and output through non-linear functions.<sup>33</sup> By having many layers and millions of trainable parameters, the system is able to model increasingly complex processes in ways that are both sensitive to minute details and invariant to noise.

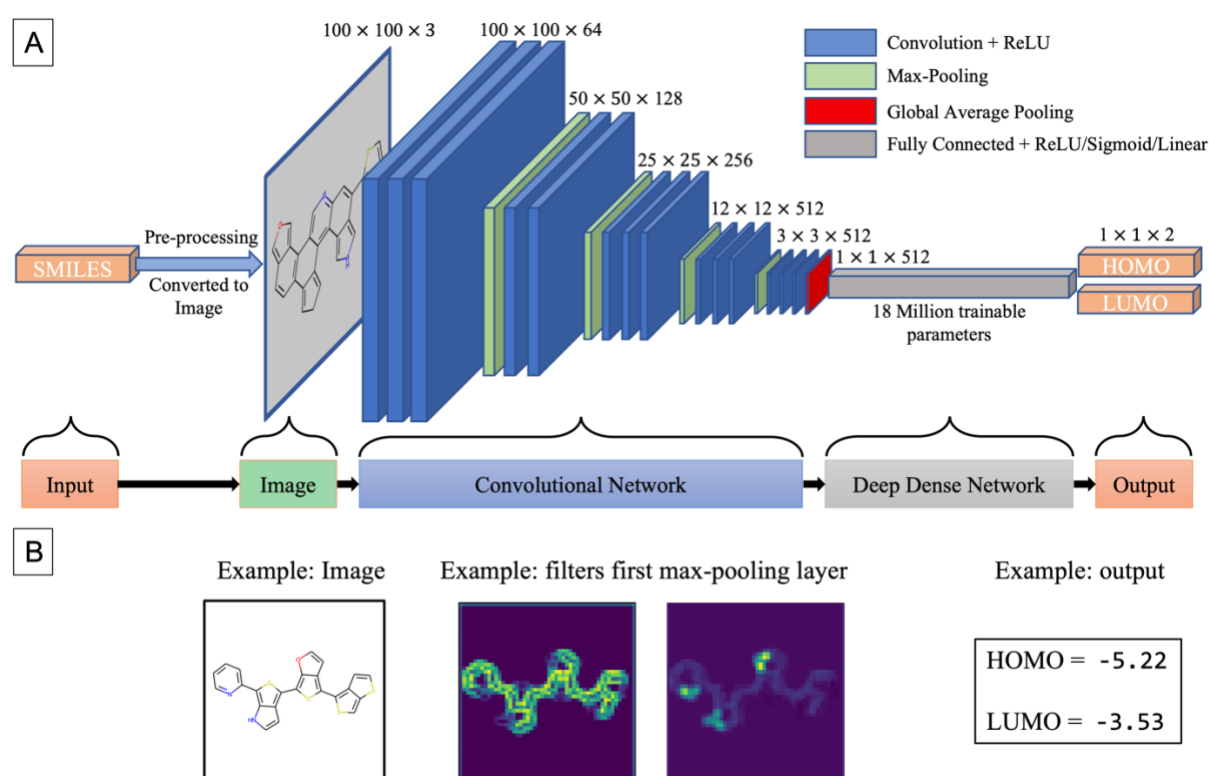


Figure 4.8-1 A) Illustration of the convolutional neural network, showing the pre-processing step, the convolutional network (with rectified linear unit (ReLU) activation function), max-pooling, global averaging, and fully connected layers (with activation functions). B) Examples of (left) a molecular image, (middle) the output of two filters after the first max-pooling layer and, (right) the output of the model.

Figure 7-1 A illustrates the architecture of the model used in this work, where it is broken up into two distinct parts, the convolutional network and the deep dense network.<sup>17</sup> This model takes SMILES (or InChI, International Chemical Identifier) as input and generates standardised RGB molecular images as a pre-processing step. The convolutional network is used as a way of automatically creating a non-linear, trainable feature extracting function without the need for explicit feature engineering or hard-coded pattern recognition. Carbons are represented in



black and each heteroatom in its own color (*e.g.*, oxygen in red, sulfur in yellow, nitrogen in blue), this allows for heteroatoms to be easily picked out as features even with the relatively low image resolution (100x100x3) which reduces the computational requirements. The convolutional layers slide multiple initially random filters over the image, transforming it such that features like edges, large shapes (*e.g.*, conjugated backbones, Figure 7-1 B middle left), or color change (*e.g.*, heteroatoms, Figure 7-1 B middle right) are highlighted. Then, it down-samples the data using a max-pooling layer until it is in a form appropriate for input into the dense network (1D array). Finally, the result of the convolutional network (or feature map) is fed into the deep dense network, which consists of layers of fully connected neurons each containing trainable weights and activation functions which introduce non-linearity into the model.<sup>33</sup> The deep dense network has around 18 million trainable parameters starting with an input array of 512 feature elements, from the convolutional network, and outputting 2 numbers that are trained to represent the HOMO and LUMO levels of the input molecule (details in section A.4.1). This work makes use of a supervised learning technique where the model parameters (or weights and biases) are iteratively optimized based on the results of a loss function which quantifies the difference between the known true output and the predicted output.<sup>33</sup> Here, the loss function is calculated as the mean squared error (MSE) between the true and predicted values (details in section A.4.2 2, Figure A.4-1 and Figure A.4-2 ).

#### 4.8.2. Datasets and Training

The ultimate objective of this work is to train a deep learning model able to predict the HOMO and LUMO energy levels of a molecule with experimental (not theoretical) values taken as ‘true’. The main constraint is the lack of a large enough dataset containing experimentally measured values. With relatively small training sets, deep learning models are unlikely to learn in a way that gives meaningful predictivity. In order to overcome this constraint a technique called transfer learning is employed.<sup>24,25,34</sup> In transfer learning, a model is trained on a large and general dataset where basic functions, which require many iterations and large amounts of data to learn, are acquired. The model is then retrained (fine-tuned) on a smaller more specific dataset using the previously learned weights to initialize the model.<sup>25,34,35</sup> The second training, or fine-tuning, is done using a significantly smaller learning rate as the weights are assumed to be already close to optimal.

Here the data used for the initial phase of training (phase I, Figure 7-2) is 500’000 randomly sampled molecules from the Harvard Clean Energy Project dataset (HCEP).<sup>36</sup> The HCEP dataset consists of around 2.3 million artificially generated potential donor molecules, for use

in OPV devices. All molecules are designed combinatorically from 26 molecular building blocks. The HOMO and LUMO levels of these molecules are estimated using DFT at different levels (details in section A.4.3.1).

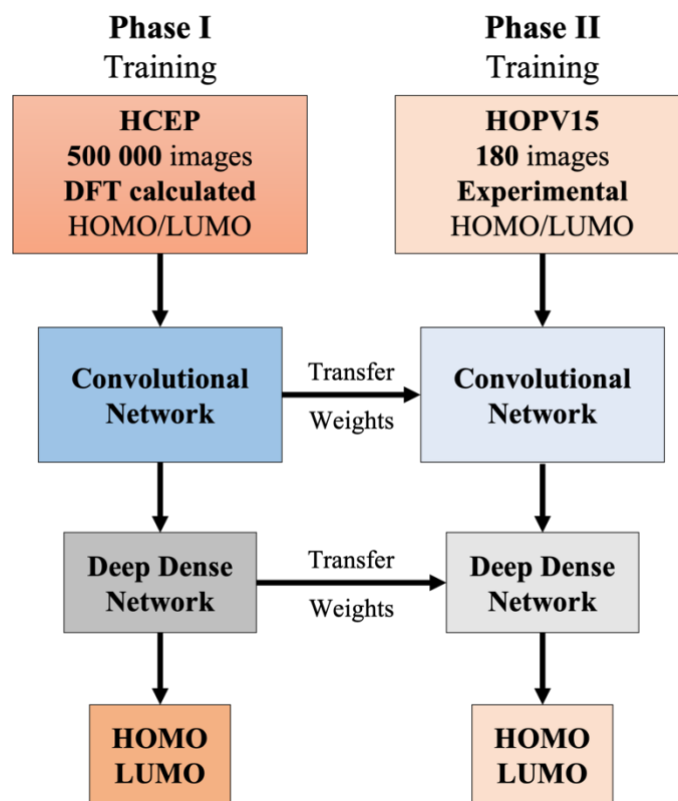


Figure 4.8-2 Schematic of phase I and phase II of training using the HCEP dataset and HOPV15 dataset respectively, with the learned weights being transferred from the first to the second phase of training.

The deep learning model is then fine-tuned (phase II, Figure 7-2) on a subset (180 molecules) of the Harvard organic photovoltaic dataset (HOPV15)<sup>37</sup> with the weights being carried over from the first Phase I. The dataset consists of around 350 molecules whose HOMO and LUMO levels have been (i) experimentally measured (extracted from literature), and (ii) estimated using DFT in a range of conformations with four different functionals used for each conformation. Phase II uses these experimental values (i) as ‘true’ for training and the resulting predictions of the model are later compared with the values from DFT (ii). The dataset was created to represent a measurably diverse range of donor molecules used in the field of OPV (details in section A.4.3.2).

#### 4.8.3. Testing and External Validation

Validation of QSPR models needs to be done rigorously in order to assess their predictivity.<sup>38</sup> Validation is done using three calculations: the square of the correlation coefficient ( $R^2$ ), the Root Mean Squared Error (RMSE) and the Standard Error of Prediction (SEP). The  $R^2$  value

is a measure of correlation between the true and predicted values, while the RMSE can be understood as the accuracy and the SEP as the precision of prediction.<sup>38</sup> The first step for validation is to split the dataset into a subset for training and a subset for testing. By doing so, the predictivity of the model can be assessed on a test set never exposed to the model and yet still representative of the entire dataset.<sup>39</sup> In this work, phase I is performed on 500'000 molecules and tested on 10'000 extra molecules (2%), and phase II on 180 molecules and tested on 40 extra molecules (~22%). In both training phases the training and testing molecules were split with random sampling, but specifically in a way that the distribution of the HOMO and LUMO values was roughly the same. Then, to ensure the robustness of the model, a Y-Scrambling test is done. Here, the dependent variables (HOMO and LUMO values) are randomly scrambled and associated to the 'wrong' structures (SMILES), in a way that the structure-property relationships no longer hold, and the model is retrained. If the deep learning model shows high  $R^2$  and the Y-scrambled model shows low  $R^2$  values, it implies that the model outputs are not overfitting or chance correlations but that there is necessarily a learnt link between the input (structure) and the output (properties).<sup>23,39</sup>

#### 4.8.4. The 'use-case' Dataset

While it would be sufficient to test the deep learning model only on the test set from the HOPV15 dataset, we built, from literature, an additional dataset with the aim of testing the model in a real use-case scenario. The so-called 'use-case' dataset consists of 27 donor molecules used in OPVs that are commercially available (*i.e.*, including Chemical Abstracts Service or CAS numbers) and have both experimentally measured and DFT-estimated HOMO/LUMO energy levels published in peer-reviewed journals. The molecules are strictly not in the HOPV15 dataset but are composed of atoms and building-blocks represented in the Phase II training set (Figure A.4-5). Note that experimental values of the 'use-case' dataset are exclusively determined by cyclic voltammetry (CV).<sup>40</sup> CV allows an estimation of HOMO/LUMO energy levels with an error margin generally considered to be about  $\pm 100$  mV.<sup>41</sup> More accurate techniques exist, such as ultraviolet photoelectron spectroscopy (UPS) or inverse photoelectron spectroscopy (IPES), however, CV is undoubtedly the most commonly used technique in the field of organic electronics due to the relative ease of measurement.<sup>42</sup> More details are given in section A.4.3 3.3 and a full list of the molecules with all values and predictions is given in Table A.4-2.

## 4.9. Results and Discussion

### 4.9.1. Phase I

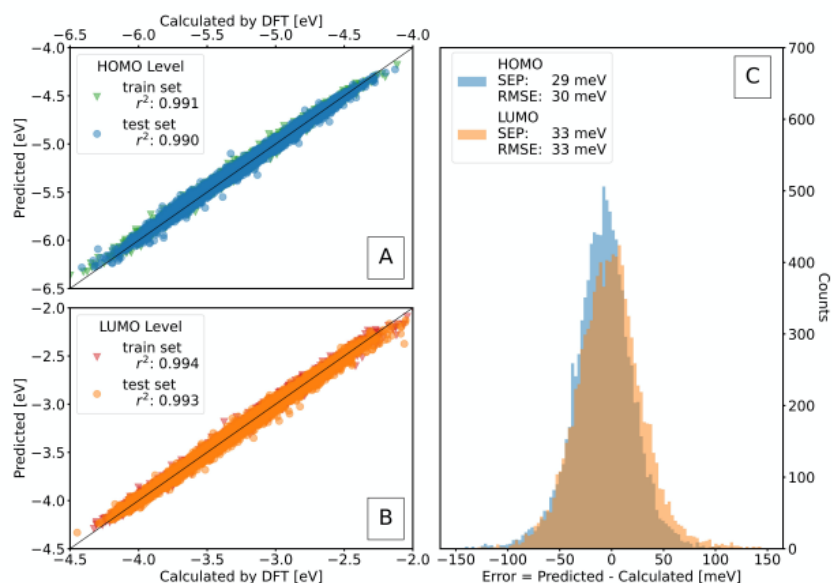
In Phase I of training, molecules with DFT-estimated HOMO and LUMO levels from the large HCEP dataset are used to train the deep learning model with randomly initialized weights (Figure A.4-1). The goal of this phase is to leverage the large amount of data so that the model learns to extract important features from the molecular images and learns to convert those features into HOMO and LUMO energy level predictions. In order to evaluate the performance of the model at this stage, we generate predictions on the test set from the HCEP dataset.  $R^2$  values close to 1 (Figure 7-3 A,B) with SEP and RMSE values around 30 meV (Figure 7-3 C) are found for the prediction of HOMO and LUMO levels, thereby illustrating the accuracy and precision of the prediction after phase I of training. This result is followed up by an  $R^2$  value of 0.990 with SEP and RMSE of around 45 meV for the band gap (Table 7-1, Figure A.4-3), showing not only the individual predictions, but also their relative positions to be highly accurate and precise. The results from the Y-Scrambling test shows  $R^2$  values of -0.922 and -0.930 for the HOMO and LUMO levels respectively (Table 7-1). The negative  $R^2$  values close to -1 indicate that a simple prediction of the mean value would have been almost double as accurate, and that the Y-Scrambling model is only able to predict random values within the range of the training data. The Y-Scrambling test confirms that there is no overfitting and, more specifically, that there is a structure-property relationship in the dataset and that this relationship is necessarily learned by the model. Note that no chemical knowledge was implemented at any time.

### 4.9.2. Phase II

After phase I of the training, the deep learning model demonstrates an ability to predict DFT-estimated frontier energy levels of molecules represented in the HCEP dataset. The goal of this work is, however, to be able to predict experimentally equivalent HOMO/LUMO values of molecules in order to increase the potential utility of this model. To do so, phase II fine-tunes the model on molecules already reported in OPVs using experimentally determined HOMO/LUMO values as ‘true’ values (Figure A.4-2). The model is fine-tuned on 180 molecules from the HOPV15 dataset. By starting with the weights learned in phase I, for both the convolutional network and the deep dense network, the model can leverage the predictive structure-property relationship learnt from phase I and fine-tune itself to have better predictability for the new, experimental, dataset used in phase II. Note that transferring the weights only for the convolutional network or only for the deep dense network does not provide

satisfying results (Table S1). Since the HCEP and HOPV15 datasets have an incomplete overlap both in atoms and molecular building blocks present in the molecules, phase II training is expected to induce fine-tuning of the weights in the convolutional layers that extract the features of the molecules. Similarly, as the HCEP uses DFT and HOPV15 uses experimental methods to define ‘true’ values, the weights in the deep dense layers are also expected to be adjusted in phase II to accommodate the new structural features and to give predictions in accordance with experimental data. For both HOMO and LUMO predictions after phase II training (Figure 7-3 D, E respectively), satisfying  $R^2$  values are obtained: greater than 0.7 for the training set, and greater than 0.5 for the test set, which indicates a good correlation between the prediction and true values. More importantly, SEP and RMSE values below 140 meV and 190 meV are achieved for the HOMO and LUMO levels respectively (Figure 7-3 F). In other words, with this model, the frontier energy levels of any newly designed donor polymer/small molecule composed of atoms and building blocks seen in the HOPV15 training set, can be predicted with, on average, an error of less than 200 meV compared to the experimental value. Such finding offers a fast and accurate tool to guide molecular engineering for OPV optimization.

## Phase I



## Phase II

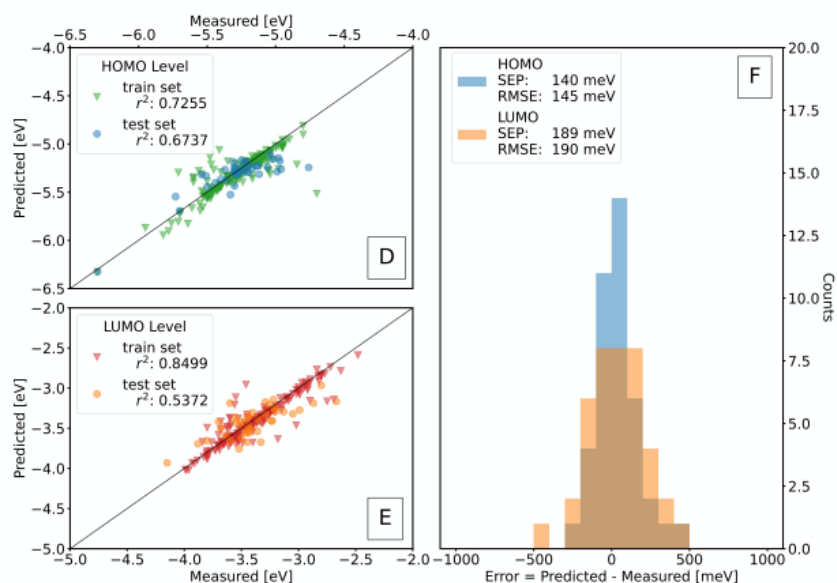


Figure 4.9-1 Results of both phases of deep learning model training. Phase I shows the predicted versus DFT-estimated (A) HOMO and (B) LUMO levels for the training set (triangles) and test set (circles). (C) Distribution of the prediction errors with the HOMO level error shown in blue and the LUMO level error in orange. Phase II shows the results of the fine-tuning on HOPV15 dataset with the predicted versus experimentally measured (D) HOMO and (E) LUMO levels. (F) Distribution of the prediction errors in phase II.

As in phase I, the validity of these results and the importance of using the transfer learning technique is confirmed by non-transfer learning and Y-Scrambling tests. Indeed, low and negative  $R^2$  values are obtained when the model is not initialized with the previously learned weights (Non-Transfer Learning, Table 7-1). This illustrates the necessity of the transfer learning and confirms that the HOPV15 dataset is not large enough to train this kind of deep

learning model alone. Lastly, the poor  $R^2$  values from the Y-Scrambling test again demonstrates the learned relationship between the new chemical structures and the experimental values of the frontier energy levels (Table 7-1).

*Table 7-1 Performance of the deep learning model trained on the HCEP dataset in phase I and HOPV15 in phase II including Y-Scrambling for both phases and training without transfer learning for phase II.*

	Phase I - HCEP		Phase II - HOPV15		
	Learning	Y-Scrambling	Transfer Learning	Non-Transfer Learning	Y-Scrambling
<b><math>R^2</math> (HOMO)</b>	0.990	-0.922	0.674	-0.00718	-0.193
<b><math>R^2</math> (LUMO)</b>	0.993	-0.930	0.537	0.0298	-0.176
<b><math>R^2</math> (Gap)</b>	0.990	-0.957	0.477	-0.119	-0.197

#### 4.9.3. Comparison with DFT from HOPV15 Dataset

After exploring the results of the phase II training against experimental data, the model is compared to the common method for energy level estimation, DFT simulations. The error distributions, *i.e.*, the distributions of the difference between predicted (deep learning model or DFT) and experimental ‘true’ values, are shown in Figure 7-4. The distributions of the absolute values are shown in Figure A.4-4. For the DFT-estimated results, we see rather poor accuracy of the prediction leading to large RMSE values (Table 7-2), which are illustrated by the shift in the error distributions from zero (Figure 7-4). The low RMSE values and the error distributions centered around zero for the deep learning model clearly indicate its better accuracy compared to this level of DFT in predicting experimental HOMO/LUMO levels. Even if the shifts in energy values obtained by DFT can conceivably be improved by an empirical correction factor, the precision remains inferior to the model as highlighted by the SEP values (Table 7-2). Indeed, all the DFT methods show comparable SEP values (between 269 meV and 407 meV) for the estimation of the HOMO and LUMO levels (Table 7-2), while the SEP values for the model predictions are around half of that (140 meV and 189 meV for the HOMO and LUMO levels, respectively). In particular, the better accuracy and precision of the deep learning model for both the HOMO and LUMO levels is emphasized by the low RMSE (accuracy, 219 meV *vs.* 637 meV) and SEP (precision, 220 meV *vs.* 449 meV) obtained for the band gap compared to the best performing DFT functional for predicting the band gap, BP86. We can therefore conclude that the deep transfer learning model is not only more accurate but also more precise than any of the DFT methods used in the HOPV15 dataset.

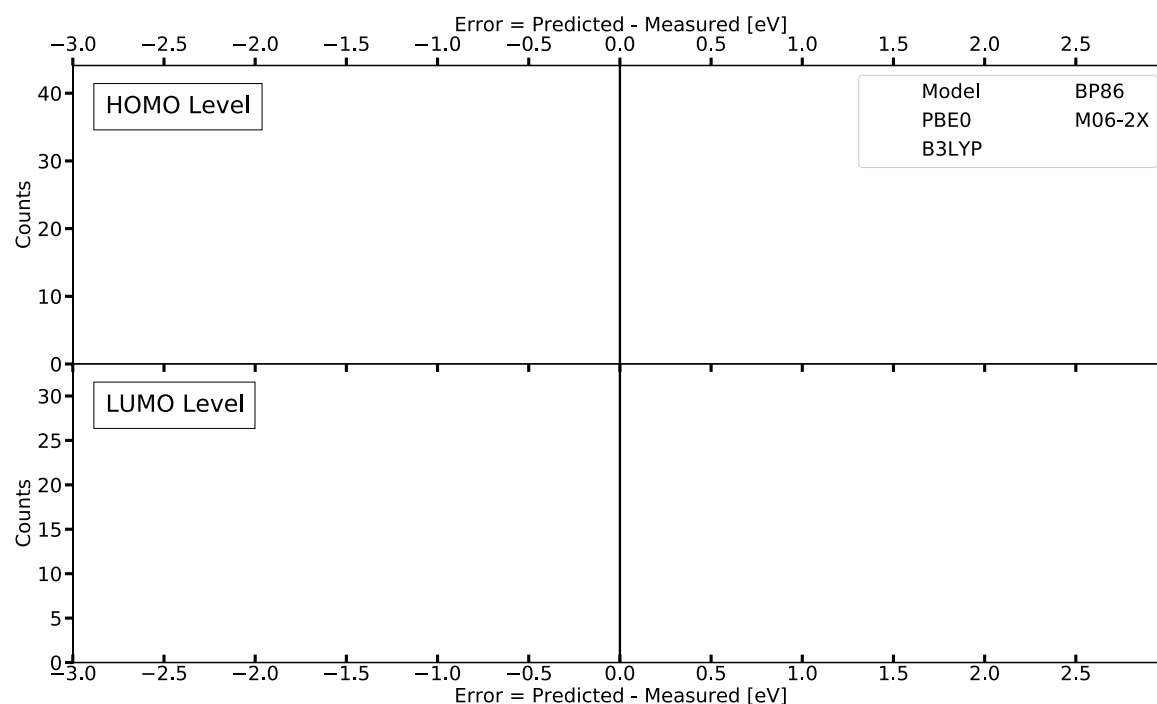


Figure 4.9-2 Distribution of the prediction errors of the HOMO (top) and LUMO (bottom) levels for the deep learning model (black) as well as DFT-estimated values for all conformers using various functionals from the HOPV15 dataset (colors). The difference in counts results from the multiple DFT values (one for each conformer) reported for a given molecule with a given functional in the HOPV15 dataset.

Table 7-2 Comparison of the performance of the deep learning model and the various DFT estimations for the HOMO level, LUMO level and the band gap (= LUMO – HOMO), showing the Standard Error of Prediction (SEP) and the Root Mean Square Error (RMSE).

Method	HOMO (meV) [SEP / RMSE]	LUMO (meV) [SEP / RMSE]	Gap (meV) [SEP / RMSE]
<b>This model</b>	140 / 150	189 / 190	220 / 219
<b>DFT: PBE0</b>	292 / 309	381 / 814	530 / 978
<b>DFT: B3LYP</b>	288 / 324	370 / 791	515 / 753
<b>DFT: BP86</b>	269 / 652	339 / 367	449 / 637
<b>DFT: M06-2X</b>	307 / 1003	407 / 1407	589 / 2376

#### 4.9.4. External Validation: Comparison with DFT from Literature ('use-case' Dataset)

In order to validate this claim, the deep learning model is tested on the 'use-case' dataset made up of 27 commercially available donor molecules whose HOMO/LUMO levels were both experimentally determined by CV measurements and calculated using DFT based on routinely used hybrid functionals (B3LYP or PBE0) and advanced basis sets (mainly 6-31G) (details in Table A.4-2). The model undergoes no further training. The predictions of both the deep learning model and DFT simulations are compared to the experimental CV data. The  $R^2$  values



of circa 0.6 for both HOMO and LUMO levels (Figure 7-5 A, B respectively) confirm the practical predictability of this model.<sup>39</sup> Again, the distribution of the prediction errors is better centered around zero than for DFT simulations (Figure 7-5 C). More importantly, the SEP and RMSE values under 150 meV for both HOMO and LUMO model predictions compared to 390 meV for DFT (Table 7-3) demonstrate the ability of the deep learning model to outperform routinely used DFT simulations in determining the frontier energy levels of this set of molecules. The list of predicted values for each molecule (including PCE11, PCDTBT, F8T2, MEH-PPV, TQ1, etc.) is given in Table A.4-2. The performance of the deep learning model compared to DFT is illustrated graphically in Figure 7-5 D for a few polymers of broad interest: P3HT, PTB7-Th, PNTz4T, J71, PM6 and D18 (PCE18).

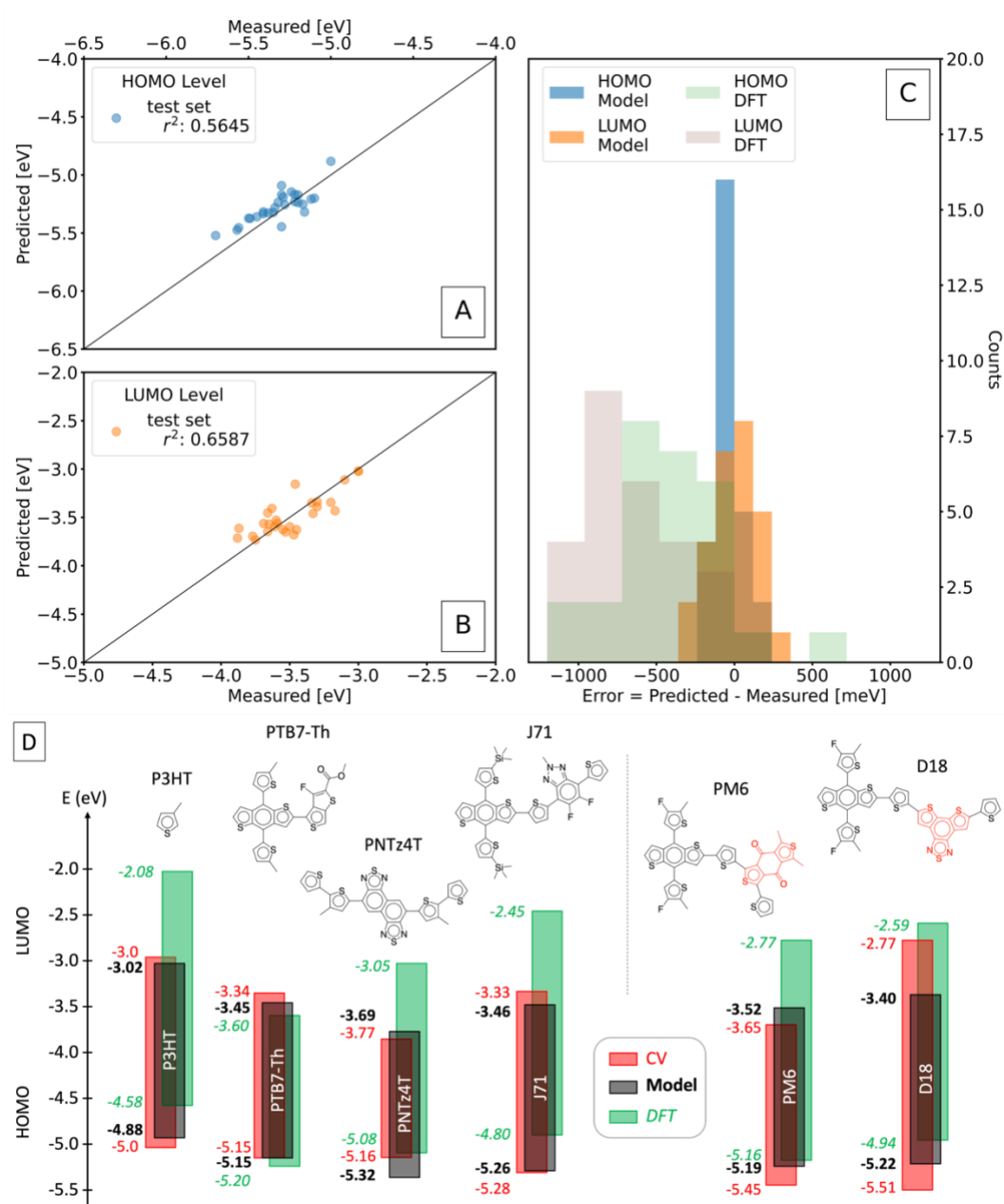


Figure 4.9-3 Results of testing the deep learning model on the 'use-case' dataset. Deviation of the (A) HOMO and (B) LUMO level predicted compared to the experimental values. (C) Distributions of the prediction errors for the values outputted by the deep learning model (**Model**) and the values estimated by DFT (DFT) extracted from literature. "Measured" correspond to energy levels determined experimentally (by cyclic voltammetry) and extracted from peer-reviewed journals. (D) Schematic comparison of the model and DFT predictions compared to experimental values of commonly used donor polymers in OPVs. PM6 and D18 are not part of the 'use-case' dataset as they are partly composed of building blocks, highlighted in red in their chemical structures, not represented in the HOPV15 training set.

Table 7-3 Comparison of the results of the deep learning model and published DFT of molecules from the ‘use-case’ testing dataset. The table shows SEP and RMSE of the HOMO, LUMO and band gap (= LUMO – HOMO).

Method	HOMO (meV) [SEP / RMSE]	LUMO (meV) [SEP / RMSE]	Gap (meV) [SEP / RMSE]
<b>This model</b>	92 / 96	146 / 146	152 / 155
<b>DFT</b>	325 / 492	387 / 716	497 / 540

The limitations of this deep transfer learning model, however, must be considered. It is mainly limited by the broadness of the training data, in that its ability to give consistently good predictions decreases when tested on molecules containing atoms or building blocks that are not represented in the training data (overlap of building blocks are shown in Figure A.4-5). As an example, D18, which has a dithienobenzothiadiazole unit not represented in the HOPV15 training set, shows a better HOMO level prediction but an overall worse model prediction than the B3LYP-based DFT estimation. Indeed, the LUMO level is significantly under-estimated most likely because wide-band gap polymers such as D18 are not present in the training set.<sup>43,44</sup> Note that PM6 contains a benzo[1,2-*c*:4,5-*c'*]dithiophene-4,8-dione unit also not represented in the HOPV15 training set and yet the deep learning model remains more accurate than B3LYP-based DFT.<sup>45,46</sup> The HOMO/LUMO predictions of 16 other polymers used in OPVs that are commercially available, but not fully represented in the training set, is given in Table A.4-3 (including PCE12, PCE13, J61, DRCN5T, PDBT-T1, etc.) with statistical analysis in Figure A.4-6 and Table A.4-4. Finally, it is crucial to remember that, unlike the model presented here, the capabilities of DFT simulations go far beyond the simple prediction of HOMO/LUMO energy levels. DFT allows the estimation of electronic distribution of each orbital, dipole moment, electronic coupling, molecular electrostatic potential, optical absorption, and many more complex properties.<sup>47-51</sup>

#### 4.10. Conclusion

In this work, a QSPR deep transfer learning model is successfully created which takes the SMILES of a molecule as input, converts it to an RGB image, and predict its HOMO/LUMO levels with an accuracy (RMSE) of below 200 meV. This model makes use of a convolutional neural network architecture and transfer learning techniques in order to train on experimental data despite the relatively small dataset. The practical use of this model is successfully validated on real-use donor molecules used in OPVs from both the HOPV15 dataset (test set) and an external ‘use-case’ dataset made up of commercially available molecules with frontier energy levels reported in literature. The model predictions are also compared to the results of DFT simulations, using four different functionals, and DFT results reported in literature, whereby the model is found to be substantially more accurate and precise. This suggests that this deep learning model performs better at predicting the frontier energies of this class of molecules than the computationally expensive and time consuming DFT simulations. As a result, this model offers a reliable and quick way of screening potential donor molecules for optimizing OPVs, thereby saving costly and time-consuming synthesis and experimental testing.

One downside of models created using deep learning techniques is our inability to extract how the model converts the image into the energy values. Nevertheless, our findings suggest that with enough data, parameters and a well optimized model, there is enough information in the 2D diagram of a molecule to predict its HOMO/LUMO energies. Currently the major limitation hindering the broad adoption of this model is the limited training set, as it does not process atoms and molecular building blocks that are not represented in the training data consistently. We believe that if one could gather the data already available in peer-reviewed journals and train this model on it, the model will grow in accuracy for a wide variety of newly designed materials. Considering that no chemical knowledge is implemented, we do not see any limitations in extending use of this model to acceptor molecules if a suitable training dataset is made available. In general, the expansion of datasets in size and diversity would greatly improve the prediction power and practical utility of these kinds of QSPR models.

## Reference

- (1) V, M.-D.; Zhai, P.; Pirani, A.; Connors, S. L.; Péan, C.; Berger, S.; Caud, N.; Chen, Y.; Goldfarb, L.; Gomis, M. I.; Huang, M.; Leitzell, K.; Lonnoy, E.; Matthews, J. B. R.; Maycock, T. K.; Waterfield, T.; Yelekçi, O.; Yu, R.; Zhou, B. *Climate Change 2021: The Physical Science Basis. Contribution of Working Group I to the Sixth Assessment Report of the Intergovernmental Panel on Climate Change* 2021.
- (2) Wang, J.; Zheng, Z.; Zu, Y.; Wang, Y.; Liu, X.; Zhang, S.; Zhang, M.; Hou, J. A Tandem Organic Photovoltaic Cell with 19.6% Efficiency Enabled by Light Distribution Control. *Advanced Materials* **2021**, 2102787.
- (3) Hou, J.; Inganas, O.; Friend, R. H.; Gao, F. Organic solar cells based on non-fullerene acceptors. *Nat. Mater.* **2018**, 17, 119-128.
- (4) Cui, Y.; Yao, H.; Hong, L.; Zhang, T.; Xu, Y.; Xian, K.; Gao, B.; Qin, J.; Zhang, J.; Wei, Z.; Hou, J. Achieving Over 15% Efficiency in Organic Photovoltaic Cells via Copolymer Design. *Adv. Mater.* **2019**, 1808356.
- (5) Fan, B.; Zhang, D.; Li, M.; Zhong, W.; Zeng, Z.; Ying, L.; Huang, F.; Cao, Y. Achieving over 16% Efficiency for Single-Junction Organic Solar Cells. *Sci China Chem* **2019**, 62.
- (6) Cui, Y.; Yao, H.; Zhang, J.; Zhang, T.; Wang, Y.; Hong, L.; Xian, K.; Xu, B.; Zhang, S.; Peng, J.; Wei, Z.; Gao, F.; Hou, J. Over 16% efficiency organic photovoltaic cells enabled by a chlorinated acceptor with increased open-circuit voltages. *Nature Communications* **2019**, 10, 2515.
- (7) Liu, Q.; Jiang, Y.; Jin, K.; Qin, J.; Xu, J.; Li, W.; Xiong, J.; Liu, J.; Xiao, Z.; Sun, K.; Yang, S.; Zhang, X.; Ding, L. 18% Efficiency organic solar cells. *Science Bulletin* **2020**.
- (8) Scharber, M. C.; Mühlbacher, D.; Koppe, M.; Denk, P.; Waldauf, C.; Heeger, A. J.; Brabec, C. J. Design Rules for Donors in Bulk-Heterojunction Solar Cells—Towards 10 % Energy-Conversion Efficiency. *Advanced Materials* **2006**, 18, 789-794.
- (9) Alharbi, F. H.; Rashkeev, S. N.; El-Mellouhi, F.; Lüthi, H. P.; Tabet, N.; Kais, S. An efficient descriptor model for designing materials for solar cells. *npj Computational Materials* **2015**, 1, 15003.
- (10) Scharber, M. C.; Sariciftci, N. S. Efficiency of bulk-heterojunction organic solar cells. *Progress in Polymer Science* **2013**, 38, 1929-1940.
- (11) Hohenberg, P.; Kohn, W. Inhomogeneous Electron Gas. *Physical Review* **1964**, 136, B864-B871.
- (12) Kohn, W.; Sham, L. J. Self-Consistent Equations Including Exchange and Correlation Effects. *Physical Review* **1965**, 140, A1133-A1138.
- (13) Mesta, M.; Chang, J. H.; Shil, S.; Thygesen, K. S.; Lastra, J. M. G. A Protocol for Fast Prediction of Electronic and Optical Properties of Donor–Acceptor Polymers Using Density Functional Theory and the Tight-Binding Method. *The Journal of Physical Chemistry A* **2019**, 123, 4980-4989.
- (14) Janesko, B. G. Replacing hybrid density functional theory: motivation and recent advances. *Chem Soc Rev* **2021**, 50, 8470-8495.
- (15) Verma, P.; Truhlar, D. G. Status and Challenges of Density Functional Theory. *Trends in Chemistry* **2020**, 2, 302-318.
- (16) He, K.; Zhang, X.; Ren, S.; Sun, J.: Identity Mappings in Deep Residual Networks. Springer International Publishing, 2016; pp 630-645.
- (17) Simonyan, K.; Zisserman, A. Very Deep Convolutional Networks for Large-Scale Image Recognition. *arXiv pre-print server* **2015**.

- (18) Padula, D.; Simpson, J. D.; Troisi, A. Combining electronic and structural features in machine learning models to predict organic solar cells properties. *Materials Horizons* **2019**, *6*, 343-349.
- (19) Sahu, H.; Rao, W.; Troisi, A.; Ma, H. Toward Predicting Efficiency of Organic Solar Cells via Machine Learning and Improved Descriptors. *Advanced Energy Materials* **2018**, *8*, 1801032.
- (20) Pereira, F.; Xiao, K.; Latino, D. A. R. S.; Wu, C.; Zhang, Q.; Aires-De-Sousa, J. Machine Learning Methods to Predict Density Functional Theory B3LYP Energies of HOMO and LUMO Orbitals. *Journal of Chemical Information and Modeling* **2017**, *57*, 11-21.
- (21) Sun, W.; Li, M.; Li, Y.; Wu, Z.; Sun, Y.; Lu, S.; Xiao, Z.; Zhao, B.; Sun, K. The Use of Deep Learning to Fast Evaluate Organic Photovoltaic Materials. *Advanced Theory and Simulations* **2019**, *2*, 1800116.
- (22) Yangali-Quintanilla, V.; Verliefde, A.; Kim, T. U.; Sadmani, A.; Kennedy, M.; Amy, G. Artificial neural network models based on QSAR for predicting rejection of neutral organic compounds by polyamide nanofiltration and reverse osmosis membranes. *Journal of Membrane Science* **2009**, *342*, 251-262.
- (23) Meftahi, N.; Klymenko, M.; Christofferson, A. J.; Bach, U.; Winkler, D. A.; Russo, S. P. Machine learning property prediction for organic photovoltaic devices. *npj Computational Materials* **2020**, *6*.
- (24) Tan, C.; Sun, F.; Kong, T.; Zhang, W.; Yang, C.; Liu, C.: A Survey on Deep Transfer Learning. Springer International Publishing, 2018; pp 270-279.
- (25) Hussain, M.; Bird, J. J.; Faria, D. R.: A Study on CNN Transfer Learning for Image Classification. Springer International Publishing, 2019; pp 191-202.
- (26) Farabet, C.; Couprie, C.; Najman, L.; LeCun, Y. Learning Hierarchical Features for Scene Labeling. *IEEE Transactions on Pattern Analysis and Machine Intelligence* **2013**, *35*, 1915-1929.
- (27) Szegedy, C.; Liu, W.; Jia, Y.; Sermanet, P.; Reed, S.; Anguelov, D.; Erhan, D.; Vanhoucke, V.; Rabinovich, A. Going Deeper with Convolutions. *arXiv pre-print server* **2014**.
- (28) Ma, J.; Sheridan, R. P.; Liaw, A.; Dahl, G. E.; Svetnik, V. Deep Neural Nets as a Method for Quantitative Structure–Activity Relationships. *Journal of Chemical Information and Modeling* **2015**, *55*, 263-274.
- (29) Ciodaro, T.; Deva, D.; de Seixas, J. M.; Damazio, D. Online particle detection with Neural Networks based on topological calorimetry information. *Journal of Physics: Conference Series* **2012**, *368*, 012030.
- (30) Helmstaedter, M.; Briggman, K. L.; Turaga, S. C.; Jain, V.; Seung, H. S.; Denk, W. Connectomic reconstruction of the inner plexiform layer in the mouse retina. *Nature* **2013**, *500*, 168-174.
- (31) Leung, M. K. K.; Xiong, H. Y.; Lee, L. J.; Frey, B. J. Deep learning of the tissue-regulated splicing code. *Bioinformatics* **2014**, *30*, i121-i129.
- (32) Xiong, H. Y.; Alipanahi, B.; Lee, L. J.; Bretschneider, H.; Merico, D.; Yuen, R. K. C.; Hua, Y.; Gueroussov, S.; Najafabadi, H. S.; Hughes, T. R.; Morris, Q.; Barash, Y.; Krainer, A. R.; Jovic, N.; Scherer, S. W.; Blencowe, B. J.; Frey, B. J. The human splicing code reveals new insights into the genetic determinants of disease. *Science* **2015**, *347*, 1254806-1254806.
- (33) Lecun, Y.; Bengio, Y.; Hinton, G. Deep learning. *Nature* **2015**, *521*, 436-444.
- (34) Vrbančič, G.; Podgorelec, V. Transfer Learning With Adaptive Fine-Tuning. *IEEE Access* **2020**, *8*, 196197-196211.
- (35) Ching, J. Y.; Wong, A. K. C.; Chan, K. C. C. Class-dependent discretization for inductive learning from continuous and mixed-mode data. *IEEE Transactions on Pattern Analysis and Machine Intelligence* **1995**, *17*, 641-651.

- (36) Hachmann, J.; Olivares-Amaya, R.; Atahan-Evrenk, S.; Amador-Bedolla, C.; Sánchez-Carrera, R. S.; Gold-Parker, A.; Vogt, L.; Brockway, A. M.; Aspuru-Guzik, A. The Harvard Clean Energy Project: Large-Scale Computational Screening and Design of Organic Photovoltaics on the World Community Grid. *The Journal of Physical Chemistry Letters* **2011**, 2, 2241-2251.
- (37) Lopez, S. A.; Pyzer-Knapp, E. O.; Simm, G. N.; Lutzow, T.; Li, K.; Seress, L. R.; Hachmann, J.; Aspuru-Guzik, A. The Harvard organic photovoltaic dataset. *Scientific Data* **2016**, 3, 160086.
- (38) Alexander, D. L. J.; Tropsha, A.; Winkler, D. A. Beware of R<sup>2</sup>: Simple, Unambiguous Assessment of the Prediction Accuracy of QSAR and QSPR Models. *Journal of Chemical Information and Modeling* **2015**, 55, 1316-1322.
- (39) Tropsha, A.; Gramatica, P.; Gombar, V. K. The Importance of Being Earnest: Validation is the Absolute Essential for Successful Application and Interpretation of QSPR Models. *QSAR & Combinatorial Science* **2003**, 22, 69-77.
- (40) Elgrishi, N.; Rountree, K. J.; McCarthy, B. D.; Rountree, E. S.; Eisenhart, T. T.; Dempsey, J. L. A Practical Beginner's Guide to Cyclic Voltammetry. *Journal of Chemical Education* **2018**, 95, 197-206.
- (41) Cardona, C. M.; Li, W.; Kaifer, A. E.; Stockdale, D.; Bazan, G. C. Electrochemical Considerations for Determining Absolute Frontier Orbital Energy Levels of Conjugated Polymers for Solar Cell Applications. *Adv Mater* **2011**, 23, 2367-2371.
- (42) Sworakowski, J. How accurate are energies of HOMO and LUMO levels in small-molecule organic semiconductors determined from cyclic voltammetry or optical spectroscopy? *Synthetic Metals* **2018**, 235, 125-130.
- (43) Liu, Q.; Jiang, Y.; Jin, K.; Qin, J.; Xu, J.; Li, W.; Xiong, J.; Liu, J.; Xiao, Z.; Sun, K.; Yang, S.; Zhang, X.; Ding, L. 18% Efficiency organic solar cells. *Science Bulletin* **2020**, 65, 272-275.
- (44) Li, X.; Xu, J.; Xiao, Z.; Wang, X.; Zhang, B.; Ding, L. Dithieno[3',2':3,4;2'',3'':5,6]benzo[1,2-c][1,2,5]oxadiazole-based polymer donors with deep HOMO levels. *Journal of Semiconductors* **2021**, 42, 060501.
- (45) Zhang, H.; Yao, H.; Hou, J.; Zhu, J.; Zhang, J.; Li, W.; Yu, R.; Gao, B.; Zhang, S.; Hou, J. Over 14% Efficiency in Organic Solar Cells Enabled by Chlorinated Nonfullerene Small-Molecule Acceptors. *Advanced Materials* **2018**, 30, 1800613.
- (46) Liu, W.; Liu, Q.; Xiang, C.; Zhou, H.; Jiang, L.; Zou, Y. Theoretical exploration of optoelectronic performance of PM6:Y6 series-based organic solar cells. *Surfaces and Interfaces* **2021**, 26, 101385.
- (47) Aboulouard, A.; Mtougui, S.; Demir, N.; Moubarik, A.; Idrissi, M. E.; Can, M. New non-fullerene electron acceptors-based on quinoxaline derivatives for organic photovoltaic cells: DFT computational study. *Synth. Met.* **2021**, 279, 116846.
- (48) Yaqoob, U.; Raza Ayub, A.; Rafiq, S.; Khalid, M.; Iqbal, J. Structural, Optical and Photovoltaic Properties of Unfused Non-Fullerene Acceptors for Efficient Solution Processable Organic Solar Cell (Estimated PCE > 12.4%): A DFT Approach. *J. Mol. Liq.* **2021**, 117428.
- (49) Guillén-López, A.; Delesma, C.; Amador-Bedolla, C.; Robles, M.; Muñoz, J. Electronic structure and nonlinear optical properties of organic photovoltaic systems with potential applications on solar cell devices: a DFT approach. *Theor. Chem. Acc.* **2018**, 137.
- (50) Rana, D.; Materny, A. Effect of static external electric field on bulk and interfaces in organic solar cell systems: A density-functional-theory-based study. *Spectrochimica Acta Part A: Molecular and Biomolecular Spectroscopy* **2021**, 253, 119565.

(51) Sumpter, B. G.; Meunier, V. Can computational approaches aid in untangling the inherent complexity of practical organic photovoltaic systems? *J. Polym. Sci., Part B: Polym. Phys.* **2012**, *50*, 1071-1089.



# 8 General Conclusions and Perspective

The morphology of efficient OPV systems is complex and plays a critical role in determining the usefulness of the blend. Breaking up the complex bulk heterojunction into different, well defined, morphologies allow us to observe the workings of each part. As we have seen, the conversion of absorbed light to photocurrent in OPVs is a constant competition: exciton quenching vs relaxation, CT state separation vs geminate recombination, charge extraction vs non-geminate recombination. Each morphology type (from phase separated to intermixed and everything in between) excels in some of these competitions but not in all. In this thesis we have mainly looked at the workings of extreme morphologies (bilayers and dilute-donor blends). Understanding the successes and limitations of these extreme systems contributes greatly to the understanding and optimisation of complex BHJ blends where these morphologies are represented.

Chapters 4 and 5 follow on from work done on neat C<sub>60</sub> films where the excitonic behaviour is well described. In chapter 4 of the thesis TAPC:C<sub>60</sub> blends with low and high TAPC concentration were investigated. These blends representing both dilute and molecularly mixed morphologies. We found that large C<sub>60</sub> domains in the dilute blends lead to exciton diffusion-limited hole transfer and assist the generation of free electrons by enhancing electron delocalization and transport. We directly visualize an energetic gradient driving electrons away from the TAPC site into the C<sub>60</sub> bulk, favouring free charge generation. We show that CT excitons within C<sub>60</sub> clusters do not play a major role in the hole transfer process, since they undergo rapid localization to Frenkel excitons before dissociating. Interestingly, we find a fast monomolecular trap-based recombination mechanism in thin films containing 5 % TAPC, where free electrons recombine with holes that are trapped on isolated TAPC molecules. From this we conclude that while large C<sub>60</sub> clusters in dilute solar cells can enhance trap-based recombination mechanisms, this can be mitigated by efficient extraction. The C<sub>60</sub> clusters are, however, overall beneficial for efficient hole transfer and most importantly charge separation most likely due to the enhanced CT state delocalisation. In chapter 5 of the thesis  $\alpha$ 6T:C<sub>60</sub> bilayer and bulk-heterojunction blends of different ratios are investigated using both TA spectroscopy and TD-DFT. The TA spectra of the bilayer and 50% blends are dominated by excitonic features, with very little charge activity. The 5% and 10% blends, however, show a

strong  $\alpha 6T$  cation signature (along with  $C_{60}$  anion signature), which agrees with the much higher photocurrent reported for the dilute blends. The  $\alpha 6T$  cation peak showed a definite and measurable red shift over time. An MCR-ALS decomposition was able to split the  $\alpha 6T$  cation signature into two and plot their relative dynamics. TD-DFT simulations were then done to simulate the  $\alpha 6T$  cation transition energies in different configurations. The  $\alpha 6T$  cation was simulated both in the vicinity of the  $C_{60}$  anion (represented the CT state) and without the presence of the anion (representing the separated charge). The transition energies of the  $\alpha 6T$  cation were indeed different in the presence of the  $C_{60}$  anion and were shown to be reasonably invariant to their relative orientations. The different  $\alpha 6T$  cation signatures were therefore assigned to CT state and separated charges. A kinetic model was then fit to the relative CT and separate charge dynamics and rates related to the physical properties of the blends. The entire TA spectra was then reconstructed with the results of the kinetic model and the simulated spectra. These results not only give insight into the charge generation mechanisms and the differences in charge absorption, but constitutes the first observation of spectrally resolved CT state and separated charges confirmed by simulations. This allowed us to fit more complete kinetic models and understand the charge generation, separation, and recombination in more detail.

The work in these two chapters on dilute fullerene based systems mainly emphasised the benefits of delocalisation in neat  $C_{60}$ . In highly dilute-donor morphologies the  $C_{60}$  clusters are able to delocalise the electrons both when bound in CT states and when charges are separated. This delocalisation facilitated CT state separation is so beneficial to the dilute blends that they exhibit higher PCEs than their 1:1 blend counterparts. This is despite the fact that the dilute blends absorb less light, require longer exciton diffusion, have lower donor/acceptor interface and have an almost completely hindered hole transport.

Chapter 6 of this thesis follows on from research done on the exciton dynamics and charge transfer mechanisms in polymer:m-ITIC blends. In chapter 6 we look at the polymer properties which effect the geminate recombination mechanisms in these blends. This was done by comparing m-ITCT blended with semi-crystalline P3HT, and amorphous J61 and PCDTBT polymers. In order to understand the efficient J61:m-ITIC 1:1 blend, three other morphologies were used as model systems for the three phase morphology found in the 1:1 blend. A bilayer was used to represent the phase separated interfaces, 5:1 blend was used to represent an intermixed acceptor neat a neat donor region and 1:10 blend for the inverse. We find that the amorphous J61 and PCDTBT maintain their packing order regardless of the morphological

regime, while P3HT varies substantially in different morphologies. It is found that remaining amorphous allows relatively efficient charge generation in all morphological scenarios. We also see that a high lying CT state slows the geminate recombination enough to make the separation/geminate recombination competition favour the separation. However, separation still requires high short range morphology in order to be efficient. In the end it is found that the optimal polymer to blend with NFAs are amorphous and have high short range mobility. This chapter mainly emphasises the importance of having desirable properties be tolerant to different morphologies. The most efficient BHJ blends have a three phase morphology and so charge separation that is efficient in all three is naturally desirable.

The last chapter in this work looks to the future where idea material properties and new material discovery is aided by big data based machine learning. In chapter 7 of this thesis a QSPR deep transfer learning model is created. The model takes SMILES of a molecule as input, converts it to an RGB image, and predict its HOMO/LUMO levels with an accuracy (RMSE) of below 200 meV. The problem of small experimental datasets is overcome by training the model on a very large DFT based dataset and later fine tuning on the more realistic experimental data. We then test the model on a dataset we created which represents modern donor molecules for OPV with reasonable success. Even though the prediction process remains somewhat of a black box for us, we are able to define the limitations of the model quite well. It seems that the model learns to identify some multi-atom building blocks in the molecules and then correlates those to the HOMO/LUMO levels. This is confirmed by the poor predictions one molecules with new building blocks. This chapter shows generally how useful big data and machine learning techniques can be for both finding new materials and designing experiments to understand the OPV process better.

Understanding and observation of the working processes OPV systems has become extremely nuanced, and the effect, in terms of efficiency improvement, is obvious. As we continue to improve our understand of what constitutes favourable material properties for photoconversion, the design and discovery of new materials becomes more and more efficient. At the same time the advances in computational power and techniques allows us to leverage large datasets to help find new materials. The future is, however, not to replace the scientific understanding of materials with black box machine learned models. The future is to use computational and data based techniques to improve the design, volume and analytical complexity of experiments and so the understanding. While the complexity of organic photovoltaics is high, this thesis constitutes an improvement in the understanding of parts the

process through rigorous experimental and analytical work, as well as gives a glimpse into the future of computer aided science.

# 9 Appendix

## A.1 Appendix for Chapter 3:

### Methods

#### A.1.1 pyMCR Template

The MCR-ALS decomposition is done in Python using a package called pyMCR whose updated documentation can be found on <https://pages.nist.gov/pyMCR>. This is meant to serve as a skeleton template to perform MCR-ALS decomposition on TA data. The main processes are fully described in Chapter 3.

```
1 from pymcr.mcr import McrAR
2 from pymcr.regressors import OLS, NNLS
3 from pymcr.constraints import *
4
5 mcr = McrAR(c_regr=NNLS(), st_regr=OLS(),           #Set regressors (OLS())
6            c_constraints = [Custom_Con(value=0.01, set_value = 0)], #Specify constrains for dynamics
7            st_constraints = [],
8            max_iter=5000,                               #maximum fitting iterations (50)
9            tol_increase=10,                             #allowed error increase factor (0.0)
10           tol_n_increase=50,                           #allowed increase iterations (10)
11           tol_err_change=1e-10,                         #break if error changes less (None)
12           tol_n_above_min=5000)                        #allowed half iterations before new min (10)
```

Figure A.1-1 Importing parts of pyMCR package and initialising McrAR object, including choosing regressors, setting constraints and specifying convergence criteria.

In Figure A.1-1 we first import the appropriate parts of the pyMCR package (lines 1-3) and then initialise the McrAR object as 'mcr'. Initialising the mcr object involves choosing regressors for both dynamics and spectral components (line 5), choosing constrains for dynamics and spectral components (lines 6,7) and setting convergence criteria (lines 8-12). The default regressor is the Ordinary Least Squares (OLS()) regression algorithm (default shown in brackets in code comments), however, as the dynamics are always positive in TA spectra a Non-Negative Least Squares (NNLS()) regression algorithm is used for the dynamics optimisation. A custom constrain is specified in line 6 specifically for the dynamics optimisation (definition of custom constraint in Figure A.1-3). Lastly the convergence criteria are defined in lines 8-12 where we define how long the algorithm can spend searching for the optimum values (max\_iter), and how much and for how long the error is allowed to increase in search of a new minimum (tol\_increase, tol\_n\_increase, tol\_err\_change and tol\_n\_above\_min).

```

1 mcr.fit(TA_Data, ST=Spectral_Guess, st_fix = [0])
2
3 Optimal_Dynamics_Output = mcr.C_opt_
4 Optimal_Spectral_Output = mcr.ST_opt_

```

Figure A.1-2 Calling the fit method from the mcr object and setting the optimal output.

Figure A.1-2 shows syntax for running the MCR-ALS fitting algorithm (line 1). To run the MCR-ALS fitting algorithm we call the ‘fit’ method of the ‘mcr’ object defined in Figure A.1-1, where the first input is the TA data block (‘TA\_Data’), the second input ‘ST’ allows us to input our initial guess for the spectral components (‘C=Dynamics\_Guess’ for initial dynamics guesses, at least one type of guess is required) and ‘st\_fix’ is a list of the indices of which are held constant (not optimised) during the fitting (‘c\_fix = []’ for fixing dynamics guesses). Running line one will perform the MCR-ALS optimisation and if successful the ‘mcr’ object will gain a number of new attributes, most importantly ‘mcr.C\_opt\_’ and ‘mcr.ST\_opt\_’ which contain the optimised dynamics and spectral components respectively.

### A.1.2 Custom Constraints

As described in Chapter 3 the optimised MCR-ALS results may result in physical unrealistic dynamics or spectral components. It is therefore important to have the ability to constrain the output of the MCR-ALS to ensure physical viability. These constraints should necessarily be enforced within each iteration of the MCR-ALS fitting and not after optimisation. Enforcing a constraint on the dynamics after each iteration, for example, allows the effects of the constraint to be carried through to the optimisation of the spectral components and vice versa. Below (Figure A.1-3) is an example of a custom constraint where the values of the dynamics components are constrained. Moving forward in time, once a specific value is crossed from above then all subsequent values are set to a specific value. The motivation for this constraint was to suppress the reformation of excitonic species at long time delays for an OPV system with a relatively high driving force (where reformation of excitons is unlikely).

```

1 class Custom_Con(Constraint):
2     """
3     Sets values less than 'value' to the 'set_value' only once 'value' has been crossed once.
4     -----
5     value : float
6         Threshold value
7     set_value : float
8         Value to which the offending data will be set.
9     copy : bool
10        Make copy of input data, A; otherwise, overwrite
11    """
12
13    def __init__(self, value=0.01, set_value = 0, copy=False):
14        super().__init__(copy)
15        self.value = value
16        self.set_value = set_value
17
18    def transform(self, A):
19        if self.copy:
20            return A
21        else:
22            A *= (A > self.value)           #Sets all values lower than 'value' to 0
23            for j in range(A.shape[1]):
24                passed = None
25                for i in range(A.shape[0]):
26                    if A[i,j] > 0:
27                        passed = i           #registers index if value is passed
28                    if (A[i,j] == 0)&(passed != None):
29                        break                #value passed from above, break
30                A[passed:,j] = self.set_value #set everything set_value after pass from above
31        return A

```

Figure A.1-3 Python code example of a custom MCR-ALS constraint in the appropriate format for the pyMCR package.

The definition of this constraint class inherits properties from the ‘Constraint’ class in the pyMCR package and follows a format compatible with the package.

### A.1.3 Custom Loss Function

```

1 class Kinetic_WFree(HessianObjective):
2     """
3     This Objective is a custom objective that fits Kinetic models of TA data of Organic Bulkhydrojunctions.
4     The difference here is that we need to fit multiple species onto one decay.
5     Symfit stores the variables in alphabetical order, so we assign these to indexes in the correct order.
6     This can be checked printing model.vars.
7     We evaluate all the functions but reassign one so that it is the sum of two.
8     The rest of the efficient LeastSquares objective can then be simply applied.
9     This includes the use of the Jacobian and Hessian.
10    """
11    @keywordonly(flatten_components=True)
12    def __call__(self, ordered_parameters=[], **parameters):
13        flatten_components = parameters.pop('flatten_components')
14        evaluated_func = super(Kinetic_WFree, self).__call__(
15            ordered_parameters, **parameters)
16
17        CT, F, Ex = 0,1,2
18
19        evaluated_func[CT] = evaluated_func[CT] + evaluated_func[F]
20
21        chi2 = [0 for _ in evaluated_func]
22        for index, (dep_var, dep_var_value) in enumerate(zip(self.model.dependent_vars, evaluated_func)):
23            dep_data = self.dependent_data.get(dep_var, None)
24            if dep_data is not None:
25                sigma = self.sigma_data[self.model.sigmas[dep_var]]
26                chi2[index] += np.sum((dep_var_value - dep_data) ** 2 / sigma ** 2)
27        chi2 = np.sum(chi2) if flatten_components else chi2
28        return chi2 / 2
29
30    def eval_jacobian(self, ordered_parameters=[], **parameters):
31        evaluated_func = super(Kinetic_WFree, self).__call__(ordered_parameters, **parameters)
32        evaluated_jac = super(Kinetic_WFree, self).eval_jacobian(ordered_parameters, **parameters)
33
34        CT, F, Ex = 0,1,2
35
36        evaluated_func[CT] = evaluated_func[CT] + evaluated_func[F]
37
38        result = 0
39        for var, f, jac_comp in zip(self.model.dependent_vars, evaluated_func, evaluated_jac):
40            y = self.dependent_data.get(var, None)
41            sigma_var = self.model.sigmas[var]
42            if y is not None:
43                sigma = self.sigma_data[sigma_var]
44                pre_sum = jac_comp * ((y - f) / sigma**2)[np.newaxis, ...]
45                axes = tuple(range(1, len(pre_sum.shape)))
46                result += np.sum(pre_sum, axis=axes, keepdims=False)
47        return np.atleast_1d(np.squeeze(np.array(result)))
48
49    def eval_hessian(self, ordered_parameters=[], **parameters):
50        evaluated_func = super(Kinetic_WFree, self).__call__(ordered_parameters, **parameters)
51        evaluated_jac = super(Kinetic_WFree, self).eval_jacobian(ordered_parameters, **parameters)
52        evaluated_hess = super(Kinetic_WFree, self).eval_hessian(ordered_parameters, **parameters)
53
54        CT, F, Ex = 0,1,2
55
56        evaluated_func[CT] = evaluated_func[CT] + evaluated_func[F]
57
58        result = 0
59        for var,f,jac_comp,hess_comp in zip(self.model.dependent_vars,evaluated_func,
60            evaluated_jac,evaluated_hess):
61            y = self.dependent_data.get(var, None)
62            sigma_var = self.model.sigmas[var]
63            if y is not None:
64                sigma = self.sigma_data[sigma_var]
65                p1 = hess_comp * ((y - f) / sigma**2)[np.newaxis, np.newaxis, ...]
66                p2 = np.einsum('i...,j...->ij...', jac_comp, jac_comp)
67                p2 = p2 / sigma[np.newaxis, np.newaxis, ...]**2
68                axes = tuple(range(2, len(p2.shape)))
69                result += np.sum(p2 - p1, axis=axes, keepdims=False)
70        return np.atleast_2d(np.squeeze(np.array(result)))

```

Figure A.1-4 Custom loss function (objective) for symfit Python package based on the existing LeastSquares objective class.

Figure A.1-4 shows an example of a custom (modified) loss function usable with the symfit Python package. The class 'Kinetic\_WFree' inherits from the 'HessianObjective' class and outputs a standard LeastSquares loss value. The modification done here is in the result of the 'evaluated\_function' in the least squares calculation as well as its Jacobian and Hessian



calculations (lines 19,36,56). In TA data on OPV active layers the CT state and Free charges are not distinguishable and so their sum is represented as one component in dynamic and spectral component in the MCR-ALS decomposition (exception being in Chapter 5 of this work). The three components of the model 'CT, F, Ex' (representing the CT state charge, Free Charge and the Exciton) are saved in alphabetical order. The evaluated function of the CT state (evaluated\_function[CT]) is the reassigned as the sum of the evaluated functions of the CT state component and the free charge component in the kinetic model (lines 19,36,56) after which the calculations for least squares, Jacobian and Hessian are made. Complete and up to date documentation of the symfit Python package used for kinetic modelling can be found at <https://symfit.readthedocs.io/en/stable/index.html>.

# Charge Generation and Recombination in Low-Donor-Content Organic Solar Cells

## Foreword

This contains the full supplementary information document from the article published in the Journal of Physical Chemistry Letters titled:

*Ultrafast Charge Dynamics in Dilute-Donor versus Highly Intermixed TAPC:C<sub>60</sub> Organic Solar Cell Blends*

### A.2.1 Experimental Methods

#### A.2.1.1 Sample preparation

TAPC (4,4'-Cyclohexylidenebis[N,N-bis(4-methylphenyl)benzenamine]) was purchased from Lumtec Corp. All organic molecules were purchased once sublimed except C<sub>60</sub>, (Creaphys GmbH, >99.99%). Films and devices for transient absorption and electro-absorption measurements were processed on glass (Eagle XG, Thin Film Devices Inc) and pre-patterned ITO (Ossila Ltd), respectively. Substrates were cleaned by sequential sonication in detergent (Hellmanex GmbH), de-ionised water (DI), acetone and iso-propanol (IPA) at 55°C for 10 minutes each and finally UV-ozone treated for 10 minutes. Thin films were evaporated onto the substrate in a custom deposition tool (Creaphys GmbH) and transferred to a nitrogen-filled glove-box without air exposure. The deposition rate was controlled by quartz crystal microbalances calibrated by X-ray reflectivity measurements with ellipsometry measurements for thickness. For blend films, the relative deposition rate of the materials was varied to obtain the desired TAPC:C<sub>60</sub> ratio. Devices were prepared in this configuration: ITO/MoOx (2 nm)/5wt.% TAPC:C<sub>60</sub> (50 nm)/BPhen (6 nm)/Al (10 nm), with MoOx evaporated at 0.1 Å/s and BPhen at 0.1-0.2 Å/s. The samples were kept under nitrogen atmosphere. During packing and transportation the samples were kept under Nitrogen atmosphere with all light blocked to avoid degradation and C<sub>60</sub> dimerization. Moreover, during TA experiments, the samples were placed into a sealed chamber under nitrogen to prevent degradation by oxygen and humidity.

#### *A.2.1.2 Steady-state absorption spectroscopy*

Absorbance spectra (1- transmission - scattering) were recorded on a UV/VIS/NIR Lambda 900 spectrometer with an integrating sphere (Perkin-Elmer). Typically, an absorbance spectrum offers a more representative measurement than an absorbance spectrum for diffusely scattering and reflecting solid-state materials. Steady-state measurements were carried out on a second set of samples, prepared in the same conditions as the ones used for TA measurements to avoid oxygen contamination prior to ultrafast experiments.

#### *A.2.1.3 Grazing-Incidence Wide-Angle X-ray Scattering (GIWAXS) measurement*

Measurements were carried out at the I07 beamline at Diamond Light Source (experiment nt13183-1), using a beam energy of 12.24 keV ( $\lambda = 1.0129 \text{ \AA}$ ) focused with a 4-bounce Si(111) monochromator to a beam width of 100  $\mu\text{m}$ . Samples were maintained in a dark environmental chamber with Kapton windows, with independently-controllable fore-beam knives and beamstop. A 0.5 sccm He flow into the chamber ensured to reduce incoherent ambient scattering. Images were acquired with a 10 s exposure time using a Pilatus 2M detector in rotated configuration. Samples were re-positioned by 100  $\mu\text{m}$  between each exposure to reduce beam damage to the area being imaged. Sample-detector distance (354 mm) and beam energy were calibrated using the first 13 peaks from a silver-behenate (Ag-Beh) sample, with the largest relative error and  $\delta q$  for Ag-Beh peak-fitting at the 1.291(51)  $\text{\AA}$  peak of 0.39% and 0.5%, respectively. The DAWn software suite[48] was used for data reduction.

#### *A.2.1.4 Femtosecond transient absorption spectroscopy*

Transient absorption (TA) experiments on the sub-picosecond time scale were performed with a home-built setup using the output pulses from a regeneratively amplified Ti:sapphire laser system (Astrella from Coherent, 35 fs pulses at 800 nm with a frequency of 1 kHz and a pulse energy of 6 mJ). The output was split into two parts that ultimately generated the pump and the probe beams. The pump beam was frequency-converted to 450 nm or 610 nm with a commercial optical parametric amplifier (OPerA Solo, Coherent). The pump energy at the sample was adjusted to be in the linear regime of the TA response without any bimolecular artefact in the dynamics, which corresponded to a fluence of 13  $\mu\text{J}/\text{cm}^2$  at 450 nm and of 93  $\mu\text{J}/\text{cm}^2$  at 610 nm (where the absorption was weak,  $< 0.1 \text{ OD}$ ). The pump pulse duration was about 60-80 fs (portable autocorrelator, pulseCheck, APE). The broadband “white light” probe beam was generated by focusing another portion of the fundamental laser output on a 5 mm sapphire plate. The probe was used to generate either a near-IR continuum (840 – 1220 nm) or a visible continuum (480 – 730 nm), selected by using either 850 nm high pass or 750 nm low

pass filters for removing the remaining 800 nm from the white light. The probe beam was split before the sample into a reference beam (to correct for laser intensity fluctuations) and a signal beam. The latter was then focused on the sample where it overlapped spatially and temporally with the pump pulses. The probe intensity was negligible compared to the pump intensity (probe energy of  $< 5$  nJ) and the spot size was much smaller allowing for a homogeneous excitation (probe diameter of  $\sim 270$   $\mu\text{m}$  and pump diameter of  $\sim 700$   $\mu\text{m}$ , precisely determined for each measurement with a beam profiler, Thorlabs). The temporal delay between the two laser beams was achieved by varying the optical pathlength of the probe pulses with respect to the pump pulses using a computer-controlled delay stage (up to 1.5 ns). The visible and near-IR parts of the TA spectra were recorded separately (and scaled if necessary) with two spectrographs, consisting each of a home-built prism spectrometer equipped with either two 512  $\times$  58 pixel back-thinned Silicon CCDs (Hamamatsu S07030-0906) and or with two InGaAs arrays (Hamamatsu) for, respectively, visible and near-IR detection of the signal and the reference beams. The spectrographs were assembled by Entwicklungsbüro Stresing, Berlin. Wavelength calibration was accomplished with a series of 10 nm bandpass filters. To improve sensitivity, the pump pulses were chopped at 500 Hz and the probe pulses were recorded shot-by-shot. The TA spectra were averaged until the appropriate signal-to-noise ratio was achieved (4000-4500 shots per time delay, the whole 4 range of time delays was scanned 4-10 times). All the TA experiments were performed with a probe polarization at magic angle with respect to the one of the excitation beam to avoid effects of the polarization of the pump pulses on the probed absorption intensity. Prior to the TA analysis, the spectra were corrected for the chirp of the white light, which was determined by measuring the pump-probe cross-correlation by the optical Kerr effect on a glass slide placed between crossed polarizers. MATLAB and IgorPro software were used for data analysis. The TA measurements on devices were done in the same way with 450 nm excitation, in transmission mode. This was possible using as the electrode a thin enough Al layer (10 nm) to be transparent. The device was placed in an orientation such that the pump and probe went through the Al electrode first so that back reflection (re-excitation) was avoided.

#### *A.2.1.5 Temperature-controlled transient absorption spectroscopy*

TA spectroscopy was carried out using a homebuilt pump-probe setup. The output of a titanium:sapphire amplifier (Coherent LEGEND DUO, 4.5 mJ, 3 kHz, 100 fs) was split into three beams (2, 1, and 1.5 mJ). Two of them were used to separately pump two optical parametric amplifiers (OPA) (Light Conversion TOPAS Prime). TOPAS 1 generates tunable

pump pulses, while TOPAS 2 generates signal (1300 nm) and idler (2000 nm) only. TOPAS 2 was used to produce a white-light super continuum from 350 to 1100 nm by sending the 1300 nm pulses through a calcium fluoride (CaF<sub>2</sub>) crystal which is mounted on continuously moving stage. For short delay TA measurements, TOPAS 1 was used to generate pump pulses, while the probe pathway length to the sample was kept constant at  $\approx 5$  m between the output of TOPAS 1 and the sample. The pump pathway length was varied between 5.12 and 2.6 m with a broadband retroreflector mounted on an automated mechanical delay stage (Newport linear stage IMS600CCHA controlled by a Newport XPS motion controller), thereby generating delays between pump and probe from  $-400$  ps to 8 ns. For the 1 ns to 300  $\mu$ s delay (long delay) TA measurement, the same probe white-light supercontinuum was used as for the 100 fs to 8 ns delays. Here the excitation light (pump pulse) was provided by an actively Q-switched Nd:YVO<sub>4</sub> laser (InnoLas piccolo AOT) frequency-doubled to provide pulses at 532 nm. The pump laser was triggered by an electronic delay generator (Stanford Research Systems DG535) itself triggered by the transistor– transistor logic (TTL) sync from the Legend DUO, allowing control of the delay between pump and probe with a jitter of roughly 100 ps. The sample was kept under a dynamic vacuum of  $<10^{-5}$  mbar in a cryostat (Optistat CFV, OXFORD Instruments). The temperature-dependent study at 300-80K was performed in a cryostat cooled by liquid nitrogen with various flow rates. A temperature controller (MercuryTC, OXFORD Instrumnets) was used to control the temperature. The transmitted fraction of the white light was guided to a custom-made prism spectrograph (Entwicklungsbüro Stresing) where it was dispersed by a prism onto a 512 pixel complementary metal-oxide semiconductor (CMOS) linear image sensor (Hamamatsu G11608- 512DA). The probe pulse repetition rate was 3 kHz, while the excitation pulses were mechanically chopped to 1.5 kHz (100 fs to 8 ns delays) or directly generated at 1.5 kHz frequency (1 ns to 300  $\mu$ s delays), while the detector array was read out at 3 kHz. Adjacent diode readings corresponding to the transmission of the sample after excitation and in the absence of an excitation pulse were used to calculate  $\Delta T/T$ . Measurements were averaged over several thousand shots to obtain a good signal-to noise ratio. The chirp induced by the transmissive optics was corrected with a homebuilt Matlab code. The delay at which pump and probe arrive simultaneously on the sample (i.e., zero time) was determined from the point of maximum positive slope of the TA signal rise for each wavelength.

#### *A.2.1.6 Electro-absorption spectroscopy*

The steady-state electro-absorption (EA) spectrum of C<sub>60</sub> was obtained on a working C<sub>60</sub> device with a similar setup as described for the TA experiments. The visible probe beam entered the device through the semi-transparent (20 nm thick) Al counter electrode, then was transmitted through the entire device (8 nm BPhen, 50 nm C<sub>60</sub> active layer, 4 nm MoO<sub>3</sub>, and ITO) before being detected by the CCD spectrograph. A similar scheme as for TA spectroscopy was implemented, but the EA technique involved the modulation of an electric field applied across the contacts of the solar cell with a function generator synchronized to the 6 laser frequency (Tetronix AFG 2021), instead of the modulation of the pump pulses as in TA (in fact, the pump beam was blocked). Thus, a square voltage pulse (up to 8 V, 100  $\mu$ s duration, corresponding to a field of 1.6 MV/cm) in reverse bias was applied at half the probe frequency of 1 kHz, and the transmitted probe was measured shot-by-shot in the presence and in the absence of electric field, averaged over 4500 shots. The EA was then calculated as the absorption difference with and without the field.

#### *A.2.1.7 EQE measurements*

Monochromatic light modulated by a chopper wheel was shone onto the device through an optical fibre and the resulting current signal measured with a lock-in amplifier (Signal Recovery 7265). Reference spectra were captured with a calibrated Si diode from the Fraunhofer ISE CalLab, Freiburg (1337-33BQ, Hamamatsu).

#### *A.2.1.8 Multi-exponential global analysis*

The strong overlap of broad spectral TA bands makes the interpretation of the single wavelength TA dynamics very complicated, because they can in general not be assigned to a unique species or process. Indeed, the time evolution of the TA signal can be affected by multiple processes, for example the CT states dynamics is mixed with spectral shifts due to relaxation. For this reason, to disentangle the spectral components present in the TA spectra, we have analysed the complete spectral (TA dynamics taken every 5 nm) and temporal (between 0.1 ps to 1.5 ns) data sets using multi-exponential global analysis. Apart from being more robust to noise-related artefacts often characterizing a single wavelength, this method allows for correlating the evolution of different signatures in the TA spectrum, greatly facilitating the interpretation. Specifically, without imposing any specific model to the results, we have performed data analysis by globally fitting a sum of exponential functions to the dynamics (time constants were linked over the probe wavelengths, while amplitudes were free). In this way, we could estimate the time scale on which processes are occurring and plot the

pre-exponential factors as a function of the probe wavelength (yielding decay-associated amplitude spectra). By considering the amplitude spectra, we could thus gain information if the processes associated with a given time constant lead to a rise or a decay of the TA signal in different parts of the transient spectrum, and thus correlate the temporal behaviour of different spectral regions. Although the exponential analysis does not necessarily have an underlying physical meaning, it can be very successful in disentangling different processes if they occur on sufficiently different time scales, as is the case for TAPC:C<sub>60</sub> blends.

In the case of TAPC:C<sub>60</sub> excited at 450 nm, the dynamics could be well reproduced using a three-exponential function and an offset ( $y_0$ ) corresponding to long-lived signals.

$$\Delta A = a_1 e^{\frac{-t}{\tau_1}} + a_2 e^{\frac{-t}{\tau_2}} + a_3 e^{\frac{-t}{\tau_3}} + y_0$$

where  $\tau_n$  are the time constants and  $a_n$  the amplitudes associated with the exponential  $n$ .

#### *A.2.1.9 Multivariate Curve Resolution using Alternating Least Squares (MCR-ALS)*

MCR-ALS is a soft-modelling technique that is able to factor out the TA data surface into spectra and their concentrations over time while removing a residual matrix (**E**).

$$\mathbf{D} = \mathbf{C}\mathbf{S}^T + \mathbf{E}$$

With **D** being the 2D TA data matrix, **C** being the concentrations and **S** the spectral components (as seen in Figure 3A and 3B). The analysis was done using a freely available MATLAB toolbox developed by Romà Tauler et al.<sup>1</sup> The constraints used were non-negativity and unimodality for the concentrations. In the case of 5% blends excited at 610 nm, known spectra of excitons and charges, from the early time neat C<sub>60</sub> TA spectra and from the long-lived global analysis amplitude spectra of the 5% blend, respectively, were fixed in the fitting.

### A.2.2 GIWAXS measurement of TAPC:C<sub>60</sub> blends

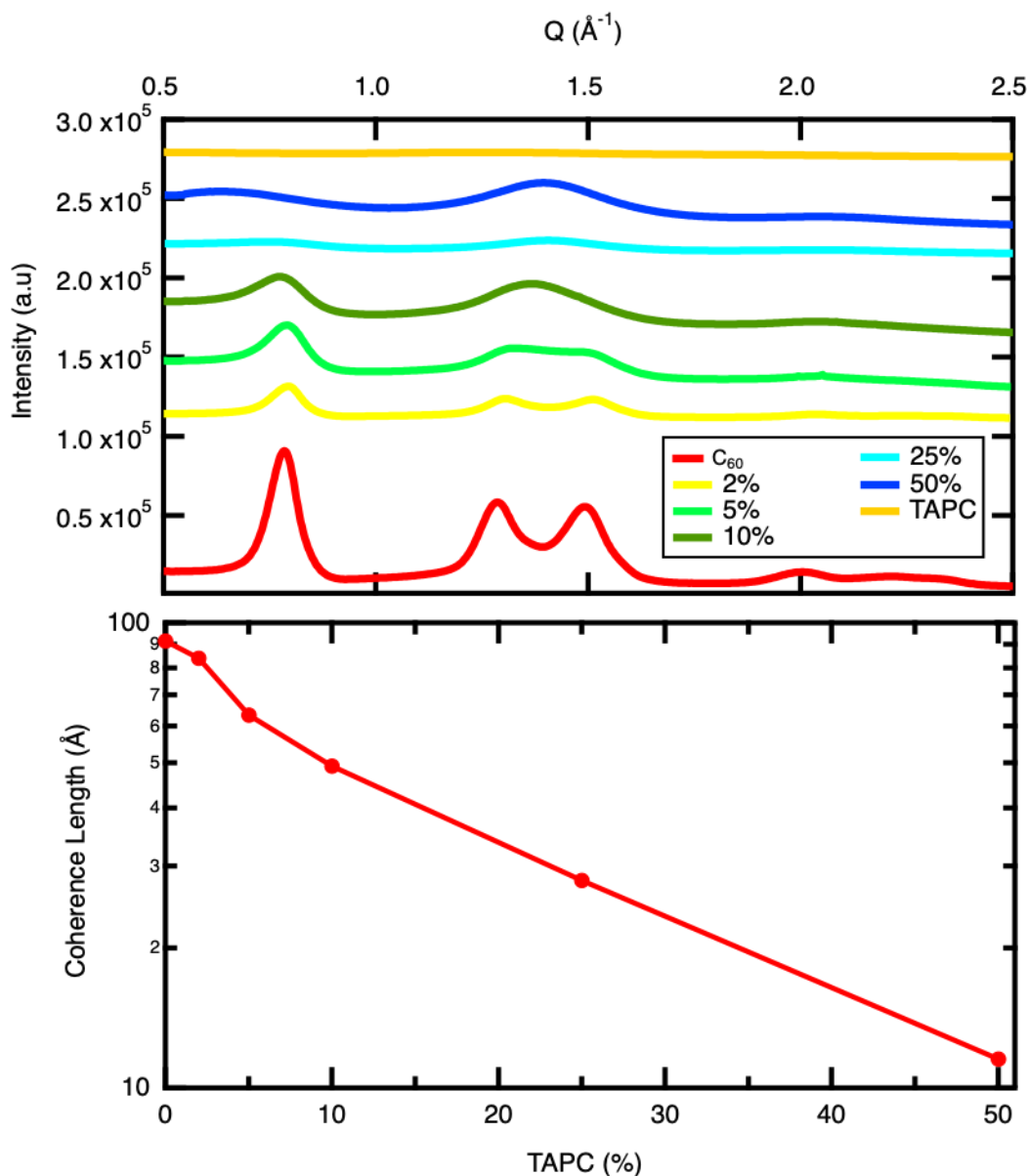


Figure A.2-1 Grazing-incidence wide-angle x-ray scattering (GIWAXS) measurements of 50 nm thick C<sub>60</sub>:TAPC thin films on glass. (top) Azimuthal integration of scattering for various TAPC concentrations. Increasing TAPC concentration is associated with reduced distinguishability of the two 220 and 300 peaks in C<sub>60</sub> in the region between 1.28 and 1.5  $\text{\AA}^{-1}$  where  $\pi$ - $\pi$  interactions are prevalent. We note that the 111 peak position exhibits a marginal increase for 2% TAPC, followed by a decrease from 0.79  $\text{\AA}^{-1}$  to 0.62  $\text{\AA}^{-1}$  at 50% TAPC. (bottom) Variation of coherence length of the C<sub>60</sub> 111 peak ( $q = 0.78 \text{\AA}^{-1}$ ) with TAPC concentration. The 111 peak is broadened ( $D_{\text{coh}} \sim 2\pi/\Delta q$ ), suggesting a decrease in C<sub>60</sub> characteristic crystallite size from 10 nm in its pure state to  $\sim 1$  nm at 50% TAPC.



### A.2.3 Transient absorption spectrum of neat C<sub>60</sub>

The TA spectrum of neat C<sub>60</sub> excited at 610 nm is shown in figure Figure B-2 with the signature of Frenkel excitons showing photoinduced absorption at 550 nm and at 930 nm. The exciton signature clearly decays with a lifetime of around 150 ps.

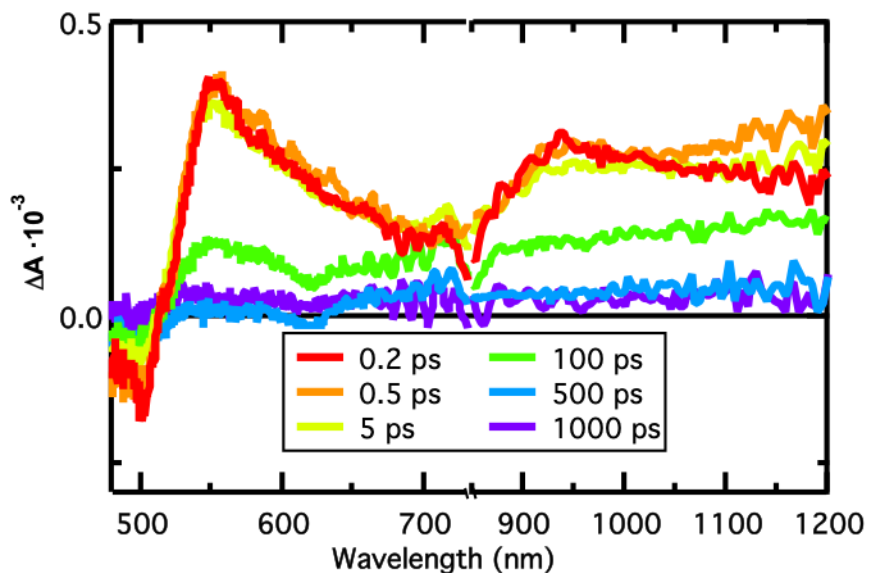


Figure A.2-2 Transient absorption (TA) spectra of neat C<sub>60</sub> film at selected time-delays (0.2 ps, 0.5 ps, 5 ps, 100 ps, 500 ps and 1 ns) at 610 nm pump excitation.

### A.2.4 Steady-state absorbance spectra for the TAPC:C<sub>60</sub> blend

From the steady-state absorbance spectra depicted in Figure B-3, we observe that the intensity of the CT absorption band (400 nm to 600 nm) is reduced in the presence of 5% TAPC, but almost suppressed at 50% TAPC loading.

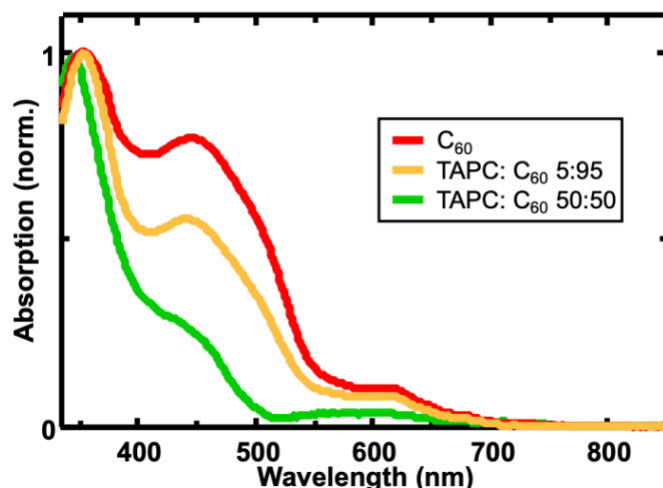


Figure A.2-3 Steady-state absorbance spectra of neat  $C_{60}$  film (red), TAPC: $C_{60}$  5% blend (yellow) and TAPC: $C_{60}$  50% blend (green).

#### A.2.5 Kinetic model used to fit the MCR-ALS decomposition dynamics

Kinetic models can be developed so that the dynamics of the species (excitons and charges) extracted from the TA data by MCR-ALS can be quantified, and to find the rate constants of the related processes. First, the MCR-ALS dynamics are normalized such that the maximum charge concentration (assumed to be equal to the total excitation density given quasi-quantitative exciton dissociation) is equal to one. The exciton dynamics are then scaled so that the sum of the initial population of excitons and charges is also unity. Then, we treat the conversion from excitons to charges by HT (which is in competition with much slower natural exciton decay to the ground state) and the ensuing charge recombining as sequential and linked processes, using linked differential equations to fit the rate of change of the  $S_1$  (exciton) and charge populations. The TA data shows a biphasic lifetime of the charges in all blends, with part of the population decaying on the sub-nanosecond time scale (with a time constant that could be linked between the different blends) and a long-lived offset of charges that recombine on a much slower time scale than our measurement window. To model this behavior, the populations of both the  $S_1$  state and charges were split into excitons that will eventually result in long-lived charges ( $Ex\_long(t)$ ) and excitons that populate charges with fast recombination ( $Ex\_rec(t)$ ), as well as, long-lived charges ( $Ch\_long(t)$ ) and those that will recombine ( $Ch\_rec(t)$ ). We note that TA spectroscopy does not allow to distinguish between signatures of bound and free charges, so that we always see the sum of the recombining and long-lived charges but cannot directly assess if the recombination occurs from bound charges (geminate process) or from free charges (trap-based recombination). For the same reason, we did not

include any specific mechanism for the generation of the long-lived charges in the model (which could be formed directly from excitons or by dissociation of initially bound charges).

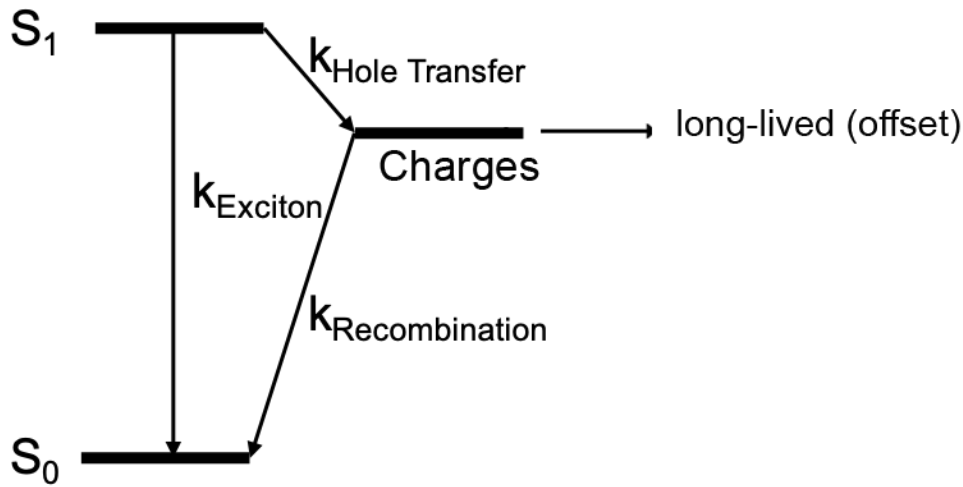


Figure A.2-4 Jablonski diagram representing the energy levels of the  $S_0$  (ground state), the  $S_1$  (first excited state or exciton) and **Charges**. The natural exciton decay rate ( $k_{\text{Exciton}}$ ), hole transfer rate ( $k_{\text{Hole Transfer}}$ ) and the charge recombination rate ( $k_{\text{Recombination}}$ ) are also represented by arrows between states.

The parameters used were:

$k_{\text{HT}}$  (hole transfer rate)

$k_{\text{Ex}}$  (natural exciton recombination rate) =  $0.00667 \text{ ps}^{-1}$  (determined from neat  $\text{C}_{60}$ )

$k_{\text{rec}}$  (sub-nanosecond charge recombination rate)

$\text{Ex}_{\text{rec}}(0) = \text{C1}$

$\text{Ex}_{\text{long}}(0) = \text{C2}$

$\text{Ch}_{\text{rec}}(0) = \text{C3}$

$\text{Ch}_{\text{long}}(0) = \text{C4}$

Rate equations and solutions:

$$\frac{d[\text{Ex}_{\text{rec}}]}{dt} = -k_{\text{HT}}[\text{Ex}_{\text{rec}}] - k_{\text{Ex}}[\text{Ex}_{\text{rec}}]$$

$$\text{Ex}_{\text{rec}}(t) = \text{C1} * \exp(-t * (k_{\text{Ex}} + k_{\text{HT}}))$$

$$\frac{d[\text{Ex}_{\text{long}}]}{dt} = -k_{\text{HT}}[\text{Ex}_{\text{long}}] - k_{\text{Ex}}[\text{Ex}_{\text{long}}]$$

$$\text{Ex}_{\text{long}}(t) = \text{C2} * \exp(-t * (k_{\text{Ex}} + k_{\text{HT}}))$$

Total exciton population =  $Ex_{rec}(t) + Ex_{long}(t)$

$$\frac{d[Ch_{rec}]}{dt} = -k_{HT}[Ex_{rec}] - k_{rec}[Ch_{rec}]$$

$$Ch_{rec}(t) = (\exp(-k_{rec}t) * (C3 * k_{Ex} + C1 * k_{HT} + C3 * k_{HT} - C3 * k_{rec})) / (k_{Ex} + k_{HT} - k_{rec}) - (C1 * k_{HT} * \exp(-t * (k_{Ex} + k_{HT}))) / (k_{Ex} + k_{HT} - k_{rec})$$

$$\frac{d[Ch_{long}]}{dt} = -k_{HT}[Ex_{long}]$$

$$Ch_{long}(t) = (C4 * k_{Ex} + C2 * k_{HT} + C4 * k_{HT}) / (k_{Ex} + k_{HT}) - (C2 * k_{HT} * \exp(-t * (k_{Ex} + k_{HT}))) / (k_{Ex} + k_{HT}) \quad (\text{no recombination})$$

Total charge population =  $Ch_{rec}(t) + Ch_{long}(t)$

Initial charge population at 0.2 ps =  $Ch_{rec}(0.2) + Ch_{long}(0.2)$

The exciton component in the MCR-ALS dynamics (Figure 1C) is then fit using the sum of  $Ex_{rec}(t)$  and  $Ex_{long}(t)$  and the charge dynamics is fit using the sum of  $Ch_{rec}(t)$  and  $Ch_{long}(t)$  with all parameters linked. The results of the fitting are shown in Table 4-1.

#### A.1.1 Intensity-dependent TA dynamics of TAPC:C<sub>60</sub> 5% blend

Figure B-5 shows the normalized TA dynamics probed at 550 nm at multiple fluences, confirming the absence of bimolecular recombination (within < 1ns) in the 5% TAPC:C<sub>60</sub> film following 450 nm excitation. The TA spectra shown in this manuscript were recorded with a pump fluence of 13  $\mu\text{J}/\text{cm}^2$ .

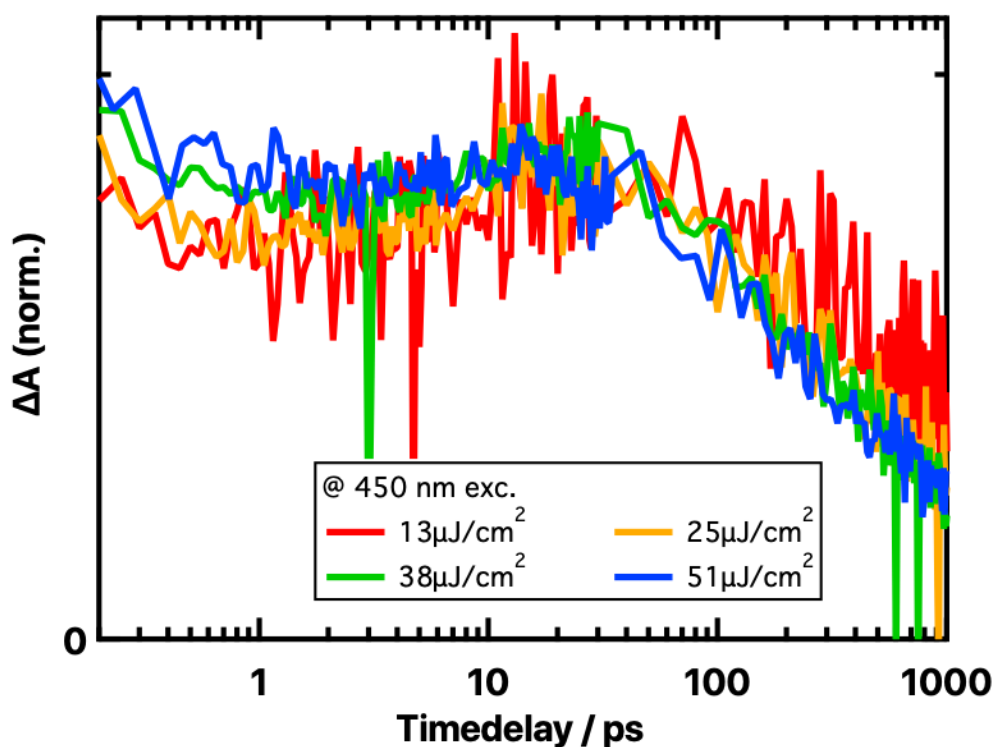


Figure A.2-5 Dynamics of the positive EA peak at 550 nm in the 5% TAPC:C<sub>60</sub> TA spectra at a range of different fluences with 450 nm excitation.

#### A.2.6 TA of the 5% TAPC:C<sub>60</sub> device

Figure B-6 on the left shows the TA spectra of the 5% blend in device configuration (with electrodes that were short-circuited with a wire). We can see a much more pronounced EA signal than in the film along with an extremely broad exciton peak at 920 nm as well as a broad charge peak at 1050 nm. The cation peak at 730 nm is obscured by the large EA signal. On the right, a comparison between the dynamics at 550 nm of the EA peak in device and film configuration is shown. In the device, the EA signal decays more slowly as a result of a longer-lasting electric field in the device.

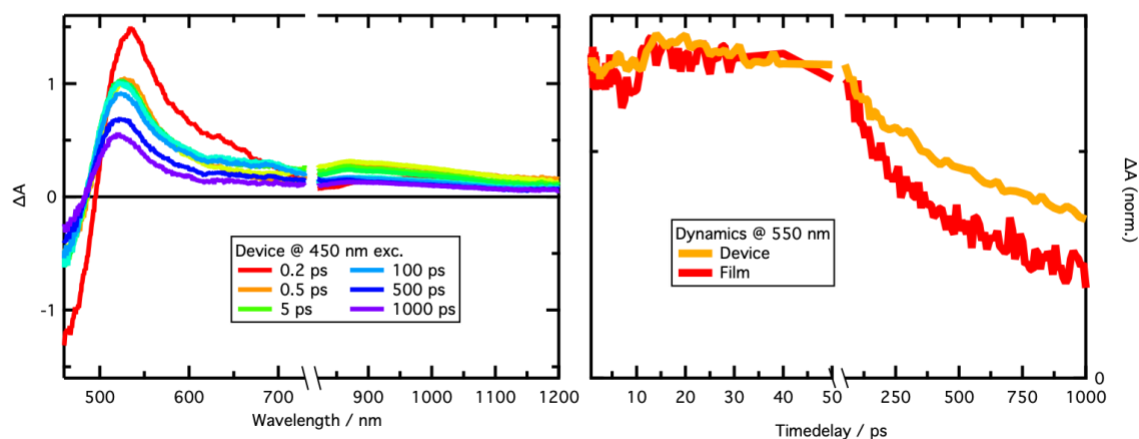


Figure A.2-6 TA spectra of the 5% blend in device configuration at selected time-delays (0.2 ps, 0.5 ps, 5 ps, 100 ps, 500 ps and 1 ns) at 450 nm pump excitation (left). The dynamics of the device and film at 550 nm (EA peak) is shown on the right.

#### A.2.7 Dynamics of the EA peak of the 50% TAPC:C<sub>60</sub> blend excited at 450 nm and 610 nm

Figure B-7 shows that unlike with the 5% blend (Figure 3C), the early time dynamics of the EA peak of TA spectra probed at 550 nm after excitation at 450 nm and 610 nm, shows very similar dynamics in the 50% blend. There is no intermolecular CT exciton signature even when exciting at 450 nm, because of the lack of large C<sub>60</sub> regions.

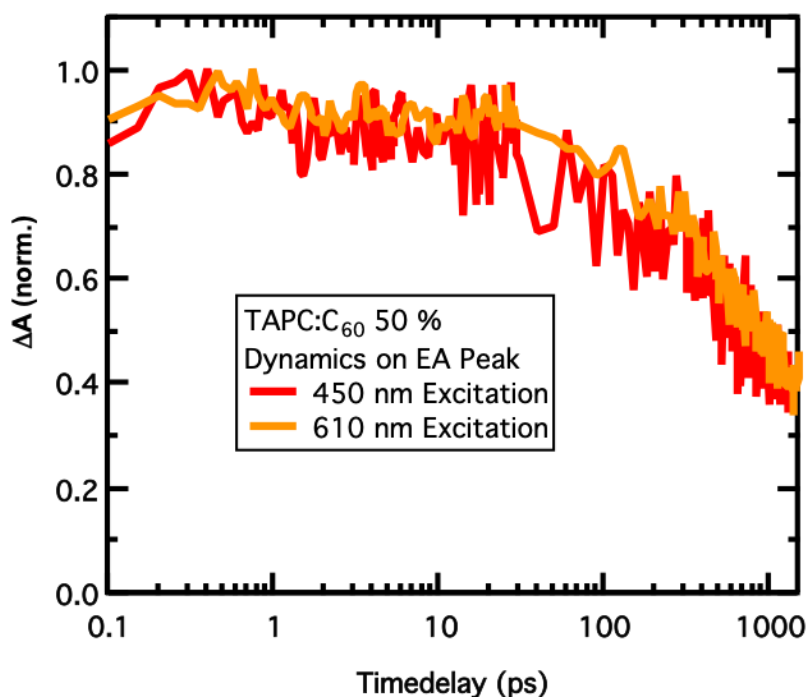


Figure A.2-7 Dynamics of the positive EA peak probed at 550 nm in TAPC:C<sub>60</sub> 50% at 450 nm (red) and 610 nm (orange) excitation.

# Pairing Non-Fullerene Acceptors with the Right Polymer: Impact of Morphology and Short-Range Mobility on Charge Generation

## A.3.1 Transient Absorption Spectra

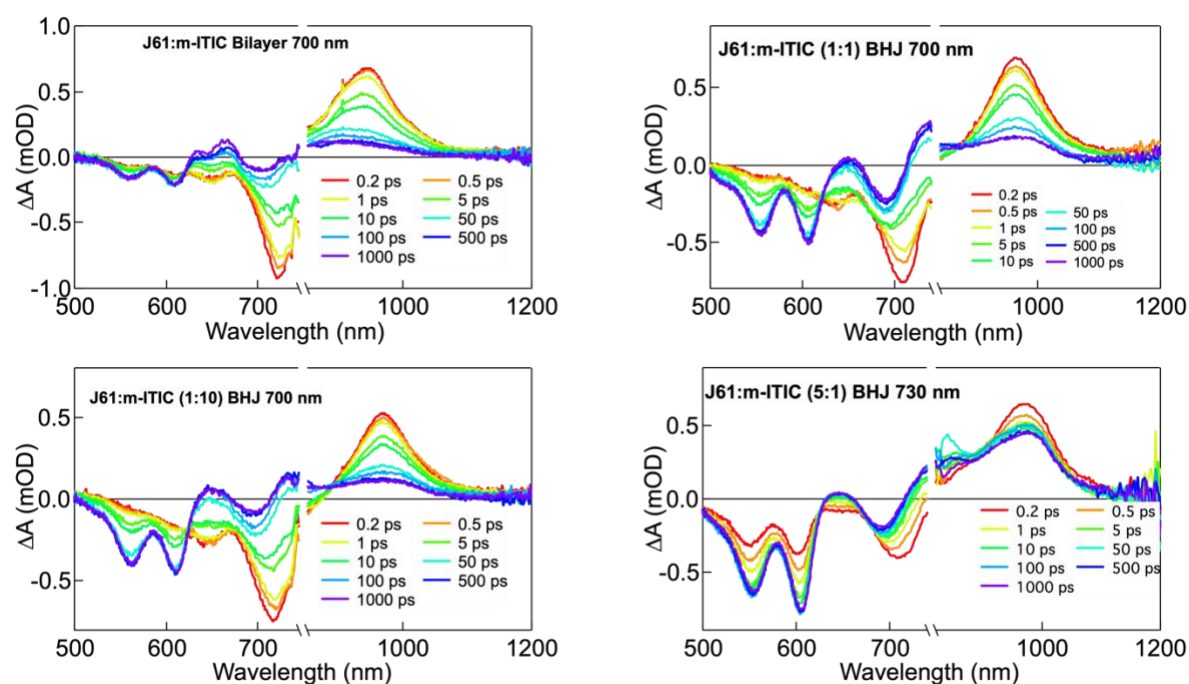


Figure A.3-1 Transient absorption spectra of J61:m-ITIC blends. Top left J61:m-ITIC bilayer excited at 700 nm. Top right J61:m-ITIC 1:1 blend excited at 700 nm. Bottom left J61:m-ITIC 1:10 blend excited at 700 nm. Bottom right J61:m-ITIC 5:1 excited at 730 nm. m-ITIC exciton excited in all samples.

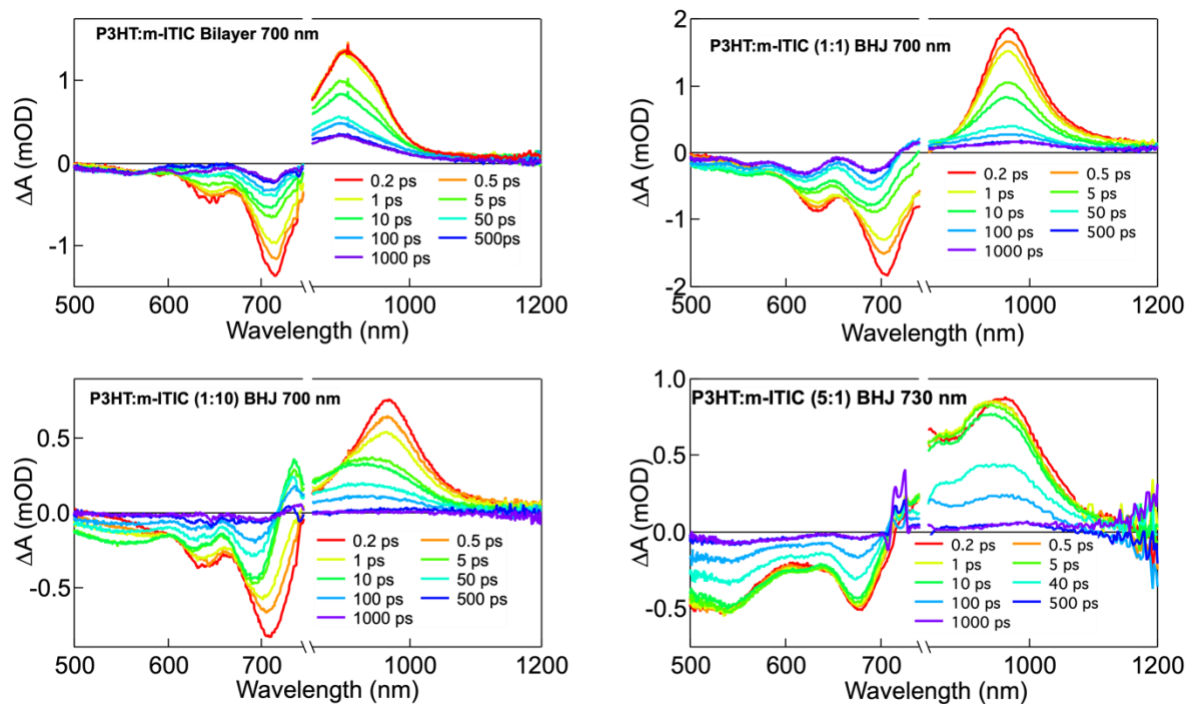


Figure A.3-2 Transient absorption spectra of P3HT:m-ITIC blends. Top left P3HT:m-ITIC bilayer excited at 700 nm. Top right P3HT:m-ITIC 1:1 blend excited at 700 nm. Bottom left P3HT:m-ITIC 1:10 blend excited at 700 nm. Bottom right P3HT:m-ITIC 5:1 excited at 730 nm. m-ITIC exciton excited in all samples.

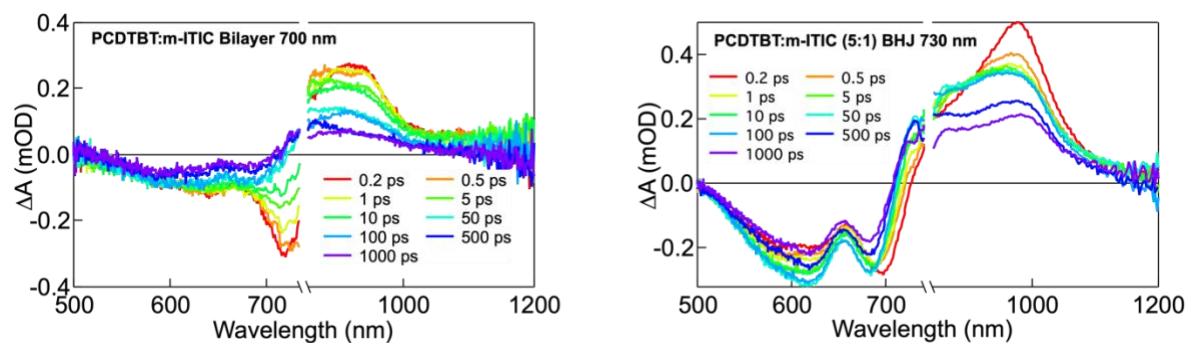


Figure A.3-3 Transient absorption spectra of PCDTBT:m-ITIC blends. Left PCDTBT:m-ITIC bilayer excited at 700 nm. Right P3HT:m-ITIC 5:1 excited at 730 nm. m-ITIC exciton excited in all samples.



# Deep transfer leaning: a fast and accurate tool to predict energy levels of donor molecules for organic photovoltaics

## Foreword

This contains the full supplementary information document from the submitted article:

*Deep transfer leaning: a fast and accurate tool to predict energy levels of donor molecules for organic photovoltaics*

### A.4.1 Deep learning methods

The deep learning model employed in this work follows a classic Convolutional Neural Network (CNN) architecture.<sup>1</sup> The model consists of two main parts: firstly, a series of convolutional and pooling layers where the features of input images are extracted and condensed and secondly, a fully connected neural network where the image features are converted through a set of weights and biases into the desired output.

The convolutional network is based on the VGG16 architecture.<sup>1</sup> The convolution layers transform the image such that features can be extracted. Here an image is convolved with a randomly initialized kernel (or filter) by sliding said kernel across the image through every special position and extracting the dot product of the kernel and the specific region of the image. An activation function and bias are then applied to the convolved feature-set resulting in a feature map. The activation function introduces nonlinearity to the network and adjusting the bias creates ability to train the value or importance of each kernel producing more meaningful feature maps. The feature maps are then subsequently treated as inputs for the next convolutional layer moving through the network. After a series convolutional layers are applied, the feature map is reduced in size by a max-pooling layer where only the maximum value in each region of the feature map is carried through. Pooling is used both to reduce the computational burden of calculation to speed up training and to make prominent features more robust by only taking the feature with the highest value thereby reducing overfitting. It is

however important to note that the kernels are randomly initialized and none of them are designed to intentionally extract specific molecular features. It would therefore be dangerous to expect to either understand the decision process of the network or to try extract meaningful scientific understanding about the connection between the molecular orbitals and the basic images by looking at these feature maps. Lastly, a global average pooling layer is applied, where the average value of each feature maps is taken such that the features are converted into a single array that can be passed through the fully connected network.

The fully connected layers of the network are used to convert the features of the image into two numbers which are trained to represent the HOMO and LUMO levels of the molecule. Layers of the fully connected network all consists of a set of neurons, with the input layer simply having the values of the feature array of the images. The input neurons are each connected to every neuron in the subsequent layer, with the value of the next neuron being a sum of each previous neuron multiplied by a unique and trainable weight with an additional bias added to each layer. An activation function is then applied to the value of each neuron in the layer in order to introduce nonlinearity to the network. This is then continued through multiple layers with varying numbers of neurons until the output layer consisting of two neurons (the HOMO and LUMO predictions). As the fully connected network is used as a regression network (as opposed to a classification network), multiple activation functions are employed so that the positive-valued feature array could be converted gradually into the negative energy values. The first part of the fully connected network uses i) the widely used ReLU<sup>2</sup> function ( $ReLU(x) = \max(0, x)$ ), followed by ii) a sigmoid function<sup>3</sup> ( $Sigmoid(x) = 1/(1 + e^{-x})$ ) which allows the values to range between 1 and  $-1$ , and (iii) a linear activation function to scale the values appropriately. Dropout layers are also included between the first few layers of the dense network in order to improve the generalizability of the model.

Data processing and training was done in Google Colab,<sup>4</sup> making use of the available Graphical Processing Units to speed up training.<sup>5</sup> The model was designed using TensorFlow<sup>6</sup> and Keras.<sup>7</sup>

#### A.4.2 Training

The loss function used in the training is the mean square of the error (MSE). Where MSE is calculated by:

$$MSE = \frac{1}{n} \sum_{i=1}^n (predicted - true)^2$$

With  $n$  being twice the number of molecules in the batch (each molecule having HOMO and LUMO predictions), *predicted* the HOMO/LUMO values predicted by the model and *true* the HOMO/LUMO values taken to be true for the molecule (DFT-estimated for Phase I training and experimentally measured for Phase II). Taking the square of the error was chosen over other loss functions (*e.g.*, mean absolute error) as it disproportionately ‘punished’ outliers. This favors for consistency of the accuracy of the model while potentially sacrificing some precision. Figures S1 and S2 show the training and validation losses for training phase I and II respectively with the root mean square error (RMSE) so that the loss values can be visualized in a meaningful unit (eV).

During training the data was split into a training and validation set (80%/20%) where the training set is used to optimize the models parameters and the validation is used to monitor the training at each epoch. Note that the validation set has nothing to do with the testing set used later. By looking at the deviation between the training loss and validation loss, we can see if the model is overfitting or staying generalized enough. Overfitting is essentially where the model learns the training data off-by-heart seeming to learn well, but when tested on the validation set the predictions are not as good. By monitoring the validation loss, we can adapt the model to minimize overfitting. This is partially done by using dropout layers between the first few layers of the dense network. Dropout layers randomly set a defined proportion of the neurons to zero after each iteration of training, spreading the prediction burden over more neurons in the layer and so making the entire network more generalizable.

The peaks in the training loss in Figure S1 come from introducing new sub-batches of data into the training set. The images of the 500’000 molecules used to train the model in Phase I are too large to fit into the random-access memory (RAM) of the system and so the model is iteratively trained on sub-batches of 50’000 molecules each.

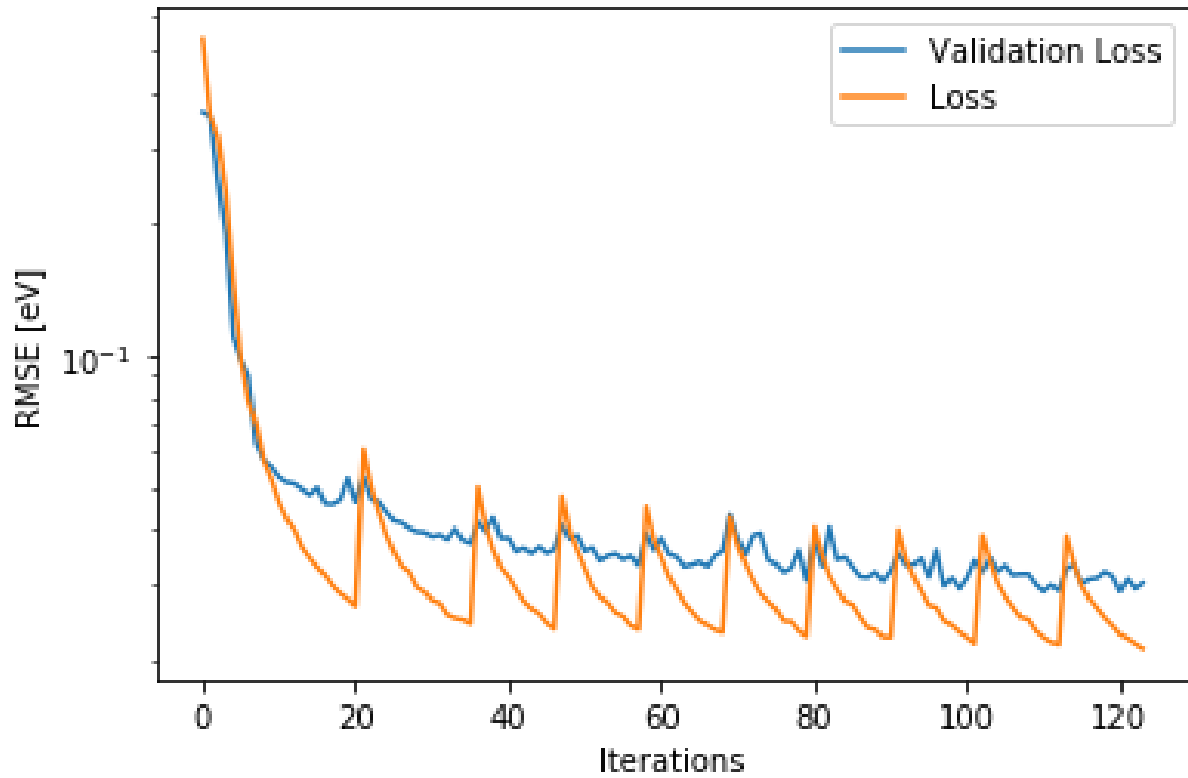


Figure A.4-1 Loss and validation loss for training on the HCEP dataset (phase I). Both the loss and validation loss relate to the training set (and not the testing set).

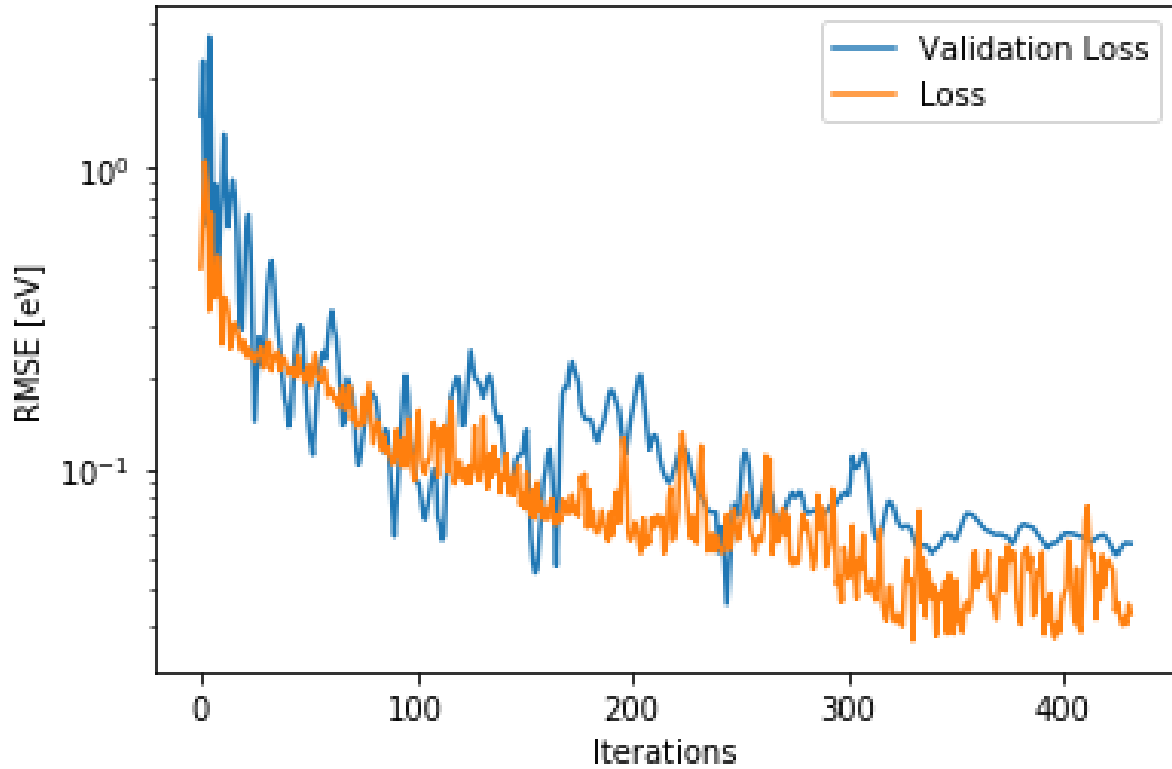


Figure A.4-2 Loss and validation loss of training on the HOPV15 dataset (phase II). Both the loss and validation loss relate to the training set (and not the testing set).

Table A.4-1 Performance of deep learning model after phase II training when weights are only transferred to the Deep Dense part of the network, the convolutional network and when normal transfer occurs.

	Only Deep weights transferred	Only CNN weights transferred	CNN and Deep weights transferred
	R <sup>2</sup> / SEP [meV]	R <sup>2</sup> / SEP [meV]	R <sup>2</sup> / SEP [meV]
<b>HOMO</b>	0.212 / 199	0.275 / 191	0.674 / 140
<b>LUMO</b>	0.390 / 246	0.791 / 146	0.537 / 189

#### A.4.3 Description of the datasets

##### A.4.3.1 HCEP as training dataset

The dataset used to train the model in this study came from the Harvard Clean Energy Project (HCEP).<sup>8</sup> The dataset consists of over 2.3 million potential donor molecules for use in OPV devices. The molecules were combinatorically generated from 26 building blocks which were systematically either linked or fused<sup>9</sup> maintaining a  $\pi$ -conjugated backbone.<sup>10</sup> The molecules were limited to five units long and represent small molecules rather than polymer monomers. The geometries of the molecules are optimized using DFT<sup>11</sup> employing BP86<sup>12, 13</sup> functionals with generalized gradient approximation (GGA) and double- $\zeta$  def2-SVP basis sets<sup>14</sup> after which the HOMO and LUMO levels are obtained. The molecules are encoded as SMILES (simplified molecular-input line-entry system)<sup>15</sup> which can be converted to 2D RGB images using the RDKit package in python.<sup>16</sup> The images are constructed with hydrogen removed, all carbon atoms in black, each non-carbon atom having a unique color and no 3D conformation representation. As loading all 2.3 million images would be very memory intensive the order of the molecules was randomly shuffled such that training on any subset of the data would be representative of the entire distribution. The first 500'000 molecules are used for model training and validation with 10'000 extra molecules used for testing.

##### A.4.3.2 HOPV15 as fine-tuning dataset

The model is fine-tuned on The Harvard organic photovoltaic dataset (HOPV15).<sup>17</sup> The HOPV15 dataset is a collection of around 350 molecules whose HOMO and LUMO levels are collected from experimental results in literature. Quantum-chemical calculations are then performed over a range on conformers with each conformer simulated with a range of functionals and basis sets in order to compare measured and calculated properties of the organic semiconductors. The only structural change made was to convert alkyl side chains to methyl groups to decrease calculation time considering that the side chains are added in order to improve solubility and do not significantly change the electronic structure of the molecule. The

HOMO and LUMO levels of each molecule is calculated with GGA BP86<sup>12, 13</sup> as well as hybrids PBE0<sup>18, 19</sup>, B3LYP<sup>12</sup> and M06-2X<sup>20, 21</sup> functionals, all with double- $\zeta$  def2-SVP<sup>14</sup> basis set. The HOPV15 dataset is designed to be representative of a wide range of molecules in the field of OPV and has become somewhat a benchmark for property prediction in this class of molecules.<sup>22</sup> Note that only 220 (180 for training and validation, and 40 for testing) molecules were used in this work: the molecules used in dye-sensitized solar cells (DSSCs), without HOMO or LUMO level reported or without relevant SMILES being excluded.

#### *A.4.3.3 'Use-case' dataset*

The 'use-case' dataset consists of 27 donor molecules (26 polymers and 1 small molecule) already reported as efficient donor materials in OPVs. To illustrate the utility of the model, only used, currently commercially available, molecules were considered. The SMILES of polymers correspond to one monomer with the alkyl side chains being simplified by methyl groups to be consistent with the structure generally used in DFT. Note that the level of computation used in DFT varies but that all the simulated HOMO/LUMO were obtained using popular hybrid B3LYP or PBE functionals. The graphic comparison of the model outputs versus DFT results is shown in Figure 5 in the main text. Table 3 in the main text highlights the accuracy obtained with the deep learning model compared to DFT at these levels.

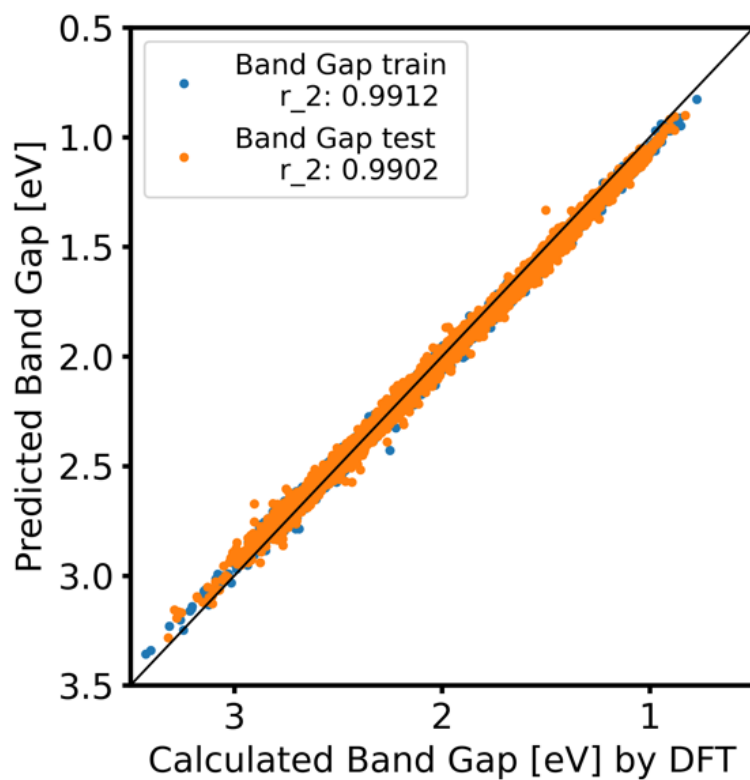


Figure A.4-3 Results of Phase I training where the band gap ( $= \text{LUMO} - \text{HOMO}$ ) predicted by the model is plotted against the band gap predicted by DFT

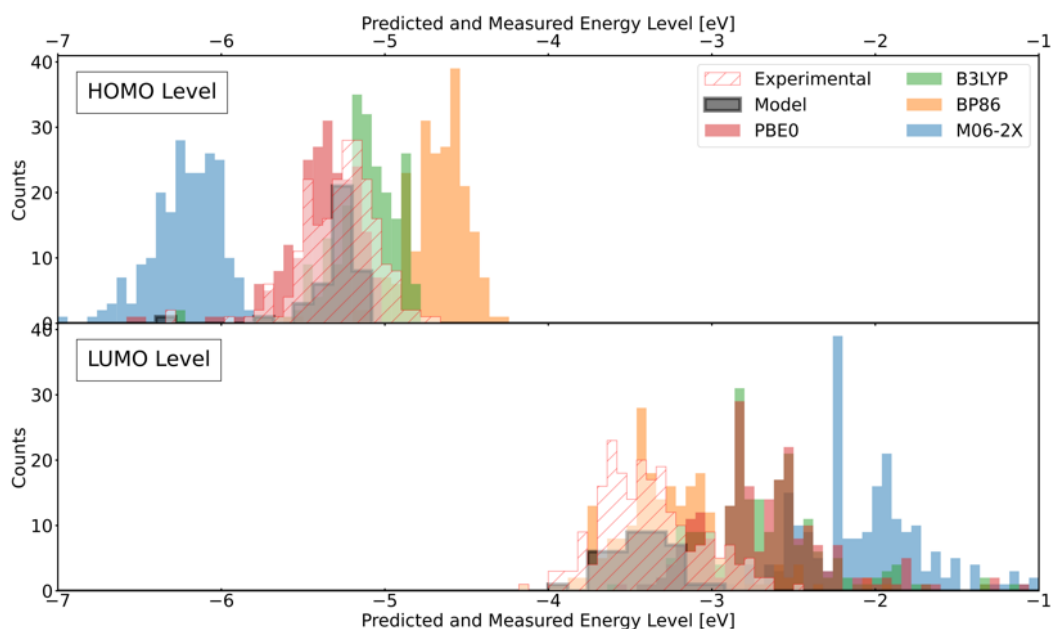


Figure A.4-4 Distribution of HOMO (top) and LUMO (bottom) levels experimentally measured (clear with red lines), predicted by the model (black) and DFT-estimated (colors) of molecules in the test set of the HOPV15 dataset.

Table A.4-2 Molecules in the ‘use-case’ dataset. DFT and experimental HOMO/LUMO values are extracted from literature. Experimental HOMO/LUMO values were determined by cyclic voltammetry (CV). Predicted HOMO/LUMO energy levels correspond to the outputs of the deep learning model after fine-tuning (phase II). Note that the entries 28 to 33 were not included in the validation of the model (Figure 5) as no corresponding DFT value was found in literature.

	Name	CAS	SMILES	HOMO (eV) (CV/model/DFT)	LUMO (eV) (CV/model/DFT)	DFT Level	Ref (CV, DFT)
1	P3HT	104934-50-1	<chem>Cc1csc1</chem>	-5.0/-4.88/-4.58	-3.0/-3.02/-2.08	B3LYP/CEP-3	23
2	PDCBT	1609536-17-5	<chem>O=C(OC)c1c(c2cccs2)sc(c3cc(C(OC)=O)c(c4cccs4)s3)c1</chem>	-5.1/-5.20/-4.87	-3.2/-3.34/-2.52	B3LYP/6-31G(d)	24, 25
3	PNTz4T	1357999-94-0	<chem>Cc1c(c2cccs2)sc(c3c(nsn4)c4c5cc(c6sc(c7cccs7)c(C)c6)c(nsn8)c8c5c3)c1</chem>	-5.16/-5.32/-5.08	-3.77/-3.69/-3.05	B3LYP/6-31G(d)	26, 27
4	DPP-DTT (PDPP2T- TT-OD)	1260685-66-2	<chem>CN1C(C2=C(N(C(C2=C1c3sc(c4sc5ccsc5c4)cc3)=O)C)c6sccc6)=O</chem>	-5.2/-5.24/-4.65	-3.5/-3.60/-2.94	B3LYP/6-31G	28, 29
5	PDPPTPT	1255939-39-9	<chem>CN1C(C2=C(c3cccs3)N(C)C(C2=C1c4cc(c5cccc5)s4)=O)=O</chem>	-5.35/-5.32/-4.29	-3.53/-3.65/-3.48	PBE	30, 31
6	PDPP3T	1198291-01-8	<chem>CN1C(C2=C(N(C(C2=C1c3sc(c4sccc4)c(c3)=O)C)c5sccc5)=O</chem>	-5.17/-5.25/-5.67	-3.61/-3.59/-3.29	B3LYP/6-31G(d)	32, 33
7	PDPP4T	1267540-03-3	<chem>CN1C(C2=C(N(C(C2=C1c3sc(c4sc(c5sc(c5)cc4)cc3)=O)C)c6sccc6)=O</chem>	-5.32/-5.24/-4.39	-3.87/-3.61/-3.61	DMol3 program	34
8	PBDTTT- CF	1379592-65-0	<chem>FC1=C(C(C)=O)Sc2c1c(c(c3)sc4c3c(OC)c(ccc5)c5c4OC)sc2</chem>	-5.22/-5.17/-5.02	-3.45/-3.63/-2.8	B3LYP/6-31G(d)	35, 36
9	PTB7	1266549-31-8	<chem>FC(c1c(c2cc3c(OC)c4sccc4c(OC)c3s2)sc(c1S5)=C5C(OC)=O</chem>	-5.15/-5.17/-5.2	-3.31/-3.56/-2.8	B3LYP/6-31G(d)	37, 38
10	PBDTTT- EFT (PTB7- Th, PCE10))	1469791-66-9	<chem>Cc1sc(c(c(sc(c2scc3c2C(F)=C(C(OC)=O)S3)c4)c4c5c6sc(C)cc6)c7c5scc7)cc1</chem>	-5.15/-5.15/-5.2	-3.34/-3.45/-3.6	B3LYP/6-31G(d, p)	39, 40
11	PfBT4T- 2OD (PCE11)	1644164-62-4	<chem>Cc1c(c2sccc2)sc(c(c(F)c(F)c3c4sc(c5scc5)c(C)c4)c6c3nsn6)c1</chem>	-5.34/-5.28/-4.66	-3.69/-3.56/-3.38	PBE	41, 42
12	PBDTT- DPP	1380582-98-8	<chem>Cc1ccc(c2c3sc(c4cc(C(N(C(C5=C(c6ccc6)N7C)=O)C)=C5C7=O)sc4)cc3c(c8ccc(C)s8)c9sccc29)s1</chem>	-5.30/-5.09/-4.89	-3.63/-3.41/-2.74	B3LYP-D3(BJ) )/def2-SVP	43, 44



1	PBDTTPD	1223479-75-1	O=C(N1C)c2c(C1=O)csc2c(c3)sc4c3c(O	-5.56/-5.45/-5.25	-3.75/-3.73/-2.9	B3LYP/6-31G(d)	45, 36
3	(PBDT(EH)-TPD(Oct))		C)c(scc5)c5c4OC				
1	PBDTTTPD	1426534-44-2	O=C(N1C)c2c(C1=O)csc2c3cc4c(c5ccc(C)s5)c6sccc6c(c7ccc(C)s7)c4s3	-5.49/-5.37/-5.13	-3.47/-3.68/-3.26	B3LYP/6-31G(d)	46, 47
4	(PBDTT(EH)-TPD(Oct))						
1	PCDTBT	958261-50-2	Cn(c1c2cccc1)c3c2ccc(c4sc(c(ccc5c6scc6)c7c5nsn7)cc4)c3	-5.45/-5.36/-4.98	-3.60/-3.53/-2.57	B3LYP/6-31G(d)	48
5							
1	PDPP4T-2F	<a href="https://www.os-sila.com/products/pdpp4t-2f">https://www.os-sila.com/products/pdpp4t-2f</a>	CN1C(C2=C(c3cccs3)N(C)C(C2=C1c4ccc(c5cc(F)c(c6c(F)ccs6)s5)s4)=O)=O	-5.22/-5.23/-4.50	-3.66/-3.65/-3.73	DMol3 program	49, 34
6	(PDQT-2F)						
1	F8T2	210347-56-1	Cc(c1c2cccc1)(C)c3c2ccc(c4sc(c5sccc5)cc4)c3	-5.5/-5.37/-5.09	-3.1/-3.11/-1.84	B3LYP/3-21G**	50, 51
7							
1	MEH-PPV	138184-36-8	C=Cc1c(OC)ccc(OC)c1	-5.3/-5.17/-4.74	-3/-3.02/-2.03	B3LYP/6-31G(d)	52, 53
8							
1	PCPDTBT	920515-34-0	CC(c1c2sc(c3c(nsn4)c4ccc3)c1)(C)c5c2scc5	-5.3/-5.45/-4.53	-3.55/-3.63/-2.93	B3LYP/6-31G(d)	54, 36
9							
2	PDTSTPD	1279109-93-1	C[Si]1(C)c2cc(c3c(C4=O)c(C(N4C)=O)cs3)sc2c5sccc15	-5.57/-5.47/-5.49	-3.88/-3.71/-3.70	PBE0/6-31G(d)	55, 56
0							
2	DTS(FBTTh2)2	1402460-84-7	C[Si]1(C)c2cc(c3c(F)cc(c4ccc(c5sc(C)cc5)s4)c6nsnc36)sc2c7sc(c8c(F)cc(c9ccc(c%10sc(C)cc%10)s9)c%11nsnc8%11)cc17	-5.12/-5.12/-4.95	-3.34/-3.35/-3.02	B3LYP/6-311G*	57, 58
2	TQ1 (PTQ1)	565228-37-7	COc1cc(c(n2)c(c3cccc(OC)c3)nc4c2c(c5sccc5)ccc4)ccc1	-5.5/-5.52/-5.12	-3.8/-3.34/-2.34	B3LYP/6-31G(d)	59
2	PPDT2FBT	1620673-07-5	Fe1c(F)c(c2cccs2)c3nsnc3c1c4ccc(c5c(OC)ccc(OC)c5)s4	-5.41/-5.33/-5.09	-3.65/-3.57/-2.60	B3LYP/6-31G**	60
3	(PCE9.3, FBT))						
2	FTAZ	<a href="https://lumtec.com.tw/product-view.php?ID=786">https://lumtec.com.tw/product-view.php?ID=786</a>	Cc1c2ccsc2c(C)c3c1sc(c4sc(c5c6=NN(C)N=c6c(c7sccc7)c(F)c5F)cc4)c3	-5.38/-5.33/-5.28	-3.17/-3.43/-2.54	B3LYP/6-311+G(d)	61, 62
4							
2	J51	1393529-03-7	Cc1cccc(c2c3sc(c4ccc(c5c(F)c(F)c6cccs6)c7c5=NN(N=7)C)s4)cc3c(c8ccc(C)s8)c9c2ccs9)s1	-5.29/-5.19/-4.8	-3.30/-3.39/-2.49	B3LYP/6-31G(d, p)	63, 64
5							

2 6	J71	2035466-89-6	<chem>C[Si](C)(C)c1sc(c2c3ccsc3c(c4sc([Si](C)(C)cc4)c5c2sc(c6sc(c7c8=NN(C)N=c8c(c9sccc9)c(F)c7F)cc6)c5)cc1</chem>	-5.28/-5.26/-4.80	-3.33/-3.46/-2.45	B3LYP/6-31G(d)	65
2 7	PBT-TTz (PTZ1)	2029196-34-5	<chem>Cc1sc(c2c3ccsc3c(c4sc(C)cc4)c5c2sc(c6sc(c7sc8nc(c9scc(C)c9)sc8n7)cc6C)c5)cc1</chem>	-5.41/-5.32/-4.88	-3.46/-3.16/-2.51	B3LYP/6-31G(d,p)	66
2 8	F8TBT	891911-18-5	<chem>Cc(C)(c1c2ccc(c3c(C)cc(c4ccc(c5cc(C)c5)c6nsnc46)s3)c1)c7c2cccc7</chem>	-5.28/-5.38/*	-3.48/-3.61/*	*	67
2 9	PSBTBT	1089687-02-4	<chem>C[Si](c1c2sc(c3c(nsn4)c4ccc3)c1)(C)c5c2scc5</chem>	-5.05/-5.33/*	-3.27/-3.65/*	*	68
3 0	PTO2 (PE12)	<a href="https://www.os-sila.com/products/pto2">https://www.os-sila.com/products/pto2</a>	<chem>Cc1c(F)cc(c2c3sc(c4cc(C(OC)=O)cs4)cc3c(c5cc(F)c(C)s5)c6sccc26)s1</chem>	-5.59/-5.16/*	-3.67/-3.35/*	*	69
3 1	PTQ10	2270233-86-6	<chem>COc1cnc2cc(F)c(F)c(c3cccs3)c2n1</chem>	-5.54/-5.56/*	-2.98/-3.46/*	*	70
3 2	TPD-3F	2499690-26-3	<chem>O=C(c1c(c2ccc(c3cc4c(c(c5cc(F)c(C)s5)c(ccs6)c6c4c7cc(F)c(C)s7)s3)s2)sc(c8ccc(s8)c1C9=O)N9C</chem>	-5.62/-5.51/*	-3.73/-3.75/*	*	71
3 3	PTFBDT-BZS	1840869-86-4	<chem>COc1c(c2cccs2)c3nsnc3c(c4ccc(c5cc6c(c(c7cc(F)c(C)c(F)c7)c(ccs8)c8c6c9cc(F)c(C)c(F)c9)s5)s4)c1OC</chem>	-5.5/-5.24/*	-3.69/-3.47/*	*	72

List of building-blocks in HOPV15 training set that are also in 'use-case' dataset.

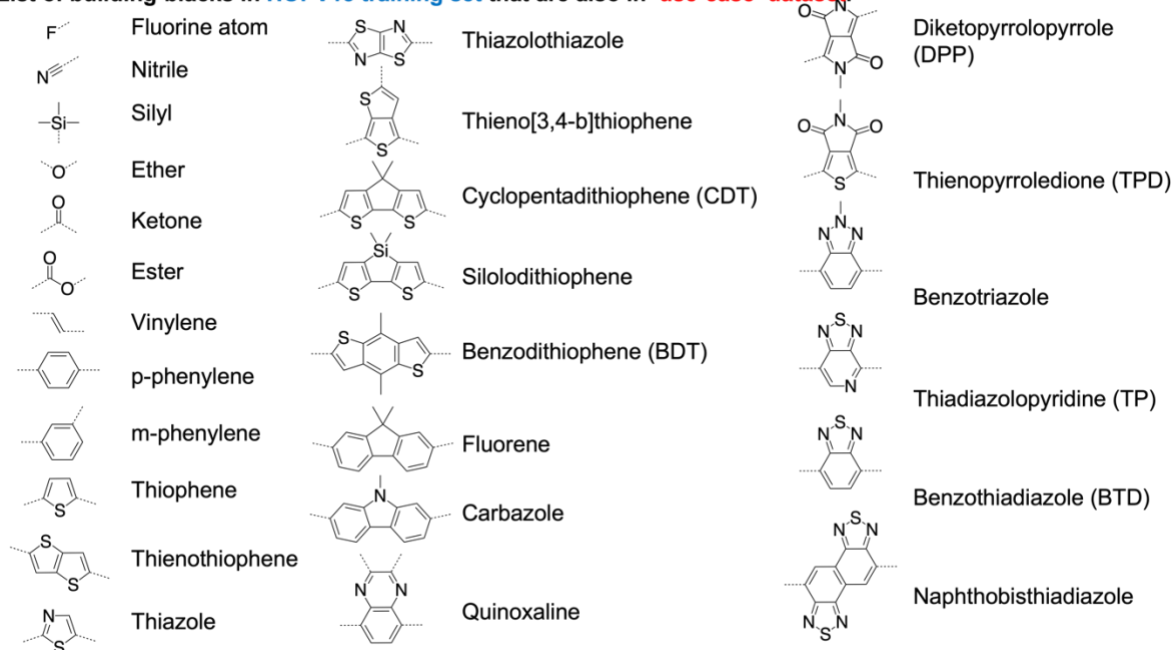


Figure A.4-5 Molecular building blocks present in both the HOPV15 training set and 'use-case' datasets. This gives an idea of the boundaries of the model predictability, in terms of molecule types.

Table A.4-3 Other commercially available molecules with experimental HOMO/LUMO values reported. Compared to Table A.3-2, the molecules in Table A.3-3 are partly composed of atoms/building blocks not represented in the HOPV15 training set, hence explaining why the predictions are not as good as for the molecules, entirely represented, of Table A.3-2.

	Name	CAS	SMILES	HOMO (eV) (CV/model/DFT)	LUMO (eV) (CV/model/DFT)	DFT Level	Ref (CV, DFT)
1	PBDB-T (PCE12)	1415929-80-4	<chem>Cc1ccc(c2c3sc(c4ccc(c5c6c(C(c7c(C)sc(C)c7C6=O)=O)c(c8cccs8)s5)s4)cc3c(c9ccc(C)s9)c%10sccc2%10)s1</chem>	-5.27/-5.33/-4.93	-3.48/-2.92/-2.30	B3LYP/6-31G(d)	73, 74
2	PBDB-T-SF (PCE13)	<a href="https://www.ossila.com/products/pbdb-t-sf">https://www.ossila.com/products/pbdb-t-sf</a>	<chem>Fc1cc(c2c3cc(c4ccc(c5c6c(C(c7c(C)sc(C)c7C6=O)=O)c(c8cccs8)s5)s4)sc3c(c9cc(F)c(SC)s9)c%10c2sc(c%10)sc1SC</chem>	-5.4/-5.16/-	-3.6/-3.63/-		75
3	PBDB-T-2F (PM6)	1802013-83-7	<chem>Cc1sc(c2c(ccs3)c3c(c4sc(C)c(F)c4)c5c2sc(c6sc(c7sc(c8sccc8)c(C(c9c%10c(C)sc9C)=O)c7C%10=O)cc6)c5)cc1F</chem>	-5.45/-5.19/-5.16	-3.65/-3.52/-2.77	B3LYP/6-31G(d,p)	76, 77
4	PBDB-T-2Cl (PM7)	2239295-71-5	<chem>Cc1c(Cl)cc(c2c3sc(c4ccc(c5c6c(C(c7c(C)sc(C)c7C6=O)=O)c(c8cccs8)s5)s4)cc3c(c9cc(Cl)c(C)s9)c%10sccc2%10)s1</chem>	-5.52/-5.15/-	-3.57/-3.58/-		78
5	PBDD4T (PBT1)	1439937-09-3	<chem>Cc1sc(C)c(C(c2c3c(c4cc(C)c(c5ccs5)s4)sc2c6cc(C)c(c7sccc7)s6)=O)c1C3=O</chem>	-5.30/-5.12/-	-3.54/-3.41/-		79
6	PBDD4T-2F	1890205-85-2	<chem>Cc1sc(C)c(C(c2c3c(c4cc(C)c(c5cc(F)cs5)s4)sc2c6cc(C)c(c7scc(F)c7)s6)=O)c1C3=O</chem>	-5.39/-5.16/-	-3.63/-3.40/-		79
7	DRCN5T	1674394-69-4	<chem>CCN(C/1=O)/C(SC1=C/c2sc(c3sc(c4sc(c5sc(c6sc(/C=C7S/C(N(C\7=O)CC)=C(C#N)\C#N)cc6C)cc5C)cc4)c(C)c3)c(C)c2)=C(C#N)/C#N</chem>	-5.22/-5.41/-5.14	-3.41/-3.65/-3.12	B3LYP/6-31G*	80
8	D18 (PCE18)	2433725-54-1	<chem>Cc1c(F)cc(c2c3sc(c4ccc(c5cc6c(c7c(c8nsnc86)cc(c9cccs9)s7)s5)s4)cc3c(c%10cc(F)c(C)s%10)c%11sccc2%11)s1</chem>	-5.51/-5.22/-4.94	-2.77/-3.40/2.59	B3LYP/6-31G(d)	81, 82
9	D18-Cl	<a href="https://www.ossila.com/products/d18-cl">https://www.ossila.com/products/d18-cl</a>	<chem>Cc1sc(c(c(sc(c2sc(c3sc4c5sc(c6sc6)cc5c(nsn7)c7c4c3)cc2)c8)c8c9c%10sc(C)c(Cl)c%10)c%11c9scc%11)cc1Cl</chem>	-5.56/-5.15/-	-2.78/-3.40/-		83

1 0	PCITO2	<a href="https://www.ossila.com/products/pclto2">https://www.ossila.com/products/pclto2</a>	<chem>Cc1sc(c(c(sc2ccc(C(OC)=O)c2)c3)c3c4c5sc(C)c(Cl)c5)c6c4scc6)cc1Cl</chem>	-5.66/-5.13/-	-3.41/-3.35/-	84
1 1	PBDTS-TDZ	<a href="https://www.sigmaaldrich.com/CH/en/product/aldrich/901871?context=product">https://www.sigmaaldrich.com/CH/en/product/aldrich/901871?context=product</a>	<chem>CSc1sc(c2c3ccc3c(c4sc(SC)cc4)c5c2sc(c6sc(c7sc(c8ccc(C)c8)nn7)c6C)c5)cc1</chem>	-5.39/-5.27/-	-2.79/-3.32/-	85
1 2	J61	1887136-03-9	<chem>Fc1c(F)c(c2cccc2)c3=NN(C)N=c3c1c4sc(c5cc6c(c7sc(SC)cc7)c8scc8c(c9sc(SC)cc9)c6s5)cc4</chem>	-5.32/-5.18/-4.82	-3.08/-3.31/-2.69	B3LYP/6-31G(d) 86, 87
1 3	PIT2FBT	2055007-82-2	<chem>CC1(C)c2cc(c3c(F)c(F)cc4nsnc34)sc2c5cc(c6sccc6)ccc51</chem>	-5.54/-5.30/-	-3.66/-3.53/-	88
1 4	PDTBDT-FBTz	<a href="https://www.1-material.com/wp-content/uploads/2017/08/1M-NFA-OPV-highlight-20170819.pdf">https://www.1-material.com/wp-content/uploads/2017/08/1M-NFA-OPV-highlight-20170819.pdf</a>	<chem>Cc1sc(c2c(sc3c4sc(c5c(=NN(C)N=6)c6ccc(F)c5F)c3)c4c(c7sc(C)c(C)c7)c8sc9ccsc9c82)cc1C</chem>	-5.47/-5.34/-	-3.25/-3.67/-	89
1 5	PDTBDT-FBT	1919055-55-2	<chem>Cc1sc(c2c(sc3c4sc(c5c(nsn6)c6ccc(F)c5F)c3)c4c(c7sc(C)c(C)c7)c8sc9ccsc9c82)cc1C</chem>	-5.51/-5.33/-	-3.54/-3.66/-	89
1 6	PDBT-T1	1701403-91-9	<chem>Cc1ccc(c(c(sc2cc(c3cc(c4c(C(c5c(C)sc(C)c5C6=O)=O)c6c(c7cccs7)s4)sc3)sc28)c8c9c%10ccc(C)s%10)c%11c9sc%12c%11sec%12)s1</chem>	-5.36/-5.16/-	-3.43/-3.33/-	90

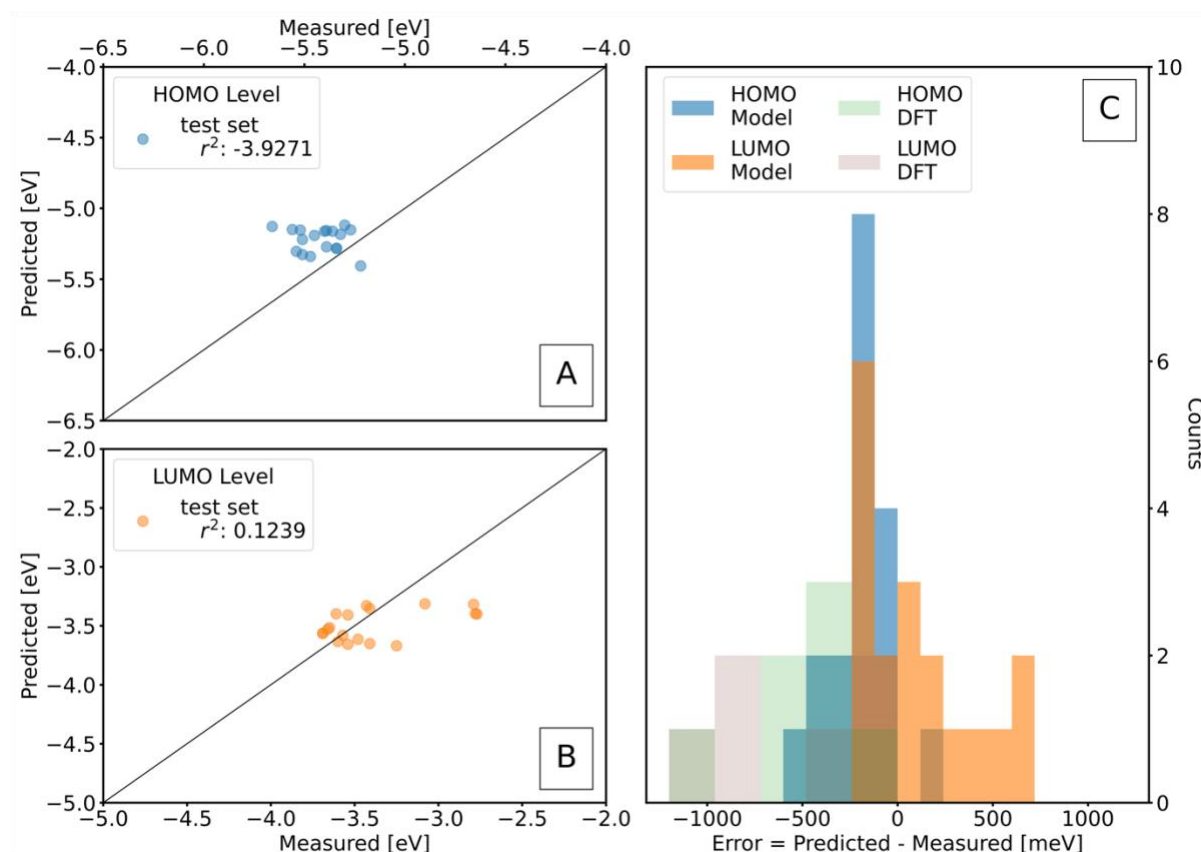


Figure A.4-6 Results of testing the deep learning model on the ‘use-case’ dataset plus the molecules reported in Table S2 that are partly composed of atoms/building blocks not represented in the HOPV15 training set. Deviation of the (a) HOMO and (b) LUMO levels predicted compared to the experimental values. (c) Distribution of the prediction errors for the values outputted by the model (Model) and the values calculated by DFT extracted from literature (DFT).

Table A.4-4 Comparison of the results of the model and published DFT of molecules from the ‘use-case’ testing dataset plus the molecules reported in Table S2 that are partly composed of atoms/building blocks not represented in the HOPV15 training set. The table shows SEP and RMSE of the HOMO, LUMO levels and the band gap (= LUMO - HOMO).

Method	HOMO (meV) [SEP / RMSE]	LUMO (meV) [SEP / RMSE]	Gap (meV) [SEP / RMSE]
Model	155 / 249	278 / 290	318 / 435
DFT	172 / 334	225 / 423	357 / 353

## References

1. Simonyan, K.; Zisserman, A., Very Deep Convolutional Networks for Large-Scale Image Recognition. *arXiv pre-print server* **2015**.
2. Abien, Deep Learning using Rectified Linear Units (ReLU). *arXiv pre-print server* **2019**.
3. Narayan, S., The generalized sigmoid activation function: Competitive supervised learning. *Information Sciences* **1997**, 99 (1), 69-82.
4. Bisong, E., Google Colaboratory. Apress: 2019; pp 59-64.
5. Ufimtsev, I. S.; Martinez, T. J., Quantum Chemistry on Graphical Processing Units. 1. Strategies for Two-Electron Integral Evaluation. *J Chem Theory Comput* **2008**, 4 (2), 222-31.
6. Martín Abadi, A. A., Paul Barham, Eugene Brevdo,; Zhifeng Chen, C. C., Greg S. Corrado, Andy Davis,; Jeffrey Dean, M. D., Sanjay Ghemawat, Ian Goodfellow,; Andrew Harp, G. I., Michael Isard, Rafal Jozefowicz, Yangqing Jia,; Lukasz Kaiser, M. K., Josh Levenberg, Dan Mané, Mike Schuster,; Rajat Monga, S. M., Derek Murray, Chris Olah, Jonathon Shlens,; Benoit Steiner, I. S., Kunal Talwar, Paul Tucker,; Vincent Vanhoucke, V. V., Fernanda Viégas,; Oriol Vinyals, P. W., Martin Wattenberg, Martin Wicke,; Yuan Yu, a. X. Z., TensorFlow: Large-scale machine learning on heterogeneous systems. In *12th USENIX Symposium on Operating Systems Design and Implementation (OSDI '16)*, Savannah, GA, USA, 2015.
7. Antonio, G.; Sujit, P., *Deep learning with Keras*. Packt Publishing Ltd: 2017.
8. Hachmann, J.; Olivares-Amaya, R.; Atahan-Evrenk, S.; Amador-Bedolla, C.; Sánchez-Carrera, R. S.; Gold-Parker, A.; Vogt, L.; Brockway, A. M.; Aspuru-Guzik, A., The Harvard Clean Energy Project: Large-Scale Computational Screening and Design of Organic Photovoltaics on the World Community Grid. *The Journal of Physical Chemistry Letters* **2011**, 2 (17), 2241-2251.
9. Pron, A.; Rannou, P., Processible conjugated polymers: from organic semiconductors to organic metals and superconductors. *Prog. Polym. Sci.* **2002**, 27 (1), 135-190.
10. Facchetti, A.,  $\pi$ -Conjugated Polymers for Organic Electronics and Photovoltaic Cell Applications. *Chemistry of Materials* **2011**, 23 (3), 733-758.
11. Koch, W.; Holthausen, M. C., *A chemist's guide to density functional theory*. John Wiley & Sons: 2015.
12. Becke, A. D., Density-functional exchange-energy approximation with correct asymptotic behavior. *Physical Review A* **1988**, 38 (6), 3098-3100.
13. Perdew, J. P., Density-functional approximation for the correlation energy of the inhomogeneous electron gas. *Physical Review B* **1986**, 33 (12), 8822-8824.
14. Weigend, F.; Ahlrichs, R., Balanced basis sets of split valence, triple zeta valence and quadruple zeta valence quality for H to Rn: Design and assessment of accuracy. *Physical Chemistry Chemical Physics* **2005**, 7 (18), 3297-3305.
15. Weininger, D., SMILES, a chemical language and information system. 1. Introduction to methodology and encoding rules. *Journal of chemical information and computer sciences* **1988**, 28 (1), 31-36.
16. G, L. RDKit: Open-source. <http://www.rdkit.org> (accessed 09/09/2021).
17. Lopez, S. A.; Pyzer-Knapp, E. O.; Simm, G. N.; Lutzow, T.; Li, K.; Seress, L. R.; Hachmann, J.; Aspuru-Guzik, A., The Harvard organic photovoltaic dataset. *Scientific Data* **2016**, 3 (1), 160086.
18. Perdew, J. P.; Burke, K.; Ernzerhof, M., Generalized gradient approximation made simple. *Physical review letters* **1996**, 77 (18), 3865.

19. Perdew, J. P.; Ernzerhof, M.; Burke, K., Rationale for mixing exact exchange with density functional approximations. *The Journal of chemical physics* **1996**, *105* (22), 9982-9985.
20. Zhao, Y.; Truhlar, D. G., The M06 suite of density functionals for main group thermochemistry, thermochemical kinetics, noncovalent interactions, excited states, and transition elements: two new functionals and systematic testing of four M06-class functionals and 12 other functionals. *Theoretical chemistry accounts* **2008**, *120* (1), 215-241.
21. Zhao, Y.; Truhlar, D. G., Density functionals for noncovalent interaction energies of biological importance. *Journal of Chemical Theory and Computation* **2007**, *3* (1), 289-300.
22. Meftahi, N.; Klymenko, M.; Christofferson, A. J.; Bach, U.; Winkler, D. A.; Russo, S. P., Machine learning property prediction for organic photovoltaic devices. *npj Computational Materials* **2020**, *6* (1).
23. Minkler, M. J.; Kim, J.; Lawson, K. E.; Ali, A.; Zhao, R.; Adamczyk, A. J.; Beckingham, B. S., Solution processible statistical poly(3-methoxythiophene)-co-poly(3-hexylthiophene) copolymer. *Materials Letters* **2019**, *256*, 126563.
24. Do Kim, H.; Shimizu, R.; Ohkita, H., Ternary Blend Polymer Solar Cells Based on Wide-bandgap Polymer PDCBT and Low-bandgap Polymer PTB7-Th. *Chemistry Letters* **2018**, *47* (8), 1059-1062.
25. Wang, Q.; Li, M.; Zhang, X.; Qin, Y.; Wang, J.; Zhang, J.; Hou, J.; Janssen, R. A. J.; Geng, Y., Carboxylate-Substituted Polythiophenes for Efficient Fullerene-Free Polymer Solar Cells: The Effect of Chlorination on Their Properties. *Macromolecules* **2019**, *52* (12), 4464-4474.
26. Osaka, I.; Shimawaki, M.; Mori, H.; Doi, I.; Miyazaki, E.; Koganezawa, T.; Takimiya, K., Synthesis, Characterization, and Transistor and Solar Cell Applications of a Naphthobisthiadiazole-Based Semiconducting Polymer. *Journal of the American Chemical Society* **2012**, *134* (7), 3498-3507.
27. Rasool, S.; Hoang, Q. V.; Van Vu, D.; Trang Bui, T. T.; Jin, S.-M.; Ho, T. T.; Song, C. E.; Lee, H. K.; Lee, S. K.; Lee, J.-C.; Moon, S.-J.; Lee, E.; Shin, W. S., High-efficiency non-halogenated solvent processable polymer/PCBM solar cells via fluorination-enabled optimized nanoscale morphology. *Journal of Materials Chemistry A* **2019**, *7* (43), 24992-25002.
28. Li, J.; Zhao, Y.; Tan, H. S.; Guo, Y.; Di, C.-A.; Yu, G.; Liu, Y.; Lin, M.; Lim, S. H.; Zhou, Y.; Su, H.; Ong, B. S., A stable solution-processed polymer semiconductor with record high-mobility for printed transistors. *Scientific Reports* **2012**, *2* (1).
29. Yang, F.; Li, C.; Zhang, J.; Feng, G.; Wei, Z.; Li, W., Methylated conjugated polymers based on diketopyrrolopyrrole and dithienothiophene for high performance field-effect transistors. *Organic Electronics* **2016**, *37*, 366-370.
30. Bijleveld, J. C.; Gevaerts, V. S.; Di Nuzzo, D.; Turbiez, M.; Mathijssen, S. G. J.; De Leeuw, D. M.; Wienk, M. M.; Janssen, R. A. J., Efficient Solar Cells Based on an Easily Accessible Diketopyrrolopyrrole Polymer. *Advanced Materials* **2010**, *22* (35), E242-E246.
31. Shen, P.; Wang, H.; Liao, P.; Wang, L., Electronic properties of donor:acceptor complexes in all-polymer solar cells based on density functional theory. *Journal of Physics D: Applied Physics* **2021**, *54* (19), 195301.
32. Dubey, A.; Adhikari, N.; Venkatesan, S.; Gu, S.; Khatiwada, D.; Wang, Q.; Mohammad, L.; Kumar, M.; Qiao, Q., Solution processed pristine PDPP3T polymer as hole transport layer for efficient perovskite solar cells with slower degradation. *Solar Energy Materials and Solar Cells* **2016**, *145*, 193-199.
33. Pan, J.; Yin, H.; Xie, Y.-Z.; Sun, G.-Y.; Su, Z.-M., The conversion of donor to acceptor and rational design for diketopyrrolopyrrole-containing small molecule acceptors by introducing nitrogen-atoms for organic solar cells. *RSC Advances* **2017**, *7* (51), 31800-31806.

34. Rasool, S.; Hoang, Q. V.; Vu, D. V.; Song, C. E.; Lee, H. K.; Lee, S. K.; Lee, J.-C.; Moon, S.-J.; Shin, W. S., High-efficiency single and tandem fullerene solar cells with asymmetric monofluorinated diketopyrrolopyrrole-based polymer. *Journal of Energy Chemistry* **2022**, *64*, 236-245.
35. Chen, H.-Y.; Hou, J.; Zhang, S.; Liang, Y.; Yang, G.; Yang, Y.; Yu, L.; Wu, Y.; Li, G., Polymer solar cells with enhanced open-circuit voltage and efficiency. *Nature Photonics* **2009**, *3* (11), 649-653.
36. Risko, C.; McGehee, M. D.; Brédas, J.-L., A quantum-chemical perspective into low optical-gap polymers for highly-efficient organic solar cells. *Chem. Sci.* **2011**, *2* (7), 1200-1218.
37. He, Z.; Zhong, C.; Su, S.; Xu, M.; Wu, H.; Cao, Y., Enhanced power-conversion efficiency in polymer solar cells using an inverted device structure. *Nature Photonics* **2012**, *6* (9), 591-595.
38. Park, S.; Jeong, J.; Hyun, G.; Kim, M.; Lee, H.; Yi, Y., The origin of high PCE in PTB7 based photovoltaics: proper charge neutrality level and free energy of charge separation at PTB7/PC71BM interface. *Scientific Reports* **2016**, *6* (1), 35262.
39. Li, C.; Yue, Q.; Wu, H.; Li, B.; Fan, H.; Zhu, X., Small bandgap non-fullerene acceptor enables efficient PTB7-Th solar cell with near 0 eV HOMO offset. *Journal of Energy Chemistry* **2021**, *52*, 60-66.
40. Aboulouard, A.; Mtougui, S.; Demir, N.; Moubarik, A.; Idrissi, M. E.; Can, M., New non-fullerene electron acceptors-based on quinoxaline derivatives for organic photovoltaic cells: DFT computational study. *Synthetic Metals* **2021**, *279*, 116846.
41. Liu, Y.; Zhao, J.; Li, Z.; Mu, C.; Ma, W.; Hu, H.; Jiang, K.; Lin, H.; Ade, H.; Yan, H., Aggregation and morphology control enables multiple cases of high-efficiency polymer solar cells. *Nature Communications* **2014**, *5* (1), 5293.
42. Boschetto, G.; Xue, H.-T.; Dziedzic, J.; Krompiec, M.; Skylaris, C.-K., Effect of Polymerization Statistics on the Electronic Properties of Copolymers for Organic Photovoltaics. *The Journal of Physical Chemistry C* **2017**, *121* (5), 2529-2538.
43. Dou, L.; You, J.; Yang, J.; Chen, C.-C.; He, Y.; Murase, S.; Moriarty, T.; Emery, K.; Li, G.; Yang, Y., Tandem polymer solar cells featuring a spectrally matched low-bandgap polymer. *Nature Photonics* **2012**, *6* (3), 180-185.
44. Zhuang, W.; Wang, S.; Tao, Q.; Ma, W.; Berggren, M.; Fabiano, S.; Zhu, W.; Wang, E., Synthesis and Electronic Properties of Diketopyrrolopyrrole-Based Polymers with and without Ring-Fusion. *Macromolecules* **2021**, *54* (2), 970-980.
45. Zou, Y.; Najari, A.; Berrouard, P.; Beaupré, S.; Réda Aïch, B.; Tao, Y.; Leclerc, M., A Thieno[3,4-c]pyrrole-4,6-dione-Based Copolymer for Efficient Solar Cells. *Journal of the American Chemical Society* **2010**, *132* (15), 5330-5331.
46. Kim, T.; Kim, J.-H.; Kang, T. E.; Lee, C.; Kang, H.; Shin, M.; Wang, C.; Ma, B.; Jeong, U.; Kim, T.-S.; Kim, B. J., Flexible, highly efficient all-polymer solar cells. *Nature Communications* **2015**, *6* (1), 8547.
47. Xie, X.-H.; Zhao, X.-W.; Li, M., Theoretical Study on the Photoelectric Properties of a Class of Copolymers Based on Benzodithiophene for Solar Cells. *International Journal of Polymer Science* **2018**, *2018*, 1-11.
48. Blouin, N.; Michaud, A.; Gendron, D.; Wakim, S.; Blair, E.; Neagu-Plesu, R.; Belletête, M.; Durocher, G.; Tao, Y.; Leclerc, M., Toward a Rational Design of Poly(2,7-Carbazole) Derivatives for Solar Cells. *Journal of the American Chemical Society* **2008**, *130* (2), 732-742.
49. Zheng, Z.; Zhang, S.; Zhang, J.; Qin, Y.; Li, W.; Yu, R.; Wei, Z.; Hou, J., Over 11% Efficiency in Tandem Polymer Solar Cells Featured by a Low-Band-Gap Polymer with Fine-Tuned Properties. *Advanced Materials* **2016**, *28* (25), 5133-5138.



50. Huang, J.-H.; Yang, C.-Y.; Ho, Z.-Y.; Kekuda, D.; Wu, M.-C.; Chien, F.-C.; Chen, P.; Chu, C.-W.; Ho, K.-C., Annealing effect of polymer bulk heterojunction solar cells based on polyfluorene and fullerene blend. *Organic Electronics* **2009**, *10* (1), 27-33.
51. Lourenco, O. D.; Benatto, L.; Marchiori, C. F. N.; Avila, H. C.; Yamamoto, N. A. D.; Oliveira, C. K.; Da Luz, M. G. E.; Cremona, M.; Koehler, M.; Roman, L. S., Conformational Change on a Bithiophene-Based Copolymer Induced by Additive Treatment: Application in Organic Photovoltaics. *The Journal of Physical Chemistry C* **2017**, *121* (29), 16035-16044.
52. Lee, S. J.; Li, J.; Lee, S. I.; Moon, C.-B.; Kim, W. Y.; Cao, J.; Jhun, C. G., Effects of MEH-PPV Molecular Ordering in the Emitting Layer on the Luminescence Efficiency of Organic Light-Emitting Diodes. *Molecules* **2021**, *26* (9), 2512.
53. Xie, X.; Liu, X.; Zeng, D.; Zhao, L., The Potentials in Solar Cells for MEH-PPV Derivatives: Molecular Design and Performance Prediction. *Bulletin of the Korean Chemical Society* **2020**, *41* (7), 719-726.
54. Mühlbacher, D.; Scharber, M.; Morana, M.; Zhu, Z.; Waller, D.; Gaudiana, R.; Brabec, C., High Photovoltaic Performance of a Low-Bandgap Polymer. *Advanced Materials* **2006**, *18* (21), 2884-2889.
55. Chu, T.-Y.; Lu, J.; Beaupré, S.; Zhang, Y.; Pouliot, J.-R.; Wakim, S.; Zhou, J.; Leclerc, M.; Li, Z.; Ding, J.; Tao, Y., Bulk Heterojunction Solar Cells Using Thieno[3,4-c]pyrrole-4,6-dione and Dithieno[3,2-b:2',3'-d]silole Copolymer with a Power Conversion Efficiency of 7.3%. *Journal of the American Chemical Society* **2011**, *133* (12), 4250-4253.
56. Liu, X.; He, R.; Shen, W.; Li, M., Molecular design of donor-acceptor conjugated copolymers based on C-, Si- and N-bridged dithiophene and thienopyrroledione derivatives units for organic solar cells. *Journal of Power Sources* **2014**, *245*, 217-223.
57. Van Der Poll, T. S.; Love, J. A.; Nguyen, T.-Q.; Bazan, G. C., Non-Basic High-Performance Molecules for Solution-Processed Organic Solar Cells. *Advanced Materials* **2012**, *24* (27), 3646-3649.
58. Shi, J.; Isakova, A.; Abudulimu, A.; Van Den Berg, M.; Kwon, O. K.; Meixner, A. J.; Park, S. Y.; Zhang, D.; Gierschner, J.; Lüer, L., Designing high performance all-small-molecule solar cells with non-fullerene acceptors: comprehensive studies on photoexcitation dynamics and charge separation kinetics. *Energy & Environmental Science* **2018**, *11* (1), 211-220.
59. Kim, Y.; Yeom, H. R.; Kim, J. Y.; Yang, C., High-efficiency polymer solar cells with a cost-effective quinoxaline polymer through nanoscale morphology control induced by practical processing additives. *Energy & Environmental Science* **2013**, *6* (6), 1909.
60. Uddin, M. A.; Lee, T. H.; Xu, S.; Park, S. Y.; Kim, T.; Song, S.; Nguyen, T. L.; Ko, S.-J.; Hwang, S.; Kim, J. Y.; Woo, H. Y., Interplay of Intramolecular Noncovalent Coulomb Interactions for Semicrystalline Photovoltaic Polymers. *Chemistry of Materials* **2015**, *27* (17), 5997-6007.
61. Zhao, F.; Dai, S.; Wu, Y.; Zhang, Q.; Wang, J.; Jiang, L.; Ling, Q.; Wei, Z.; Ma, W.; You, W.; Wang, C.; Zhan, X., Single-Junction Binary-Blend Nonfullerene Polymer Solar Cells with 12.1% Efficiency. *Advanced Materials* **2017**, *29* (18), 1700144.
62. Zhang, Q.; Yan, L.; Jiao, X.; Peng, Z.; Liu, S.; Rech, J. J.; Klump, E.; Ade, H.; So, F.; You, W., Fluorinated Thiophene Units Improve Photovoltaic Device Performance of Donor-Acceptor Copolymers. *Chemistry of Materials* **2017**, *29* (14), 5990-6002.
63. Li, Y.; Qian, D.; Zhong, L.; Lin, J.-D.; Jiang, Z.-Q.; Zhang, Z.-G.; Zhang, Z.; Li, Y.; Liao, L.-S.; Zhang, F., A fused-ring based electron acceptor for efficient non-fullerene polymer solar cells with small HOMO offset. *Nano Energy* **2016**, *27*, 430-438.
64. Yu, L.; Li, Y.; Wang, Y.; Wang, X.; Cui, W.; Wen, S.; Zheng, N.; Sun, M.; Yang, R., Fuse the  $\pi$ -Bridge to Acceptor Moiety of Donor- $\pi$ -Acceptor Conjugated Polymer: Enabling

an All-Round Enhancement in Photovoltaic Parameters of Nonfullerene Organic Solar Cells. *ACS Applied Materials & Interfaces* **2019**, *11* (34), 31087-31095.

65. Du, M.; Geng, Y.; Ji, H.; Li, G.; Xiao, Y.; Zuo, K.; Liu, Y.; Guo, Q.; Tang, A.; Zhou, E., The optimization of  $\pi$ -bridge for trialkylsilyl substituted D- $\pi$ -A photovoltaic polymers. *Dyes and Pigments* **2021**, *194*, 109609.

66. Zhao, K.; Wang, Q.; Xu, B.; Zhao, W.; Liu, X.; Yang, B.; Sun, M.; Hou, J., Efficient fullerene-based and fullerene-free polymer solar cells using two wide band gap thiophene-thiazolothiazole-based photovoltaic materials. *Journal of Materials Chemistry A* **2016**, *4* (24), 9511-9518.

67. Wang, L.; Pan, C.; Liang, A.; Zhou, X.; Zhou, W.; Wan, T.; Wang, L., The effect of the backbone structure on the thermoelectric properties of donor-acceptor conjugated polymers. *Polymer Chemistry* **2017**, *8* (32), 4644-4650.

68. Hou, J.; Chen, H.-Y.; Zhang, S.; Li, G.; Yang, Y., Synthesis, Characterization, and Photovoltaic Properties of a Low Band Gap Polymer Based on Silole-Containing Polythiophenes and 2,1,3-Benzothiadiazole. *Journal of the American Chemical Society* **2008**, *130* (48), 16144-16145.

69. Yao, H.; Cui, Y.; Qian, D.; Ponseca, C. S.; Honarfar, A.; Xu, Y.; Xin, J.; Chen, Z.; Hong, L.; Gao, B.; Yu, R.; Zu, Y.; Ma, W.; Chabera, P.; Pullerits, T.; Yartsev, A.; Gao, F.; Hou, J., 14.7% Efficiency Organic Photovoltaic Cells Enabled by Active Materials with a Large Electrostatic Potential Difference. *Journal of the American Chemical Society* **2019**, *141* (19), 7743-7750.

70. Sun, C.; Pan, F.; Bin, H.; Zhang, J.; Xue, L.; Qiu, B.; Wei, Z.; Zhang, Z.-G.; Li, Y., A low cost and high performance polymer donor material for polymer solar cells. *Nature Communications* **2018**, *9* (1).

71. Jiang, B.-H.; Wang, Y.-P.; Liao, C.-Y.; Chang, Y.-M.; Su, Y.-W.; Jeng, R.-J.; Chen, C.-P., Improved Blend Film Morphology and Free Carrier Generation Provide a High-Performance Ternary Polymer Solar Cell. *ACS Applied Materials & Interfaces* **2021**, *13* (1), 1076-1085.

72. Li, G.; Gong, X.; Zhang, J.; Liu, Y.; Feng, S.; Li, C.; Bo, Z., 4-Alkyl-3,5-difluorophenyl-Substituted Benzodithiophene-Based Wide Band Gap Polymers for High-Efficiency Polymer Solar Cells. *ACS Applied Materials & Interfaces* **2016**, *8* (6), 3686-3692.

73. Li, X.; Ma, R.; Liu, T.; Xiao, Y.; Chai, G.; Lu, X.; Yan, H.; Li, Y., Fine-tuning HOMO energy levels between PM6 and PBDB-T polymer donors via ternary copolymerization. *Science China Chemistry* **2020**, *63* (9), 1256-1261.

74. Lu, Q.; Qiu, M.; Zhao, M.; Li, Z.; Li, Y., Modification of NFA-Conjugated Bridges with Symmetric Structures for High-Efficiency Non-Fullerene PSCs. *Polymers* **2019**, *11* (6), 958.

75. Zhao, W.; Li, S.; Yao, H.; Zhang, S.; Zhang, Y.; Yang, B.; Hou, J., Molecular Optimization Enables over 13% Efficiency in Organic Solar Cells. *Journal of the American Chemical Society* **2017**, *139* (21), 7148-7151.

76. Zhang, H.; Yao, H.; Hou, J.; Zhu, J.; Zhang, J.; Li, W.; Yu, R.; Gao, B.; Zhang, S.; Hou, J., Over 14% Efficiency in Organic Solar Cells Enabled by Chlorinated Nonfullerene Small-Molecule Acceptors. *Adv. Mater.* **2018**, *30* (28), 1800613.

77. Liu, W.; Liu, Q.; Xiang, C.; Zhou, H.; Jiang, L.; Zou, Y., Theoretical exploration of optoelectronic performance of PM6:Y6 series-based organic solar cells. *Surfaces and Interfaces* **2021**, *26*, 101385.

78. Fan, Q.; Zhu, Q.; Xu, Z.; Su, W.; Chen, J.; Wu, J.; Guo, X.; Ma, W.; Zhang, M.; Li, Y., Chlorine substituted 2D-conjugated polymer for high-performance polymer solar cells with 13.1% efficiency via toluene processing. *Nano Energy* **2018**, *48*, 413-420.

79. Zhang, S.; Qin, Y.; Uddin, M. A.; Jang, B.; Zhao, W.; Liu, D.; Woo, H. Y.; Hou, J., A Fluorinated Polythiophene Derivative with Stabilized Backbone Conformation for Highly Efficient Fullerene and Non-Fullerene Polymer Solar Cells. *Macromolecules* **2016**, *49* (8), 2993-3000.
80. Kan, B.; Li, M.; Zhang, Q.; Liu, F.; Wan, X.; Wang, Y.; Ni, W.; Long, G.; Yang, X.; Feng, H.; Zuo, Y.; Zhang, M.; Huang, F.; Cao, Y.; Russell, T. P.; Chen, Y., A Series of Simple Oligomer-like Small Molecules Based on Oligothiophenes for Solution-Processed Solar Cells with High Efficiency. *Journal of the American Chemical Society* **2015**, *137* (11), 3886-3893.
81. Liu, Q.; Jiang, Y.; Jin, K.; Qin, J.; Xu, J.; Li, W.; Xiong, J.; Liu, J.; Xiao, Z.; Sun, K.; Yang, S.; Zhang, X.; Ding, L., 18% Efficiency organic solar cells. *Science Bulletin* **2020**, *65* (4), 272-275.
82. Li, X.; Xu, J.; Xiao, Z.; Wang, X.; Zhang, B.; Ding, L., Dithieno[3',2':3,4;2'',3'':5,6]benzo[1,2-c][1,2,5]oxadiazole-based polymer donors with deep HOMO levels. *Journal of Semiconductors* **2021**, *42* (6), 060501.
83. Qin, J.; Zhang, L.; Zuo, C.; Xiao, Z.; Yuan, Y.; Yang, S.; Hao, F.; Cheng, M.; Sun, K.; Bao, Q.; Bin, Z.; Jin, Z.; Ding, L., A chlorinated copolymer donor demonstrates a 18.13% power conversion efficiency. *Journal of Semiconductors* **2021**, *42* (1), 010501.
84. Ossila, C. f. <https://www.ossila.com/products/pclto2> (accessed 09/09/2021).
85. Xu, X.; Yu, T.; Bi, Z.; Ma, W.; Li, Y.; Peng, Q., Realizing Over 13% Efficiency in Green-Solvent-Processed Nonfullerene Organic Solar Cells Enabled by 1,3,4-Thiadiazole-Based Wide-Bandgap Copolymers. *Advanced Materials* **2018**, *30* (3), 1703973.
86. Bin, H.; Zhang, Z.-G.; Gao, L.; Chen, S.; Zhong, L.; Xue, L.; Yang, C.; Li, Y., Non-Fullerene Polymer Solar Cells Based on Alkylthio and Fluorine Substituted 2D-Conjugated Polymers Reach 9.5% Efficiency. *Journal of the American Chemical Society* **2016**, *138* (13), 4657-4664.
87. Tang, A.; Xiao, B.; Wang, Y.; Gao, F.; Tajima, K.; Bin, H.; Zhang, Z. G.; Li, Y.; Wei, Z.; Zhou, E., Simultaneously Achieved High Open-Circuit Voltage and Efficient Charge Generation by Fine-Tuning Charge-Transfer Driving Force in Nonfullerene Polymer Solar Cells. *Advanced Functional Materials* **2018**, *28* (6), 1704507.
88. Wang, M.; Wang, Z.; Ma, W.; Chen, S.-C.; Zheng, Q., Indenothiophene-Based Wide Bandgap Copolymer for Polymer Fullerene Solar Cells with 9.01% Efficiency and 1.0 V Open Circuit Voltage. *Advanced Electronic Materials* **2016**, *2* (11), 1600340.
89. Zhong, W.; Xiao, J.; Sun, S.; Jiang, X.-F.; Lan, L.; Ying, L.; Yang, W.; Yip, H.-L.; Huang, F.; Cao, Y., Wide bandgap dithienobenzodithiophene-based  $\pi$ -conjugated polymers consisting of fluorinated benzotriazole and benzothiadiazole for polymer solar cells. *Journal of Materials Chemistry C* **2016**, *4* (21), 4719-4727.
90. Luo, Z.; Xiong, W.; Liu, T.; Cheng, W.; Wu, K.; Sun, Y.; Yang, C., Triphenylamine-cored star-shape compounds as non-fullerene acceptor for high-efficiency organic solar cells: Tuning the optoelectronic properties by S/Se-annulated perylene diimide. *Organic Electronics* **2017**, *41*, 166-172.



# 10 Acknowledgements

I would like to acknowledge and say a special thanks to my supervisor Prof. Dr. Natalie Banerji for firstly accepting me into the FemtoMat group, but mainly for her support, encouragement and time during the last four years. I have particularly appreciated her balance of guidance along with freedom and trust, which has been invaluable to both my scientific and personal development.

I would also like to thank Prof. Dr. Koen Vandewal for being the external examiner for this work as well as Prof. Dr. Prof. Dr. Jean-Louis Reymond for heading the examination.

I am grateful to my BSc. Hons. and MSc. supervisors Prof. Dr. Mmanstae Diale and Dr. Artur Braun whose blind trust and belief kicked off this entire journey.

I would like to extend my sincere thanks to the entire FemtoMat group (both past and present) in general but particularly Julien, Martina, Yufei, Olivier, Rishi, Phillip and Kaila for the scientific interactions and support. I would like to point out Olivier's particular encouragement in the work of Chapter 7, without you the project would still be sitting in a file on my computer. I would also like to specifically thank first Phillip and then Rishi for their particular patience in our invaluable scientific discussions.

On a more personal note, my time here was greatly enriched by the friendships I have made, and for that I would like to especially thank Gonzague, Phillip, Rishi, Olivier and Daniel, along with Julien, Kaila and Lisa. Your time and acceptance has allowed me to find home so far from my own.

I would like to thank Moira for her immeasurable emotional and practical support as well as her patience, especially towards the end.

Lastly, I would like to give my biggest thanks and the dedication of this work to my Mom, Dad, Megan, Linda, Richard, Granny M, Granny B and Grandpa for their endless love, support both emotionally and financially since the beginning, I love you all very much.



## **Declaration of consent**

on the basis of Article 18 of the PromR Phil.-nat. 19

Name/First Name: Moore, Gareth John

Registration Number: 17-102-674

Study program: PhD in CHemistry and Molecular Sciences

Bachelor ☐ Master ☐ Dissertation ☒

Title of the thesis: Charge Dynamics in Organic Photovoltaics:  
Effects of Morphology on Formation, Separation and  
Recombination.

Supervisor: Prof. Dr. Natalie Banerji

I declare herewith that this thesis is my own work and that I have not used any sources other than those stated. I have indicated the adoption of quotations as well as thoughts taken from other authors as such in the thesis. I am aware that the Senate pursuant to Article 36 paragraph 1 litera r of the University Act of September 5th, 1996 and Article 69 of the University Statute of June 7th, 2011 is authorized to revoke the doctoral degree awarded on the basis of this thesis.

For the purposes of evaluation and verification of compliance with the declaration of originality and the regulations governing plagiarism, I hereby grant the University of Bern the right to process my personal data and to perform the acts of use this requires, in particular, to reproduce the written thesis and to store it permanently in a database, and to use said database, or to make said database available, to enable comparison with theses submitted by others.

Place/Date

Bern, 13.12.2022

  
Signature





# Curriculum Vitae

## Gareth John Moore

---

---

### Personal Information:

Date of Birth: 22.08.1991  
Nationality: South African  
Email: garethjohnmoore01@gmail.com

---

### Education:

12/2017-02/2022	PhD Physical Chemistry and Molecular Sciences University of Bern Advisor: Prof. Dr. N. Banerji
08/2019-06/2021	CAS in Applied Data Science University of Bern
01/2016-12/2016	MSc. Physics University of Pretoria Advisors: Prof. Dr. M. Diale and Dr. A. Braun
2014-2015	BSc. Hons. Physics University of Pretoria
2011-2014	BSc. Physics University of Pretoria

---

### Publications:

R. Shivhare, G.J. Moore, A. Hofacker, S. Hutsch, Y. Zhong, M. Hambsch, T. Erdmann, A. Kiriya, S. C. B. Mannsfeld, F. Ortman, N. Banerji; 'Short excited-state lifetimes mediate charge-recombination losses in organic solar cell blends with low charge-transfer driving force' *Advanced Materials* (2021)

G. J. Moore, M. Causa', J. F. M. Hardigree, S. Karuthedath, I. R. Ramirez, A. Jungbluth, F. Laquai, M. K. Riede, and N. Banerji; 'Ultrafast Charge Dynamics in Dilute-Donor versus Highly Intermixed TAPC:C60 Organic Solar Cell Blends' *Journal of Physical Chemistry Letters* (2020)

Y. Zhong, M. Causa', Gareth J. Moore, P. Krauspe, B. Xiao, F. Günther, J. Kublitski, R. Shivhare, J. Benduhn, E. BarOr, S. Mukherjee, K. M. Yallum, J. Réhault, S. C. B. Mannsfeld, D. Neher, L. J. Richter, D. M. DeLongchamp, F. Ortman, K. Vandewal, E. Zhou & N. Banerji; 'Sub-picosecond charge-transfer at near-zero driving force in polymer:non-fullerene acceptor blends and bilayers' *Nature Communications* (2020)